Predictive Models of Tissue Outcome in Acute Human Cerebral Ischemia Using Diffusion and Perfusion Weighted MRI

by

Ona Wu

B. S. History, MIT (1992)
B. S. Electrical Science & Engineering, MIT (1994)
S. M. Electrical Engineering & Computer Science, MIT (1994)

SUBMITTED TO THE DEPARTMENT OF ELECTRICAL ENGINEERING AND COMPUTER SCIENCE IN PARTIAL FULFILLMENT OF THE REQUIREMENTS FOR THE DEGREE OF

DOCTOR OF PHILOSOPHY IN ELECTRICAL ENGINEERING
AT THE
MASSACHUSETTS INSTITUTE OF TECHNOLOGY
FEBRUARY 2002

Author .....
Department of Electrical Engineering and Computer Science
December 18, 2001

Certified by.....
Martha L. Gray
Edward Hood Taplin Professor of Medical & Electrical Engineering, Thesis Supervisor

Certified by.....
A. Gregory Sorensen
Associate Professor of Radiology, Harvard Medical School, Thesis Supervisor

Accepted by.....
Arthur C. Smith
Chairman, Departmental Committee on Graduate Students

Predictive Models of Tissue Outcome in Acute Human Cerebral Ischemia Using Diffusion and Perfusion Weighted MRI

by Ona Wu

Submitted to the Department of Electrical Engineering and Computer Science
on December 18, 2001, in Partial Fulfillment of the Requirements for the
Degree of Doctor of Philosophy in Electrical Engineering

ABSTRACT

Diffusion (DWI) and perfusion weighted (PWI) magnetic resonance imaging (MRI) provide significant insight into acute stroke and can potentially be useful for clinical decision-making. In particular, current therapeutic decisions for acute human cerebral ischemia are typically based on time of symptom onset, limiting the number of patients treated. Imaging, however, offers insight into the physiologic integrity of brain tissue that is not attainable with time of symptom onset alone. This thesis extends existing imaging techniques for acute human stroke in order to improve identification of tissue at risk of infarction, thereby assisting clinical decision-making at the stage when intervention may be most effective.

DWI and PWI have both been shown to identify infarcted tissue earlier than conventional stroke imaging. However, these techniques are limited in their existing implementations. DWI in most acute stroke settings has been restricted to isotropic imaging, measuring only mean diffusivity. In this thesis, DWI is extended to diffusion tensor imaging (DTI) with results demonstrating that DTI can detect ultrastructural changes in acute human stroke. PWI measures perfusion status by tracking the first pass of a bolus of contrast agent. In this dissertation, using numerical simulations, delay in contrast agent arrival is found to result in biased estimates of perfusion indices. A deconvolution technique using a block-circulant matrix is therefore proposed to compensate for delayed arrival, and its performance is compared to non-block circulant techniques in simulations as well as in clinically acquired human data sets. The results show that decoupling delay-associated effects reduces bias in tissue perfusion estimates.

Algorithms combining DWI and PWI information are also evaluated to determine whether they predict tissue outcome in acute stroke better than models using only subsets of these parameters. Results show that algorithms combining DWI and PWI on a voxel-by-voxel basis predict tissue that infarct with higher specificity and sensitivity than algorithms using DWI or PWI individually. These combination algorithms are then used to investigate the efficacy of a novel therapeutic agent by evaluating the performance of the model as a function of treatment dose. Findings suggest that predictive models allow evaluation of novel therapies using smaller sample sizes than traditional endpoints.

The results of this dissertation demonstrate that imaging can be used to identify tissue at risk of infarction, which may aid diagnosis and prognosis by providing clinicians unique insight into the underlying pathophysiology of stroke.

Thesis Supervisor: Martha L. Gray, Ph. D.
Title: Edward Hood Taplin Professor of
Medical & Electrical Engineering

Thesis Supervisor: A. Gregory Sorensen, M. D.
Title: Associate Professor of Radiology,
Harvard Medical School

Contents

Acknowledgments

Over five years have passed since I followed the White Rabbit down the rabbit hole and emerged in the Wonderland known as the MGH-NMR Center, and henceforth my life has never been the same. Through Mad Tea Parties, I have met characters as wondrous as any Alice has encountered, albeit with NMR Center own unique versions of Caterpillars and Cheshire Cats. I am truly appreciative of my entire experience here, which has taught me much about science and about life.

To Greg Sorensen, my mentor and thesis supervisor, I am deeply indebted to, not only for all the financial and academic support that he has provided me over these many years, but also for believing in me. I do not know how I can repay his generosity except to try to be as good as a scientist and as good as a person as he is in my own life.

To the members of my thesis committee, Martha Gray, Bruce Rosen, Robert Weisskoff and Eric Grimson, I owe many thanks for your constructive criticisms and valuable feedback and for each of your unique contributions that made this thesis possible. My gratitude goes to Martha Gray for co-supervising this thesis and shepherding this work through the MIT Electrical Engineering Department. I would also like to thank Bruce Rosen, for not only introducing me to Greg, but also for fine collaboration experiences. Robert Weisskoff has my gratitude for providing valuable guidance for my many many numerical simulations for my plethora of projects. Eric Grimson has my appreciation for his sage advice on statistical modeling and expert systems.

This work would not have been possible without the collaboration of the MGH Department of Radiology and Department of Neurology. In the Department of Radiology, I would like to especially thank Gil Gonzalez for his support over the years. In the Department of Neurology, I would like to thank the NeuroICU staff and in particular Dr. Walter Koroshetz, Dr. Lee Schwamm, Dr. Ferdy Buonanno and Dr. Seth Finklestein for their many stimulating discussions on how to push the clinical envelope with new technology. Without question, my gratitude goes to Joanie O'Donnell for never tiring of responding to my questions and e-mails.

At MIT, my gratitude is owed to my faculty advisor Roger Mark for making sure I met all the MIT requirements. I give special thanks to Marilyn Pierce and Monica Bell at the Graduate Office in the Department of Electrical Engineering and Computer Science for their unfailing support and assistance over these nine years.

There are too many people to list that I am indebted to at the MGH-NMR Center. However, I will try to name but a few. My gratitude goes to Mike Moskowitz, Ken Kwong, Lino Becerra, Lani Lee, Tim Reese, Tim Davis, Dick Bakker and Bill Copen for enlightening conversations and support over the years. I thank Dick Ziegler, Verdene Smith and Tara Ullrich for their administrative assistance. I would like to thank all of my past and present collaborators without whose help this thesis would not be possible. In particular, I am very grateful to Rick Dijkhuizen, for not only sitting with me for three hours reviewing my thesis presentation, but also for providing solid support as a fellow researcher and as a friend over these years. I am also indebted to Evelina Busa for proofreading my thesis abstract more times than I did and for keeping me focused on what really matters in life with her challenging late night discourses. I am grateful to

Thomas Benner, my co-conspirator in making sure all the computers are running, for the many informative brainstorming sessions we shared. Special thanks go to Leif Østergaard whose generosity and sage advice were of incredible assistance despite his being thousands of miles away.

I would also like to thank all my friends not already mentioned above for their support over the years. In particular, Sylvia Isler for showing me engineering's role in medicine and to Shirley Yang, for her continuous support and helpful advice over the seventeen years that we have known each other. I would also like to thank the Thursday nights' Mad Tea Party participants, Sridhar Kalluri and John Iversen, for providing support and stimulating conversations throughout graduate school.

Finally, my heartfelt thanks go to my family for giving me the freedom to pursue my dreams regardless of which paths or rabbit holes they may lead.

This study was supported in part by grants PHS R01NS38477 and P01NS35611, and a grant from Scios, Inc.

Chapter 1

Introduction

"Where shall I begin, please your Majesty?" he asked.

"Begin at the beginning," the King said, very gravely, "and go on till you come to the end: then stop."

—Lewis Carroll
(*Alice's Adventures in Wonderland*)

1.1 Time is brain

Stroke is the third leading cause of death and a leading cause of serious long-term disability in the United States with 600,000 new or recurring cases annually (1). In stroke, the cerebrovascular system is impaired due to the obstruction (ischemic stroke) or rupture (hemorrhagic stroke) of cerebral blood vessels that results in focal metabolic impairment and neurological dysfunction (2). The majority of stroke types is ischemic (77%) (3) with the remaining (23%) hemorrhagic. Previously considered a non-emergency condition due to lack of available treatment options (4), recent advances have shown that ischemic stroke patients have an improved outcome if treated early with thrombolytic or clot busting agents (5). The possibility of treatment has changed the outlook of acute stroke care from therapeutic nihilism to therapeutic optimism (4, 6). It has also changed the management of acute stroke patients such that early detection and therefore treatment of an ischemic event is critical given that the only currently FDA approved therapy, recombinant tissue plasminogen activator (rt-PA), has been shown to be effective only if administered within 3 hours of symptom onset (7). Outside of this therapeutic time window, it has been demonstrated that there is an increased risk of hemorrhage resulting in a worsened outcome (7). This critical dependence of administration of treatment within a narrow therapeutic time window has led to the coining of the phrase "Time is Brain".

Accurately assessing the exact onset time, however, is often difficult to determine, thereby limiting the number of patients eligible for treatment. Critics argue that the rt-PA therapeutic time window is too stringent and does not take into consideration individual patient variability such as presence of collateral flow, lesion location, lesion volume and other factors. (8-10). Some argue that a three-hour time window was not specific enough for identifying treatable patients since some patients may not have lysable clots although they are seen within the time frame (8). Others argue that the time window is not sensitive enough for identifying potentially treatable patients and that the window should be expanded (11). Both parties agree, however, that imaging may be the solution to both of their concerns since it would replace the concept of a "ticking clock" as a surrogate for tissue viability with a more accurate "tissue clock" (10, 12). An imaging surrogate for the ischemic penumbra, i.e. hypoperfused or oligemic but still therapeutically treatable tissue, could allow identification of patients whom although seen within the three hour time window should not be treated with thrombolysis due to the lack of presence of salvageable tissue. In another scenario where a patient is seen outside the three-hour time frame, an imaging surrogate may identify still salvageable tissue suggesting the potential benefits of treatment even though the therapeutic time window has lapsed.

More and more stroke investigators are advocating the use of imaging as an inclusion or exclusion criterion for clinical trials and also for monitoring patients' individual responses to therapy (11-16). This is a logical extension of the experimental animal stroke models experience where the majority of these pre-clinical trials has been using imaging criteria. In these studies, differences in lesion volumes between treatment groups are used to evaluate efficacy, with a positive result reported if the treatment group has smaller lesion volumes than the control placebo group. However, much work has been invested in experimental animal models to insure the reproducibility of lesion size and location in the animals. For humans, on the other hand, due to large inter-patient variability in stroke severity and location, large numbers of patients are often necessary in order to detect a statistically significant effect. Since intra-patient variability is presumably lower than the inter-patient variability, statistical power may be increased if one

measures change in lesion size from baseline (13). A logical extension would be to compare individual voxels to their baseline state. Such a method might provide even lower variability and thereby further increase the statistical power for detecting a treatment-related change.

By acutely identifying tissue at risk of infarction, salvageable tissue can then be identified. Without knowing how much tissue is at risk of infarction prior to treatment, assessing the efficacy of a therapy is complicated by physiologic variations and choices of treatment. By distinguishing tissue likely to infarct without treatment, tissue that was saved post-treatment can then be identified. This identification should be done with both high sensitivity and specificity. While current imaging technologies have hinted at some promise, the methodological framework to carry out this process remains to be developed. This is one of the goals of this thesis.

1.2 The Role of Imaging in Acute Stroke

Imaging occupies an essential but limited role in the routine care of acute ischemic stroke patients, namely for the exclusion of hemorrhage, a contraindication for rt-PA. One reason for this limited role has been due to the low sensitivity of imaging techniques in acutely detecting stroke lesions and therefore obviating their use for early diagnosis and therapy guidance. Typical imaging techniques used to evaluate the extent and severity of an infarct such as computed tomography (CT) and conventional magnetic resonance imaging (MRI) reflect anatomical changes wrought by damage due to the ischemic process. In general, however, both techniques are insufficient in the acute setting, only showing abnormalities hours after onset. Conventional imaging techniques therefore may not be optimal for the guidance of early intervention due to their lack of acute sensitivity (17, 18).

With the advent of high speed functional MRI, the underlying physiology of tissue can be better investigated. In particular, diffusion weighted imaging (DWI), a reflection of extent of cellular injury and ionic homeostasis, and perfusion weighted (PWI) magnetic resonance (MR) imaging, a measurement of hemodynamic status, have both been shown to identify infarcted tissue earlier than conventional stroke imaging with greater sensitivity and specificity (19). The lesion volumes identified by perfusion and diffusion imaging, however, often do not match. Because DWI and PWI measure different aspects of ischemia and infarction, it has been postulated that this area of mismatch may help identify the ischemic penumbra. However, lesion volume mismatches may be overly sensitive and not specific due to intralesional heterogeneity in both diffusion (20) and perfusion parameters (21). There have been several studies investigating thresholds of diffusion (12, 22) or perfusion parameters (23-25) that may distinguish the ischemic penumbra. However, in an acute clinical setting, readily identifying regions of tissue within the pertinent thresholds in multiple images may be a cumbersome process. A single image reflecting tissue that has already infarcted, tissue likely to infarct without treatment and tissue not at risk would be an ideal tool in assisting clinical decision making. The question is therefore how to optimally combine these multiple images to assess risk of infarct accurately and objectively.

1.3 Overview

The goal of this study is to extend existing imaging techniques to acutely identify tissue at risk of infarction in stroke to better identify tissue that can be saved. Identifying salvageable tissue is ill

defined without specifying which treatment is to be attempted since some tissue may respond better to one therapy than another. However, identifying tissue that will infarct without novel intervention is a tractable problem and the target of this dissertation.

This study is organized into three major components:

- Extension of diffusion weighted imaging techniques to diffusion tensor imaging in acute stroke patients.

- Extension of perfusion weighted imaging techniques to decouple "delayed flow" from reduced flow.

- Development of algorithms that combine acute diffusion and perfusion weighted images into a single map of the estimated risk of infarction on a voxel-by-voxel basis.

The first two components seek to better characterize the underlying pathophysiology in acute stroke and to identify with greater specificity tissue that is at risk of infarction. The first section examines tissue status and risk of infarction with the second section investigating perfusion status of the tissue and risk of infarction. The third section, on the other hand, seeks to identify tissue that is at risk of infarction with sensitivity and specificity by providing a single index of probability of infarction.

The organization of this thesis is therefore as follows:

Chapter 2 investigates the extension of diffusion weighted imaging to diffusion tensor imaging in acute stroke to gain insight into ultrastructural changes that may lead to greater understanding of the contrast provided by diffusion weighted imaging than can be elucidated from mean diffusivity alone. Diffusion weighted imaging has been shown to be a highly sensitive and specific indicator of tissue that is likely to infarct. (26). However with the advent of rt-PA, cases where the initial DWI abnormality has reversed and cases where the initial DWI abnormality hemorrhages have been reported (12). Figure 1.3.1 shows an example lesion that reversed on follow-up exam following intravenous thrombolysis and Figure 1.3.2 shows an example where the patient went on to hemorrhage following intra-arterial thrombolysis. To differentiate between these two conditions, a marker that is more sensitive to ultrastructure may be more useful. For example, as shown in Figure 1.3.3, an image that uses only mean diffusivity shows very little gray white matter contrast. However, an image derived from diffusion tensor imaging data clearly distinguishes gray from white matter. We hypothesize that diffusion tensor imaging can better capture any structural changes that may occur in acute stroke and therefore, by reflecting extent of tissue damage, may be useful for aiding decisions to treat or not treat.

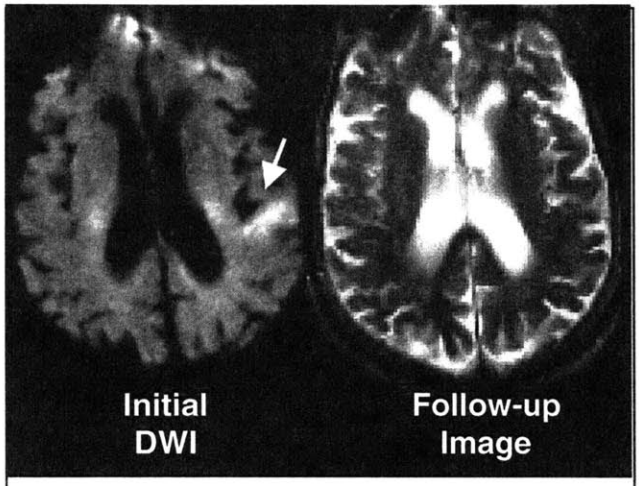

Figure 1.3.1 Example of a patient who was treated with intravenous thrombolysis and whose initial DWI lesion (arrow) reversed leaving no identifiable lesion on the follow-up imaging study.

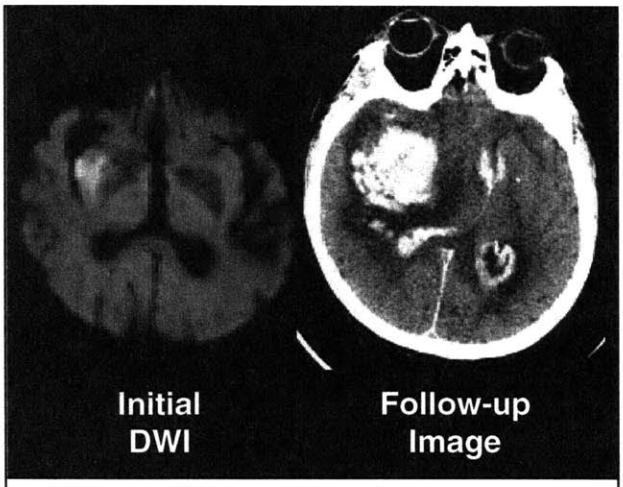

Figure 1.3.2 Example of a patient who was treated with intra-arterial thrombolysis resulting in hemorrhage (arrow) as evidenced on the follow-up CT imaging study.

In Chapter 2, a brief background in isotropic diffusion weighted imaging is first provided followed by a description of its extension to diffusion tensor imaging (DTI). The chapter is divided into DTI technical development and DTI applications in acute stroke. Results show that ultrastructural changes occur in hyperacute stroke, which are detectable with DTI. These changes are complimentary to changes in mean diffusivity and may provide insight into cellular structural integrity. For example, reductions in anisotropy were found on average in DWI lesions that infarcted whereas elevations and preserved anisotropy were observed within reversible DWI lesions.

Chapter 3 concentrates on improving existing perfusion analysis techniques. Perfusion imaging measures cerebral blood flow (CBF), cerebral blood volume (CBV) and mean transit time (MTT) using tracking of the first pass of a bolus of high magnetic susceptibility contrast agent. Perfusion indices of CBF and MTT have been shown to be very sensitive for identifying tissue at risk of infarction but not very specific (27). We speculate that this may be partly due to sensitivity of the existing perfusion analysis technique to tracer arrival delay. For example, Figure 1.3.4 shows the calculated flow maps for a patient where two very different hemispheres are identified as abnormal depending on whether one chooses the diseased hemisphere for the arterial input function (LMCA CBF) or the normal hemisphere for the arterial input function (RMCA CBF). We see that using an

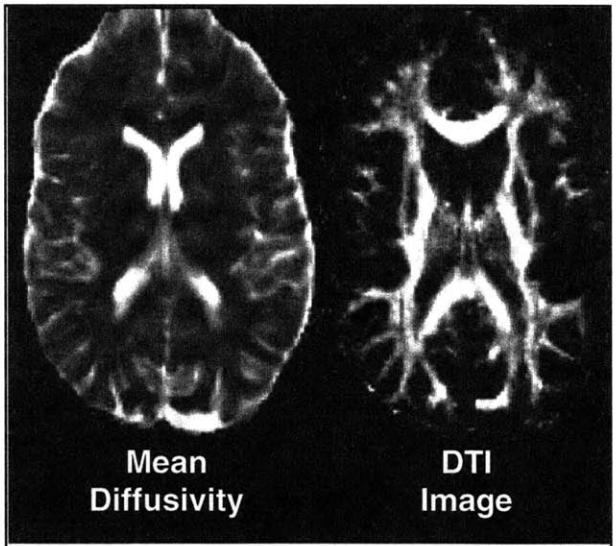

Figure 1.3.3 Structural differences between white and gray matter are more evident in the image derived from DTI than in the image of mean diffusivity from the same subject.

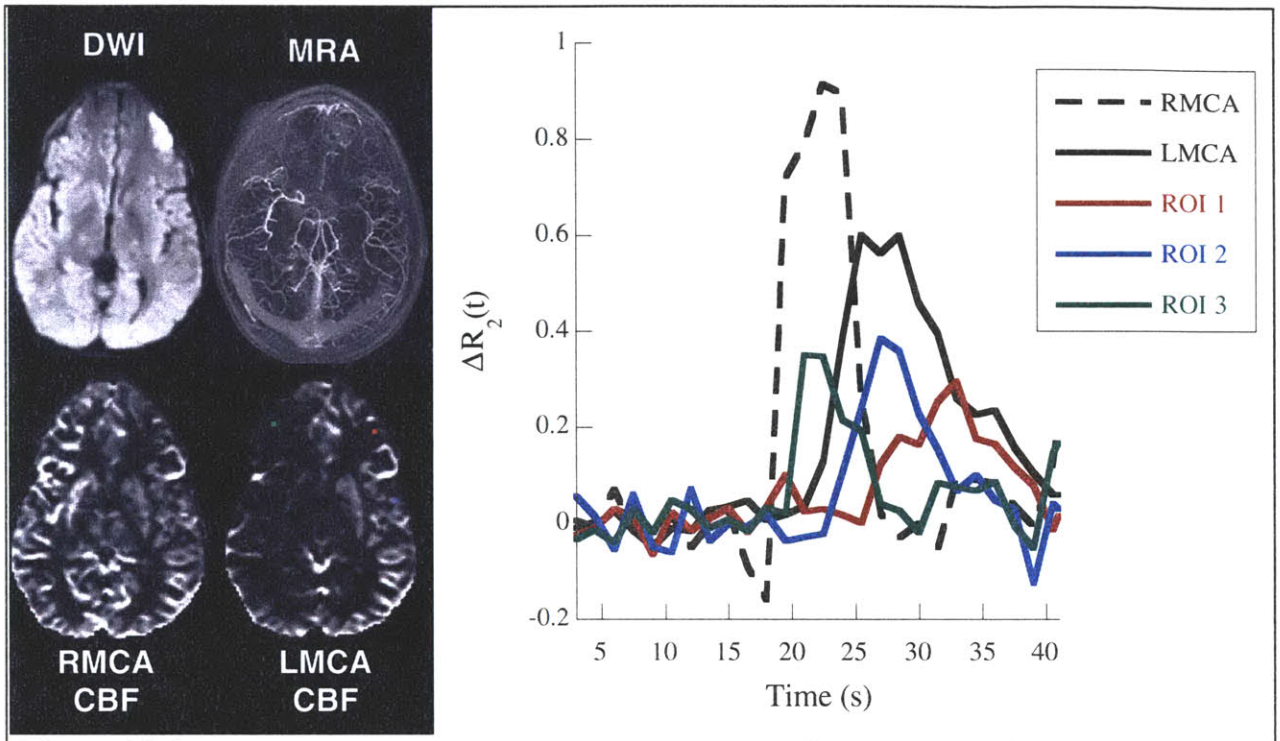

Figure 1.3.4 Example case where AIF selection results in different regions of tissue being identified as hypoperfused.
Diffusion and perfusion studies for a 12 year-old sickle cell anemia patient within 35 hours of symptom onset of left MCA stroke. Clearly evident is diminished flow in the MRA as well as an area of infarct in the left frontal lobe (DWI). CBF maps using RMCA and LMCA for the AIF produce very disparate flow estimates. The graph on the left hand side shows the signal change, $\Delta R2(t)$, for three ROIs: ipsilateral in area of DWI abnormality (ROI 1 - red), ipsilateral normal perfused territory (ROI 2 - blue) and normal contralateral (ROI 3- green).

arterial input function (AIF) from the diseased hemisphere leads to the wrong hemisphere identified as abnormal, which from clinical symptoms and images of the vasculature in the magnetic resonance angiogram (MRA) and the DWI is determined to be the left hemisphere. The signal curves measured from three different regions are observed to have different tracer arrival times that may have contributed to the differences in the estimated flow rates. Although this example is an extreme case of tracer arrival delay, because the current technique for estimating CBF and MTT use a single AIF for all voxels, tracer delay may be occurring on an individual voxel basis. We therefore investigated the contribution of tracer arrival timing in CBF estimates using both numerical simulations and simulations with acquired human data. Results show that the existing technique for calculating perfusion parameters is sensitive to delay in tracer arrival time and selection of the arterial input function. For that reason, a deconvolution technique using a block-circulant matrix is presented to compensate for delayed arrival, and it is compared to the current deconvolution technique by using numerical simulations as well as in clinically acquired human data sets. Using this new technique to analyze the data shown in Figure 1.3.4, a more robust assessment of tissue perfusion status is obtained as shown in Figure 1.3.5. Decoupling delay-associated effects on calculated CBF is shown to result in less bias in estimates of tissue perfusion status.

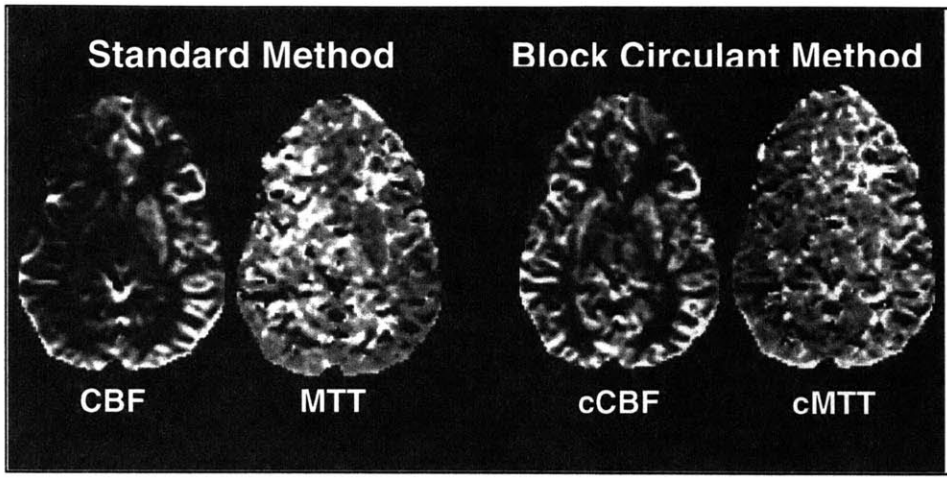

Figure 1.3.5 Results of deconvolution using a block-circulant compared to standard techniques for patient seen in Figure 1.3.4. The new technique provides an estimate of tissue perfusion status that is more consistent with clinical symptoms and follow-up exam.

Chapter 4 describes algorithms that combine DWI and PWI values where they are evaluated to determine whether they are more sensitive and specific predictors of tissue outcome than algorithms using only subsets of these values. Ideally, one would like to be able to take the initial acute imaging studies consisting of DWI and PWI and predict the infarct volume when no novel intervention occurs, an example of which is shown in Figure 1.3.6. Towards this goal, DWI and PWI images from acute human stroke patients not receiving thrombolytic or novel pharmaceutical intervention were retrospectively analyzed to create statistical models of the likelihood of infarction of an individual patient on a voxel-by-voxel basis. Maps of risk of tissue infarction in acute human cerebral ischemia using statistical techniques such as thresholding

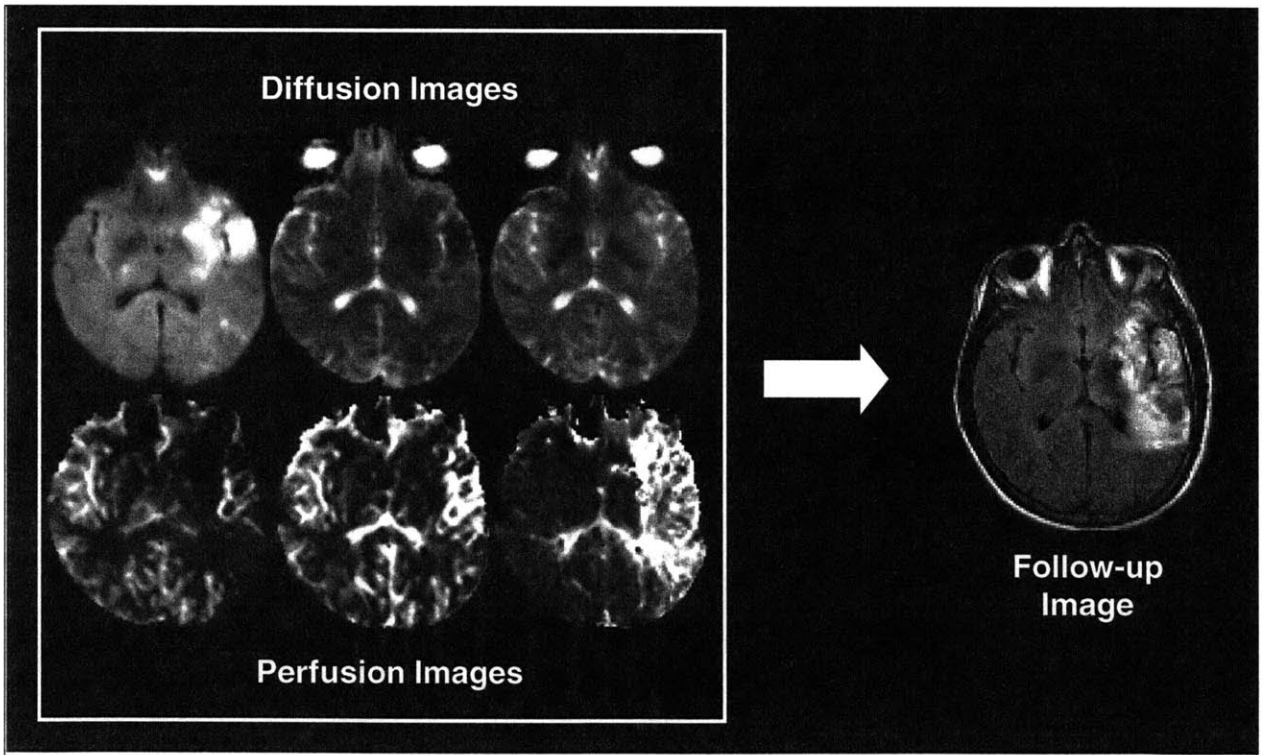

Figure 1.3.6 Ideally, one would like to be able to take as input an acute imaging data set consisting of diffusion and perfusion images and predict the infarct volume if no intervention occurs.

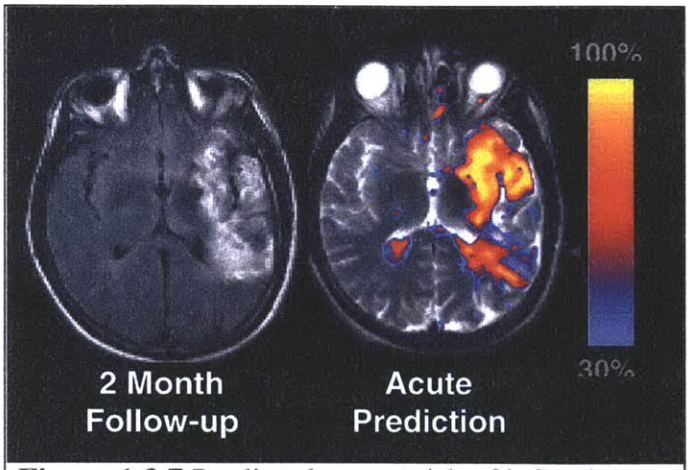

Figure 1.3.7 Predicted area at risk of infarction using acute imaging data shown in Figure 1.3.6 as input to a generalized linear model. The predicted area at risk of infarction spatially correlates well with the infarct volume seen in the follow-up exam.

models, generalized linear models, generalized additive models and hierarchical mixtures of experts are presented, an example of which is shown in Figure 1.3.7. The performances of these models are compared using receiver operator curve analysis. Results show that algorithms combining acute DWI and PWI predicted tissue at risk of infarction with higher specificity and sensitivity than algorithms using DWI or PWI individually. Furthermore, non-linear models perform more accurately than linear models.

Chapter 5 applies the combined generalized linear model algorithm described in Chapter 4 to evaluate outcomes for patients receiving a novel

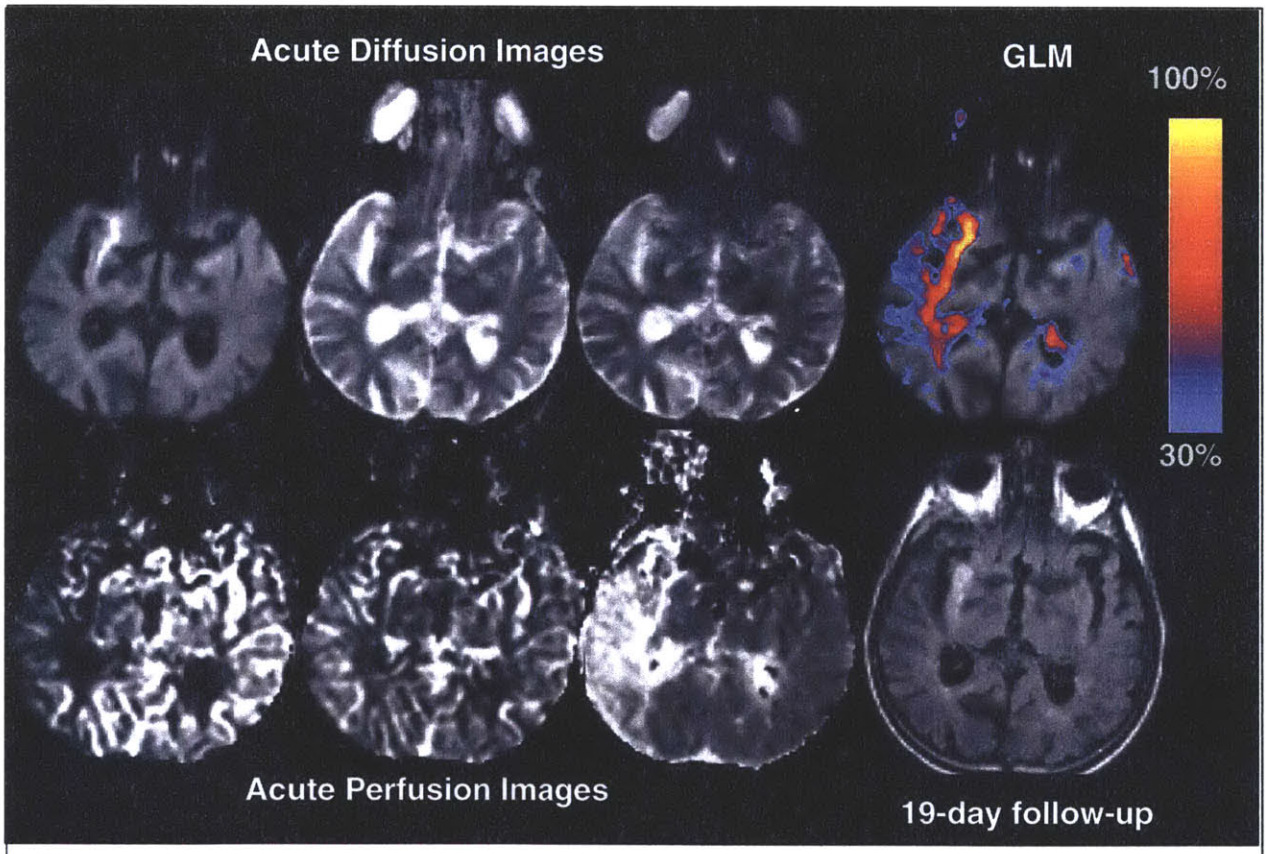

Figure 1.3.8 Baseline estimate of tissue at risk of infarction using models developed in Chapter 4 and acute imaging studies for a patient who received 150 μg/kg of bFGF. The top row shows a much larger predicted infarct volume than what was demonstrated in the follow-up study, suggesting tissue at risk of infarction did not due to the therapy.

therapeutic treatment, basic fibrinogen growth factor (bFGF). The positive-predictive-value of the model is evaluated on a voxel-by-voxel basis as a dose-dependent function of a neuroprotective agent in a small patient population. Using each voxel of tissue as its own baseline risk assessment, for example as seen in Figure 1.3.8, may reduce the number of patients required to statistically identify a biologic effect due to therapeutic intervention by reducing interpatient as well as intervoxel variability. Although additional patients are needed to demonstrate statistical significance for bFGF, findings suggest that predictive models may allow evaluation of novel therapies using smaller sample sizes than traditional clinical endpoints.

1.4 References

1. American Heart Association. *2001 Heart and Stroke Statistical Update.* Dallas, Texas:American Heart Association, 2000.

2. Ginsburg M, Bougousslavsky J. *Cerebrovascular Diseaase: Pathophysiology, Diagnosis, and Management.* Malden, MA: Blackwell Science, 1988.

3. Sacco RL, Boden-Albala B, Gan R, Chen X, Kargman DE, Shea S, Paik MC, Hauser WA. Stroke incidence among white, black, and Hispanic residents of an urban community: the Northern Manhattan Stroke Study. *Am J Epidemiol.* 1998;147:259-268.

4. Barnett HJ, Buchan AM. The imperative to develop dedicated stroke centers. *JAMA.* 2000;283:3125-3126.

5. Marler J, Jones P, Emr M. Proceedings of a National Symposium on Rapid Identification and Treatment of Acute Stroke. Bethesda, Maryland 1997;

6. Buchan AM, Feasby TE. Stroke thrombolysis: is tissue plasminogen activator a defibrillator for the brain? *Cmaj.* 2000;162:47-48.

7. National Institute of Neurological Disorders and Stroke rt-PA Stroke Study Group. Tissue plasminogen activator for acute ischemic stroke. *N Engl J Med.* 1995;333:1581-1587.

8. Caplan L, Mohr M, Kistler J, Koroshetz W. Thrombolysis - not a panacea for ischemic stroke. *N Engl J Med.* 1997;337:1309-1310.

9. Baron JC, von Kummer R, del Zoppo GJ. Treatment of acute ischemic stroke. Challenging the concept of a rigid and universal time window. *Stroke.* 1995;26:2219-2221.

10. Koroshetz WJ, Gonzalez G. Diffusion-weighted MRI: an ECG for "brain attack"? *Ann Neurol.* 1997;41:565-566.

11. Albers GW. Expanding the window for thrombolytic therapy in acute stroke. The potential role of acute MRI for patient selection. *Stroke.* 1999;30:2230-2237.

12. Kidwell CS, Saver JL, Mattiello J, Starkman S, Vinuela F, Duckwiler G, Gobin YP, Jahan R, Vespa P, Kalafut M, Alger JR. Thrombolytic reversal of acute human cerebral ischemic injury shown by diffusion/perfusion magnetic resonance imaging. *Ann Neurol.* 2000;47:462-469.

13. Stroke Therapy Academic Industry Roundtable II (STAIR-II). Recommendations for Clinical Trial Evaluation of Acute Stroke Therapies. *Stroke.* 2001;32:1598-1606.

14. Kidwell CS, Liebeskind DS, Starkman S, Saver JL. Trends in acute ischemic stroke trials through the 20th century. *Stroke.* 2001;32:1349-1359.

15. Heiss WD. Ischemic penumbra: evidence from functional imaging in man. *J Cereb Blood Flow Metab.* 2000;20:1276-1293.

16. Warach S, Pettigrew LC, Dashe JF, Pullicino P, Lefkowitz DM, Sabounjian L, Harnett K, Schwiderski U, Gammans R. Effect of citicoline on ischemic lesions as measured by diffusion-weighted magnetic resonance imaging. Citicoline 010 Investigators. *Ann Neurol.* 2000;48:713-722.

17. Sorensen AG, Rosen BR. Functional MRI of the Brain. In: Atlas Scott W., eds. *Magnetic Resonance Imaging of the Brain and Spine*,. Second Edition Philadelphia: Lippincott-Raven Publishers, 1996;

18. Fisher M, Prichard JW, Warach S. New magnetic resonance techniques for acute ischemic stroke. *JAMA.* 1995;274:908-911.

19. Baird AE, Warach S. Magnetic resonance imaging of acute stroke. *J Cereb Blood Flow Metab.* 1998;18:583-609.

20. Nagesh V, Welch KMA, Windham JP, Patel S, Levine SR, Hearshen D, Peck D, Robbins K, D'Olhaberriague L, Soltanian-Zadeh H, Boska MD. Time course of ADCw changes in ischemic stroke: Beyond the Human Eye! *Stroke.* 1998;29:1778-1782.

21. Østergaard L, Sorensen AG, Chesler DA, Weisskoff RM, Koroshetz WJ, Wu O, Gyldensted C, Rosen BR. Combined diffusion-weighted and perfusion-weighted flow heterogeneity magnetic resonance imaging in acute stroke. *Stroke.* 2000;31:1097-1103.

22. Pillekamp F, Grune M, Brinker G, Franke C, Uhlenkuken U, Hoehn M, Hossmann K. Magnetic resonance prediction of outcome after thrombolytic treatment. *Magn Reson Imaging.* 2001;19:143-152.

23. Schlaug G, Benfield A, Baird AE, Siewert B, Lovblad KO, Parker RA, Edelman RR, Warach S. The ischemic penumbra: operationally defined by diffusion and perfusion MRI. *Neurology.* 1999;53:1528-1537.

24. Neumann-Haefelin T, Wittsack HJ, Wenserski F, Siebler M, Seitz RJ, Modder U, Freund HJ. Diffusion- and perfusion-weighted MRI. The DWI/PWI mismatch region in acute stroke. *Stroke*. 1999;30:1591-1597.

25. Parsons MW, Yang Q, Barber PA, Darby DG, Desmond PM, Gerraty RP, Tress BM, Davis SM. Perfusion magnetic resonance imaging maps in hyperacute stroke : relative cerebral blood flow most accurately identifies tissue destined to infarct. *Stroke*. 2001;32:1581-1587.

26. Gonzalez RG, Schaefer PW, Buonanno FS, Schwamm LH, Budzik RF, Rordorf G, Wang B, Sorensen AG, Koroshetz WJ. Diffusion-weighted MR imaging: diagnostic accuracy in patients imaged within 6 hours of stroke symptom onset. *Radiology*. 1999;210:155-162.

27. Sorensen AG, Copen WA, Ostergaard L, Buonanno FS, Gonzalez RG, Rordorf G, Rosen BR, Schwamm LH, Weisskoff RM, Koroshetz WJ. Hyperacute stroke: simultaneous measurement of relative cerebral blood volume, relative cerebral blood flow, and mean tissue transit time. *Radiology*. 1999;210:519-527.

Chapter 2

Diffusion-Weighted Imaging

Never imagine yourself not to be otherwise than what it might appear to others that what you were or might have been was not otherwise than what you had been would have appeared to them to be otherwise.

—Lewis Carroll
(*Alice's Adventures in Wonderland*)

Diffusion weighted imaging (DWI) has been shown by several studies to be a highly sensitive and specific identifier of lesion and clinical outcome for patients with acute cerebral ischemia (1-3). However, the precise pathophysiological mechanisms underlying the evolution of the diffusion signal and its associated apparent diffusion coefficient (ADC) is not fully understood. Studies have hypothesized that the initial decline of ADC is related to the shift of water from extracellular space (ECS) to intracellular space (ICS) due to cytotoxic edema with the subsequent pseudonormalization and elevation of ADC to be due to vasogenic edema and cell lysis. However, this may be an oversimplification of a complex and heterogeneous process. For example, in cases where patients received thrombolytic therapy, DWI lesions either completely reversed, stayed abnormal or reversed temporarily only to suffer secondary ADC reduction in subsequent imaging studies (4). These findings suggest that ADC alone may not be a suitable marker of irreversibly damaged tissue and that there may be better markers that are more sensitive to ultrastructural changes.

The direction-dependence or anisotropy of the diffusion process in tissue has been demonstrated in both *ex vivo* measurements (5-8) and *in vivo* animal (9-11) and human studies (12-16). The diffusion process in three-dimensional space can be characterized by a tensor to take into consideration its direction-dependence. Diffusion tensor imaging therefore provides a means for examining microscopic water diffusion in 3D space as well as a technique for extracting ultrastructural information in both normal and pathologic tissue (14, 15, 17-20). By extending diffusion weighted imaging in acute stroke to diffusion tensor imaging, additional understanding into ultrastructural changes and ultimately salvageability may be attained than can be gleaned from mean diffusivity alone.

This chapter is divided into two sections. In the first section, **Technical Development**, diffusion tensor imaging acquisition and analysis techniques are described. Techniques for solving for the elements of the diffusion tensor are presented. In order to simplify visualizing and to provide a numerical index to reflect changes in the shape of the tensor during ischemia, scalar metrics of anisotropy are evaluated rather than vector metrics. Because calculation of diffusion tensor values is complicated by the presence of noise, Monte Carlo simulations are used to validate and compare anisotropy metrics. Additionally, the stability and reproducibility of the metrics are assessed using data from normal human subjects. The second section, **Applications**, describes the application of diffusion tensor imaging to a clinical setting. The first study, *Acute Human Cerebral Ischemia: Detection of Changes in Water Diffusion Anisotropy*, diffusion tensor images from patients presenting with acute cerebral ischemia are retrospectively analyzed to investigate acute changes in the shape and magnitude of the diffusion tensor in stroke. The second study, *Anisotropy Changes in Reversible DWI Lesions*, examines changes in the diffusion tensor in cases of reversible DWI lesions in order to gain insight into ultrastructural viability.

2.1 Technical Development

2.1.1 Diffusion Tensor Imaging

Diffusion is the process by which particles from a region of high concentration are transported to a region of low concentration. According to Fick's first law of diffusion, the flux of particles is proportional to the gradient of the concentration, that is:

$$\Phi = -D\nabla c \qquad \textbf{(2.1.1.1)}$$

where D, the diffusion coefficient, is the proportionality constant and c is the concentration of the particles as a function of space and time. The diffusion coefficient is typically a function of the physical characteristics of the solute as well as the solvent in which it is diffusing. The rate at which the concentration changes follows Fick's second law:

$$\frac{\partial c}{\partial t} = -D\nabla^2 c. \qquad \textbf{(2.1.1.2)}$$

The mechanism by which the particles diffuse has been shown to be the result of random translational motion of molecules due to their thermal energy (21). Thus, even in a one-phase system, the molecules are moving at a rate that can be characterized by its self-diffusion coefficient. The self-diffusion of water molecules causes the transverse magnetization in a nuclear magnetic resonance (NMR) experiment to be dephased which results in the reduction of the measured signal. In a standard spin-echo (SE) sequence, the effects due to diffusion are minimized by keeping the imaging gradients small. However, by applying a large gradient over a long duration, the diffusion effects become significant. In 1965, Stejskal and Tanner developed a NMR technique to measure the self-diffusion coefficient of water by adding pulsed field gradients to a SE sequence (22). An example of such a sequence is shown in Figure 2.1.1.1. In this experiment, the measured signal, S is:

$$\ln\frac{S}{S_0} = -D\,\gamma^2\,G^2\,\delta^2\left(\Delta - \frac{\delta}{3}\right) \qquad \textbf{(2.1.1.3)}$$

where S_0 is the non-diffusion weighted signal, D is the diffusion coefficient, γ is the gyromagnetic ratio for hydrogen (42.6 MHz/Tesla), G is the amplitude of the diffusion gradient, δ is the duration of the diffusion gradient and Δ is the intertemporal pulse offset. The $\gamma^2\,G^2\,\delta^2\,(\Delta - \delta/3)$ factor is termed the diffusion sequence's b-value, a measure of the amount of diffusion weighting applied (23).

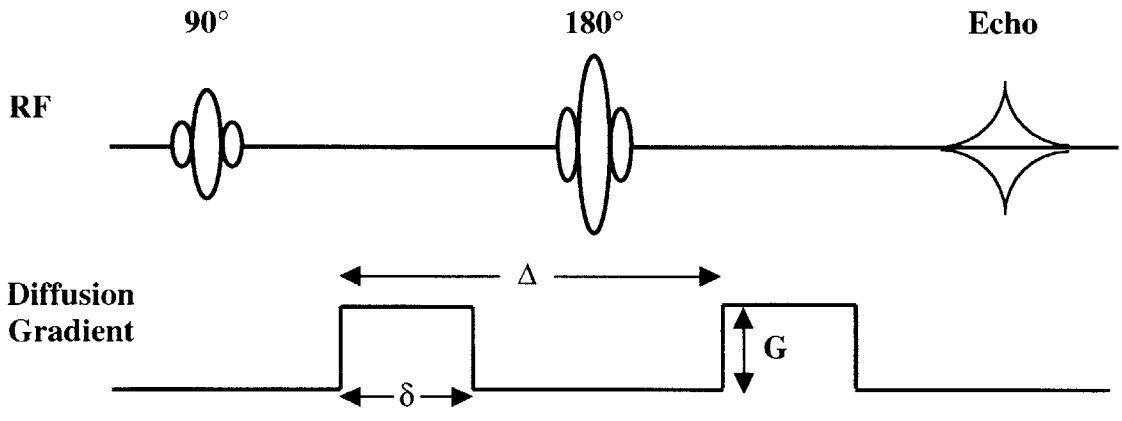

Figure 2.1.1.1 Pulsed field gradient spin-echo NMR sequence.

Equation 2.1.1.3 is used to characterize diffusion measured in a single direction. The diffusion process in three-dimensional space can be characterized by a tensor to take into consideration its direction-dependence. This tensor has six degrees of freedom and thus can be represented by **D**, a 3×3 symmetric matrix[1]:

$$\mathbf{D} = \begin{bmatrix} D_{xx} & D_{xy} & D_{xz} \\ D_{yx} & D_{yy} & D_{yz} \\ D_{zx} & D_{zy} & D_{zz} \end{bmatrix}$$

where $D_{xy}=D_{yx}$, $D_{xz}=D_{zx}$, and $D_{yz}=D_{zy}$, assuming rate of diffusion is symmetrical along the same axis. In isotropic media, **D** reduces to an identity matrix scaled by a constant, D, because the rate of diffusion is independent of direction, meaning that the probability that a particle moves to another point follows the behavior of a spherically symmetric Gaussian function (21). However, in the case of restricted diffusion, the diffusing particles encounter barriers that are direction dependent. The probability that a particle moves to another point then becomes a function of the geometry of the diffusion barriers (5) and results in diffusion coefficients that are anisotropic or direction dependent. In order to accurately characterize the underlying diffusion process, the full-diffusion tensor should therefore be sampled as opposed to measured in only one, two or three orthogonal directions. Sampling in only one-direction measures the rate of diffusion only in the sampled direction. Using only two directions for characterizing anisotropy, e.g. $D_{||}/D_{\perp}$, results in an underestimation of anisotropy (18). Sampling in only three directions results in measurements dependent on the imaging frame. Only in isotropic media can one safely assume that the off-diagonal terms are zero. In anisotropic media, the off-diagonal terms are comparable to the diagonal terms (24) and therefore need to be sampled using full diffusion tensor imaging.

The diffusion tensor is sampled on a voxel-by-voxel basis by generalizing the original Stejskal-Tanner sequence (Eqn. 2.1.1.3) to include the condition of anisotropic, restricted diffusion (25, 26) when applying a diffusion gradient in direction **r**:

$$\ln \frac{S(\mathbf{r})}{S_o} = -\gamma^2 \int_0^{TE} \left(\mathbf{F}(t) - 2\zeta(t)\,\mathbf{f}\right) \cdot \mathbf{D} \cdot \left(\mathbf{F}(t) - 2\zeta(t)\,\mathbf{f}\right) dt \qquad \textbf{(2.1.1.4)}$$

with

$$\zeta(t) = \begin{cases} 0 & 0 < t < \tau \\ 1 & t > \tau \end{cases} \qquad \textbf{(2.1.1.5)}$$

$$\mathbf{F}(t) = \int_o^t \mathbf{G}(x)\, dx$$

where TE is the echo time, τ=1/2 TE or refocus time, **f**=**F**(τ), **G**(t) is the applied diffusion gradient sequence, such as the one shown in Figure 2.1.1.2 with **r**=(1,-1,0) G/cm, and **D** is the

[1] Vector and tensor quantities are denoted in boldface.

diffusion tensor to be determined. Piecewise linear analysis of Equation 2.1.1.4 produces an analytical expression that can be used to solve for the elements of the diffusion tensor. Assuming **G**(t) is the sequence shown in Figure 2.1.1.2, and letting:

$\mathbf{G}_d(\mathbf{r})$ = Diffusion gradients on from T_2 to T_3 and T_7 to T_8
g_1 = Gradients on from 0 to T_0
g_2 = Gradients on from T_1 to T_2
g_3 = Gradients on from T_4 to T_5 and from T_5 to T_6

$$d = \mathbf{G}_d \cdot \mathbf{D} \cdot \mathbf{G}_d$$

$$\Delta = T_7 - T_2 \qquad \alpha_i = g_i \cdot \mathbf{D} \cdot g_i$$

$$\delta = T_3 - T_2 = T_8 - T_7 \qquad \beta_i = 2\, g_i \cdot \mathbf{D} \cdot g_i$$

$$\zeta = T_5 - T_4 = T_6 - T_5 \qquad \gamma_{ij} = 2\, g_i \cdot \mathbf{D} \cdot g_j$$

$$\varepsilon = T_1 - T_0 \qquad \text{where i, j} = 1, 2, 3$$

and substituting into Equation 2.1.1.4 and 2.1.1.5, the following analytical expression can be obtained:

$$\ln \frac{S(\mathbf{r})}{S_0} = -\gamma^2 \left\{ \begin{array}{l} d\,\delta^2\left(\Delta - \frac{1}{3}\delta\right) + \beta_1\, T_0\, \delta\, \Delta + \beta_2\, \varepsilon\, \delta\, \Delta + \beta_3\, \delta\, \zeta^2 \\ +\alpha_1\, T_0^2\left[(t - T_1) + (T_1 - T_0) + \frac{1}{3}T_0\right] \\ +\alpha_2\,(T_1 - T_0)^2\left[(t - T_1) + \frac{1}{3}(T_1 - T_0)\right] \\ +\frac{2}{3}\alpha_3\,\zeta^3 \\ +\gamma_{12}\, T_0\, \varepsilon\left[(t - T_1) + \frac{1}{2}\varepsilon\right] \\ +\gamma_{13}\, T_0\, \zeta^3 + \gamma_{23}\, \varepsilon\, \zeta^2 \end{array} \right\} \qquad \textbf{(2.1.1.6)}$$

Equation 2.1.1.6 reduces to Equation 2.1.1.3 if imaging gradients are assumed to have no effect on the measured signal, by setting the imaging gradients' amplitudes and durations to zero. It should also be noted that the largest contributions are due to interactions between the imaging gradients and the diffusion gradients (β_i) as opposed to interactions between the imaging gradients (α_i and γ_{ij}) due to the magnitude and duration of G_D compared to g_i.

By rearranging terms, Equation 2.1.1.6 can be expressed more compactly as:

$$\ln \frac{S(\mathbf{r})}{S_0} = -\mathbf{B}\,\mathbf{V} \qquad \textbf{(2.1.1.7)}$$

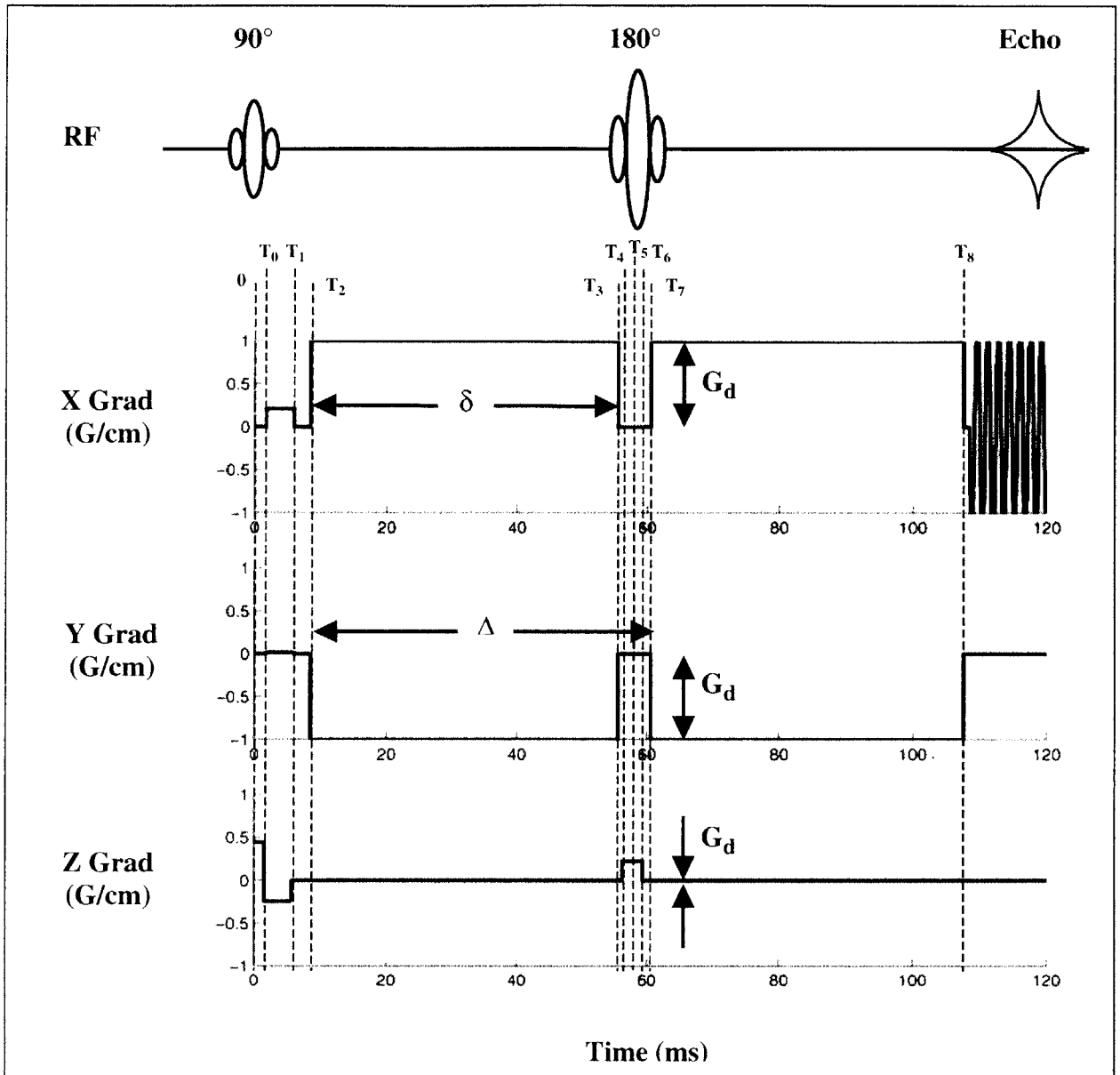

Figure 2.1.1.2 Pulsed field gradient spin-echo NMR sequence extended to three-dimensional space using echo planar imaging. This diffusion sequence applies a diffusion gradient in the direction **r(x,y,z)** = (1, -1, 0) with an amplitude of 1 G/cm.

where **V** is a vector of the six-elements of the symmetric diffusion tensor and **B** is a matrix of weighting coefficients that is not only a function of the imaging gradients, but is also a function of the direction and magnitude of the applied diffusion gradient sequence **r**. Each row of the **B** matrix is due to a different applied diffusion gradient **r**. Therefore, by applying six non-collinear diffusion gradients, we can solve for the six elements of the diffusion tensor, **V**, for an individual voxel by:

$$\mathbf{V} = - \mathbf{B}^{-1} \ln\left(\frac{S(\mathbf{r})}{S_0}\right). \qquad \textbf{(2.1.1.8)}$$

As long as the imaging gradient sequence is not modified, $\mathbf{B^{-1}}$ can be calculated *a priori* given the timing parameters of the diffusion sequence and does not need to be recalculated for each newly acquired dataset following the same protocol. A unique solution for **D** can be obtained provided $\mathbf{r}_i$, i = 1, . . ., 6, are linearly independent and S_0 is known.

Once the diffusion tensor (**D**) coefficients are calculated, the diffusion tensor's eigenvalues, λ_i, and eigenvectors, $\mathbf{v}_i$, can be derived using eigenanalysis. The eigenvectors of the symmetric diffusion tensor, a set of orthonormal vectors, define the orientation of the principal axes of the diffusion tensor ellipsoid in space. Their corresponding eigenvalues represent the lengths of the axes. These quantities define the size and shape of the ellipsoids of **D** and are independent of a voxel's orientation in its frame of measurement.

To demonstrate the feasibility of measuring the diffusion tensor in humans, datasets acquired from a normal human volunteer as well as an acute stroke patient are presented.

Materials and Methods

To reduce artifacts due to patient movement (12), echo planar imaging (EPI) was used in this study to allow the acquisition of the full diffusion tensor for multiple slices of the head in a short time period (15). However, EPI introduces additional artifacts in the form of eddy current distortion (27, 28). These eddy currents are scanner dependent and are generated on the surfaces of the scanner equipment due to high switching fields from the large amplitude diffusion gradients (29). Residual eddy currents lead to a translation in the slice select direction, shearing in the read direction and scaling in the phase encode direction which are dependent on the inhomogeneities in individual MR scanners (27, 28). Warping due to eddy currents was compensated for by an affine transformation of the warped high b-value images using an automated image registration software package, AIR 3.08 (UCLA, CA) (30, 31). Eddy currents may also contribute additional diffusion weighting, however, for the high b-values used in this study they were not considered significant.

The full diffusion tensor was sampled using a T2-weighted one-shot echo-planar imaging (EPI) technique (32) repeated seven times, the minimum required for solving for the diffusion coefficients that characterizes the diffusion tensor (26, 33-35). Diffusion gradients were applied in turn at $\mathbf{r}_o$ = (x,y,z) = (0.05, 0.05, 0.0) and the six $\mathbf{r}_i$ = {(1,1,0), (1,-1,0), (0,1,1), (0,-1,1), (1,0,1), (-1,0,1)}, which corresponded to the centers of the non-opposed edges of a cube.

Due to the retrospective nature of this study, which spanned over the years 1996-2001, imaging was performed on a variety of platforms. Imaging was performed on a 1.5T MR instrument with 5.4.2 software (Signa; GE Medical Systems, Milwaukee, Wis.) and EPI capabilities by means of a hardware upgrade (ANMR, Wilmington, MA), including "catch and hold" modification. T2-weighted single-shot pulsed field gradient spin-echo sequences consisted of diffusion encoding pulses of amplitudes 1 G/cm, durations δ = 47 ms, with an interpulse temporal offset Δ = 52 ms, placed symmetrically about the 180° radio-frequency pulse resulting in a b-value=1221 sec/mm^2. With catch-and-hold enabled, the echo time (TE) was 118 ms. A repetition time (TR) of 6,000

ms was used and up to 20 axial sections were obtained with a 6-mm section thickness and a 1-mm spacing between sections. A fixed field of view (FOV) of 40×20 cm^2 and an acquisition matrix of 256×128 pixels was used resulting in an in-plane resolution of 1.56×1.56 cm^2. Total acquisition time for a single complete tensor was 42 seconds for imaging the whole head. To increase the signal-to-noise ratio (SNR) multiple tensor samples was acquired and averaged. After averaging, the SNR in this study was estimated from non-diffusion-weighted images by calculating the ratio of the mean signal intensity of a 5×5 region of interest (ROI) in the thalamus to the standard deviation (SD) of the noise measured in artifact free background areas outside the head. At this institution, a typical clinical study consisted of three averages resulting in an estimated SNR of 20 and a total acquisition time of 2 minutes and 6 seconds.

The more recent imaging studies were performed on a 1.5T GE Signa Horizon LX BRM and CRM systems (GE Medical Systems, Milwaukee, Wis.) with echo planar imaging capabilities. On the LX system, TR=7500 ms and FOV=22×22 cm^2 or 20×20 cm^2 and acquisition matrix size128×128 pixels and up to 23 slices with slice thickness of 5–6 mm and interslice gap of 1mm. Some systems were BRM systems with TE=99 ms, δ = 32.5 ms, Δ=38.4 ms with gradient amplitudes of 1.6 G/cm in each direction resulting in b-value=1000 sec/mm^2. For CRM systems, TE=73 ms, δ = 21.1 ms, Δ=27.2 ms with gradient amplitudes of 2.8 G/cm in each direction resulting in b-value=1000 sec/mm^2. For both systems, typical clinical studies consisted of three averages resulting in a total acquisition time of 2 minutes and 38 seconds. Data acquired from the BRM systems typically have an SNR of 35 while data from the CRM systems have an SNR of approximately 40.

A normal 34-year-old male underwent diffusion imaging on the 1.5T MR ANMR system using the previously described protocol after providing informed consent. An estimated SNR of 65 was obtained by averaging 30 full diffusion tensor samples for one axial section, with a total acquisition time of 21 minutes. For comparison, diffusion tensor data from a 48-year-old female stroke patient imaged on the 1.5T ANMR system within 2 hours of onset of aphasia and right hemiplegia is also presented. Diffusion data is also shown for a 66-year old male stroke patient whom was imaged on a 1.5T GE BRM system.

In addition to the raw diffusion data, images that were used for clinical diagnosis, the mean diffusivity and associated isotropic DWI, were also calculated. The isotropic DWI was the geometric mean of the six diffusion-weighted images. Using this isotropic DWI and the low b-value image, a monoexponential fit can be calculated where the rate of decay is the "apparent diffusion coefficient" (ADC). To demonstrate the effect of eddy current distortion on diffusion tensor calculation, fractional anisotropy maps were also calculated (19). Fractional anisotropy will be discussed in more detail in Section 2.1.2.

The diffusion tensor, **D**, was calculated on a voxel-by-voxel basis using Eqn. 2.1.1.8. In the calculation, the effects of the imaging gradients were corrected by using techniques described above which were similar to those described in other reports (26, 34, 35). The eigenvalues and eigenvectors of **D** were calculated on an individual voxel basis. Images of the eigenvalues were generated as grayscale scalar images where the intensity reflects the magnitude of the eigenvalue. Since the eigenvectors were a three-dimensional quantity, for visualization, their directions were color-coded with their normalized <x,y,z> components in the image coordinates mapped to red, green and blue intensity values respectively (36). To mask out isotropic structures

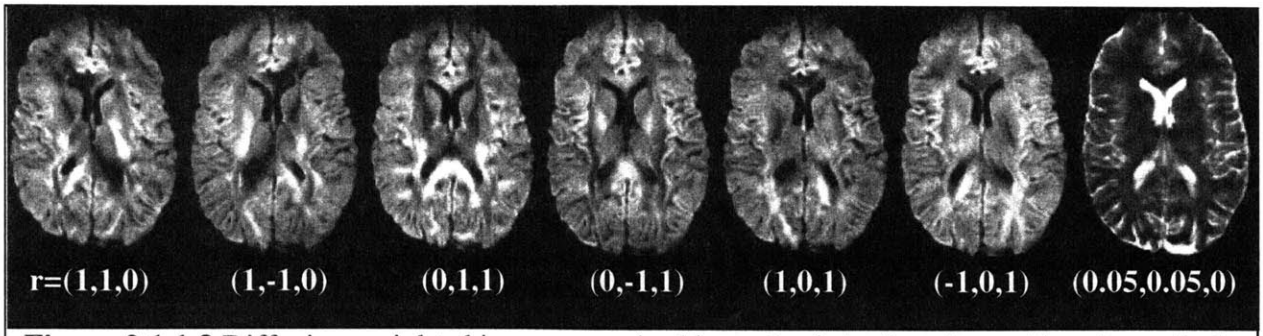

Figure 2.1.1.3 Diffusion weighted images acquired in each of six directions. Also shown is the low b-value image that is used as the EPI T2 image. Clearly seen is the dependence of the diffusion signal on the direction of the applied diffusion gradient.

where fiber orientation is meaningless (37), the images were scaled according to their level of fractional anisotropy (19).

Results

Figure 2.1.1.3 shows the diffusion weighted images acquired in each of the six directions along with the EPI T2 image for the normal volunteer. Clearly seen is the dependence of the diffusion signal on the direction of the applied diffusion gradient. Greater restriction, as evident by regions of hyperintensity, is seen in areas corresponding to fiber tracts. Figure 2.1.1.4 shows the distortions from eddy current effects. The first high b-value image was subtracted from the other five high b-value image. The "halos" around the edges of the cortex are due to the mismatch between diffusion images resulting from eddy current distortions. Figure 2.1.1.5 shows the same images after correcting for eddy current distortions. The halos around the edges are less noticeable. Figure 2.1.1.6 shows the effects eddy current distortions have on the isotropic DWI. The isotropic DWI image without correction appears blurry especially in the areas corresponding to the "halo" regions in Figure 2.1.1.4. After correcting for eddy current distortions, one sees that the gyri appear much sharper than in the uncorrected image (arrowheads). Figure 2.1.1.7 shows the effects of eddy current distortions on fractional anisotropy calculations. Due to the mismatch in the tensor images, tissue regions appear artificially anisotropic (arrowheads). After correction, the fractional anisotropy image appears sharper, with greater contrast between gray and white matter.

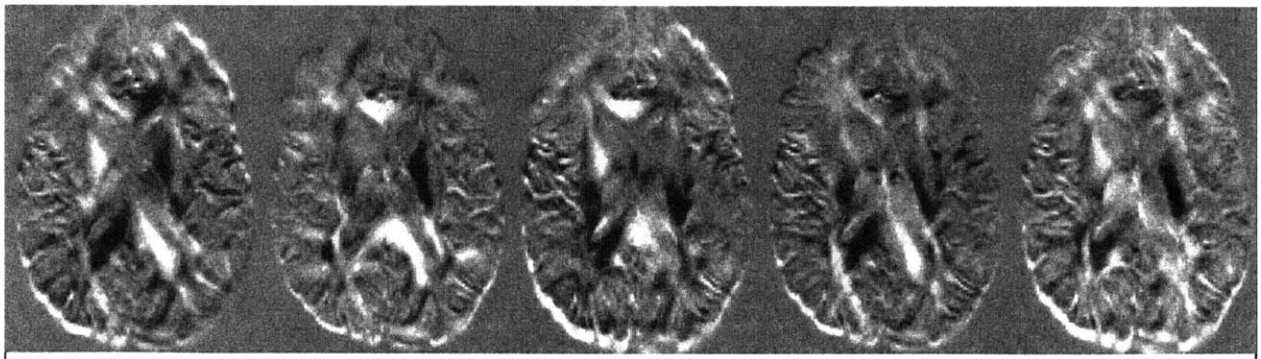

Figure 2.1.1.4 Eddy current distortions are clearly visible when subtracting the first high b-value image from the other five as evidenced by the "halos" around the edges

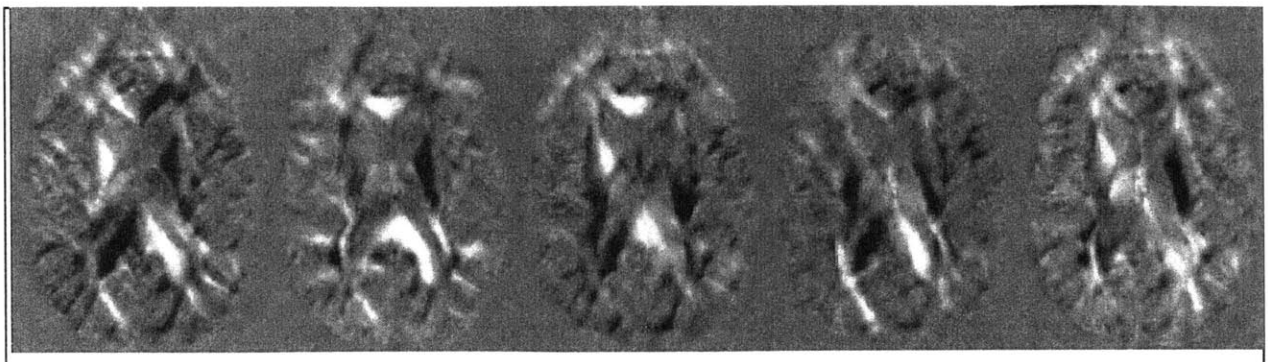

Figure 2.1.1.5 Results of eddy current compensation. The halos around the edges are less noticeable than in Figure 2.1.1.4.

A potential clinical impact of not correcting for eddy current distortions is shown in Figure 2.1.1.8. This figure shows the DWI image created with and without eddy current corrections for a 66-year-old male patient imaged within 3 hours of presenting with symptoms of left-sided weakness. The effects of eddy current distortions on a stroke patient may blur small lesions reducing the conspicuity of the abnormal area. With eddy current corrections, the areas of abnormalities in this patient are much better delineated (arrowheads). The gyri are again noted to be sharper in the corrected DWI than in the uncorrected DWI (arrows).

To demonstrate the effects anisotropy has on clinical decision making, Figure 2.1.1.9 shows the eddy-current corrected diffusion weighted images acquired at the same gradient directions used

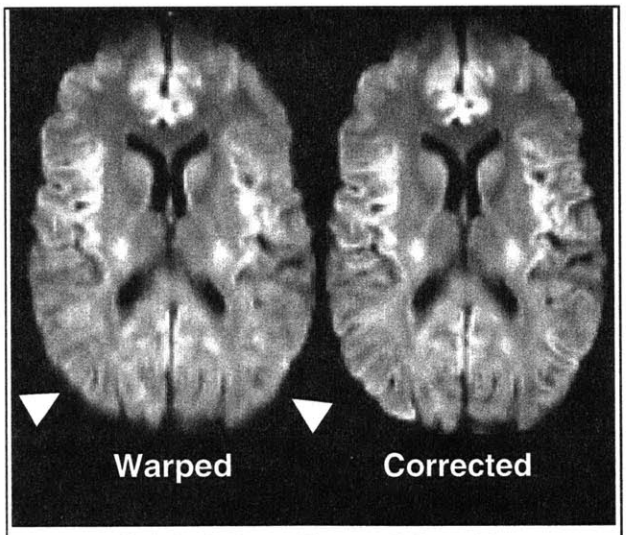

Figure 2.1.1.6 The effects of the eddy current distortions result in blurring of the isotropic DWI generated from the data shown in Figure 2.1.1.3. With compensation for eddy current distortions, one sees that the gyri in the cortex appears sharper compared to the DWI calculated without correction. This may be especially important for detecting small lesions.

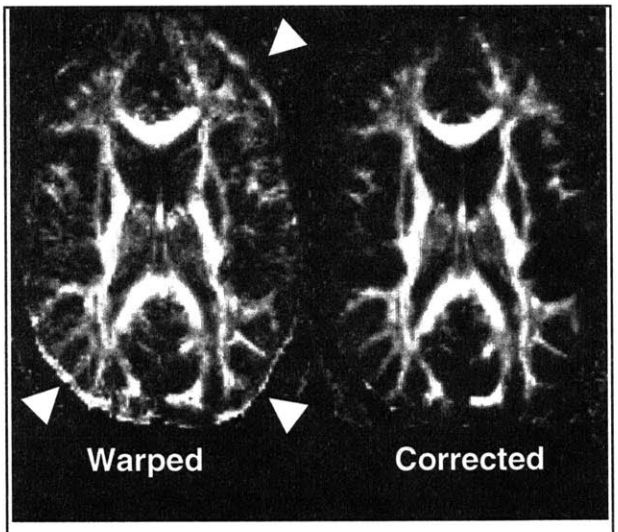

Figure 2.1.1.7 The effects of the eddy current distortions result in inaccurate anisotropy maps, especially noticeable around the edges (arrowheads). Tissue has artificially elevated anisotropy in areas where the DWI do not match. With compensation, the anisotropy image appears sharper with greater contrast between white and gray matter.

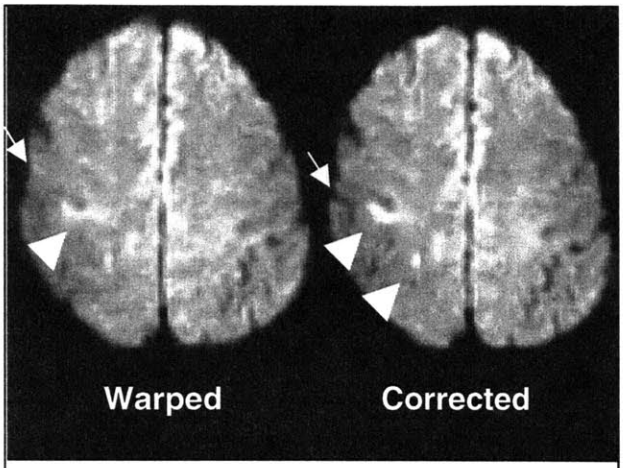

Figure 2.1.1.8 The effects of eddy current distortions on a stroke patient may blur small lesions reducing the conspicuity of the abnormal area. With eddy current corrections the area of abnormalities in this patient are much bet! ·r delineated (arrowheads) The gyri are again noted to be sharper in the corrected DWI than in the uncorrected DWI (arrows).

in Figure 2.1.1.3 but for an acute stroke patient seen within 2 hours of symptom onset and using only 3 averages. Again we see hyperintensities corresponding to greater restriction in white matter tracts. However, an area of hyperintensity is seen in the left[2] lentiform nucleus (arrowhead) in each of the diffusion weighted images that is not seen for the normal volunteer (Figure 2.1.1.3). One can deduce from the asymmetry that this region of increased restriction is likely due to a pathophysiological cause but identifying this abnormality using a single diffusion weighted image is complicated by anisotropy occurring in the normal brain. Imaging in only one direction therefore would have been inadequate for this patient.

Figure 2.1.1.10 shows the isotropic DWI and ADC maps calculated from Figure 2.1.1.9 as well as the seven-day follow-up T2 weighted MR study. From the isotropic DWI, the lesion is clearly delineated as a hyperintense region. In the ADC, this translates into a region of hypointensity reflecting the reduction in the diffusivity. The area of reduced ADC becomes infarcted as evidenced by the corresponding hyperintensity in the 7-day follow-up T2 MR. From Figure 2.1.1.9, we note that this reduction is independent of the direction of the applied diffusion gradient. For comparison, the isotropic DWI for the normal volunteer (Figure 2.1.1.6) does not show an abnormality on either DWI map.

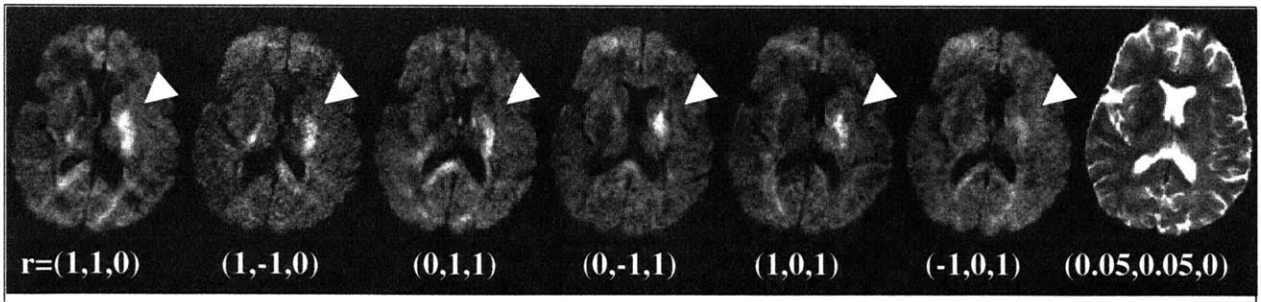

Figure 2.1.1.9 Diffusion weighted images acquired in each of the six directions for an acute stroke patient. The anisotropy of the white matter tracts causes restricted diffusion that can be confused for reduced diffusion due to acute stroke.

[2] According to radiologic convention, the right half of the image corresponds anatomically to the left half of the brain and vice-versa.

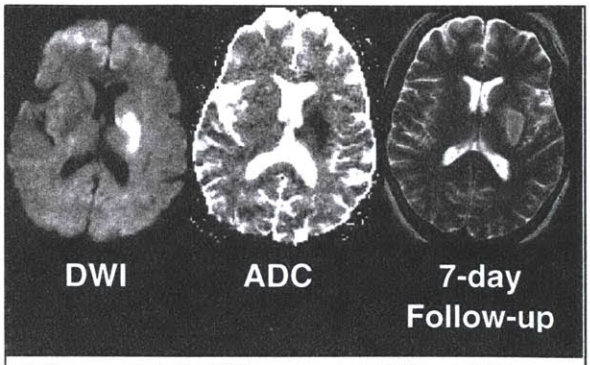

Figure 2.1.1.10 Isotropic DWI, ADC and 7-day follow-up T2 image for the patient shown in Figure 2.1.1.9. The area of hyperintensity on the DWI and hypointensity on the ADC corresponds well to the area of infarct as seen on the 7-day follow-up study.

Figure 2.1.1.11 shows the calculated elements of the diffusion tensor, D_{xx}, D_{yy}, D_{zz}, D_{xy}, D_{xz}, and D_{yz} for the acquired images shown in Figure 2.1.1.3. The images representing each of the diffusion tensor elements are placed in accordance to their corresponding location in the diffusion tensor:

$$\mathbf{D} = \begin{bmatrix} D_{xx} & D_{xy} & D_{xz} \\ D_{yx} & D_{yy} & D_{yz} \\ D_{zx} & D_{zy} & D_{zz} \end{bmatrix}$$

From this image, it is evident that off-diagonal terms are not zero and may be quite high in areas corresponding to white matter fiber tracts, thereby justifying the necessity of full-tensor sampling.

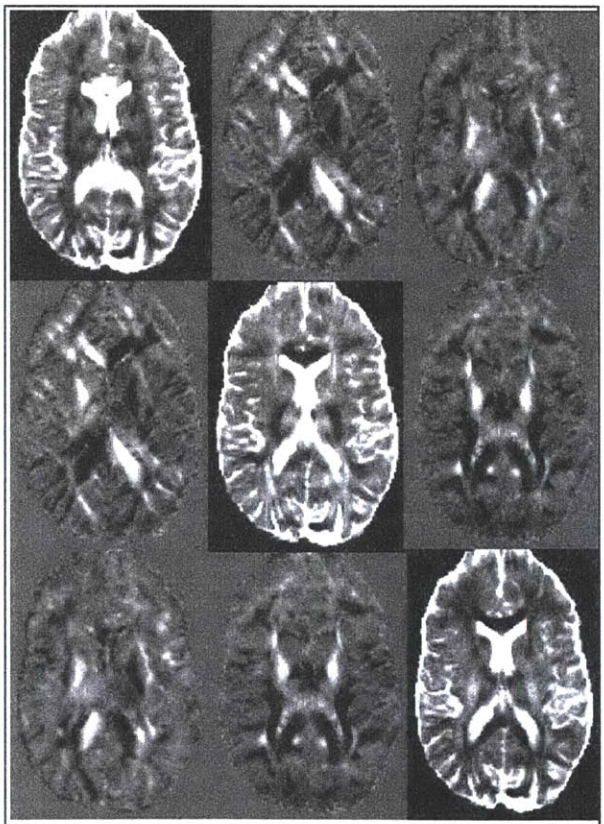

Figure 2.1.1.11 Calculated components of the diffusion tensor using acquired images shown in Figure 2.1.1.3. The order of the images corresponds to the elements of the diffusion tensor. Non-brain tissue has been masked out.

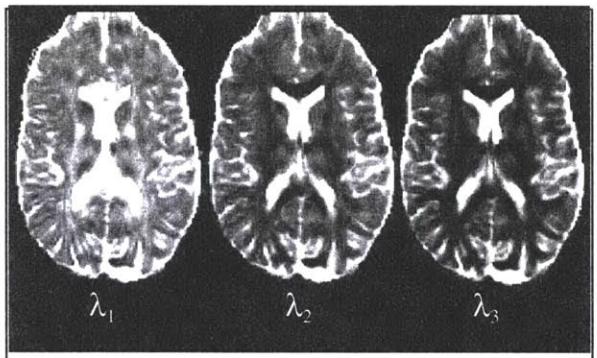

Figure 2.1.1.12 Eigenvalues calculated from Figure 2.1.1.11. Non-brain tissue has been masked out

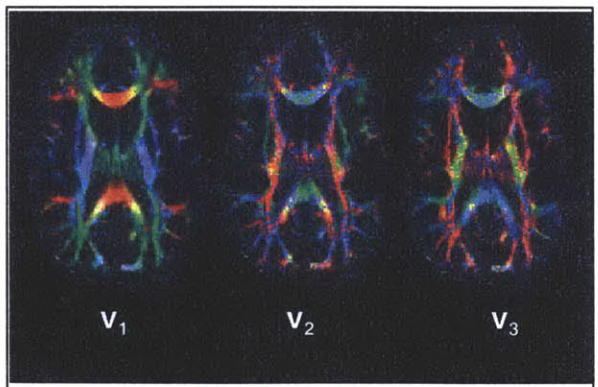

Figure 2.1.1.13 Eigenvectors calculated from Figure 2.1.4. Non-brain tissue has been masked out.

Figure 2.1.1.12 shows the eigenvalues of the diffusion tensor for each voxel in Figure 2.1.1.11. The same image intensity scale was used for each image to ease comparison. As expected, cerebral spinal fluid (CSF) appears the same intensity for all images since it is an isotropic medium. A clear difference is seen in areas corresponding to white matter tracts across the eigenvalue images.

Figure 2.1.1.13 shows the associated eigenvectors for the eigenvalues shown in Figure 2.1.1.12. One sees that the orientations of the principal eigenvectors, $\mathbf{v}_1$, are parallel to the known orientations of the fiber bundles. From the color-coding, one sees that $\mathbf{v}_2$ and $\mathbf{v}_3$ are perpendicular to $\mathbf{v}_1$ and one another. This suggests that, in white matter, the direction of greatest rate of diffusion, as represented by $\mathbf{v}_1$, is along the fiber bundle whereas the direction of greatest restriction, as represented by $\mathbf{v}_3$, is perpendicular to it.

2.1.2 Evaluation of Scalar Metrics of Diffusion Anisotropy

Because the diffusion tensor is a 3D quantity, visualizing and measuring changes is not a straightforward task, as demonstrated by the results in Section 2.1.1. As a first estimate of tracking changes in the diffusion tensor, alterations in the shape of the diffusion tensor, as measured by its anisotropy, and changes in its mean diffusivity, as reflected by its trace apparent diffusion coefficient (ADC), are examined. Using the calculated eigenvalues, coordinate independent scalar functions of **D** can be constructed that measure the tensor's degree of anisotropy.

A challenge to measuring anisotropy from the calculated eigenvalues arises from noise contamination (20). For example, even in an isotropic sample, measurement noise makes the calculated eigenvalues unequal, with the resultant implication of some anisotropy. For anisotropy metrics that rely on sorting of the eigenvalues, a bias and a variance that depend on the diffusion properties of the tissue are introduced (20). To reduce partial volume artifacts, only intravoxel scalar indices that do not involve averaging anisotropy metrics with neighbors are examined. Therefore, in this study, evaluation of anisotropy metrics is limited to intravoxel scalar indices that do not require the sorting of eigenvalues. Maps of fractional anisotropy (FA), relative anisotropy (RA) and volume ratio (VR) indices are calculated. FA, the ratio of the anisotropic component of the diffusion tensor to the magnitude of the whole diffusion tensor, is defined by (19) as:

$$\mathrm{FA}(\mathbf{D}) = \sqrt{\frac{3}{2}}\,\frac{\sqrt{\left(\lambda_1 - \langle\mathbf{D}\rangle\right)^2 + \left(\lambda_2 - \langle\mathbf{D}\rangle\right)^2 + \left(\lambda_3 - \langle\mathbf{D}\rangle\right)^2}}{\sqrt{\lambda_1^2 + \lambda_2^2 + \lambda_3^2}} \qquad \textbf{(2.1.2.1)}$$

with

$$\langle\mathbf{D}\rangle = \frac{\lambda_1 + \lambda_2 + \lambda_3}{3} \qquad \textbf{(2.1.2.2)}$$

which is the trace apparent diffusion coefficient (ADC) or mean diffusivity. RA, the ratio of the variance of the computed eigenvalues to their mean is defined by (19) to be:

$$\mathrm{RA}(\mathbf{D}) = \sqrt{\frac{1}{3}}\frac{\sqrt{\left(\lambda_1 - \langle\mathbf{D}\rangle\right)^2 + \left(\lambda_2 - \langle\mathbf{D}\rangle\right)^2 + \left(\lambda_3 - \langle\mathbf{D}\rangle\right)^2}}{\langle\mathbf{D}\rangle} \qquad \textbf{(2.1.2.3)}$$

VR, the ratio of the volume of the diffusion tensor ellipsoid to the volume of a sphere whose radius is the mean diffusivity, is defined by (20) as:

$$\mathrm{VR}(\mathbf{D}) = 1 - \frac{\lambda_1\lambda_2\lambda_3}{\langle\mathbf{D}\rangle^3}\ . \qquad \textbf{(2.1.2.4)}$$

Methods

Scalar diffusion anisotropy metrics were evaluated using Monte Carlo methods to simulate diffusion-weighted images over a range of SNRs of 0.1–100. Anisotropy maps are generated using the three metrics described, and the contrast-to-noise ratio (CNR) between the anisotropic and isotropic region calculated. The CNR is defined as

$$\mathrm{CNR}(x, y) = \frac{|\bar{x} - \bar{y}|}{\sqrt{\sigma_x^2 + \sigma_y^2}}, \qquad \textbf{(2.1.2.5)}$$

where x and y are calculated anisotropy values for anisotropic and isotropic media respectively and σ_x and σ_y are their SDs.

The diffusion-weighted images are simulated using eigenvalues typical for a healthy volunteer in two homogeneous white matter regions — 1.7, 0.3, and 0.1×10^{-3} mm^2/sec for the corpus callosum and 1.2, 0.9, and 0.3×10^{-3} mm^2/sec for the left forceps major. Monte Carlo simulations were used to synthesize diffusion-weighted images. The simulated diffusion-weighted images consisted of 128×128-pixel regions of anisotropic white matter media and 128×128-pixel regions of isotropic media. For the isotropic media, eigenvalues of 0.8, 0.8, and 0.8×10^{-3} mm^2/sec were used because they were representative of values measured in cortical gray matter and also corresponded well with values reported by another group (20). The mean and standard deviation (SD) of each anisotropy measure as a function of image SNR were then calculated.

The CNR between the white matter regions and the isotropic regions are calculated for SNR levels of 0.1–100.0. The SNR is varied by changing the statistical characteristics of the noise added to the real and imaginary components of the noise-free diffusion-weighted images (20, 38). These random noise values are normally distributed with a mean of zero and different variances, depending on the desired SNR. The simulated acquired signal was set to the magnitude of the complex images. These steps are repeated 10 times to assess the variability of results between different simulations. In addition, the contribution of noise bias and variance to the calculated eigenvalues are estimated.

To investigate the variability of ADC and anisotropy metrics between different imaging sessions in the same subject, a healthy 34-year-old male volunteer, the same subject in Section 2.1.1, underwent imaging three times in three separate sessions, with a resultant total of nine full-head tensor data sets. The imaging parameters were the same as reported in Section 2.1.1 with the

exception that three averages were used, the same protocol that was used clinically for the 1.5T ANMR systems, resulting in an imaging time of 2 minutes and 6 seconds for each scan. The trace ADC values, anisotropy index values, and eigenvalues are measured in 2×2 ROIs. The mean±SD of ADC and anisotropy values are calculated in ROIs placed in deep gray matter in the thalamus; deep white matter in the corpus callosum; and cerebrospinal fluid in the atrium of the right lateral ventricle.

For statistical comparison, two-tailed heteroscedastic Student t-tests were used for calculating the significance of differences in fractional anisotropy, eigenvalues, and ADC values between normal white and gray matter and cerebrospinal fluid. $P<.05$ was considered to indicate a statistically significant difference.

Results

The results of the Monte Carlo simulations are shown in Figure 2.1.2.1. The corpus callosum has a higher level of anisotropy than the left forceps major, with a resultant higher CNR when the simulated corpus callosum tissue was compared with simulated isotropic tissue. On the basis of empiric measurements, the clinically acquired diffusion data was estimated to have an SNR of approximately 20. At this SNR, the three anisotropy metrics perform approximately the same. However, at a higher SNR, the volume ratio performs poorer than the other two metrics. From the Monte Carlo simulations, one notes that of the anisotropy metrics examined, fractional anisotropy (FA) provided the best contrast-to-noise ratio (CNR) as a function of SNR.

Table 2.1.2.1 summarizes the trace ADC values, fractional anisotropy index values, and eigenvalues measured in the healthy volunteer in 2×2 ROIs. ADC values in gray matter, white matter, and cerebrospinal fluid are stable at repeated measures. Moving from cerebrospinal fluid to normal gray matter to normal white matter, a stepwise increase in anisotropy was observed.

Table 2.1.2.1 Stability of Mean of the ADC, Fractional Anisotropy, and Eigenvalue Measurements

	Thalamus	Splenium	CSF
ADC Mean	0.76 (0.05)	0.65 (0.06)	2.69 (0.08)
FA Mean	0.36 (0.04)	0.86 (0.04)	0.21 (0.03)
λ_1 Mean	1.06 (0.08)	1.54 (0.13)	3.29 (0.20)
λ_2 Mean	0.74 (0.05)	0.31 (0.08)	2.61 (0.08)
λ_3 Mean	0.49 (0.06)	0.11 (0.04)	2.16 (0.08)

Stability of gray and white matter measurements of the ADC, fractional anisotropy, and eigenvalues in nine separate scanning sessions in the same volunteer for three imaging acquisitions at three different dates; 2×2 ROIs were placed for each study in the thalamus, the splenium of the corpus callosum, and the cerebrospinal fluid (atrium of the right lateral ventricle). Data are the mean of the ROIs for the nine images. Numbers in parentheses are the SD of the means.

FA = fractional anisotropy. The units of ADC, λ_1, λ_2, and λ_3 are in 10^{-3} mm2/sec. Fractional anisotropy values are unitless.

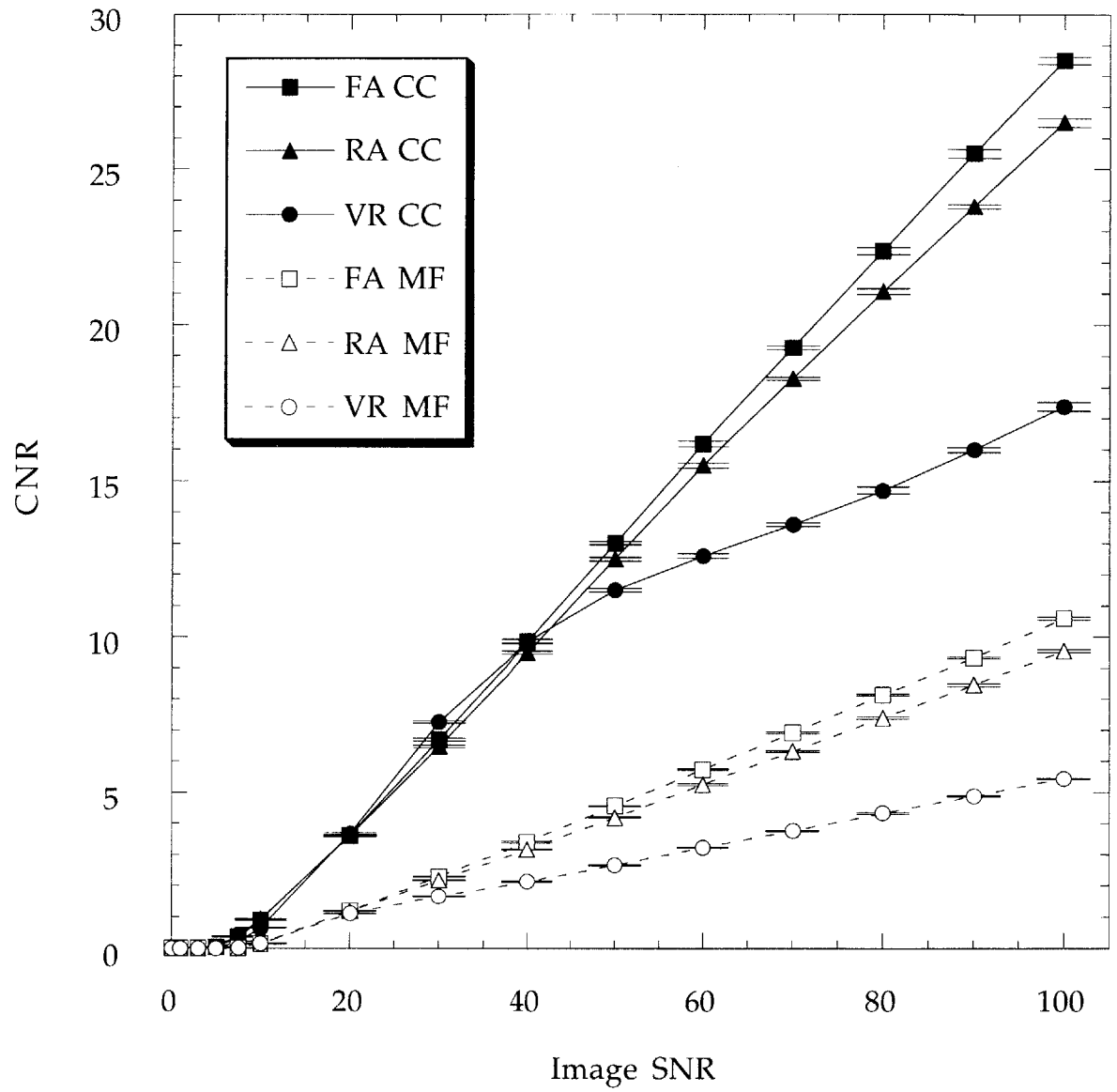

Figure 2.1.2.1 Graph shows CNR as a function of SNR for fractional anisotropy (FA), relative anisotropy (RA), and volume ratio (VR) indices computed from Monte Carlo simulations of two tissue types with different levels of anisotropy. The eigenvalues for the two tissue types were based on typical *in vivo* values of the splenium of the corpus callosum (CC) (1.7, 0.3, and 0.1 x 10^{-3} mm2/sec) and the left forceps major (MF) (1.2, 0.9, and 0.3 x 10^{-3} mm^2/sec) in healthy volunteers. The error bars represent the SD in computed CNR over 10 different simulations.

While white matter was more anisotropic than gray matter or cerebrospinal fluid, deep gray matter voxels were not completely isotropic. Deep gray matter had almost twice the fractional anisotropy value of isotropic cerebrospinal fluid, a significant difference ($P < .001$). The differences between deep gray matter and deep white matter fractional anisotropy values were significant ($P < .001$). For ADC, the difference between deep gray matter and deep white matter was also significant ($P = .001$).

Discussion

We extend the results of earlier studies of scalar metrics of anisotropy (14, 19, 20) by identifying fractional anisotropy as the metric with the best performance characteristics over the range of available SNRs in both the corpus callosum and left forceps major. Fractional anisotropy is therefore used as the anisotropy metric of choice for investigation of changes in anisotropy in the remainder of this dissertation.

As Table 2.1.2.1 and Figure 2.1.1.7 demonstrate, anisotropy maps can be used to differentiate clearly between gray and white matter. The distance scale to which our sequence is sensitive can be derived from the Einstein relation (21), which states that the time scale (Δ) is sensitive to diffusion on the length scale, $L = (2D\Delta)^{1/2}$. For our implementation, assuming D ranges from 1 to 1.5 $\times 10^{-3}$ mm^2/sec (range of λ_1 values from Table 2.1.2.1) at a Δ=47 ms, L = 10 to 12 μm. This distance scale is comparable to typical neuroglial cell soma diameters of 7–15 μm (39) suggesting that the diffusion images are different from those obtained with conventional MR imaging in that they are based on microscopic diffusion properties rather than on relaxation properties.

2.2 Applications

2.2.1 Acute Human Cerebral Ischemia[3]

Magnetic resonance imaging (MRI) has excelled at depicting the macroscopic anatomy of the human brain. However, many normal cellular functions as well as disease processes that occur at the microscopic level do not affect conventional MR relaxation parameters. As a result, certain disease processes such as early acute cerebral ischemia are poorly assessed with conventional MRI. Routine diagnosis could be improved if MR imaging could be used to investigate events at the microscopic level; this has been shown to be possible with acute ischemic stroke, where diffusion and perfusion weighted MR imaging have documented abnormalities, even when conventional MR imaging shows no abnormality (17, 41, 42).

To date, most diffusion imaging of humans in a clinical setting measured either a single direction of the diffusion tensor (17, 23, 41, 43-46) or averaged the diffusion coefficient measured in three orthogonal directions (41, 42, 47-52). Several studies have documented marked anisotropy in the normal human brain particularly in regions of white matter (12, 13, 53-56). However, only a few studies have measured the full diffusion-tensor in human cerebral ischemia. Studies sampling the full diffusion tensor have been limited to chronic stroke patients. In one study, anisotropy reductions were detected in chronic stroke patients in regions corresponding to areas of gliosis and to areas of Wallerian degeneration (57). In another study, changes in tensor orientation were observed in a chronic embolic stroke patient (36).

Based on evidence of anisotropy changes in chronic stroke patients, one can hypothesize that changes in anisotropy will also occur in cases of acute cerebral ischemia particularly in white

[3] This section is based on a previous study (40). Results differ slightly due to improved eddy current compensation techniques used in this present study not used in the previous study. The overall conclusions, however, remain unchanged.

matter. Measuring the entire diffusion tensor during ischemia may thus provide insight regarding the mechanisms involved in acute ischemia and ultimately improve diagnosis. Two earlier stroke studies using middle cerebral artery occlusion (MCAO) in cats did not detect anisotropy changes over a 15-hour period post-occlusion (10, 58). However, one study utilizing MCAO in rats demonstrated a reduction in anisotropy 24-48 hours after occlusion (59). None of these animal studies, however, measured the full diffusion tensor. In this study, changes in the shape of the diffusion tensor in white and gray matter were investigated in acute human cerebral ischemia. It is hypothesized that acute ischemic tissue will show changes in anisotropy compared to tissue that is not infarcted, particularly in areas normally exhibiting anisotropy such as white matter.

Methods

Patient Selection

Patients who presented with symptoms of acute cerebral ischemia underwent imaging with an acute stroke protocol similar to that previously published (42). The protocol included evaluation by the hospital stroke service, computed tomographic scanning, and MR imaging, which may involve both diffusion and, at the discretion of the radiologist and neurologist, perfusion weighted functional MR imaging. For this study, patients were selected at random retrospectively from patients with acute stroke who underwent full diffusion tensor imaging. This study included only patients who underwent imaging less than 24 hours after they were last known to be asymptomatic. All patients underwent full diffusion tensor imaging as described in Section 2.1.1 using an average of three data sets for a total acquisition time of 126 seconds. Isotropic diffusion-weighted images were calculated by taking the geometric mean of the six images obtained with a b-value of 1,221 sec/mm^2. Calculation of the diffusion coefficients was done as described in Section 2.1.1.

No head restraints or navigator echoes were used to control or correct for patient motion. Patients were excluded if the data contained image artifacts due to motion or other technical reasons. Patients were excluded if their isotropic diffusion-weighted images were normal. Patients were also excluded if the time of onset of symptoms was not available or not determinable to be less than 24 hours. Fifty patients (33 men, 17 women; age distribution, 62.9 years ± 21 (mean ± SD)) met the inclusion criteria, with 25 white matter infarcts and 35 gray matter infarcts. Ten patients had lesions in both gray and white matter. The mean time±SD to imaging from the time the patient was last seen to be healthy was 7.8 hours ± 3.7.

Data Analysis

In this study, the ischemic focus was defined as an area of hyperintensity on the initial isotropic diffusion-weighted images. 2×2 ROIs were placed in the following areas: ischemic gray matter, contralateral normal-appearing gray matter, ischemic white matter, and contralateral normal-appearing white matter. In the ischemic regions, the ROIs were placed in the geometric center. Care was taken that the same type of gray or white matter (e. g., deep or cortical) was chosen in the contralateral hemisphere as in the ischemic focus. If the lesion did not involve both gray and white matter as determined by a neuroradiologist (A.G.S.), then only the appropriate ROI and its corresponding contralateral ROI were placed. The mean and SD for trace ADC and anisotropy values were obtained for each ROI.

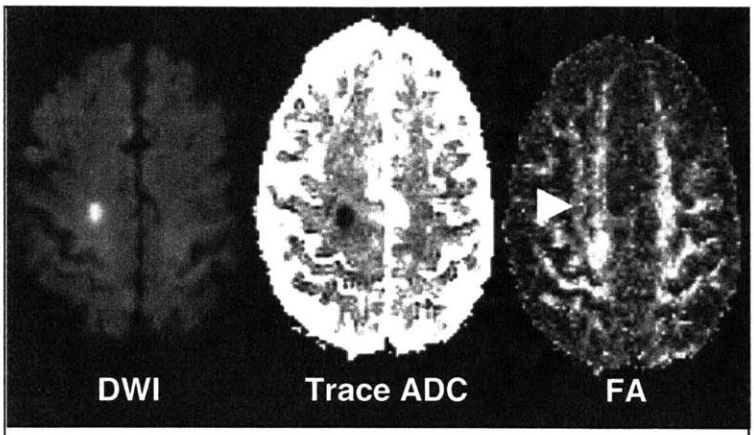

Figure 2.2.1.1 Images obtained axially in a 76-year-old man 12 hours after the onset of symptoms. The conspicuity of the ischemic zone is greatest in the DWI owing to the homogeneity of the background. The white matter in the area of ischemia (arrowhead) shows a subtle decrease in FA.

The statistical analysis was either nonparametric two-tailed Wilcoxon signed rank tests for paired comparisons or Student t tests, assuming heteroscedasticity for nonpaired comparisons. Wilcoxon signed rank tests were used for comparing differences in anisotropy, eigenvalues, and trace ADC between ipsilateral and contralateral hemispheres. A one-way analysis of variance (ANOVA) was performed followed by a two-tailed Student t-test, assuming heteroscedasticity to compare group differences between λ_1, λ_2, and λ_3. An F-test was performed to compare variances between gray and white matter eigenvalues. $P<.05$ was considered statistically significant.

Results

Figure 2.2.1.1 displays the isotropic DWI, trace ADC and fractional anisotropy (FA) images acquired at an SNR of 20 for an example case of acute ischemic stroke in a 76 year-old man imaged 12 hours after the onset of symptoms. Consistent with expectations from results of Monte Carlo simulations (Figure 2.1.2.1), a higher CNR was seen in the high-SNR brain image from the healthy volunteer (Figure 2.1.1.7) than in the ischemic brain image (Figure 2.2.1.1). The white matter in the area of ischemia (arrowhead) shows a subtle decrease in FA. The conspicuity of the ischemic zone is greatest in the DWI and ADC owing to the homogeneity of the surrounding tissue.

Figure 2.2.1.2 shows the eigenvalues of the normal contralateral regions in the patients with acute stroke. Using a one-way analysis of variance, the eigenvalues were all significantly different ($P < .001$) from each other in both normal gray matter and normal white matter. Performing a post-hoc two-tailed heteroscedastic Student t-test further demonstrated a significant difference between all pairs of eigenvalues ($P < .001$). Consistent with previous reports (14), eigenvalues from normal white matter have slightly larger variability than those from normal gray matter. The differences in variances between gray and white matter for our data set were significant for λ_1 but not for λ_2 nor λ_3 (F test for λ_1, $P = .04$; λ_2, $P = .06$; and λ_3, $P = .1$).

Table 2.2.1.1 summarizes the results from patients presenting with acute ischemic stroke. There was a significant decrease in ADC between ischemic brain and normal brain, for both white and gray matter ischemia ($P < .001$). A significant decrease in fractional anisotropy ($P = .007$) between the contralateral and ipsilateral hemispheres was detected in only white matter but not in gray matter ($P = .4$). Figure 2.2.1.3 displays the differences between abnormal and contralateral fractional anisotropy values for all of the patients. Figure 2.2.1.4 shows the eigenvalues

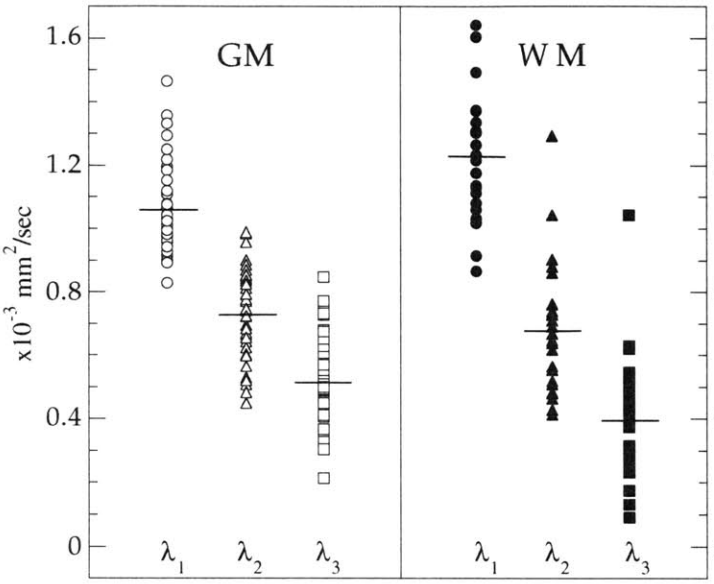

Figure 2.2.1.2 Graph shows eigenvalues in normal contralateral regions of the brain in patients with acute ischemia. The horizontal lines indicate the sample means. Normal mean λ_1, $\lambda_2$and $\lambda_3$values are all significantly different from each other for both gray matter (GM) and white matter (WM) ($P < .001$). A post-hoc two-tailed heteroscedastic Student t-test further demonstrated a significant difference between all pairs of eigenvalues ($P < .001$).

Table 2.2.1.1 Changes in ADC and Fractional Anisotropy in Normal and Ischemic Gray Matter and White Matter

A. Mean (SD) values of 2×2 ROIs

Measurement	Normal GM	Ischemic GM	Normal WM	Ischemic WM
ADC	0.77 (0.11)	0.48 (0.14)	0.77 (0.18)	0.55 (0.22)
FA	0.35 (0.13)	0.33 (0.13)	0.52 (0.14)	0.44 (0.16)

B. Statistical significance between populations (P-value)

	Normal Differences	Ischemic Differences	
Measurement	GM vs. WM	GM vs. GM Infarct	WM vs. WM Infarct
ADC	1.0	<0.001	<0.001
FA	<0.001	0.4	0.007

FA = fractional anisotropy. GM=gray matter, WM=white matter

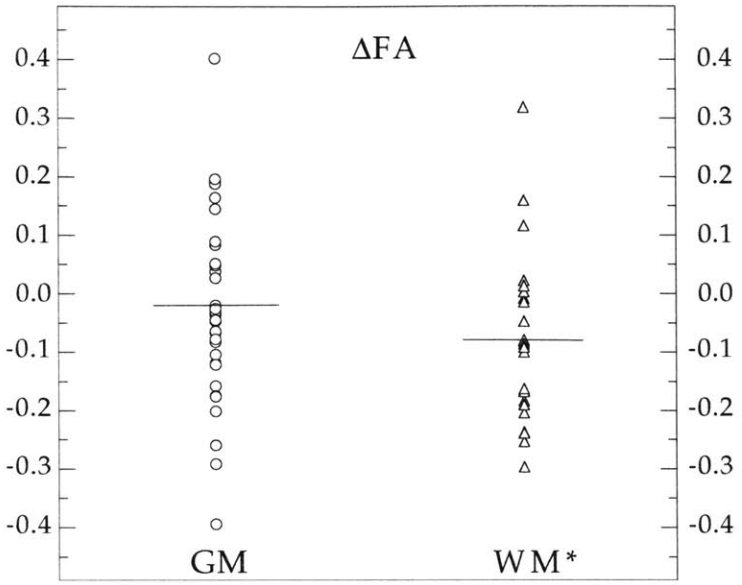

Figure 2.2.1.3 Graph shows fractional anisotropic differences (FA) between ischemic gray matter (GM) and ischemic white matter (WM) and normal contralateral regions. Regions that were abnormal on initial diffusion-weighted images and their contralateral regions were selected. The values plotted are the difference between the abnormal and contralateral values in unitless dimensions. The change in white matter was significant (P = .007). The horizontal lines indicate the sample means.

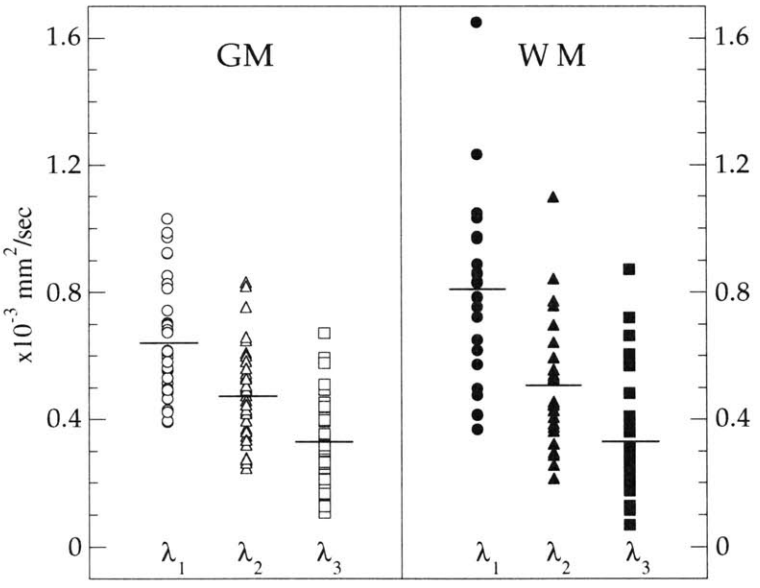

Figure 2.2.1.4 Graph shows eigenvalues in abnormal regions in patients with acute ischemia. The horizontal lines indicate the sample means. Abnormal mean λ_1, λ_2, and λ_3 values are still significantly different from each other in both gray matter (GM) and white matter (WM). With the exception of the significance between λ_2 and λ_3 in white matter, the level of significance between the other eigenvalues is $P < .001$ as determined by using heteroscedastic Student t tests. In the case of λ_2 and λ_3 for white matter, the differences are significant at P=0.004.

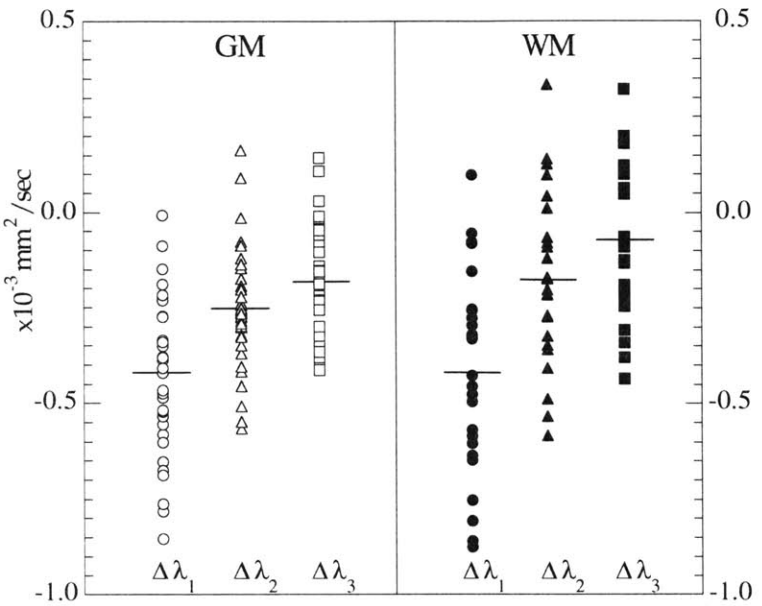

Figure 2.2.1.5 Changes in λ_1, λ_2, and λ_3 during ischemia in gray matter (GM) and white matter (WM). The horizontal lines indicate the sample means. The plotted data points are the difference between eigenvalues measured in the ipsilateral and contralateral hemispheres. All eigenvalues significantly decrease in gray matter (P<.001). In white matter, λ_1 and λ_2 have significant changes but not λ_3 (λ_1:P ≤.001; λ_2:P=.001; λ_3: P=.06).

measured in the abnormal ischemic ROIs. F-tests comparing the observed variabilities between gray matter and white matter ischemic tissue were significant for λ_1 (P=.01) and λ_3 (P=.02) but not for λ_2 (P=.1).In Figure 2.2.1.5, the differences in eigenvalues between the ischemic and normal contralateral hemispheres are plotted. Significant decreases for the first (P < .001 for both gray and white matter) and second (P < .001 for gray matter and P =.001 for white matter) eigenvalues were found. A significant decrease in the third eigenvalue (λ_3) was found in gray matter (P < .001) but only a trend towards significance was found in white matter (P = .06).

Discussion

While the focus of clinical studies (17, 41, 46, 48, 49, 51, 60) appropriately has been on the decrease in the trace or single-direction ADC in acute cerebral ischemia, our results confirm those of earlier reports of changes in anisotropy in animal models of cerebral ischemia (59) and in patients with chronic stroke (36, 57). Our data extend previous work by documenting acute changes in the eigenvalues of white and gray matter; thus demonstrating that measurement of the full tensor can provide additional microanatomic information in human tissue.

The exact mechanisms underlying ADC changes in the ischemic brain remain controversial. Anisotropy has not been a major component of the proposed models to date. However, such information may prove useful as the models used to understand the ADC changes in early cerebral ischemia are refined. For example, the ADC decrease in ischemic white matter was largest in λ_1, the direction of which has been shown to align with white matter tracts (36). One thus can speculate that ADC principally decreases along the long axis of the white matter fiber tracts.

Our data in both our high SNR and lower SNR clinical data demonstrated a significant difference between λ_2 and λ_3 in non-ischemic gray matter and non-ischemic white matter (P <.001). These findings of nonaxisymmetry have also been detected by other groups (14). Furthermore, our data

indicate that during ischemia, λ_2 and λ_3 may behave differently, which suggests that the assumption of axisymmetry may prevent an accurate description of water diffusion behavior in acute cerebral ischemia. Although this difference may be due to noise-related bias and variance (14) it may be nonetheless prudent to acquire the full six diffusion directions in tensor studies.

As can be seen in Figure 2.2.1.4, the variance of the eigenvalues in the ischemic white matter ROIs is quite high, which suggests that some biologic heterogeneity may exist. While the variance may be due to noise, Monte Carlo simulation results from Pierpaoli et al (20) have shown the expected deviation due to noise in a single eigenvalue direction to be less than $\pm 0.15 \times 10^{-3}$ mm^2/s for SNR=20, which is less than the standard deviation we measured for the individual eigenvalues in the ipsilateral hemisphere. This suggests that the variance we measured is more due to biology than noise. We speculate that the changes in anisotropy may occur to a different degree in different white matter locations; further subset analyses await collection of additional data. In addition, to better characterize changes in eigenvalues additional studies should be performed evaluating the variance in estimated eigenvalues over a greater range of possible eigenvalues than used in this study as well as previous others (20). While the anisotropy maps were sensitive to changes in white matter anisotropy, the visual conspicuity of early ischemia is still highest on the trace diffusion-weighted images. These images normally have little or no gray-white contrast. In addition, on the basis of our Monte Carlo simulations, fluctuations in noise have greater effects on anisotropy metrics than they do on ADC values.

Anisotropy maps provide useful information not captured in ADC values. One example is the ability to differentiate between white and gray matter in cases in which the biology of ischemic injury may well differ. Water can diffuse into the neuronal cell bodies that make up gray matter through neurotransmitter-gated ion channels, synapses, and a concentration of voltage-gated ion channels not found in white matter. The dense arrays of parallel white matter tracts create a structured extracellular space that differs substantially from that found in the meshwork of gray matter. It may be that diffusion tensor changes in shape are more evident in white matter than in gray matter owing to the greater structure and hence anisotropy present in normal white matter as compared with normal gray matter.

Careful evaluation of anisotropy metrics is needed. There are at least four causes for variability: (a) anisotropy metrics, themselves, are sensitive to noise contamination (Figure 2.1.2.1); (b) anisotropy itself is quite variable throughout white matter (Figure 2.1.1.7); (c) incomplete eddy current compensation can lead to artifactual anisotropy measurements (Figure 2.1.1.7) and (d) just as ADC values first decrease and later pseudo-normalize, anisotropy values may also vary in different stages of stroke. These many causes of variability may contribute to the fractional anisotropy changes in our sample size. Changes in anisotropy and the eigenvalues that characterize the full diffusion tensor therefore need further investigation.

2.2.2 Anisotropy Changes in Reversible DWI

Almost, but not quite all acute DWI lesions proceed to infarction on follow-up imaging, suggesting that perhaps some DWI lesions may include salvageable tissue. In both experimental animal stroke models with reperfusion (61-64) and in patients receiving thrombolytic therapy (4), the outcome of DWI lesions varied from reversing completely, staying abnormal or

reversing temporarily only to suffer secondary ADC reduction. This suggests that ADC alone may not be a suitable marker for inevitable tissue infarction. Elevations in anisotropy of the diffusion tensor have been observed in early stages of ischemia in both animals (65) and humans (66, 67). One study suggested that elevations in the anisotropy might be related to tissue salvage (67). We therefore sought to determine if anisotropy indices of the diffusion-tensor might reveal additional information about reversibility of ADC lesions.

Subjects and Methods

Full-tensor diffusion-weighted images of patients acquired between November 1995 and May 1999 were examined retrospectively. Due to the rarity of imaging "ADC reversal" in acute stroke patients, this study was not limited to arterial stroke patients and all cases of ADC reversal during this time period were examined. Imaging was performed on a 1.5T General Electric Signa MR instrument, with 5.4.2 software (General Electric Medical Systems, Waukesha, WI) and retrofitted with echo planar imaging (EPI) capabilities via an Advanced NMR Systems (Wilmington, MA) hardware upgrade, that included the "catch and hold" modification. Each patient was also imaged with conventional MR sequences that included sagittal T1-weighted localizers, axial T2-weighted fast spin echo (FSE), fluid attenuated inversion recovery (FLAIR) or proton-density (PD) images. Axial full-tensor diffusion-weighted images with b-value=1221 s/mm2 were acquired using six single-shot pulsed field gradient spin-echo sequences consisting of diffusion encoding pulses of duration 47 ms, with interpulse intervals of 52 ms, placed symmetrically about the 180° RF pulse. A low b-value (b=3 s/mm2) was used in place of crusher gradients for the non-diffusion-weighted image. For all images, TR/TE=6000/118 ms with 6 mm slice thickness and 1 mm slice gap. A fixed field of view (FOV) of 400×200 mm^2 with an acquisition matrix of 256×128 voxels was used. Three tensor sequences were acquired and averaged to increase the signal to noise ratio of the diffusion weighted images. The apparent diffusion coefficient (ADC), fractional anisotropy (FA) and eigenvalues (λ_1, λ_2, λ_3) of the diffusion tensor were calculated on a voxel-by-voxel basis using techniques described in the previous section.

Cases of "ADC reversal" were operationally defined in this study as cases where an initial ADC region of abnormality demonstrated a reduction greater than or equal to 10% of the values in the normal appearing contralateral hemisphere where the follow-up T2 FSE or FLAIR lesion volumes were less than 10% of the initial ADC lesion volume. Follow-up T2 FSE or FLAIR studies for these patients were required to show no volume loss. Furthermore, resolution of the clinical symptoms associated with the initial ADC lesions was required.

For patients meeting the inclusion criteria for "ADC reversal", regions of interest (ROI) were outlined in the initial studies in areas exhibiting reduced ADC along with matching normal appearing contralateral anatomical areas. If no matching non-affected contralateral region could be found, ROI analysis was not performed for those lesions and the lesions excluded from this study. Regions that demonstrated T2 prolongation on follow-up T2 FSE or FLAIR studies were also omitted in the ROI analysis of this study. In one patient who demonstrated both reversible and irreversible ADC reductions, regions that demonstrated T2 prolongation on the co-registered F/U images were outlined and compared with tissue with reversed ADC reduction.

Table 2.2.2.1 Patient diagnoses and scan times.

Pt	Diagnosis	First Scan	Second Scan	Lesion Type
1	Status Epilepticus	6 days	5 days	Cortical
2	Venous sinus thrombosis	11 hours	3 days	White Matter
3	Hemiplegic migraine	3 days	4 days	White Matter
4	Venous sinus thrombosis	11 days	28 days	Cortical
5	Acute MCA Stroke	2 hours	5 days	Both

Initial scan is the time the patient received the first MRI since presenting with symptoms. Follow-up scans are the days since initial scan. Five distinct lesions were outlined in the five patients (two white matter lesions and three gray matter lesions).

†Time from symptom onset
‡Time from first scan

The mean and standard deviation of the ADC, FA, λ_1, λ_2, and $\lambda_3$values in the outlined ROIs were calculated. One-sided non-parametric paired Wilcoxon signed-rank tests were performed on the initial MR studies between the means of the ADC, FA, λ_1, λ_2, and $\lambda_3$values in the lesion ROIs and their matching anatomical normal appearing contralateral ROIs. For intrasubject lesion values, a non-paired one-tailed Wilcoxon signed-rank test was performed comparing ADC, FA and eigenvalues in tissue that infarcted versus tissue that demonstrated ADC reversal.

Results

Six patients fulfilled the criteria for ADC reversal as defined operationally in this study. These were all the cases that had come to the attention of the neuroradiologists at this institution. The small number of patients for this study is due to the rarity of "ADC reversal", estimated to be 0.2-0.4% by a previous study on the frequency of "ADC reversal" (68). Preliminary data for these six patients have been reported in an earlier study of the frequency of "ADC reversal" (68) and in a case report (69). Neither study, however, investigated changes in anisotropy. One patient was excluded in the both studies due to motion artifacts. In this study, ROI analysis involved the entire lesion rather than one section as performed in the previous study (68). One patient was included in this study but not in the previous one (Patient 1). The clinical settings of the patients studied are summarized in Table 2.2.2.1. Five distinct lesions were outlined in the five patients (two white matter lesions and three gray matter lesions). One patient (Patient 4) demonstrated a second area of ADC reversal in the left thalamus. However, since the right thalamus was also abnormal, no normal matching anatomical contralateral region could be outlined and the region not included in this study. The area of initial DWI abnormality for Patient 5 encompassed both white and gray matter. However, the white matter lesion infarcted and was therefore not considered a reversible ADC lesion and excluded from ROI analysis.

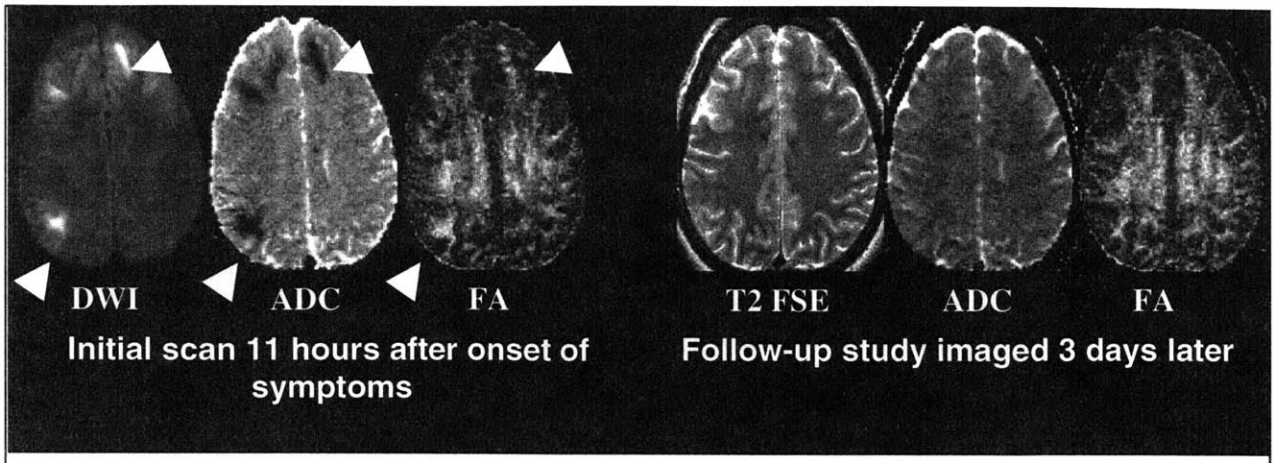

Figure 2.2.2.1 A 31-year-old male (Patient 2) was imaged 11 hours after the onset of left - sided weakness and seizures, including a seizure in the magnet. DWI shows marked bilateral abnormalities (arrowheads). FA is elevated in multiple areas (arrowheads). Average ADC reduction is 50% and average FA increase is 20% with respect to contralateral. The patient was diagnosed with venous sinus thrombosis, treated with transverse sinus thrombolysis with urokinase the following day. His follow-up MRI acquired 3 days later shows minimal damage, with reversal of the majority of the DWI, ADC and FA abnormalities, consistent with the patient's clinical recovery of movement.

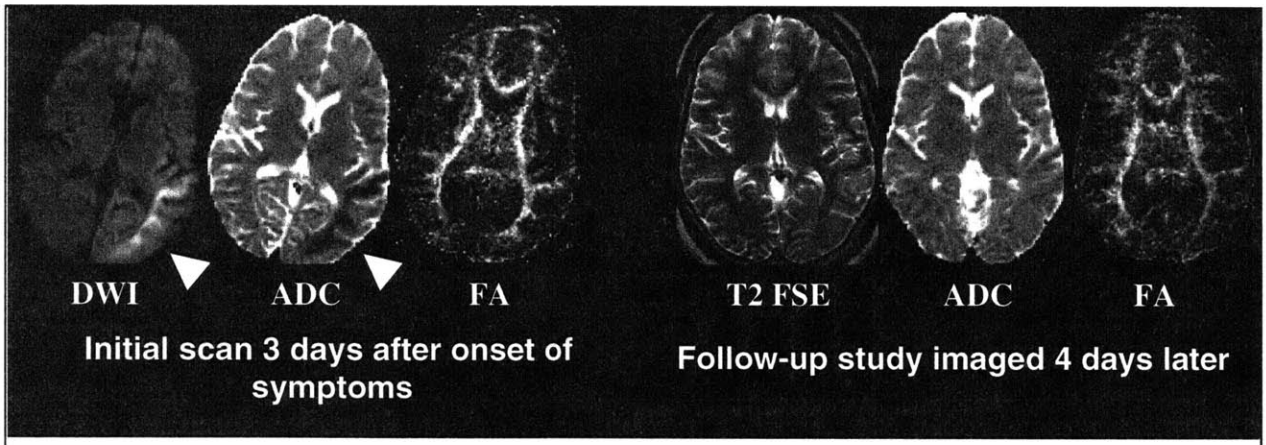

Figure 2.2.2.2 A 23-year old female (Patient 3) presented with right-sided weakness due to hemiplegic migraine. Her initial scan (not shown) taken the same day as admission was normal. The second study acquired 3 days later demonstrates marked white matter abnormalities in the DWI and ADC maps (arrowheads) that are typically associated with infarction. In this case, FA appears normal. The average reduction in ADC was 41% while FA had an average decrease of 8% with respect to contralateral. The patient's hemiplegia resolved consistent with the follow-up MRI taken 4 days later which show recovery of ADC in previously abnormal regions.

Figure 2.2.2.1 shows an example case of a reversible ADC reduction for a patient diagnosed with venous sinus thrombosis and treated with transverse sinus thrombolysis with urokinase the following day (Patient 2). The DWI shows marked bilateral abnormalities (arrowheads). This patient had a mean overall 50% reduction in ADC. Elevations in FA are also noticeable with a mean increase of 20% over contralateral values. His follow-up MRI acquired 3-days later shows minimal damage with reversal of the majority of the DWI, ADC and FA abnormalities, consistent with the patient's clinical recovery of movement.

Figure 2.2.2.2 shows an example of reversible ADC reduction for a patient with hemiplegic migraine. This patient was imaged 3 days after presenting with symptoms. There exists marked ADC reductions, with an average reduction of 41%. FA, however appears normal, with a measured average reduction of 8% with respect to the normal hemisphere.

Figure 2.2.2.3 shows the fractional change in ADC, λ_1, λ_2, λ_3 and FA from normal appearing matched anatomical contralateral regions for all five patients studied. The average and standard deviation of the fractional changes in these values were respectively -36±11, -35±11, -35±11, -39±13, and +7±13. From the one-sided non-parametric paired Wilcoxon signed-rank tests, ADC, λ_1, λ_2, λ_3 were found significantly reduced (P=.03). FA changes were not significant (P=0.2). Three out of the five patients had overall elevated anisotropy (20%, 17% and 8%) while two remaining showed mild reductions (8% and 5%) with respect to the normal contralateral hemisphere. In all cases, eigenvalues were reduced but to different degrees. For the three patients demonstrating elevated anisotropy, λ_1 reductions (46%, 26%, and 25%) and λ_2 reductions (51%, 27%, and 26%) were less than λ_3 reductions (60%, 36%, and 28%) in two of the cases. For the two patients with mild reductions, λ_1 reductions (46% and 31%) and λ_2 reductions (42% and 30%) were comparable to λ_3 reductions (40% and 30%). This suggests that the elevated anisotropy in two of three cases were associated with greater reduction in λ_3 compared to the other two eigenvalues.

Figure 2.2.2.4 shows the initial DWI, ADC and FA for Patient 5 who was imaged within 3 hrs of symptom onset of acute stroke. The patient received intravenous thrombolytic therapy, reversing the majority of the initial ADC reduction (green arrows) but not all (red arrows) as reflected by the 5-day T2 follow-up MRI. In the tissue that reversed, ADC was reduce by 29%, while FA was

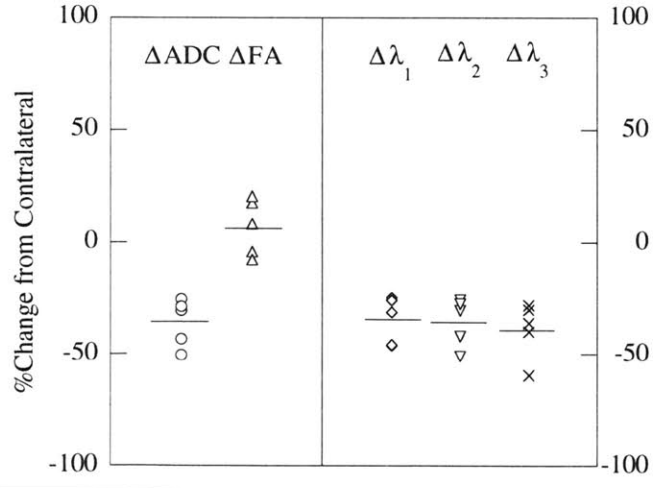

Figure 2.2.2.3 shows the percent changes in ADC, λ_1, λ_2, λ_3 and FA from normal contralateral values. Average±SD percent changes were respectively -36±11, -35±11, -35±11, -39±13, and +7±13. ADC, λ_1, λ_2, λ_3 were found to be significantly reduced (P=0.03) in all five lesions. FA changes, on the other hand, were not significant.

elevated by 17%. In the total lesion that presented with ADC reduction on the initial scan, ADC and FA were significantly less in tissue that infarcted (P<.01) than tissue that reversed. In terms of eigenvalues, for tissue that infarcted, λ_1 and λ_2 were significantly less (P<.001), while λ_3 was not significantly reduced.

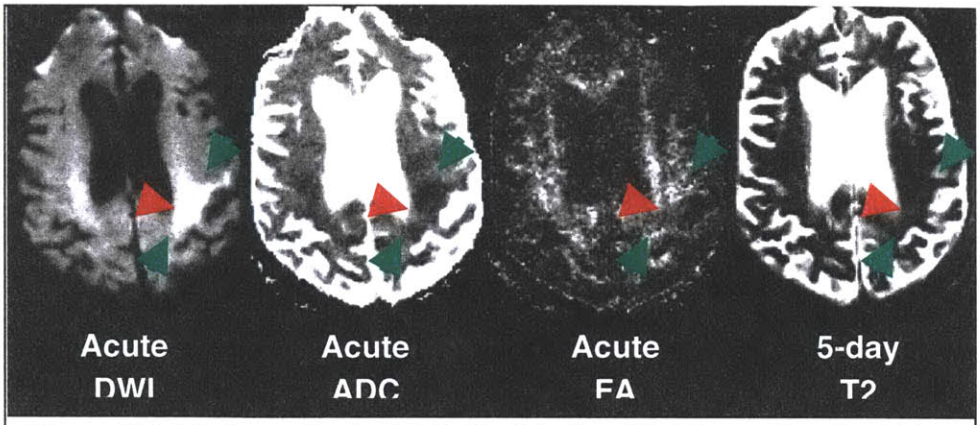

Figure 2.2.2.4 shows the initial DWI, ADC and FA for Patient 5 within 3 hours of symptom onset. The patient received rt-PA reversing the majority of the initial ADC reduction (green arrows) but not all (red arrows) as reflected by the 5-day T2 follow-up MRI.

Discussion

In the rare event when reduced ADC reverses with minimal associated permanent T2 changes no significant change in anisotropy was found. This is most likely due to the limited sample size of this study. This study extends previous research by examining anisotropy changes in tissue with reversible ADC reductions in various clinical settings including arterial infarction. Our findings, although clearly preliminary, suggest that FA may be elevated or preserved in these cases even though significant reductions in ADC and individual eigenvalues were found. In the 2 of the 3 cases with elevated anisotropy, λ_3 had greater reductions, which would result in the change in anisotropy. In cases with mild changes in anisotropy, the changes in the individual eigenvalues were comparable. For an rt-PA treated patient, tissue that recovered had significantly higher ADC and FA than tissue that became infarcted. This is in contrast to reductions in anisotropy reported for tissue with reduced ADC that infarcted (40, 70). The eigenvalues in this case were significantly less in infarcted tissue compared to reversible tissue only for λ_1 and λ_2. One can speculate that the more severe drop in λ_1 and λ_2 may reflect tissue at greater risk of irreversible infarction.

Anisotropy metrics may provide complimentary information to that gleaned from ADC. The biophysical mechanisms underlying ADC changes in stroke have been the target of several studies. In acute brain injury, the decrease in ADC is principally due to cellular swelling or cytotoxic edema (71-73) where upon failure of the transmembrane pump due to ATP depletion and energy failure, water shifts from the extracellular space (ECS) to the intracellular space (ICS). This shift has been posited to reduce ADC in principally three ways: (1) normal intracellular water has a lower ADC than normal extracellular water and therefore a water shift will result in net reduction of ADC (72) (although recent studies have shown intracellular ADC may not be significantly lower (73-75)); (2) increased tortuosity due to cellular swelling reduces extracellular diffusion (76); (3) intracellular diffusion is reduced due to the ischemic insult which leads to breakdown of the cytoarchitecture (74, 75) and increased intracellular viscosity (77, 78). However, in a recent study (73) examining histological and ADC changes in an experimental rat

stroke model, Liu et al demonstrated that ADC reductions were associated with tissue that demonstrated both cytotoxic edema, where ADC could be elevated intracellullarly due to swollen cells but reduced extracellularly due to increased viscosity, and neuronal shrinkage, with an overall measured reduced ADC. Therefore measured ADC values may be the ensemble average of processes that both reduce and increase ADC, possibly explaining the heterogeneity in ADC values. However, this study does not actually measure intracellular diffusion but infers it from measured ADC and expected extracellular changes. They also demonstrated that although the ADC was reduced, no signs of irreversible infarction were visible on histology and therefore the reduction in ADC was still potentially reversible.

In this study, three out of five patients showed elevated FA in conjunction with reversible ADC reductions. The cause of elevated FA remains to be determined. However, our findings are not contradictory to the above hypotheses for ADC reductions. Shift of water to intracellular space with reduced diffusion due to increased restriction may also result in increased anisotropy (67). The increased tortuosity associated with reduced ADC may result in direction dependent increased restriction and increased anisotropy. Reduction of intracellular diffusion may also be direction dependent, for example reduction of diffusion parallel to the fiber bundles due to impairment of fast axonal transport, and therefore also lead to an increase in anisotropy.

Our observations of elevated FA in three reversible ADC lesions are consistent with previous studies that found increases in anisotropy in early acute cerebral ischemia (66, 67). In these two studies, the authors hypothesized the elevation of anisotropy at hyperacute stroke was an indicator of membrane viability in the setting of increased water restriction due to water shift. Yang et al (67) hypothesized that anisotropy, at first elevated in the acute stage, pseudonormalizes before finally becoming reduced due to increased membrane permeability, onset of vasogenic edema and finally lysis. Pseudonormalization of anisotropy was shown to occur much sooner than that of ADC which has been shown by serial studies (60) to persist as long as two weeks.

Therefore, we speculate that FA elevation or preservation in conjunction with ADC reduction may indicate tissue at risk of infarction that may still salvageable due to an intact structural membrane or preserved cytoarchitecture. Increased FA, however, has also been observed in tissue that infarcts (66, 67). Therefore, although elevated or preserved anisotropy may be a sensitive marker for salvageability in tissue with reduced ADC but it may not be specific and as such, is not a definitive marker for reversibility or irreversibility. The utility of FA in identifying tissue with reversible ADC reductions remains to be proved with studies involving larger patient populations. With additional information, such as the tissue's state of perfusion, the temporal characteristics of anisotropy and ADC in reversible and irreversible tissue can perhaps be better understood.

The findings of this study may be confounded by the inherent spatial heterogeneity of FA present in even normal subjects (14). To better characterize changes in FA, a comparison to baseline values would be preferred. Such an analysis was used in an experimental animal model of ischemia (65) that found bilateral elevation of anisotropy compared to baseline early after occlusion. The technique used in this study, comparison with contralateral regions, would not be sensitive to such bilateral changes. Furthermore, comparison with contralateral regions may be confounded with partial volume effects since it is difficult to outline identical regions of tissue in

human patients. Since ADC values are more homogeneous at baseline compared to FA (Table 2.2.1.1), comparison of ADC values to contralateral regions are perhaps less sensitive to partial volume effects than FA. Clarification of anisotropy's role in hyperacute ischemia may be better determined with additional studies in animal models of ischemia where baseline data are readily available.

This study is clearly limited by its small sample size. Given that reversible ADC lesions are rare events (68), an alternate approach may be to use serial studies of patients demonstrating mismatches in diffusion and perfusion lesion volumes which have been speculated to represent salvageable tissue. Serial studies which characterize ADC and FA evolution on an individual voxel basis in the area of mismatch may provide additional insight over previous volumetric based approaches (66, 67) due to the known temporal heterogeneity of ADC evolution (60, 79) and spatial heterogeneity of FA even in normal subjects (14). Techniques which takes into consideration white and gray matter differences may also be needed to accurately characterize the nature of anisotropy and ADC changes in acute stroke.

In this post-rt-PA era, the role of anisotropy as a marker of salvageability may be best elucidated with additional imaging studies of patients receiving interventional therapies, and correlating anisotropy to which tissue reverses and to which tissue infarcts after treatment. If anisotropy is shown persistently preserved or elevated in tissue that is successfully salvaged, and reduced in tissue that infarct, one can then speculate that anisotropy is a specific indicator for salvageable tissue.

2.3 Conclusions

In conclusion, this chapter demonstrates that full-tensor imaging is feasible in the clinical setting of stroke imaging. Even at the low SNR available clinically, maps of anisotropy metrics can be generated. As scanner equipment improve with greater gradient strengths, greater SNR will become available and subtler changes may be better discerned.

This chapter has also demonstrated that acute human cerebral ischemia changes the anisotropy or shape of the diffusion tensor in white matter. Furthermore, it has demonstrated that diffusion tensor imaging may provide valuable insight into the ultrastructural information and changes that occur with tissue damage. This in turn may prove useful for evaluating the integrity of ischemic tissue. With additional studies from patients receiving interventional therapy, which should become more readily available, as more and more patients receive rt-PA, anisotropy may prove to be useful in assessing tissue integrity. We eagerly await these future studies that can evaluate anisotropy metrics sensitivity and specificity as a diagnostic marker of salvageable tissue that can be used to assist therapeutic strategies.

2.4 References

1. Gonzalez RG, Schaefer PW, Buonanno FS, Schwamm LH, Budzik RF, Rordorf G, Wang B, Sorensen AG, Koroshetz WJ. Diffusion-weighted MR imaging: diagnostic accuracy in patients imaged within 6 hours of stroke symptom onset. *Radiology*. 1999;210:155-162.

2. Warach S, Dashe JF, Edelman RR. Clinical outcome in ischemic stroke predicted by early diffusion-weighted and perfusion magnetic resonance imaging: A Preliminary Analysis. *J Cereb Blood Flow Metab.* 1996;16:53-59.

3. Baird AE, Warach S. Magnetic resonance imaging of acute stroke. *J Cereb Blood Flow Metab.* 1998;18:583-609.

4. Kidwell CS, Saver JL, Mattiello J, Starkman S, Vinuela F, Duckwiler G, Gobin YP, Jahan R, Vespa P, Kalafut M, Alger JR. Thrombolytic reversal of acute human cerebral ischemic injury shown by diffusion/perfusion magnetic resonance imaging. *Ann Neurol.* 2000;47:462-469.

5. Tanner JE, Stejskal EO. Restricted self-diffusion of protons in colloidal systems by the pulsed-gradient, spin-echo methods. *Journal of Chemical Physics.* 1968;49:1768-1777.

6. Cleveland GG, Chang DC, Hazlewood CF, Rorschach HE. Nuclear magnetic resonance measurement of skeletal muscle: anisotropy of the diffusion coefficient of the intracellular water. *Biophys J.* 1976;16:1043-1053.

7. Cooper RL, Chang DB, Young AC, Martin CJ, Ancker-Johnson D. Restricted diffusion in biophysical systems. *Biophys J.* 1974;14:161-177.

8. Henkelman RM, Stanisz GJ, Kim JK, Bronskill MJ. Anisotropy of NMR Properties of Tissues. *Magnetic Resonance in Medicine.* 1994;32:592-601.

9. Moseley ME, Cohen Y, Kucharczyk J, Mintorovitch J, Asgari HS, Wendland ME, Tsuruda J, Norman D. Diffusion weighted MRI of anisotropic water diffusion in cat central nervous system. *Radiology.* 1990;176:439-445.

10. Moonen CT, Pekar J, de Vleeschouwer MH, van Gelderen P, van Zijl PC, Des Pres D. Restricted and anisotropic displacement of water in healthy cat brain and in stroke studied by NMR diffusion imaging. *Magnetic Resonance in Medicine.* 1991;19:327-332.

11. Wimberger DM, Roberts TP, Barkovich AJ, Prayer LM, Moseley ME, Kucharczyk J. Identification of "Premyelination" by diffusion-weighted MRI. *Journal of Computer Assisted Tomography.* 1995;19:28-33.

12. Chien D, Buxton RB, Kwong KK, Rosen BR. MR diffusion imaging of the human brain. *Journal of Computer Assisted Tomography.* 1990;14:514-520.

13. Douek P, Turner R, Pekar J, Patronas N, Le Bihan D. MR Color mapping of myelin fiber orientation. *Journal of Computer Assisted Tomography.* 1991;15:923-929.

14. Pierpaoli C, Jezzard P, Basser PJ, Barnett A. Diffusion Tensor MR Imaging of the Human Brain. *Radiology.* 1996;201:637-648.

15. Turner R, Le Bihan D, Maier J, Vavrek R, Hedges LK, Pekar J. Echo-planar imaging of intravoxel incoherent motion. *Radiology*. 1990;177:407-414.

16. Hajnal J, Doran M, Hall A, Collins A, Oatridge A, Pennock J, Young I, Bydder G. MR imaging of anisotropically restricted diffusion of water in the nervous system: technical, anatomic, and pathologic considerations. *Journal of Computer Assisted Tomography*. 1991;15:1-18.

17. Warach S, Gaa J, Siewert B, Wielopolski P, Edelman R. Acute human stroke studied by whole brain echo planar diffusion-weighted magnetic resonance imaging. *Ann Neurol*. 1995;37:231-241.

18. Garrido L, Wedeen VJ, Kwong KK, Spencer UM, Kantor HL. Anisotropy of Water Diffusion in the Myocardium of the Rat. *Circulation Research*. 1994;74:789-793.

19. Basser PJ, Pierpaoli C. Microstructural and Physiological Features of Tissues Elucidated by Quantitative-Diffusion-Tensor MRI. *Journal of Magnetic Resonance Series B*. 1996;111:209-219.

20. Pierpaoli C, Basser PJ. Toward a Quantitative Assessment of Diffusion Anisotropy. *Magnetic Resonance in Medicine*. 1996;36:893-906.

21. Einstein A. *Investigations on the theory of the brownian movement*. New York: Dover Publications, Inc., 1956.

22. Stejskal EO, Tanner JE. Spin diffusion measurements: spin echoes in the presence of a time-dependent field gradient. *Journal of Chemical Physics*. 1965;42:288-292.

23. Le Bihan D, Breton E, Lallemand D, Grenier P, Cabanis E, Laval-Jeantet M. MR imaging of intravoxel incoherent motions: application to diffusion and perfusion in neurologic disorders. *Radiology*. 1986;161:401-407.

24. Basser PJ. New histological and physiological stains derived from diffusion-tensor MR images. *Ann N Y Acad Sci*. 1997;820:123-138.

25. Stejskal EO. Use of spin echoes in a pulsed magnetic-field gradient to study anisotropic, restricted diffusion and flow. *Journal of Chemical Physics*. 1965;43:3597-3603.

26. Mattiello J, Basser PJ, Le Bihan D. Analytical Expressions for the b Matrix in NMR Diffusion Imaging and Spectroscopy. *Journal of Magnetic Resonance Series A*. 1994;108:131-141.

27. Jezzard P, Barnett AS, Pierpaoli C. Characterization of and correction for eddy current artifacts in echo planar diffusion imaging. *Magn Reson Med*. 1998;39:801-812.

28. Bastin ME. Correction of eddy current-induced artefacts in diffusion tensor imaging using iterative cross-correlation. *Magn Reson Imaging*. 1999;17:1011-1024.

29. Schmitt F, Stehling MK, Turner R. *Echo-planar imaging: theory, technique and application.* New York: Springer Verlag, 1998.

30. Woods RP, Cherry SR, Mazziotta JC. Rapid automated algorithm for aligning and reslicing PET images. *J Comput Assist Tomogr*. 1992;16:620-633.

31. Woods RP, Grafton ST, Holmes CJ, Cherry SR, Mazziotta JC. Automated image registration: I. General methods and intrasubject, intramodality validation. *J Comput Assist Tomogr*. 1998;22:139-152.

32. McKinstry RC, Weiskoff RM, Belliveau JW, Vevea JM, Moore JB, Kwong KW, Halpern EF, Rosen BR. Ultrafast MR imaging of water mobility: animal models of altered cerebral perfusion. *J Magn Reson Imaging*. 1992;2:377-384.

33. Basser PJ, Mattiello J, Le Bihan D. MR diffusion tensor spectroscopy and imaging. *Biophysical Journal*. 1994;66:259-267.

34. Basser PJ, Mattiello J, Le Bihan D. Estimation of the Effective Self-Diffusion Tensor from the NMR Spin Echo. *Journal of Magnetic Resonance Series B*. 1994;103:247-254.

35. Mattiello J, Basser PJ, Le Bihan D. The b Matrix in Diffusion Tensor Echo-Planar Imaging. *Magnetic Resonance in Medicine*. 1997;37:292-300.

36. Makris N, Worth AJ, Sorensen AG, Papadimitriou GM, Wu O, Reese TG, Wedeen VJ, Davis TL, Stakes JW, Caviness VS, Kaplan E, Rosen BR, Pandya DN, Kennedy DN. Morphometry of in vivo human white matter association pathways with diffusion-weighted magnetic resonance imaging. *Ann Neurol*. 1997;42:951-962.

37. Pajevic S, Pierpaoli C. Color schemes to represent the orientation of anisotropic tissues from diffusion tensor data: application to white matter fiber tract mapping in the human brain. *Magn Reson Med*. 1999;42:526-540.

38. Henkelman RM. Measurement of signal intensities in the presence of noise in MR images. *Med Phys*. 1985;12:232-233.

39. Gray H. *Anatomy, Descriptive and Surgical*. 1901 edition Philadelphia, PA: Running Press, 1974.

40. Sorensen AG, Wu O, Copen WA, Davis TL, Gonzalez RG, Koroshetz WJ, Reese TG, Rosen BR, Wedeen VJ, Weisskoff RM. Human acute cerebral ischemia: detection of changes in water diffusion anisotropy by using MR imaging. *Radiology*. 1999;212:785-792.

41. Warach S, Chien D, Li W, Ronthal M, Edelman RR. Fast magnetic resonance diffusion-weighted imaging of acute human stroke. *Neurology*. 1992;42:1717-1723.

42. Sorensen AG, Buonanno FS, Gonzalez RG, et al. Hyperacute stroke: Evaluation with combined multisection diffusion-weighted and hemodynamically weighted echo-planar MR imaging. *Radiology*. 1996;199:391-401.

43. Thomsen C, Henriksen O, Ring P. In vivo measurement of water self-diffusion in the human brain by magnetic resonance imaging. *Acta Radiologica*. 1987;28:353-361.

44. Chien D, Kwong KK, Gress DR, Buononno FS, Buxton RB, Rosen BR. MR diffusion imaging of cerebral infarction in humans. *AJNR Am J Neuroradiol*. 1992;13:1097-1102.

45. Welch KMA, Windham J, Knight RA, Nagesh V, Hugg JW, Jacobs M, Peck D, Booker P, Dereski MO, Levine SR. A model to predict the histopathology of human stroke using diffusion and T2-weighted magnetic resonance imaging. *Stroke*. 1995;26:1983-1989.

46. Lutsep HL, Albers GW, DeCrespigny A, Kamat GN, Marks MP, Moseley ME. Clinical utility of diffusion-weighted magnetic resonance imaging in the assessment of ischemic stroke. *Ann Neurol*. 1997;41:574-580.

47. de Crespigny AJ, Marks MP, Enzmann DR, Moseley ME. Navigated diffusion imaging of normal and ischemic human brain. *Magnetic Resonance in Medicine*. 1995;33:720-728.

48. Baird AE, Benfield A, Schlaug G, Siewert B, Lovblad KO, Edelman RR, Warach S. Enlargement of human cerebral ischemic lesion volumes measured by diffusion-weighted magnetic resonance imaging. *Ann Neurol*. 1997;41:581-589.

49. Lovblad KO, Baird AE, Schlaug G, Benfield A, Siewert B, Voetsch B, Connor A, Burzynski C, Edelman RR, Warach S. Ischemic lesion volumes in acute stroke by diffusion-weighted magnetic resonance imaging correlate with clinical outcome. *Ann Neurol*. 1997;42:164-170.

50. Lovblad KO, Laubach HJ, Baird AE, Curtin F, Schlaug G, Edelman RR, Warach S. Clinical experience with diffusion-weighted MR in patients with acute stroke. *AJNR Am J Neuroradiol*. 1998;19:1061-1066.

51. Schlaug G, Siewert B, Benfield A, Edelman RR, Warach S. Time course of the apparent diffusion coefficient (ADC) abnormality in human stroke. *Neurology*. 1997;49:113-119.

52. Ulug AM, Beauchamp N, Bryan RN, van Zijl PCM. Absolute quantitation of diffusion constants in human stroke. *Stroke*. 1997;28:483-490.

53. Chenevert TL, Brunberg JA, Pipe JG. Anisotropic diffusion in human white matter: Demonstration with MR techniques in vivo. *Radiology*. 1990;177:401-405.

54. Coremans J, Luypaert R, Verhelle F, Stadnik T, Osteaux M. A method for myelin fiber orientation mapping using diffusion-weighted MR images. *Magnetic Resonance Imaging.* 1994;12:443-454.

55. Nomura Y, Sakuma H, Takeda K, Tagami T, Okuda Y, Nakagawa T. Diffusional anisotropy of the human brain assessed with diffusion-weighted MR: Relation with normal brain development and aging. *AJNR American Journal of Neuroradiology.* 1994;15:231-238.

56. Sakuma H, Nomura Y, Takeda K, Tagami T, Nakagawa T, Tamagawa Y, Ishii Y, Tsukamoto T. Adult and neonatal human brain: diffusional anisotropy and myelination with diffusion - weighted MR imaging. *Radiology.* 1991;180:229-233.

57. Pierpaoli C, Penix L, De Graba T, Basser PJ, Di Chiro G. Identification of Fiber Degeneration and Organized Gliosis in Stroke Patients by Diffusion Tensor MRI (abstr). *Proceedings of the International Society of Magnetic Resonance in Medicine Fourth Scientific Meeting*, New York 1996; 563.

58. van Gelderen P, de Vleeschouwer MHM, Des Pres D, Pekar J, van Zijl PCM, Moonen CTW. Water diffusion and acute stroke. *Magnetic Resonance in Medicine.* 1994;31:154-163.

59. Kajima T, Azuma K, Itoh K, Kagawa R, Yamane K, Okada Y, Shima T. Diffusion Anisotropy of Cerebral Ischemia. *Acta Neurochirurgica. Supplementum.* 1994;60:216-219.

60. Schwamm LH, Koroshetz WJ, Sorensen AG, Wang B, Copen WA, Budzik R, Rordorf G, Buonanno FS, Schaefer PW, Gonzalez RG. Time course of lesion development in patients with acute stroke: Serial diffusion- and hemodynamic-weighted magnetic resonance imaging. *Stroke.* 1998;29:2268-2276.

61. Dijkhuizen RM, Knollema S, van der Worp HB, Ter Horst GJ, De Wildt DJ, Berkelbach van der Sprenkel JW, Tulleken KA, Nicolay K. Dynamics of cerebral tissue injury and perfusion after temporary hypoxia-ischemia in the rat: evidence for region-specific sensitivity and delayed damage. *Stroke.* 1998;29:695-704.

62. van Lookeren Campagne M, Thomas GR, Thibodeaux H, Palmer JT, Williams SP, Lowe DG, van Bruggen N. Secondary reduction in the apparent diffusion coefficient of water, increase in cerebral blood volume, and delayed neuronal death after middle cerebral artery occlusion and early reperfusion in the rat. *J Cereb Blood Flow Metab.* 1999;19:1354-1364.

63. Li F, Han SS, Tatlisumak T, Liu KF, Garcia JH, Sotak CH, Fisher M. Reversal of acute apparent diffusion coefficient abnormalities and delayed neuronal death following transient focal cerebral ischemia in rats. *Ann Neurol.* 1999;46:333-342.

64. Li F, Silva MD, Sotak CH, Fisher M. Temporal evolution of ischemic injury evaluated with diffusion-, perfusion-, and T2-weighted MRI. *Neurology.* 2000;54:689-696.

65. Carano RA, Li F, Irie K, Helmer KG, Silva MD, Fisher M, Sotak CH. Multispectral analysis of the temporal evolution of cerebral ischemia in the rat brain. *J Magn Reson Imaging.* 2000;12:842-858.

66. Zelaya F, Flood N, Chalk JB, Wang D, Doddrell DM, Strugnell W, Benson M, Ostergaard L, Semple J, Eagle S. An evaluation of the time dependence of the anisotropy of the water diffusion tensor in acute human ischemia. *Magn Reson Imaging.* 1999;17:331-348.

67. Yang Q, Tress BM, Barber PA, Desmond PM, Darby DG, Gerraty RP, Li T, Davis SM. Serial study of apparent diffusion coefficient and anisotropy in patients with acute stroke. *Stroke.* 1999;30:2382-2390.

68. Grant PE, He J, Halpern EF, Wu O, Schaefer PW, Schwamm LH, Budzik RF, Sorensen AG, Koroshetz WJ, Gonzalez RG. Frequency and clinical context of decreased apparent diffusion coefficient reversal in the human brain. *Radiology.* 2001;221:43-50.

69. Soman TB, Singhal AB, Wang B, Koroshetz WJ. Reversible, white matter hyperintensity on diffusion-weighted imaging (DWI) in a patient with hemiplegic migraine. *Neurology.* 1999;52:A87.

70. Mukherjee P, Bahn MM, McKinstry RC, Shimony JS, Cull TS, Akbudak E, Snyder AZ, Conturo TE. Differences between gray matter and white matter water diffusion in stroke: diffusion-tensor MR imaging in 12 patients. *Radiology.* 2000;215:211-220.

71. Moseley ME, Kucharczyk J, Mintorovitch J, Cohen Y, Kurhanewicz J, Derugin N, Asgari H, Norman D. Diffusion-weighted MR imaging of acute stroke: correlation with T2-weighted and magnetic susceptibility-enhanced MR imaging in cats. *AJNR Am J Neuroradiol.* 1990;11:423-429.

72. Benveniste H, Hedlund LW, Johnson GA. Mechanism of detection of acute cerebral ischemia in rats by diffusion- weighted magnetic resonance microscopy. *Stroke.* 1992;23:746-754.

73. Liu KF, Li F, Tatlisumak T, Garcia JH, Sotak CH, Fisher M, Fenstermacher JD. Regional variations in the apparent diffusion coefficient and the intracellular distribution of water in rat brain during acute focal ischemia. *Stroke.* 2001;32:1897-1905.

74. Duong TQ, Ackerman JJ, Ying HS, Neil JJ. Evaluation of extra- and intracellular apparent diffusion in normal and globally ischemic rat brain via 19F NMR. *Magn Reson Med.* 1998;40:1-13.

75. Duong TQ, Sehy JV, Yablonskiy DA, Snider BJ, Ackerman JJ, Neil JJ. Extracellular apparent diffusion in rat brain. *Magn Reson Med.* 2001;45:801-810.

76. Sykova E, Svoboda J, Polak J, Chvatal A. Extracellular volume fraction and diffusion characteristics during progressive ischemia and terminal anoxia in the spinal cord of the rat. *J Cereb Blood Flow Metab.* 1994;14:301-311.

77. van der Toorn A, Dijkhuizen RM, Tulleken CA, Nicolay K. Diffusion of metabolites in normal and ischemic rat brain measured by localized 1H MRS. *Magn Reson Med.* 1996;36:914-922.

78. Neil JJ, Duong TQ, Ackerman JJ. Evaluation of intracellular diffusion in normal and globally-ischemic rat brain via 133Cs NMR. *Magn Reson Med.* 1996;35:329-335.

79. Nagesh V, Welch KMA, Windham JP, Patel S, Levine SR, Hearshen D, Peck D, Robbins K, D'Olhaberriague L, Soltanian-Zadeh H, Boska MD. Time course of ADCw changes in ischemic stroke: Beyond the Human Eye! *Stroke.* 1998;29:1778-1782.

Chapter 3

Perfusion-Weighted Imaging

"Oh dear! Oh dear! I shall be too late!"

—Lewis Carroll
(*Alice's Adventures in Wonderland*)

Ischemia is the reduction of cerebral blood flow resulting in metabolic impairment and neurological dysfunction. The previous chapter describes techniques used to image the microstructural damage resulting from ischemia on a voxel-by-voxel basis. A logical extension is to directly image cerebral blood flow on a voxel-by-voxel basis. One of the research goals in stroke imaging is to identify the imaging correlate to the ischemic penumbra — tissue that is oligemic but still viable. It is this tissue that has been speculated to maximally benefit from therapeutic intervention. An accurate *in vivo* measure of cerebral blood flow (CBF) may assist guiding therapeutic strategies on an individual patient basis.

By strict definition, the ischemic penumbra, the term first coined by Astrup in 1981 (1), consists of tissue that is oligemic at a flow level leading to electrical failure but above that leading to structural membrane damage. It has been recently suggested that the ischemic penumbra can perhaps be more usefully redefined as tissue that is still therapeutically treatable (2). Critical thresholds of CBF are summarized in Figure 3.1. The reader is directed to an excellent review article by Siesjö (2) for a detailed description of the cascade of metabolic events that occur in ischemia. In brief, the studies showed that metabolic dysfunction occurs at flow levels below critical thresholds of 40 - 50% of normal flow. Electrical failure occurs at values of 15-18 ml/100 g/min while membrane failure occurs at 10 ml/100 g/min. Thus the threshold for metabolic failure and infarction are not necessarily equivalent. A gradient of ischemia density exists from the core of the infarction to the periphery, where electrically silent but still viable tissue may be present. In both *in vivo* and *in vitro* models of focal ischemia, the ability for oligemic tissue to recover is a function of both density and duration of ischemia (Figure 3.2). Therefore, although quantitative CBF may not be absolutely necessary for guiding therapy (3), an accurate assessment of relative CBF may be useful for measuring depth of ischemia and thereby assessing whether tissue is salvageable or not.

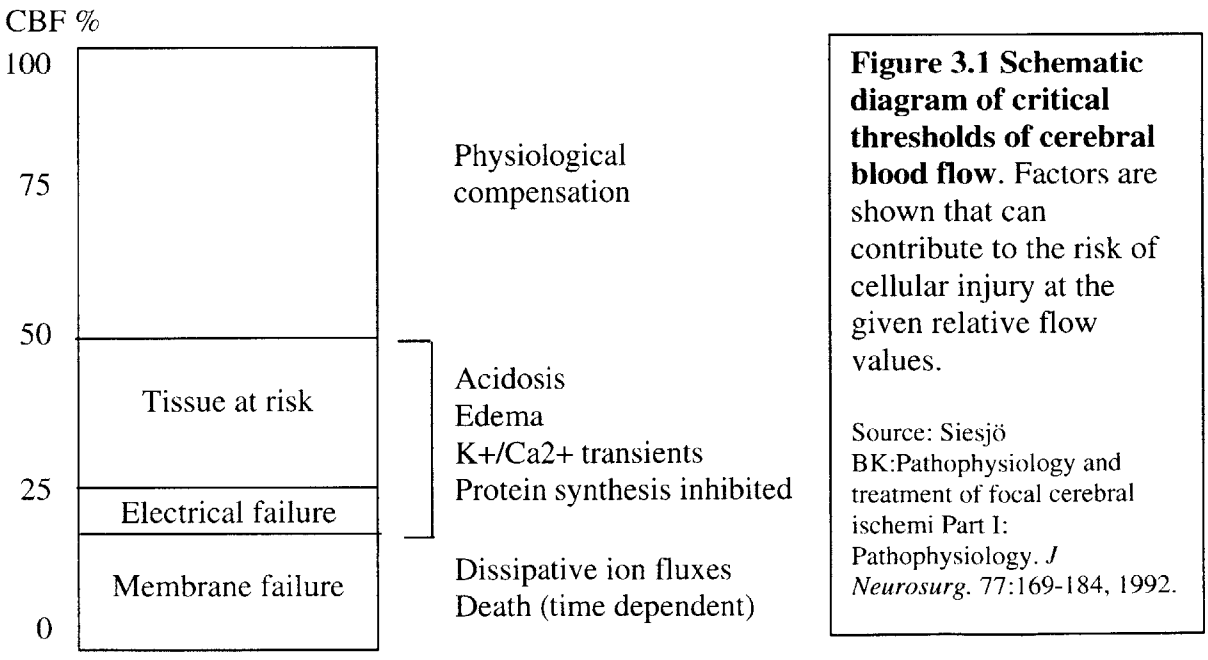

Figure 3.1 Schematic diagram of critical thresholds of cerebral blood flow. Factors are shown that can contribute to the risk of cellular injury at the given relative flow values.

Source: Siesjö BK:Pathophysiology and treatment of focal cerebral ischemi Part I: Pathophysiology. *J Neurosurg.* 77:169-184, 1992.

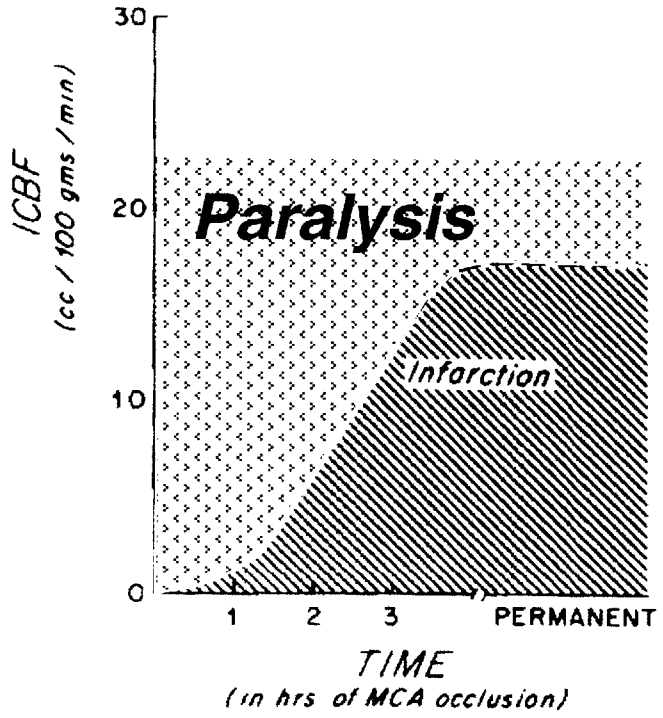

Figure 3.2 Thresholds of tissue viability
Ischemic thresholds in monkey brain as defined by level of local cerebral blood flow (lCBF) below which reversible (stippled) and irreversible (cross-hatched) ischemic changes occur. (Reprinted from Jones TH, Morawetz RB, Crowell RM et al: Thresholds of focal cerebral ischemia in awake monkeys. J Neurosurg 54:773, 1981.)

Source: Barnett, et al., *Stroke: Pathophysiology, Diagnosis, and Management*, New York: Churchill Livingstone Inc. 1986, p. 98.

Perfusion weighted (PWI) magnetic resonance imaging using tracking of the first pass of a bolus of high magnetic susceptibility contrast agent has been demonstrated to be highly sensitive in detecting tissue at risk of infarction (see review by Baird (4)). CBF maps are estimated by deconvolving tissue concentration curves with an arterial input function (AIF). This technique has been shown to be both sensitive to delay and dispersion between the AIF and the tissue concentration curve (5, 6). Because the perfusion maps depend highly on the selection of the AIF, determination of a threshold of irreversible ischemia is complicated and makes identification of tissue at risk of infarction sensitive to user variability. Furthermore, such artifacts may negatively affect patient management. For example, a vascular territory whose feeding artery is occluded will suffer delayed flow as well as reduced flow. However, even if the territory has sufficient collateral flow, the tissue may have an estimated CBF that is artificially oligemic due to these technical limitations. One can speculate that the lack of specificity of CBF and MTT in identifying salvageable tissue may be due to contamination by delay in tracer arrival and AIF selection. A technique that decoupled delay from flow estimations may provide a better estimation of existing hemodynamic injury by measuring depth of ischemia as well as distinguishing vascular territory that is downstream from a stenosis.

This chapter seeks (1) to evaluate the effects of delay on calculated CBF, (2) to correct for the delay and (3) to determine if CBF values decoupled from delay provide better insight into the pathophysiology of tissue at risk of infarction. This chapter is divided into two sections. The first section, **Background**, provides a brief overview of the current technique used for estimating cerebral blood flow (CBF), cerebral blood volume (CBV) and mean transit time (MTT) by deconvolution with an arterial input function using singular value decomposition (SVD). The second section, **Technical Development**, is in turn divided into two subsections. The first

subsection evaluates the effects of delay between the arterial input function and tissue arrival curve on flow estimates in numerical simulations and in acquired human data. In the human data, the AIF is artificially shifted with respect to the tissue arrival curve. In the second subsection, a technique less sensitive to timing shifts between the AIF and measured signal is proposed using deconvolution with a block-circulant matrix. This technique as well as SVD is evaluated for performance in terms of bias and variance as a function of noise and timing delay using numerical simulations. In addition, an additional perfusion parameter, delay, is evaluated as a supplemental marker of tissue downstream from an occlusion and therefore at risk of infarction. The performance of the deconvolution technique with the block-circulant matrix is also compared to SVD qualitatively in acquired clinical human data.

3.1 Background

Lathanide chelate contrast agents produce changes in transverse relaxation time (ΔR_2) proportional to its concentration in magnetic susceptibility MR imaging (7). During the passage of a bolus of a high magnetic susceptibility contrast agent, tissue surrounding the vessels produce a transient loss of signal due to the intravascular compartmentalization of the contrast agent. The relationship between image intensity and change in susceptibility ΔR_2 (or ΔR_2^* in a gradient echo experiment) has been shown to be (8):

$$S(t) = S_0 \, e^{-TE \cdot \Delta R_2} \tag{3.1.1}$$

where S_0 is the baseline MR image intensity prior to administration of contrast agent. The contrast agent concentration over time in a volume of tissue, *C(t)* has been demonstrated to be linearly related to ΔR_2 (8):

$$C(t) \propto \Delta R_2(t) = -\frac{1}{TE} \ln \frac{S(t)}{S_0}. \tag{3.1.2}$$

Traditional tracer kinetic models for intravascular agents (9, 10) can be extended to dynamic susceptibility contrast MRI data to calculate cerebral blood flow (CBF) and tracer mean transit time (MTT). Modeling the vascular bed as a fluid dynamic system consisting of a single in-flow and single out-flow with multiple capillary branches in between (11), the distribution of transit times can be characterized by a transfer function, *h(t)*, as shown in Figure 3.1.1 where $C_a(t)$ is the concentration flowing in, $C_v(t)$ the concentration flowing out, and *h(t)* has the following property:

$$\int_0^\infty h(t)\, dt = 1. \tag{3.1.3}$$

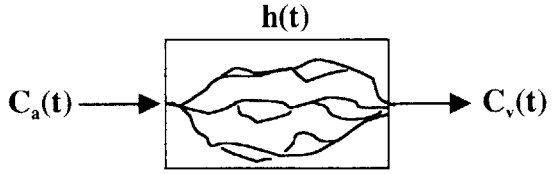

Figure 3.1.1 Simplified model of relationship tracer influx and tracer outflux.

This relationship can be formulated as,

$$C_v(t) = C_a(t) \otimes h(t) \tag{3.1.4}$$

where $\otimes$ represents linear convolution operator.

Furthermore, by defining the fraction of tracer remaining in the system, also known as the residue function, *R(t)* as

$$R(t) = 1 - \int_0^t h(\tau)\, d\tau, \tag{3.1.5}$$

the concentration of tracer remaining within the voxel of tissue can then be modeled as (12):

$$C(t) = F_t\, C_a(t) \otimes R(t) = F_t \int_0^t C_a(\tau)\, R(t-\tau)\, d\tau \tag{3.1.6}$$

where $C_a(t)$ is the concentration at the input artery (the arterial input function) and F_t is the flow within the tissue system. Flow can then be determined if one has knowledge of the arterial input function, $C_a(t)$ and concentration remaining in the voxel, *C(t)*.

Previous studies have shown that estimating the arterial input function (AIF) measured from MR images correlated well with values measured directly from arterial blood samples (13). The arterial input function is obtained by averaging the signal changes in pixels selected from regions near large cerebral vessels in the MR images that showed early large increases in ΔR_2 after contrast injection. The AIF cannot be measured directly in a large vessel, for example the middle cerebral artery (MCA), since the change in signal does not follow Eqn. 3.1.2 due to large flow effects and dependence of signal change on orientation of the large vessel (14). Instead, the AIF is typically selected in voxels near the large vessel where the signal change has been demostrated to follow Eqn. 3.1.2. Without knowledge of the concentration of contrast agent passing through the vessels resulting in the measured AIF, true quantitative CBF in terms of ml/100 g/min is not possible with the current techniques and one is relegated to use relative flow values which will differ from true CBF by a scale factor. Typically a single AIF is then used for deconvolving Eqn. 3.1.6 to calculate relative CBF for all of the voxels in the brain.

Assuming a scaled $C_a(t)$ can be measured, *R(t)* can then be estimated via deconvolution with the measured concentration versus time curve. Østergaard investigated both model-based and model-independent methods to estimate *R(t)* (12). Briefly, using Monte Carlo simulations, he showed that model based methods produced reasonable estimates of flow only if the modeled residue function matched the true residue function. In cases of pathophysiology, this assumption often does not hold true. In terms of model-independent approaches, deconvolution methods using Fourier, regularization and singular value decomposition (SVD) were examined. Fourier based methods were found to generate flow values whose accuracy was a function of flow rate, resulting in the underestimation of true flow at high flow rates. The regularization technique's performance was found to be dependent on the vascular volume of the tissue. The SVD approach, on the other hand, provided estimates that were independent of both the flow and

volume being measured. For these reasons, SVD is used to investigate CBF and MTT in this study.

The SVD technique entails expressing Eqn. 3.1.6 in discretized format:

$$c(t_j) = \Delta t\, F_t \sum_{i=0}^{j} C_a(t_i)\, R(t_j - t_i). \tag{3.1.7}$$

By expanding Eqn. 3.1.7 into matrix notation, the deconvolution problem can be expressed as an inverse matrix problem:

$$\begin{pmatrix} c(t_0) \\ c(t_1) \\ \vdots \\ c(t_{N-1}) \end{pmatrix} = \Delta t \begin{pmatrix} C_a(t_0) & 0 & \cdots & 0 \\ C_a(t_1) & C_a(t_0) & \cdots & 0 \\ \vdots & \vdots & \ddots & \vdots \\ C_a(t_{N-1}) & C_a(t_{N-2}) & \cdots & C_a(t_0) \end{pmatrix} \cdot \begin{pmatrix} R(t_0) \\ R(t_1) \\ \vdots \\ R(t_{N-1}) \end{pmatrix} \cdot F_t \,. \tag{3.1.8}$$

Simplifying the above equation to:

$$\mathbf{c} = F_t\, \mathbf{A} \cdot \mathbf{b} \tag{3.1.9}$$

one can solve for **b**, the elements of $R(t)$. The measured AIF, $C_a(t)$, can be prefiltered to reduce noise contributions and compensate for quantization errors (12), resulting in **A** with elements:

$$a_{ij} = \begin{cases} \Delta t\, (C_a(t_{i-j-1}) + 4C_a(t_{i-j}) + C_a(t_{i-j+1})) & 0 \le j \le i \\ 0 & \text{otherwise} \end{cases}. \tag{3.1.10}$$

Since **A** may be close to singular, the inverse of **A** is calculated using singular value decomposition (15). In SVD, **A** is decomposed to:

$$\mathbf{A} = \mathbf{U} \cdot \mathbf{S} \cdot \mathbf{V} \tag{3.1.11}$$

where **U** and **V** are orthogonal matrices and **S** a non-negative square diagonal matrix The inverse is then simply:

$$\mathbf{A}^{-1} = \mathbf{V} \cdot \mathbf{W} \cdot \mathbf{U}^{\mathrm{T}} \tag{3.1.12}$$

where **W**=1/**S** along the diagonals, and zero elsewhere. Values of **W** corresponding to values where **S** is smaller than a preset tolerance threshold (usually a percentage of the maximum value of **S**) are set to zero in order to eliminate singular values and to produce a more stable result. The residue function scaled by flow, **b**, can then be estimated by:

$$\mathbf{b} = F_t\, \mathbf{V} \cdot \mathbf{W} \cdot \mathbf{U}^{\mathrm{T}} \cdot \mathbf{c}. \tag{3.1.13}$$

From **b**, which is the estimated $R(t)$, rCBF is set equal to its maximum value which often does not occur at the zero time point due to tracer arrival delay.

By integrating Eqn. 3.1.2 with respect to time, relative CBV (rCBV) can be obtained (8, 16):

$$\mathrm{rCBV} = \frac{\int_0^\infty C(t)\,dt}{\int_0^\infty C_a(t)\,dt} \tag{3.1.14}$$

assuming no recirculation or consumption of the contrast agent.

MTT can then be calculated using the Central Volume Theorem (17):

$$\mathrm{MTT} = \frac{\mathrm{rCBV}}{\mathrm{rCBF}}. \tag{3.1.15}$$

From these equations, maps of perfusion indices have been calculated to assist in clinical diagnosis.

Methods

Dynamic susceptibility contrast weighted images were obtained by acquiring either spin-echo (SE) or gradient-echo (GRE) EPI images during the first pass of 0.1-0.2 mmol/kg of a gadolinium-based contrast agent injected 10 seconds after the start of imaging at a rate of 5 ml/s with the use an MR imaging-compatible power injector (Medrad, Pittsburgh, PA). The contrast agent was followed by a comparable volume of normal saline injected at the same rate. Datasets of 10-11 slices over 46 timepoints were obtained. The in-plane resolution of the images were 1.56×1.56 mm^2. Each slice was 6 mm thick with a 1 mm interslice gap. TR=1500 ms and TE=75 ms were used for SE images. TR=1499 and TE=50 ms were used for GRE images. Images were obtained on the same 1.5 T equipment used for diffusion tensor imaging (Chapter 2). From these images, the perfusion indices of cerebral blood flow (CBF), cerebral blood volume (CBV) and mean transit time (MTT) were calculated using the techniques described above.

Results

Figure 3.1.2 shows the CBF, CBV and MTT maps for a 78-year old woman imaged within 4 hours of presenting with symptoms. For comparison the acute DWI acquired in the same imaging session is also shown. Regions of abnormality are seen in the left operculum (arrows) on all acute studies. However, an additional area of abnormality can be seen in the CBF and MTT maps in the left temporal parietal lobe (arrowheads) that is shown to have infarcted on the 5-day follow-up study. The initial DWI is normal as well as the CBV. These areas of mismatch have often been hypothesized as areas of salvageable tissue and the clinical relevance of the mismatch is still the subject of active debate and investigation.

Figure 3.1.3 shows the associated concentration versus time curve derived from the measured MR signal in three regions of interest (ROIs) along with the arterial input function for Figure 3.1.2 selected in the diseased hemisphere from the right MCA. The three ROIs correspond to

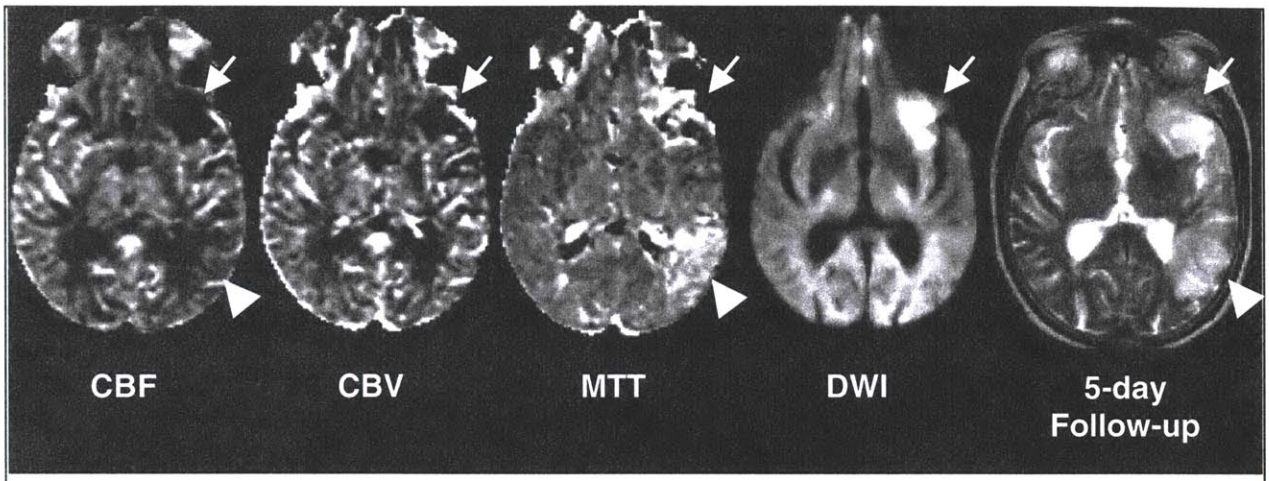

Figure 3.1.2 Example perfusion maps using SVD for an acute stroke patient
Acute CBF, CBV and MTT maps for 78-year-old woman imaged within 4 hours of presenting with symptoms. The acute DWI acquired in the same imaging session is also shown. Regions of abnormality are seen in the left operculum (arrows) on all acute studies. However, an additional area of abnormality can be seen in the CBF and MTT maps in the left temporal parietal lobe (arrowheads) that is shown to have infarcted on the 5-day follow-up study.

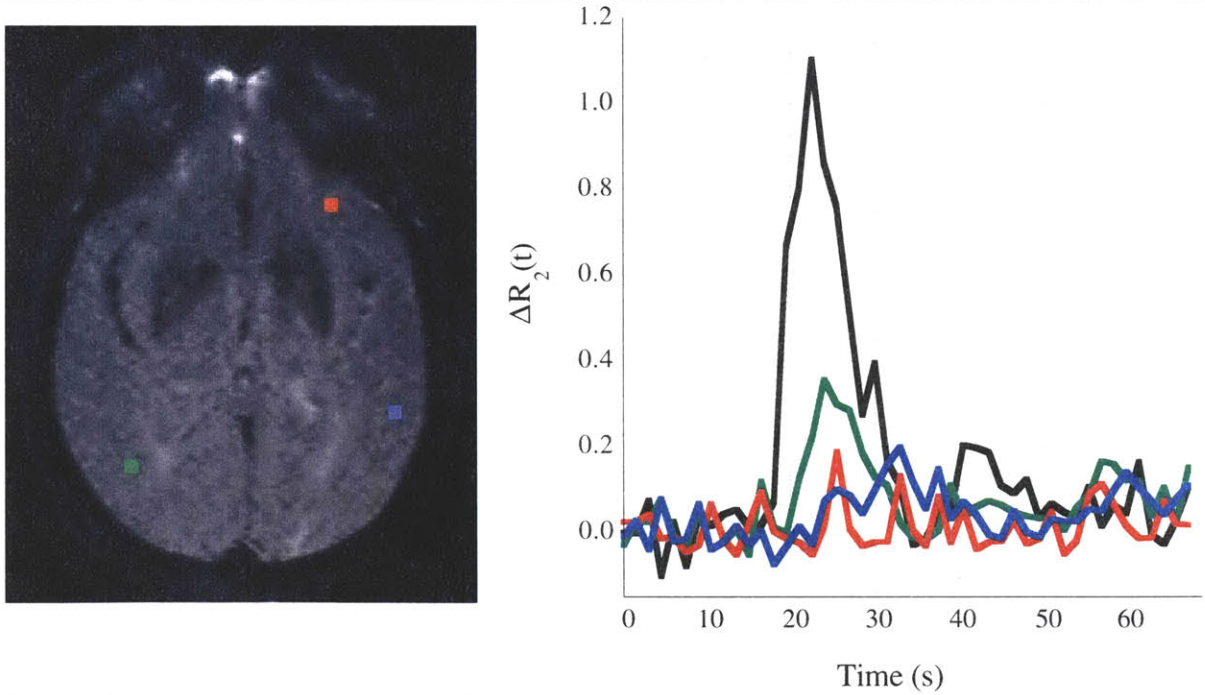

Figure 3.1.3 ΔR2(t) for the arterial input function selected in the diseased hemisphere from the right MCA (black) and for three ROIS: normal contralateral (green), ipsilateral operculum (red), and ipsilateral temporo-parietal lobe (blue). The blue and red ROIs both have much smaller amplitudes than the green ROI. The red ROI signal is almost at the level of noise.

normal contralateral hemisphere (green), ipsilateral tissue that was abnormal on the initial DWI and CBV (red) and ipsilateral tissue that was CBF and MTT abnormal (blue). Clearly reduced amplitudes are seen in the ischemic regions compared to the ROI measured in the normal contralateral hemisphere. In addition, the red ROI signal, which corresponds to tissue already DWI and CBV abnormal, is almost at the level of noise. In addition to reduced amplitude, the arrival of tracer for the ischemic tissue is greater than that in the contralateral region resulting in a delayed time-to-peak.

3.2 Technical Development

A limitation of using SVD has been the underestimation of flow due to dispersion and delay of the arterial input function (5, 6, 18). To demonstrate the potential clinical relevance of such an underestimation, an example case is shown in Figure 3.2.1, of a 39 year old woman with right internal carotid artery (ICA) stenosis experiencing recurring symptoms of numbness on the left side. Two very different CBF and MTT maps are derived depending on the selection of the AIF. By using an arterial input function from the left MCA (LMCA) in the non-occluded contralateral hemisphere, one overestimates the area of abnormality. A follow-up PET study (not shown) reported an area of abnormality in deep white matter, which correlates better with the MTT map generated using the AIF from the right MCA (RMCA). As observed from the time course graphs in Figure 3.2.1, some differences between the RMCA and LMCA AIFs are that the RMCA AIF has a larger signal change, arrives later than the LMCA AIF and experiences greater dispersion. However, as the feeding artery to the vascular territory of interest, the right hemisphere, the RMCA AIF generated maps that provide better estimates of tissue at risk of infarction.

Ideally, one would like to select an AIF on an individual voxel-by-voxel basis. However, this is not feasible in current practice. Instead, techniques have been proposed for modifying the selected AIF to compensate for delay and dispersion between where the AIF is sampled and the individual voxels are measured. One study proposes to compensate for vascular dispersion through the use of vascular transport operators (5). As shown in data from normal volunteers, a model-based approach has the benefit of being less sensitive to delay and dispersion since the vascular operators take these parameters into account. However, in pathophysiological conditions, the model may no longer be accurate if flow heterogeneity becomes disrupted (18). Another proposal for correcting for delay has been to shift the AIF by the amount it appears delayed until it is synchronized with $C(t)$ for each voxel (6, 12, 19). However, this technique has yet to be performed on a voxel-by-voxel basis, most likely due to the necessity of each voxel requiring an individual shift. Schemes for correcting for dispersion are more complicated and involve modeling the vasculature (6) and as such will not be discussed here.

Our goals are therefore two-fold: (1) to examine the effects of delayed tracer arrival time in $C(t)$ with respect to AIF on calculated CBF in both simulations and acquired human data and (2) to compensate for these effects. For the first part, the effects of timing offsets independent of noise contamination are examined using numerical simulations where "true" CBF is known and SNR is infinity. These effects are then examined in acquired human data by artificially shifting an acquired AIF over time and estimating CBF and MTT for each shift. For the second part, to correct for delay artifacts, circular convolution is used in place of linear convolution since linear convolution is constrained by assumptions of causality. However, circular convolution is known

to be sensitive to oscillatory artifacts, and therefore was further modified to include smoothness constraints (20). This technique is compared to the standard deconvolution technique as well as to deconvolution with a block-circulant matrix without smoothness constraints by using Monte Carlo simulations where "true" CBF is known. The performance of the new technique is also compared qualitatively on clinically acquired human data.

In addition, it is speculated that the sensitivity and lack of specificity of current perfusion indices (CBF and MTT) in identifying infarct volumes may be related to delay in arrival times. Therefore, techniques for estimating delay are also evaluated. We propose using the phase offset from SVD, that is the time when the maximum of *R(t)* is reached, as a delay term. Since both phase offsets are readily calculated from the deconvolution techniques, delay estimated from circular deconvolution techniques are compared with delay estimated with deconvolution.

3.2.1 Effects of delayed tracer arrival on flow estimates using singular value decomposition

Methods

Simulations

An arterial input function was simulated using a gamma variate function that has been shown in

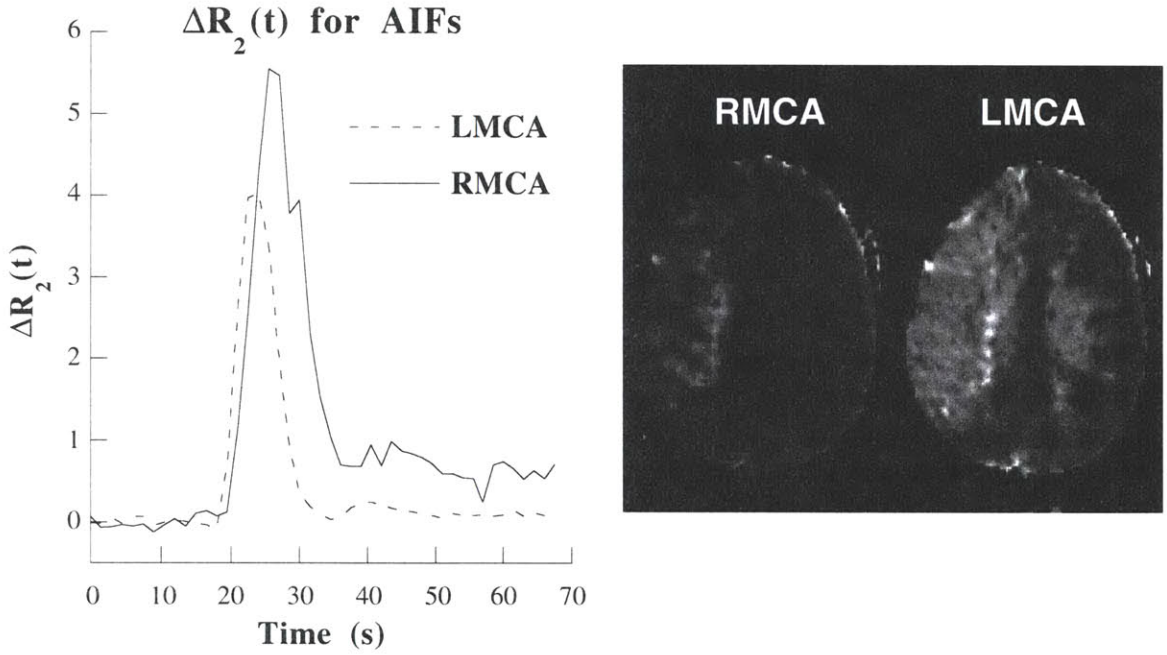

Figure 3.2.1 Sensitivity of perfusion maps to AIF selection
MTT maps for a 39-year old woman with a history of right internal carotid artery stenosis. The graph shows the measured $\Delta R_2(t)$ for the arterial input functions used to generate the MTT maps. The MTT maps generated using LMCA from the non-diseased hemisphere results in an overestimation of abnormal tissue, whereas the maps made using the RMCA from the diseased hemisphere shows a much smaller area that better correlates with a follow-up PET study (not shown) report of an area of perfusion deficit limited to deep white matter.

previous studies to correlate well with physiologically measured AIFs (6, 12). The analytical expression for the AIF was:

$$C_a(t) = \begin{cases} 0 & t \le t_0 \\ (t - t_0)^r \; e^{-(t-t_0)/s} & t > t_0 \end{cases} \qquad \textbf{(3.2.1.1)}$$

with r=3.0 and s=1.5 s representative of data from normal adult volunteers. t_0=20 s with maximum t=200 s to insure $C(t)$ was not truncated for the longest MTT used in this study (24 s). By assuming the vasculature bed was a single well-mixed compartment (6, 12), the residue function was modeled as:

$$R(t) = e^{-t/\mathrm{MTT}}. \qquad \textbf{(3.2.1.2)}$$

The tissue concentration curves, $C(t)$, were generated using Eqn. 3.1.6 in conjunction with Eqn. 3.2.1.1 and Eqn. 3.2.1.2. Flow values were varied between 10-70 ml/100 g/min. Blood volume was kept constant at either 4% or 2%, values that are typical for gray and white matter respectively (6). MTT was calculated using Eqn. 3.1.15 and then used to estimate the residue function according to Eqn. 3.2.1.2. Signal enhancement curves were generated by combining Eqn. 3.1.1, Eqn. 3.1.2 and Eqn. 3.1.6 with the simulated $C(t)$:

$$S(t) = S_0 \, e^{-k\,C(t)\,\mathrm{TE}}. \qquad \textbf{(3.2.1.3)}$$

S_0 was set to 100. The proportionality constant, k, was determined from the desired peak drop in the signal enhancement curve. For all simulations, a k was selected that resulted in a 40% change at a flow rate of 60 ml/100 g/min, corresponding to values measured in human gray matter and used in other previously published reports (6, 12). The signal enhancement curve for the arterial input function, $S_a(t)$, was similarly simulated using Eqn. 3.2.1.3, substituting $C_a(t)$ for $C(t)$. The proportionality constant, k, in this respect was selected to generate a peak signal change of 60%, typically measured signal reductions for selected AIFs at this institution using double-dose spin-echo perfusion imaging. The sampling rate (TR) was set to 1 sec with a TE=65 ms.

To evaluate the sensitivity of the flow estimation techniques to delay times, $S(t)$ was shifted -5 to +5 seconds in time. In a previous study $S(t)$ was delayed up to maximally 6 seconds (6), however, S(t) was not shifted forward in time such that $S(t)$ led the $S_a(t)$. Such a condition can potentially occur naturally if the AIF is selected downstream from a stenotic vessel, as in the case of ICA stenosis and therefore such conditions were modeled in our study. This study investigates shifts in both directions. No noise was added to $S(t)$ in order to better evaluate the effects of delay on flow estimates independent of noise contamination.

Effects of delay in AIF in acquired human data

Effects of delay in clinically acquired human data are examined by artificially shifting a measured AIF with respect to tissue arrival curves. CBF and MTT are calculated for each shift using techniques described in Section 3.1. Using methods described in Section 3.1, dynamic susceptibility contrast weighted images were obtained by acquiring spin-echo (SE) EPI images within 10 hours of symptom onset of left-sided weakness in a 65-year old male patient with a

history of right internal carotid artery stenosis and who was diagnosed with right middle cerebral artery (RMCA) stroke.

Results

Monte Carlo Simulations

Figure 3.2.1.1 shows the result of simulations assuming noiseless data. An example of the simulated AIF and simulated *C(t)* are shown for time shift of -5 s and 5 s (A). The ratio of the estimated flow using standard deconvolution is shown in (B). The flow estimate is persistently underestimated for short MTTs. For long MTTs, flow is grossly overestimated for negative shifts but flow is accurately estimated for positive delays. When $C_a(t)$ leads *C(t)* (positive shifts), we see a persistent underestimation of flow for all shifts, with slight oscillation. When $C_a(t)$ lags *C(t)* (negative shifts), however, flow is both overestimated and underestimated depending on the MTT and length of shift.

Effects of delay in AIF in acquired human data

Figure 3.2.1.2 shows acute CBV and DWI maps acquired within 10 hours of symptom onset along with the one-year follow-up (F/U) T_2 FSE study for a 65-year old male with a history of right ICA stenosis presenting with symptoms of left-sided weakness and diagnosed with right

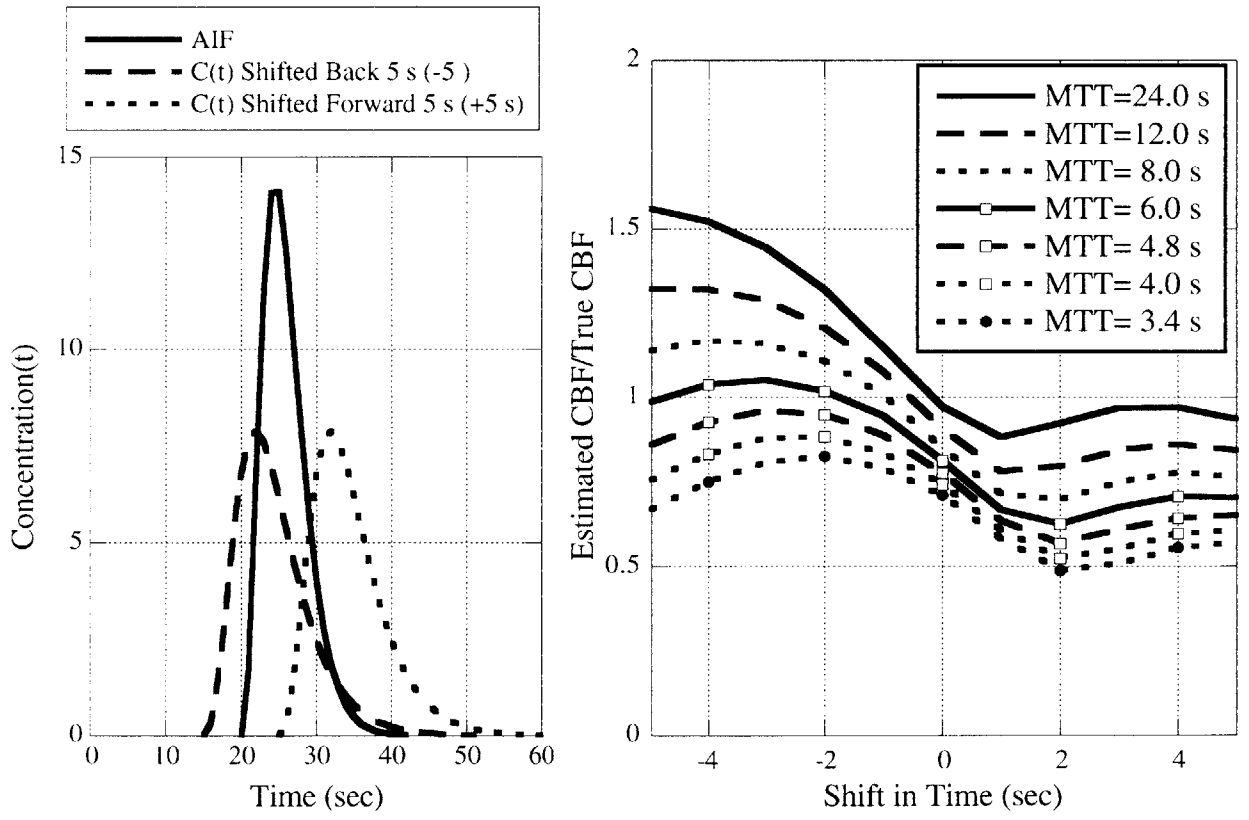

Figure 3.2.1.1 Effects of time shifts between AIF and concentration versus time curve assuming noiseless data.
(A) Example AIF and *C(t)* curves. (B) Ratio of estimated flow using standard linear deconvolution to its true flow value as a function of timing shift.

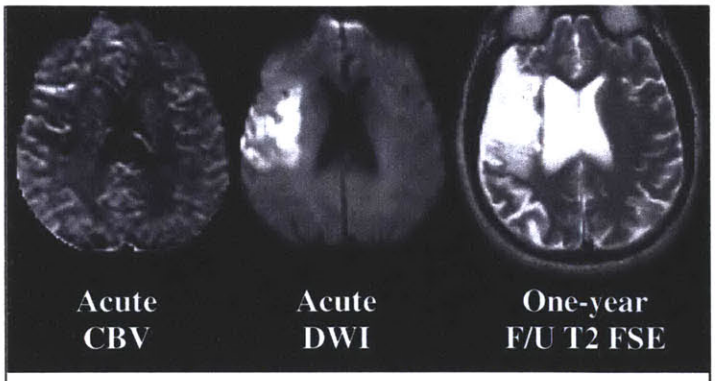

Figure 3.2.1.2 Acute DWI imaged within 10 hours of symptom onset and 1 year follow-up study for a 65 year-old male presenting with symptoms of left-sided weakness.

MCA stroke. Based on the follow-up study, the initial lesion volume seen in the acute DWI is observed to have grown slightly.

Figure 3.2.1.3 shows the estimated CBF and MTT maps acquired in the same scan session as the acute DWI. The AIF selected from the right MCA in the diseased hemisphere was artificially shifted forward and backward in time and CBF and MTT maps calculated. Also shown are the concentration versus time curves for two 5×5 regions of interest, one outlined in the ipsilateral affected right hemisphere

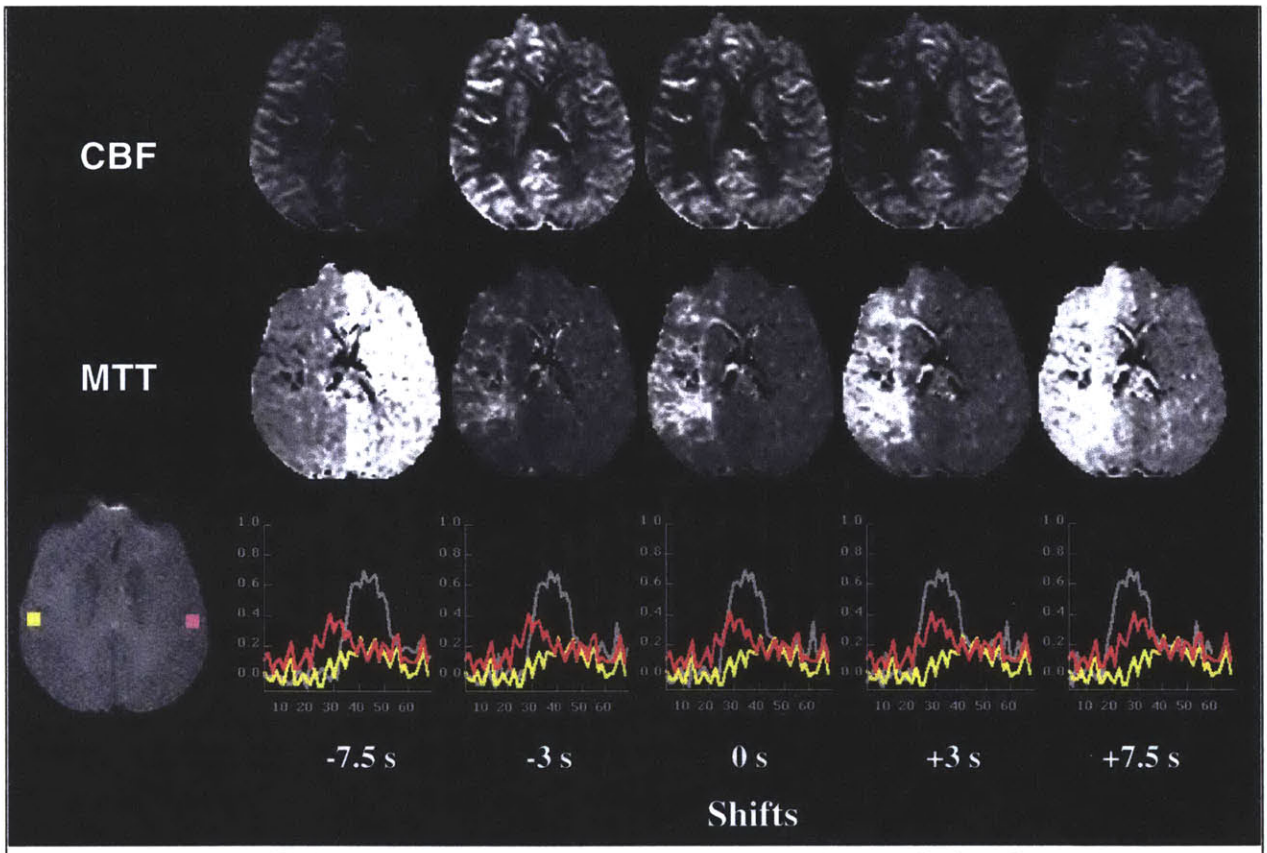

Figure 3.2.1.3 Artificially shifting the AIF with respect to the voxel signals can lead to both over and under estimation of flow.
The bottom row shows the RMCA AIF and average signals in the two ROIs, one drawn in the ipsilateral diseased right hemisphere (yellow-ROI1) and one in the contralateral normal appearing left hemisphere (magenta-ROI2). Each column represents the estimated flow and MTT and signals for a particular shift of the AIF. One sees that the area of abnormality changes considerably as the AIFs relative position to the $C_v(t)$ changes.

(yellow–ROI1) and one outlined in the contralateral normal appearing left hemisphere (magenta–ROI2). Each column represents the calculated CBF and MTT for each shift along with the AIF signal with respect to each ROI signal. All images are scaled using the same dynamic range for better comparison. The middle column shows the CBF and MTT maps that is calculated if the AIF is not shifted. One sees that the final infarct volume (Figure 3.2.1.2) correlates well with the perfusion defect seen in both the CBF and MTT maps in the middle column. However, if the AIF is advanced forward in time to an extent such that it lags the ROI2 signal, CBF is underestimated and the wrong hemisphere may even be identified as tissue at risk (Figure 3.2.1.3 -7.5 s). Even for time shifts as small as -3 s, one can potentially underestimate the volume of tissue at risk since some of the surrounding tissue in the affected hemisphere appears hyperintense, suggesting overestimation of flow in those regions. This is consistent with our results for the Monte Carlo simulations for negative shifts (Figure 3.2.1.1). Furthermore, if one decides to shift the AIF backwards in time in an attempt to ensure that the AIF will not lag a *C(t)* signal, one may overestimate the volume of tissue at risk of infarction due to underestimation of flow as a result of positive timing shifts (as is seen in Figure 3.2.1.3 +7.5 s).

Although in the example presented in Figure 3.2.1.3 the AIF was artificially manipulated, such delays may occur naturally due to the fact that the measure AIF is not the true AIF. From the time course graphs in Figure 3.2.1.3 one sees that ROI1 not only has smaller amplitude than ROI2, but also lags ROI2, potentially due to the patient's angiographically diagnosed right ICA stenosis. Figure 3.2.1.4 shows the estimated CBF and MTT using the left MCA from the non-diseased hemisphere as an arterial input function. These maps appear similar to the maps in Figure 3.2.1.3 generated when the RMCA AIF selected from the diseased hemisphere leads the

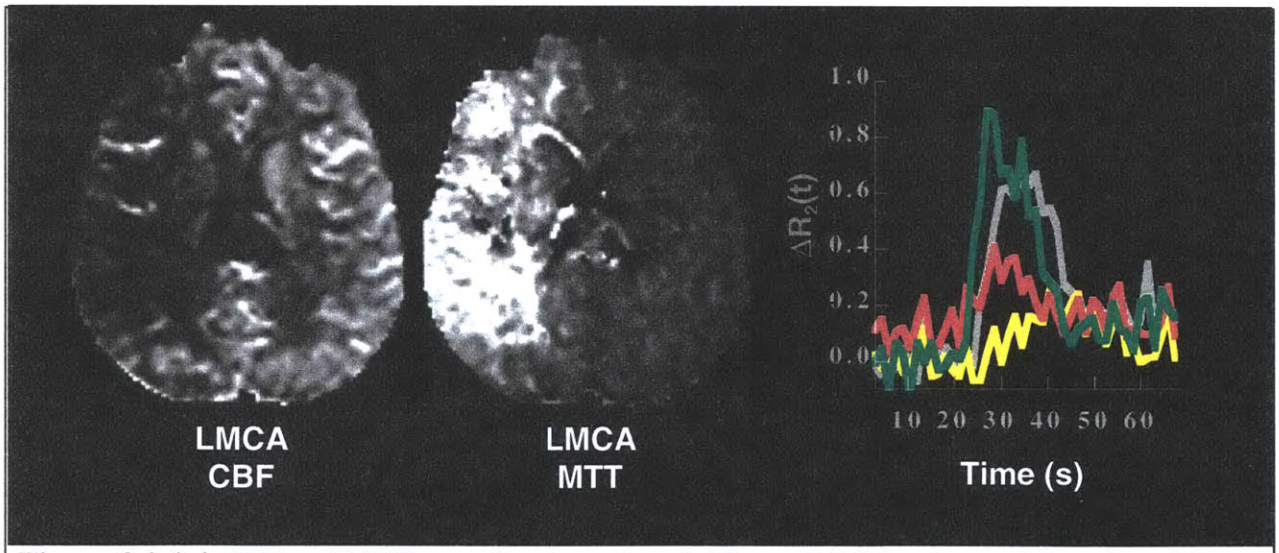

Figure 3.2.1.4 CBF and MTT maps for the patient in Figure 3.2.1.3 using an AIF selected from the left MCA in the non-diseased hemisphere. Comparing the CBF and MTT maps in this figure with those in Fig 3.2.1.3, one sees that these maps appear similar to those generated when the RMCA AIF selected from the diseased hemisphere leads the tissue curves by 3 s (+3s). Also shown is the time course for the LMCA AIF (green) overlaid on the RMCA AIF (gray) and left (magenta) and right (yellow) ROIs' (shown in Fig 3.2.1.3) time courses. The LMCA AIF (green) is slightly shifted in time with respect to the other curves, corresponding well to the time course when the RMCA AIF leads the time curves by +3s.

tissue curves by 3 s (+3s). The time course is also shown for the LMCA AIF (green) overlaid on the RMCA AIF (gray) and left (magenta) and right (yellow) ROIs' (shown in Figure 3.2.1.3) time courses. From this graph, the left MCA AIF (green) is observed to lead the right MCA AIF (gray) most likely due to less-delayed tracer arrival and appears much like the time course graph in Figure 3.2.1.3 at +3s.

Discussion

We have shown that delay between the arterial input function and measured tissue signal can result in inaccurate estimation of flow regardless of SNR. This is consistent with findings from other reports (6, 12). This is the first study that investigates the condition when the AIF lags the tissue signal, a situation that may occur naturally when the AIF is selected downstream from an occlusion. Therefore, with the existing technique, relative flows within an imaging session may not be accurate since a shifted AIF may result in overestimated CBF in some voxels and underestimated CBF in other voxels. As a result, oligemic tissue may be incorrectly diagnosed as ischemic. This has implications in clinical settings where the mismatch between DWI and PWI lesion volumes may be overestimated resulting in greater amounts of tissue categorized as at risk of infarction than is truly at risk.

Naïve approaches that grossly shift the AIF may result in flow estimates being over or underestimated if the amount of shift is not accurate. For example, to avoid negative shifts, one may be tempted to shift the AIF back in time such that it always leads the tissue curve. However, this may result in the overestimation of tissue volume at risk of infarction due to underestimation of flow, as seen in Figure 3.2.1.3. Ideally, as the delay is variable across voxels, such a correction technique would need to be on an individual voxel-by-voxel basis. Correcting for timing shifts on an individual voxel basis is a difficult task and may also be sensitive to noise. It may also be complicated by the sampling rate currently available due to TR limitations. For example, if the time shifts between the tissue concentration curve and the AIF were less than the sampling rate, accurate time shift corrections would be difficult without interpolating the acquired data. The degree of interpolation may require an *a priori* estimate of minimum expected time shift that is typically not readily available. A better technique, perhaps would be one which is insensitive to timing shifts between the $C(t)$ and AIF.

3.2.2. Correcting for and estimating delay between AIF and tissue curve

As shown in the previous section, the current SVD technique is sensitive to timing shifts between the tissue curve, $C(t)$ and the AIF which can lead to both overestimation and underestimation of flows. In this section, an extension is proposed of the standard SVD technique to a deconvolution technique with a block-circulant matrix whose flow estimates are delay invariant. To compare this new method with the existing deconvolution technique we use Monte Carlo simulations where "true" CBF is known. Since the performance of both techniques depend on the selection of free parameters to discard singular values, the performance of the two models are first evaluated as a function of the free parameters assuming zero delay between the AIF and tissue time course curves and a threshold selected which minimizes bias. Having selected optimum parameters for the respective techniques, the performances of the different deconvolution techniques are then evaluated as a function of simulated SNR and timing shifts. The performances are evaluated as a function of both mean and standard deviation of the bias of

estimated flows from true flows. The distribution of the bias is also examined when assuming no timing delay in order to determine if the algorithms systematically underestimate or overestimate high or low flow values. This analysis is repeated for estimates of timing delay between the AIF and $C(t)$. The performance of these techniques will also be evaluated qualitatively on clinically acquired human data.

Methods

Deconvolution using a block-circulant matrix

One of the limitations of Eqn. 3.1.8 is the assumption of causality. This assumption is violated when $C_a(t)$ lags $C(t)$ as shown in Figure 3.2.2.1 and which may occur naturally as described in the previous section . In this condition, the measured $C_a'(t)=C_a(t-t_0)$. Therefore, the calculated $R'(t)=R(t+t_0)$ for $C(t)$. By using circular convolution, instead of linear convolution, $R'(t)$ will be $R(t+t_0)$ circularly time shifted by t_0. Circular convolution is equivalent to linear convolution with time aliasing (21). If one assumes that the signal was sampled for a sufficient duration such that $C(t)$ is not truncated, then time aliasing will not be a consideration. In addition, by zero-padding the N-point time series $C_a(t)$ and $C(t)$ to length L, where $L \geq 2N-1$, time aliasing can be avoided. Therefore, replacing matrix **A** in Eqn. 3.1.8 and Eqn. 3.1.9 with a block-circulant matrix, **D**:

$$\mathbf{D} = \begin{pmatrix} a_{1,1} & a_{L,1} & \cdots & a_{2,1} \\ a_{2,1} & a_{2,2} & \cdots & a_{3,1} \\ \vdots & \vdots & \ddots & \vdots \\ a_{L,1} & a_{L-1,2} & \cdots & a_{L,L} \end{pmatrix} \qquad \textbf{(3.2.2.1)}$$

Eqn. 3.1.9 can be reformulated as:

$$\mathbf{g} = F_t\, \mathbf{D} \cdot \mathbf{f}, \qquad \textbf{(3.2.2.2)}$$

where **g** is the zero-padded **c** and **f** is the residue function to be determined. However, a more accurate representation of the signal to be measured can be obtained by modifying Eqn. 3.2.2.2

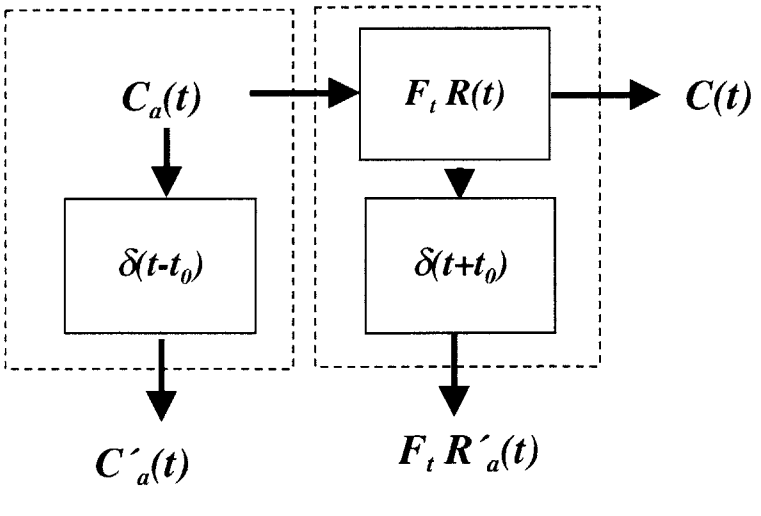

Figure 3.2.2.1 Block diagram of measured AIF that is delayed with respect to true $C_a(t)$. The calculated residue function will be shifted the reverse direction.

to take into consideration the presence of noise, **w**, in the measurement of **f**:

$$\mathbf{g} = F_t\ \mathbf{D} \cdot \mathbf{f} + \mathbf{w}. \qquad \textbf{(3.2.2.3)}$$

As a result, simply multiplying by the inverse matrix **D**, which will still be ill-conditioned if **A** was ill-conditioned, will result in noise amplification if one assumes **w** is white noise:

$$\mathbf{f}' = F_t\ \mathbf{f} + \mathbf{D}^{-1}\mathbf{w} \qquad \textbf{(3.2.2.4)}$$

resulting in **f′**, the estimated residue function, differing greatly from **f**, the true residue function. Therefore, one can again make use of singular value decomposition techniques to solve for **f** substituting **D** for **A** and **g** for **c**.

When using circular deconvolution, however, due to the discontinuity between $t=0$ and $t=L$, leakage frequencies may be amplified giving rise to spurious oscillations dominating the deconvolved signal (20). Increasing the cutoff in the SVD decomposition can reduce these oscillations. Using a modified oscillation index from that described by Gobbel (22):

$$O = \frac{1}{L}\frac{1}{f'_{\max}}\left(\sum_{k=1}^{L} f'[k] - f'[k-1]\right) \qquad \textbf{(3.2.2.5)}$$

where **f′(t)** is the estimated residue function and L is the number of sample points, the SVD threshold was varied until the estimated residue function's oscillation index fell below a user specified value.

Monte Carlo Simulations

Tissue signals, $S(t)$ and $S_a(t)$ were simulated using the same techniques described in Section 3.2.1. To evaluate the performance of the deconvolution algorithms in the presence of noise, the signal-to-noise ratio (SNR) was varied between infinity (no noise) to 10 by adding noise to the real and imaginary components of the noise-free $S_a(t)$ and $S(t)$ (23). These random noise values were normally distributed with a mean of zero and variances ranging from 1 to 10. The magnitude of the complex data with added noise was then used in the simulations. For each level of SNR, 1024 iterations were performed, except for the noiseless condition where only two iterations were used to demonstrate that the results did not change over iterations. The same noisy signal was used by each of the techniques for each shift in each iteration.

The performances of standard SVD, corrected SVD (cSVD) and corrected SVD with minimal oscillation index (oSVD) were evaluated as a function of bias and variance. The error at each iteration, i, was calculated as the sum of the absolute difference between calculated flow values (F') from true flow values (F) over the range of simulated flow values (10 to 70 ml/100 g/min) at delays ranging from -5 to 5 s:

$$\text{Error} = \sum_{F} |F' - F| . \qquad \textbf{(3.2.2.6)}$$

The bias or mean, and standard deviation of the error over all N iterations were calculated and compared as a function of shift for the different SNR levels:

$$\text{Bias} = \frac{1}{N}\sum_{t=1}^{N} \text{Error}_t . \qquad \textbf{(3.2.2.7)}$$

One can then estimate the amount each flow estimate differs from its true flow value by dividing Bias by the number of flow values evaluated, in this case seven.

The performances of SVD, cSVD and oSVD depend on the selection of free parameters. For SVD and cSVD, the selection of the cutoff threshold or tolerance level of values considered close to singular determines the accuracy of the deconvolved residue function. A threshold that is too low can result in instability as the matrix becomes close to singular while a threshold that is too high will result in not enough values used for accurately determining the residue function. For the oSVD, the choice of minimal oscillation index also affects the accuracy of the deconvolved residue function. In this case a high threshold results in instability and a low threshold in insufficient values for calculating the residue function accurately. At each noise level, for SVD and cSVD, the cutoff threshold was varied between 1 and 95% whereas for oSVD, the minimum oscillation index was varied between 0.001 and 0.2. The bias is evaluated as a function of threshold and noise for the condition of no time shift. The threshold that produced the minimum bias at each noise level is then used in the remaining simulations where the tissue curves are shifted with respect to the AIF.

Delay was estimated as the time point when the maximum $R(t)$ occurs. For the circular deconvolution techniques, the following algorithm was used to estimate shift, D':

$$D' = \begin{cases} k \cdot \text{TR} & k \le N/2 \\ (k - N) \cdot \text{TR} & k > N/2 \end{cases} \qquad \textbf{(3.2.2.8)}$$

assuming k is the sample when the maximum $R(t)$ occurs and N is the total number of points. For standard deconvolution, $D'=k$. The calculation of the error in the delay estimate is similar to that used for the flow estimate (Eqn. 3.2.2.6):

$$\text{Delay error} = \sum_{D} |D' - D| \qquad \textbf{(3.2.2.9)}$$

where the absolute error between estimated D' and true D are summed over all applied shifts. The same tolerance level or minimum oscillation index used for estimating flow was used to estimate delay. The bias of the delay estimate was taken as the mean of the delay error over all iterations and the deviance as the standard deviation of the error over all iterations:

$$\text{Delay Bias} = \frac{1}{N}\sum_{t=1}^{N} \text{Delay Error}_t . \qquad \textbf{(3.2.2.10)}$$

To estimate the amount each delay estimate differs from its true delay value, one can divide by the number of shifts evaluated, in this case eleven.

Assessments of error of fit are also estimated on individual voxel bases by calculating the error of the fitted $C(t)$ compared to the measured $C(t)$:

$$\text{EOF} = \sum_{i}^{L}\left(\left(\Delta t\, F_t \sum_{j}^{i} C_a(j)\; R(j-i)\right) - C(i)\right)^2 \qquad \textbf{(3.2.2.11)}$$

where $R(t)$ is the deconvolved residue function, $C_a(t)$ is the user defined AIF, Δt is the sampling rate, F_t is the estimated flow and $C(t)$ is the concentration versus time curve. A larger EOF value represents a larger error between fitted signal and the measured signal and therefore a reflection of poorer fit.

Image Acquisition

Dynamic susceptibility contrast weighted images were obtained by acquiring spin-echo (SE) EPI or gradient echo (GRE) images as described in Section 3.1. All data analysis was performed retrospectively. Due to the retrospective nature of this study, which spanned over the years 1996 until 2001, imaging was performed on a variety of platforms. The imaging hardware consisted of 1.5 T with 5.4.2 software (Signa; GE Medical Systems, Milwaukee, Wis.) and 3.0 T MR instrument with EPI capabilities by means of a hardware upgrade (ANMR, Wilmington, MA), including "catch and hold" modification. On the 3.0 T system, single doses of gadolinium contrast agent were used. Imaging was also performed on a 1.5T GE Signa Horizon LX (GE Medical Systems, Milwaukee, Wis.) system with echo planar imaging capabilities. On the LX systems, TR/TE=1520/65 ms and a FOV of 22×22 cm^2 or 20×20 cm^2 and acquisition matrix of 128×128 was used with slice thickness of 6 mm and interslice gap of 1 mm. All perfusion studies on the LX were SE EPI. Studies were performed on 1.5 T unless otherwise noted.

Results

Monte Carlo Simulations

Figure 3.2.2.2 shows the bias and variance as a function of tolerance and noise levels assuming no delay for standard deconvolution (SVD) and deconvolution with the block-circulant matrix (cSVD). The effects of choice of oscillation cutoff for deconvolution with the block-circulant matrix with minimum oscillation (oSVD) are also shown. The x-axis is reversed for oSVD in order to be consistent with the SVD and cSVD graphs that are plotted as functions of increasing stringency. Each graph shows the bias and variance at SNR=infinity (i.e. no noise), SNR=100, SNR=50, SNR=20 and SNR=10. As expected, with increasing stringency, the deviance of the estimations is reduced. For bias, there is a tolerance value that minimizes bias at each noise level. Selecting a tolerance value that is too low not only results in greater variance of the flow estimate but also results in greater bias as the matrix in the SVD stays ill-conditioned. A tolerance cutoff that is too high also results in increased bias as too many values are considered singular and removed, therefore leaving not enough values to accurately characterize the matrix. The tolerance cutoff that minimizes bias is observed to increase as a function of noise. The threshold for cSVD is lower than for SVD, but the resulting bias is larger in cSVD. The minimum bias for

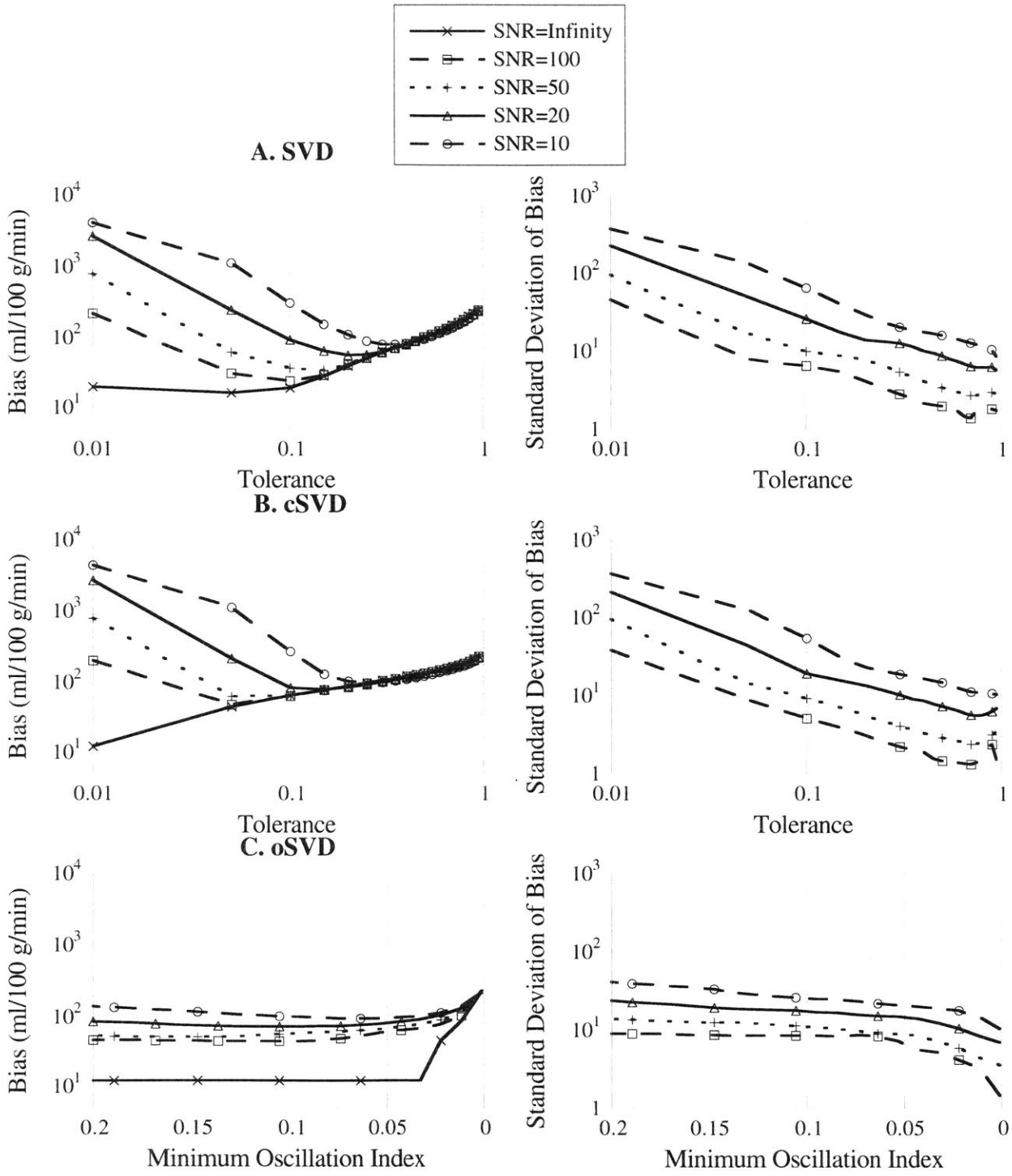

Figure 3.2.2.2 Bias (first column) and deviance (second column) of flow estimates assuming zero time delay for (A) standard SVD, (B) cSVD and (C) oSVD techniques. The deviance for SNR=Infinity was zero for all techniques. Minimum oscillation index is plotted on reverse x-axis to demonstrate effects of increasing stringency.

oSVD is comparable in magnitude to that of SVD, though oSVD's variance is larger. In oSVD, minimizing oscillations reduces variance in the flow estimates; however, this is at the cost of larger bias.

Figure 3.2.2.3 shows the estimated bias as a function of timing shift and noise for the standard decovolution technique (SVD), for the circular deconvolution (cSVD) and for the circular deconvolution with minimization of oscillation index (oSVD) (Eqn. 3.2.2.5) for SNR levels of (A) infinity, (B) SNR=100, (C) SNR=50, (D) SNR=20 and (E) SNR=10. Even when no noise is added, the bias is small (overall Bias=16 or 2.2 ml/100 g/min for each flow estimate for SVD and overall Bias=12 or 1.7 ml/100 g/min for cSVD and oSVD) but not zero, due to the pre-filtering of the AIF function that produces more accurate flow estimates in the presence of noise and coarse sampling (12) but distorts the estimate when no noise is present. From the graphs, one notes that when the delay is zero and in the presence of noise, standard deconvolution (SVD) provides the best estimate in terms of bias. However, in the presence of timing shifts, bias is observed to depend on the magnitude of the delay and can be quite considerable. Interestingly, as the SNR decreases, the amount of bias due to negative shifts relative to non-delayed bias is reduced, potentially due to the higher tolerance level used to minimize bias for lower SNR as seen in Figure 3.2.2.2. The magnitude of the bias, at zero delay, nonetheless, increases with noise (overall Bias=77 or 11 ml/100 g/min at SNR=10 compared to 2.2 ml/100 g/min at SNR=Infinity). At low SNR, the effects of delay on flow estimation using SVD appears less than the effects due to noise, resulting in apparently less variations as a function of delay. For both circular deconvolution techniques, bias is delay independent but increases with decreasing SNR. For all SNR levels in the presence of noise, oSVD consistently provides less bias than cSVD, for example for SNR=10 overall Bias=91 or 13 ml/100 g/min compared to overall Bias=95 or 13.6 ml/100 g/min.

In terms of variance, oSVD, at low SNR (SNR=10 to 20) has slightly larger variance (Figure 3.2.2.4) than cSVD. For positive or small delays, flow estimates using SVD is observed to have less variance than the other two techniques. However, the amount of variance is again dependent on the magnitude and sign of the timing shift.

Figure 3.2.2.5 plots the estimated flow as a function of true flow assuming zero delay at an SNR=20, a typical SNR for a SE acquired human perfusion study at this center. The overall Bias=77 or 11 ml/100 g/min for cSVD while for oSVD the overall Bias=70 or 10 ml/100 g/min for each flow estimate. However, the difference between estimated flow and true flow is dependent on the flow being estimated, with larger errors for very high and very low flow values. From Figure 3.2.2.5, it is observed that oSVD better characterizes extremely low and high flow rates than cSVD with SVD providing the overall best estimate.

Figure 3.2.2.6 plots the estimated flow as a function of true flow under the same conditions as Figure 3.2.2.5 except a vascular volume of 2% is used. Flows were evaluated over a range from 5 to 35 ml/100 g/min in order to maintain the same range of MTT values used for the previous simulations assuming a vascular volume of 4%. The same tolerance levels and minimum oscillation factors used for Figure 3.2.2.5 were used for Figure 3.2.2.6. cSVD seems to have a stronger dependence on vascular volume, as seen by the larger error for low flow values. On the other hand, both SVD and oSVD have only slightly poorer performance, with oSVD again underestimating high flow values more than SVD.

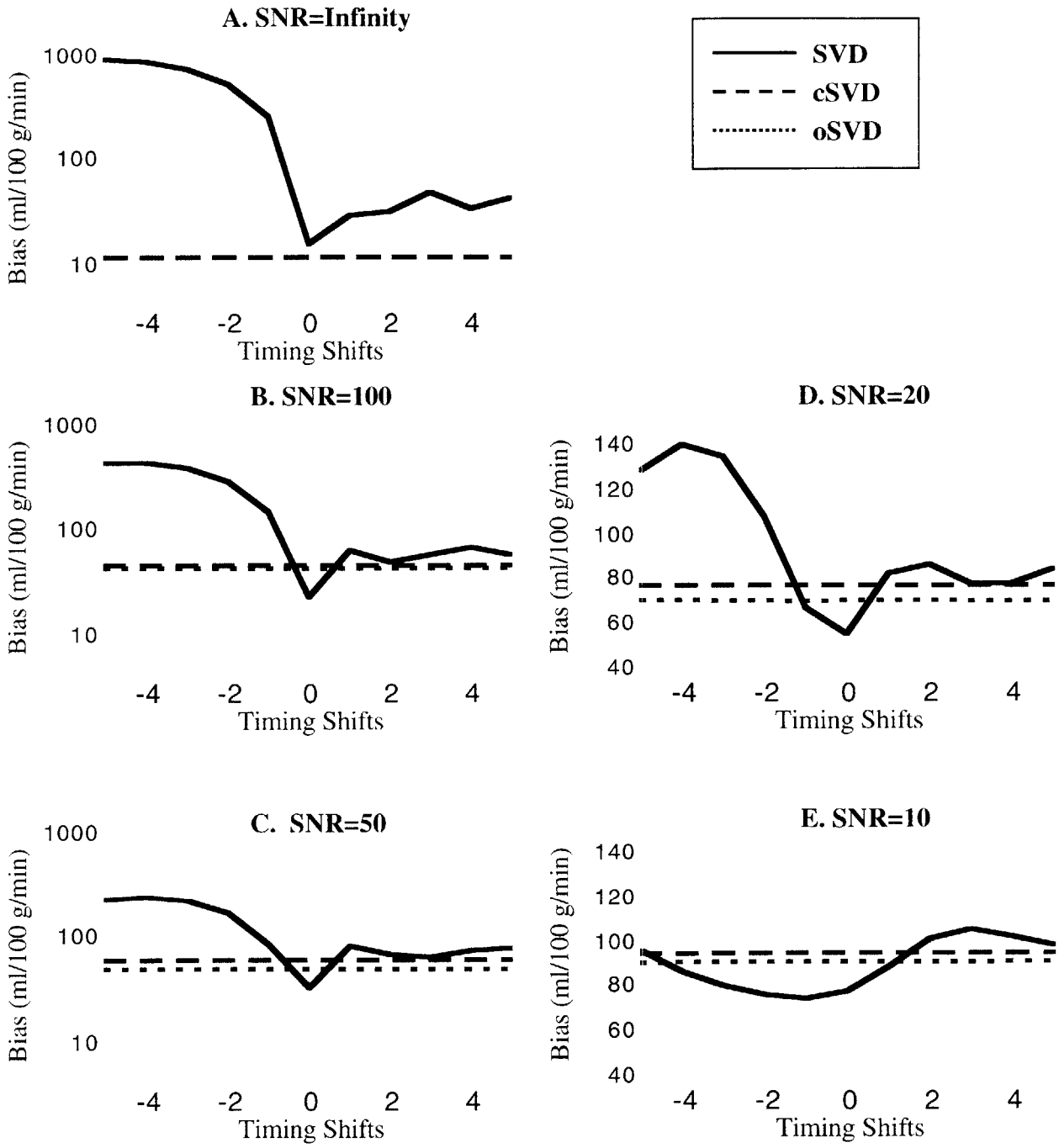

Figure 3.2.2.3 Simulation results for standard linear deconvolution (SVD), circular deconvolution (cSVD), and circular deconvolution with minimization of oscillation index (oSVD) at different SNR levels. In the first column, the bias is plotted on a log scale due to the large range of bias. The second column, with a smaller range of bias as a function of delay, is plotted on a linear scale. Flow estimates using SVD clearly are dependent on delay. Both cSVD and oSVD are independent of shift, with oSVD consistently having the smaller bias in the presence of noise.

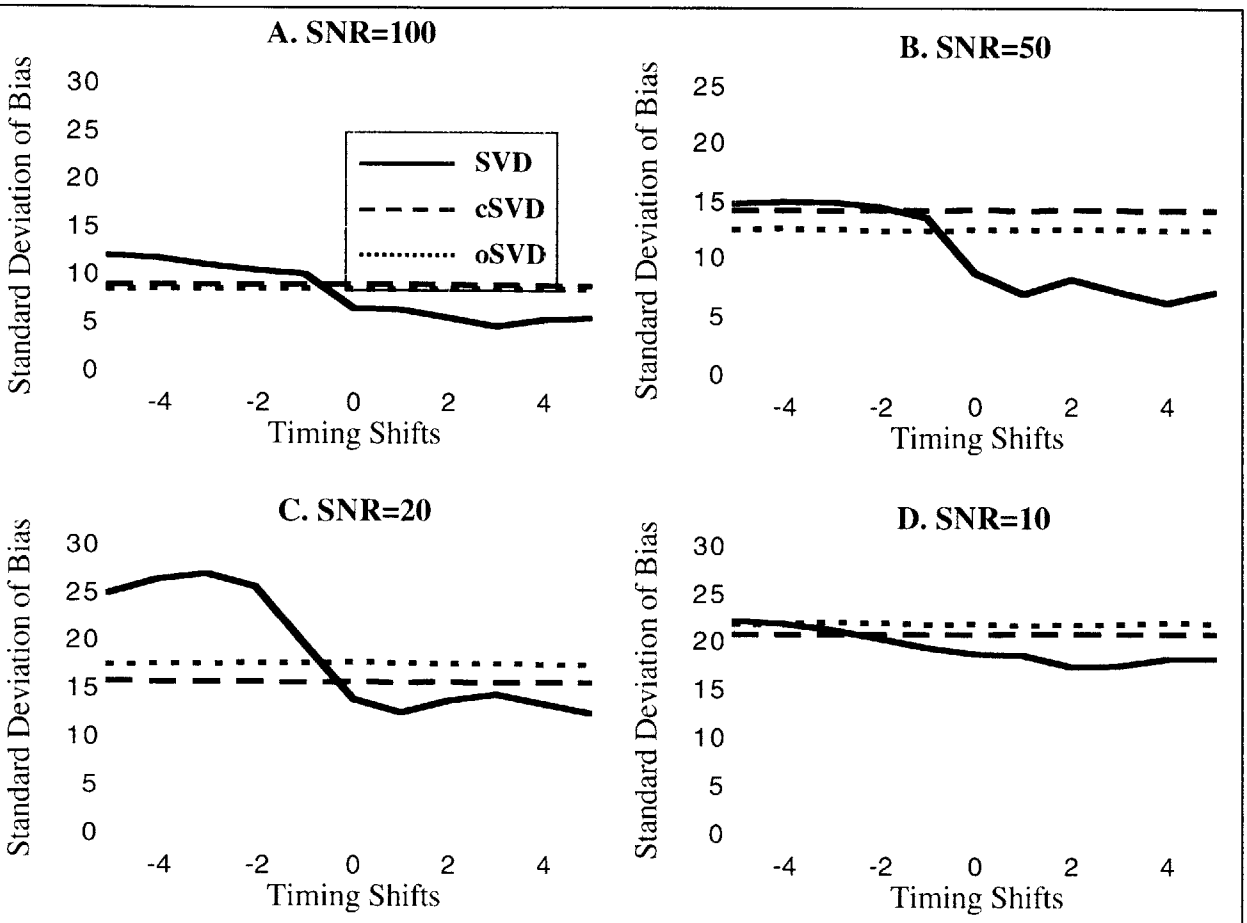

Figure 3.2.2.4 Standard deviation of errors in flow estimations from true flow as a function of delay. The standard deviation for SNR=Infinity was zero for all three techniques (not shown). For SNR=100, the standard deviation of the bias for cSVD and oSVD are superimposed with oSVD slightly reduced. Clearly seen is the delay independence for the deviance of the flow estimation for cSVD and oSVD but not so for SVD where positive timing shifts have smaller variance.

Figure 3.2.2.7 shows the estimated delay using SVD, cSVD and oSVD as a function of flow at SNR levels of (A) infinity, (B) SNR=100, (C) SNR=50, (D) SNR=20, (E) SNR=10. From the graphs, it is noted that estimation of delay is affected by flow rate, with low flow rates producing the worst estimates. For low flows, SVD provides the smallest bias for moderate SNR. For moderate to high flow levels, SVD has a larger bias than the other two techniques. At high SNR, the oSVD and cSVD techniques have better performances at low flow, which suggests that their performances are limited by noise rather than systematic error. Of the two circular deconvolution techniques, oSVD provides less bias over cSVD. Figure 3.2.2.8 shows the standard deviation of the estimated delay where SVD has the least variance. Figure 3.2.2.9 shows the estimated delay at a flow rate of 60 and SNR=20. Both cSVD and oSVD techniques perform comparably. For positive delay values, the SVD technique performs comparably to cSVD and oSVD. However, when the shift is negative, the standard deconvolution technique has a systematic bias since it is unable to distinguish negative time shifts from zero time shifts.

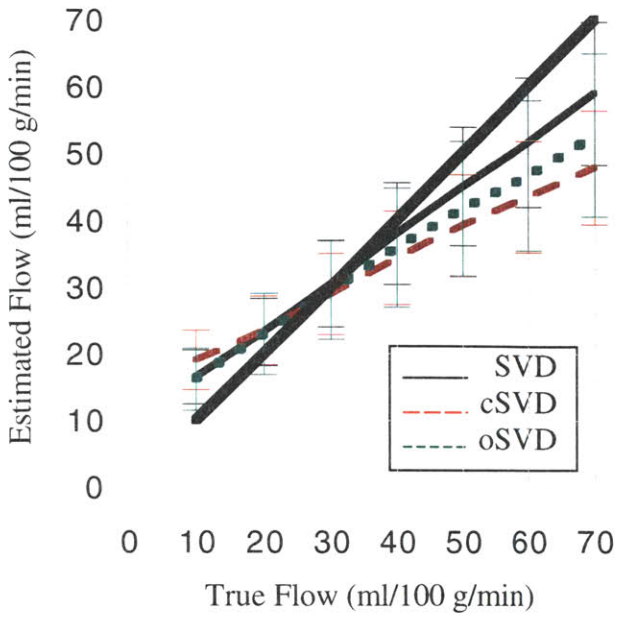

Figure 3.2.2.5 Estimated flow as a function of true flow at SNR=20 assuming no delay between AIF and voxel signal and vascular volume=4%. The oSVD technique is observed to perform comparably to the SVD technique for low flows, however with larger error bars. For high flows the oSVD technique underestimates flows more than the SVD technique. The cSVD technique both overestimates low flow and underestimates high flow values to a greater extent than both SVD and oSVD.

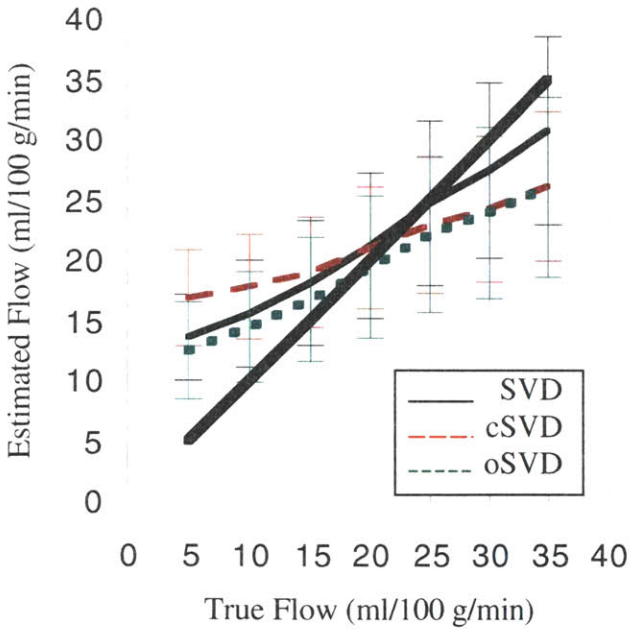

Figure 3.2.2.6 Estimated flow as a function of true flow at SNR=20 assuming no delay between AIF and voxel signal and vascular volume=2%. SVD performs comparably to Figure 3.2.2.5 with volume=4%, with greater overestimation of low flow values. cSVD performs considerably worse, while oSVDs performance is reduced at higher flow values. A lower range of flow values were evaluated in order to compare calculations using the same MTTs as used in Figure 3.2.2.5.

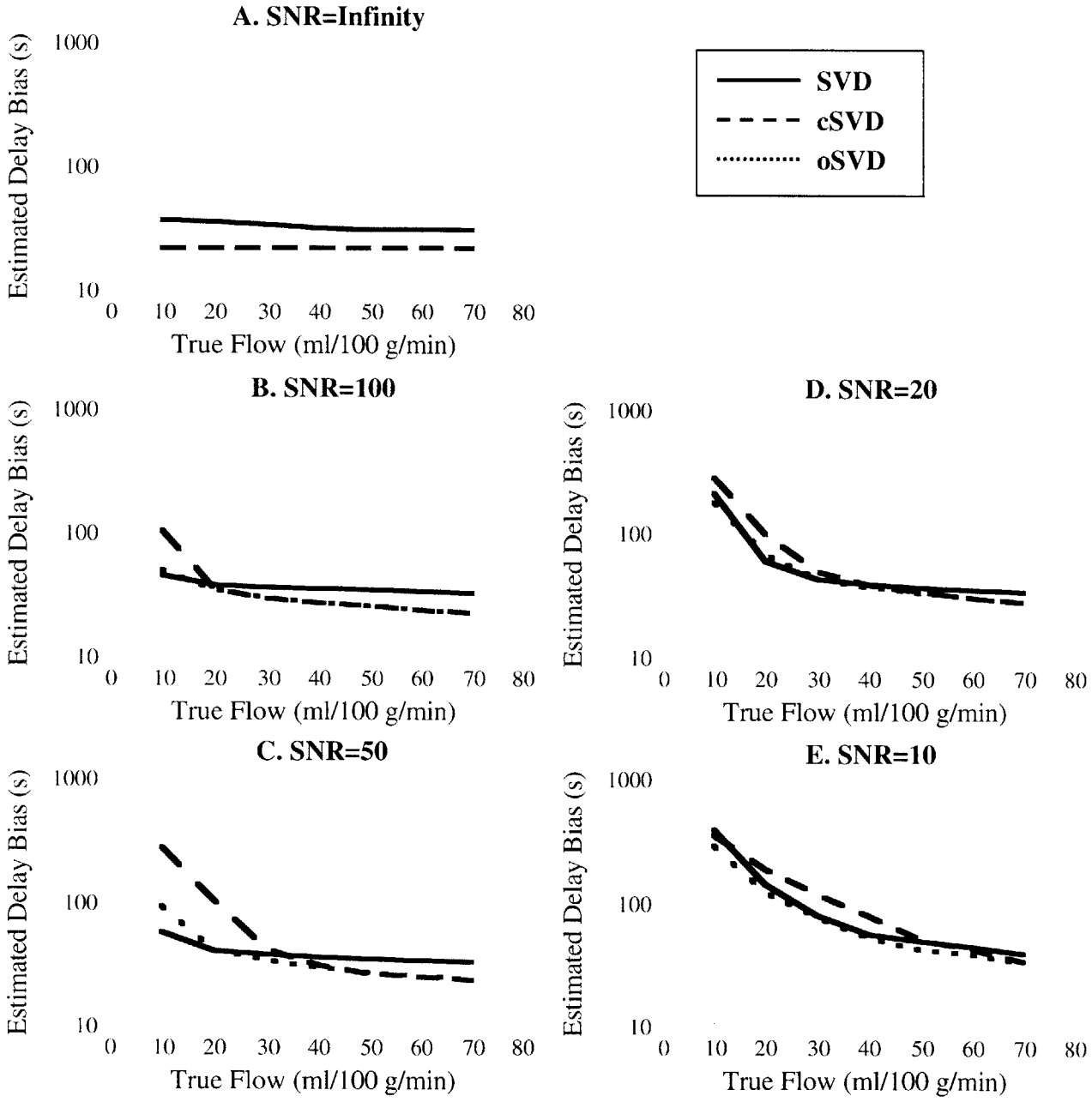

Figure 3.2.2.7 Estimation of delay bias as a function of flow at SNR of (A) infinity, (B) SNR=100, (C) SNR=50, (D) SNR=20 and (E) SNR=10. All abscissas are drawn on a logarithmic scale. Of cSVD and oSVD, oSVD estimates delay with less bias especially at low flow values. For all techniques estimation of delay is affected by flow rate. SVD produces less bias at low flow rates, however this error is summed across all delays.

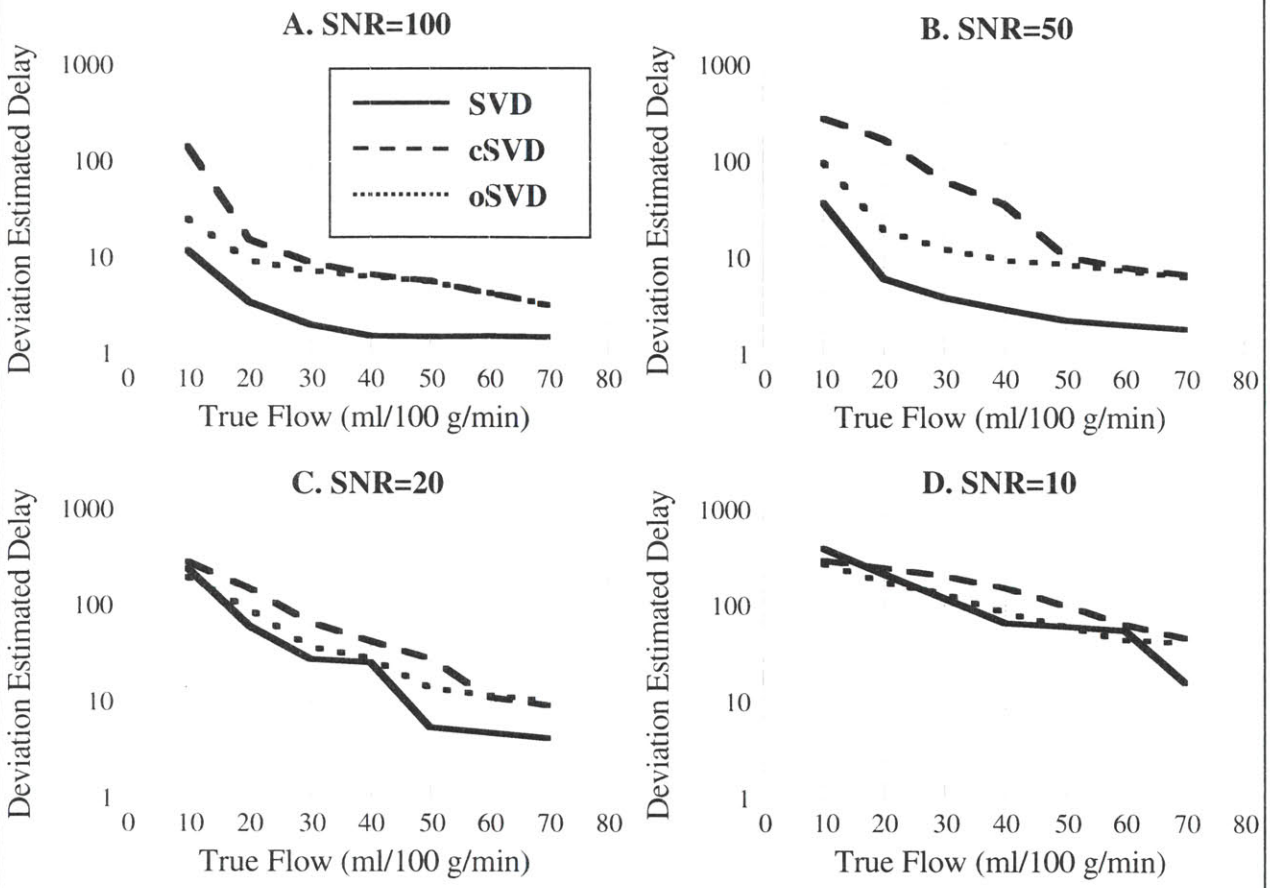

Figure 3.2.2.8 Standard deviation of biases in tracer arrival delay estimates. Standard deviation was zero at SNR=Infinity for all techniques. SVD technique provides the least variance in estimation of delay.

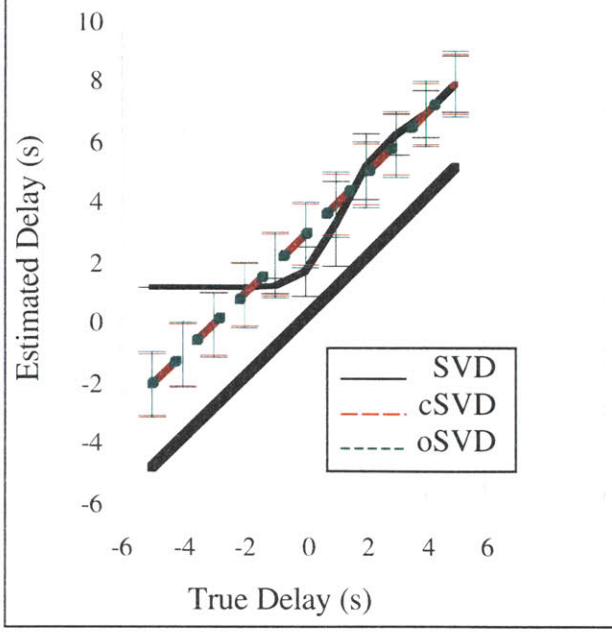

Figure 3.2.2.9 Estimated delay as a function of true delay at SNR=20 and flow value of 60 ml/100 g/min. We see that the oSVD technique performs similar to the cSVD technique. For positive shifts, the SVD technique performs comparably to cSVD and oSVD. However, when the shift is negative, it has a systematic error due to limitations of the technique.

Comparison of SVD and oSVD on clinically acquired human data

To qualitatively compare the performance of the oSVD with SVD technique, we retrospectively evaluated perfusion studies from a 30-year-old healthy female volunteer acquired on a 3.0 T MR system. CBF, MTT, CBV and Delay maps using SVD are shown in the first row of Figure 3.2.2.10. The second row consists of the oSVD results of cCBF, cMTT, cCBV and cDelay maps. All studies were evaluated using the same right MCA AIF. The CBV and cCBV maps are both normal and as expected the two maps appear similar. Consistent with the simulation results, the estimates of cCBF are slightly noisier than that of CBF. However, the uncorrected CBF map shows areas of low flow in the occipital lobes (arrowheads), which are more clearly demonstrated on the MTT map as areas of hyperintensities (arrowheads). In the corrected cCBF and cMTT maps both regions appear normal although they were calculated using the same data set that produced the first row of images. Comparing MTT with cDelay and Delay, however, one observes that the area of hyperintensities in the MTT map correspond to areas with increased delay (arrowheads). This leads one to suspect that the reduced flow is due to delayed tracer arrival compared to the AIF rather than hypoperfusion since the subject was an asymptomatic volunteer who most likely had slower posterior circulation, a normal variant. The EOF appears to be homogeneous for both techniques.

To examine the performance of oSVD in pathologic conditions not involving reduced flow, we retrospectively studied a tumor patient. Figure 3.2.2.11 shows the perfusion maps for a 39-year-old female patient with a history of oligodendroglioma with a left frontal craniotomy and partial resection of the tumor. Using a left MCA AIF, the CBF and cCBF maps appear similar as do MTT and cMTT. As expected CBV and cCBV also appear similar. Both the corrected and uncorrected maps were able to discern the areas of high volume which are indicative of a high grade tumor. A delay is detected in the left hemisphere using both techniques, which may be due to low flow. In simulations results (Figure 3.2.2.7), delay is overestimated in conditions of low flow. The EOF for SVD appears to be more heterogeneous with larger errors in the contralateral hemisphere opposite to where the AIF was selected whereas oSVD appears to be more uniform. This suggests that CBF in regions corresponding to areas with high EOF may be a poorer estimation possibly confounding relative estimates of flow changes.

To examine the effects of a naturally occurring delayed AIF on SVD and oSVD, we retrospectively examine a clinical perfusion study which had markedly different maps depending on the selection of the AIF using SVD. Figure 3.2.2.12 shows the diffusion and perfusion maps for a 12-year-old boy with a history of sickle cell anemia imaged 35 hours after onset of a left middle cerebral artery stroke. Diminished flow in the MRA is clearly seen as well as an area of infarct in the left frontal lobe as evidenced by the region of hyperintensity in the DWI. A slight flow defect is present (arrowhead) in the CBF map constructed using the right MCA for an AIF. However, contrary to previous results, where the ipsilateral AIF produced more accurate estimates of tissue flow, the resulting CBF estimate using the ipsilateral LMCA, in this case, generates a CBF map that suggests either hypoperfusion in the contralateral hemisphere or hyperemia in the ipsilateral hemisphere. Examining the $\Delta R_2(t)$ provides insight into the results. Three 2×2 ROIs were selected in the ipsilateral area of DWI abnormality (ROI 1 – red), ipsilateral normal perfused territory (ROI 2 – blue), and normal contralateral area (ROI 3 – green). From the graphs, one sees that ROI 2 and ROI 3 have the same signal amplitude with

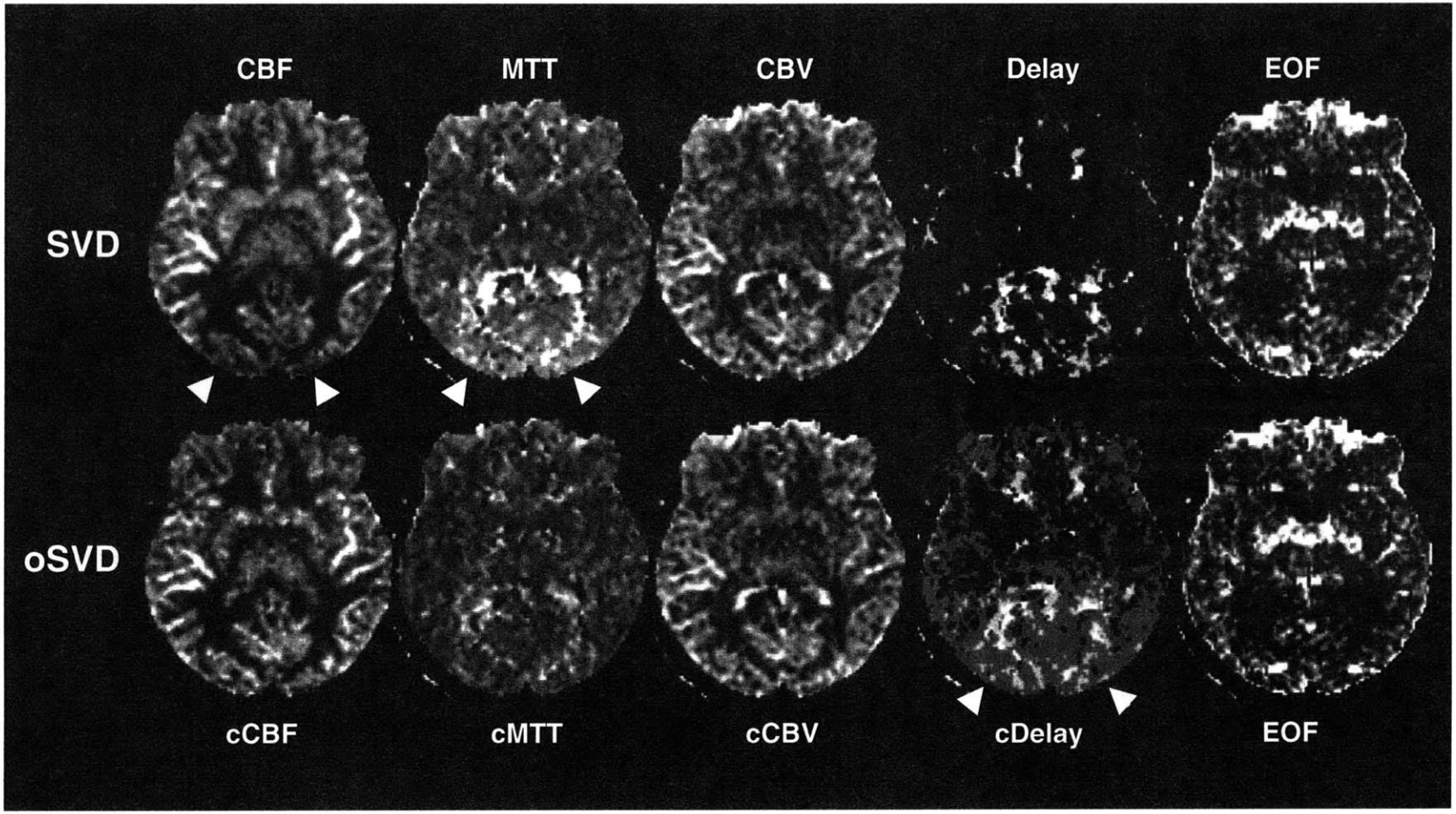

Figure 3.2.2.10 Example case of oSVD showing less artifacts than SVD maps in a normal volunteer.
CBF and MTT for a normal volunteer using both SVD and oSVD techniques with a right MCA AIF. The maps corrected for delay (oSVD) appear more homogeneous than uncorrected maps (SVD). The results using regular SVD appear artificially hypoperfused (arrows) in regions corresponding to delayed tracer arrival (arrows).

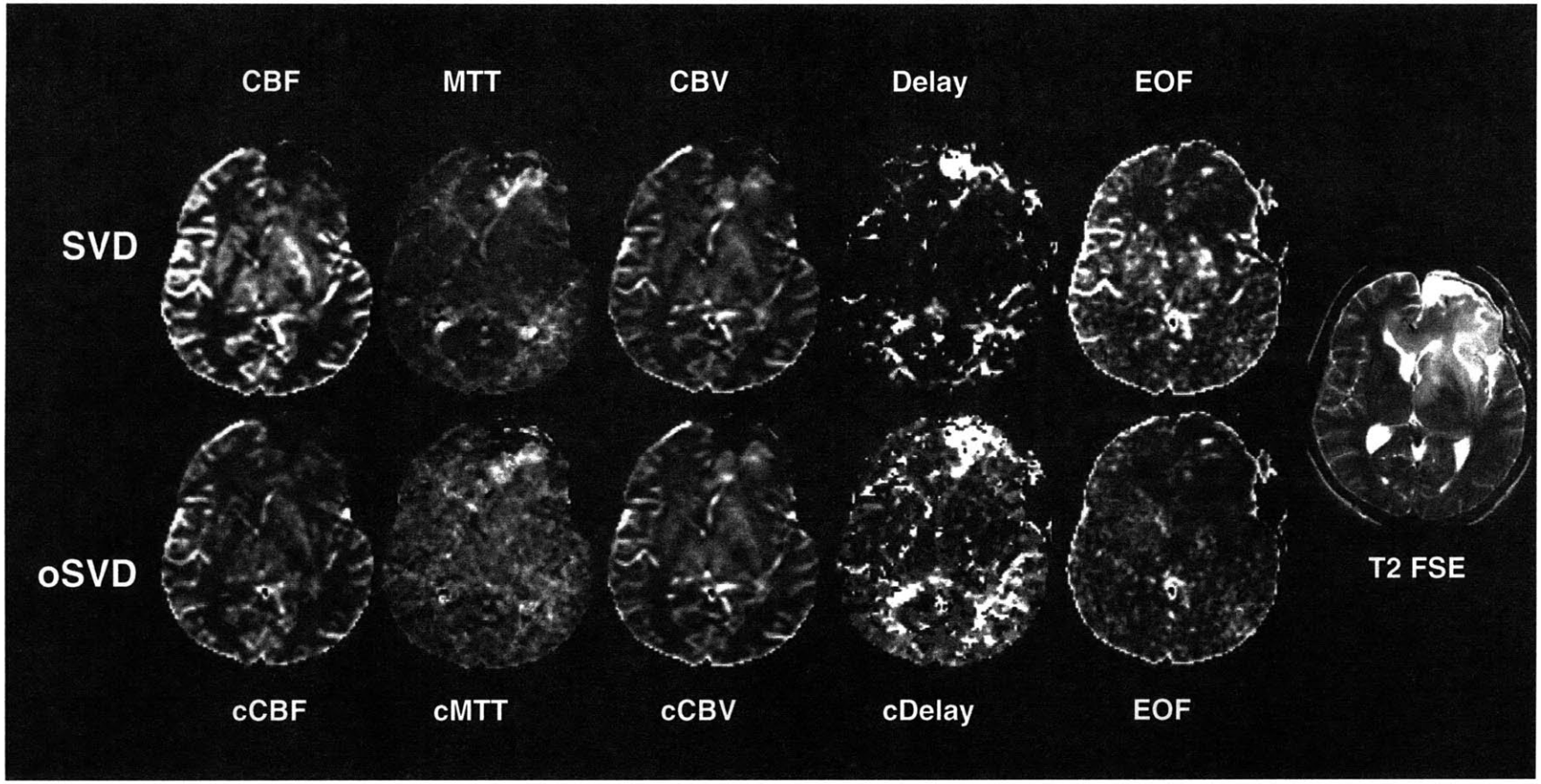

Figure 3.2.2.11 Example case of comparable performance of oSVD and SVD in tumor patient.
Perfusion maps for a 39-year-old female patient with a history of oligodendroglioma and left frontal craniotomy and partial resection of a tumor. Both SVD and oSVD perfusion studies provide similar results using the left MCA AIF. A substantial delay is shown in the left hemisphere, which may be due to the measured low flow in the area.

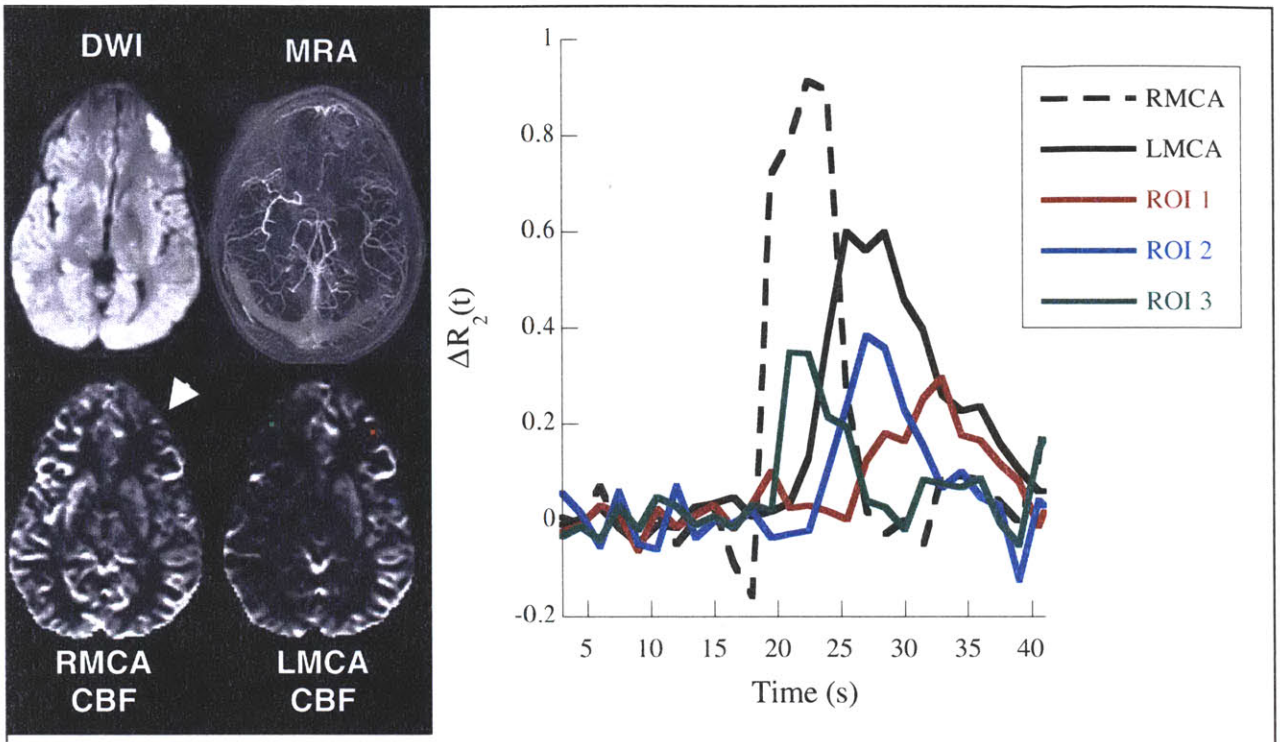

Figure 3.2.2.12 Example case where AIF selection results in different regions of tissue being identified as hypoperfused.
Diffusion and perfusion studies for a 12 year-old sickle cell anemia patient within 35 hours of symptom onset of left MCA stroke. Clearly evident is diminished flow in the MRA as well as an area of infarct in the left frontal lobe (DWI). CBF maps using RMCA and LMCA for the AIF produce very disparate flow estimates. The graph on the left hand side shows the ΔR2(t) for three ROIs: ipsilateral in area of DWI abnormality (ROI 1 - red), ipsilateral normal perfused territory (ROI 2 - blue) and normal contralateral (ROI 3- green).

ROI 2 shifted more in time suggesting that the flow in these two regions should be equivalent, which was not the case in the LMCA CBF maps. ROI 1, however, is also shifted but its amplitude is also reduced which suggests truly reduced flow that is reflected in both RMCA and LMCA CBF. Furthermore, the ROI3 signal curve lags the RMCA AIF but leads the LMCA AIF. Since the LMCA AIF lags ROI 3, we get the behavior predicted by the Monte Carlo simulations.

Figure 3.2.2.13 shows SVD and oSVD maps for this patient using the ipsilateral LMCA for the AIF. His four month follow-up imaging study is shown in the last column. The CBF and MTT maps appear abnomal on the contralateral side that appears normal in other imaging studies and in follow-up studies.. However, in the oSVD cCBF maps, a perfusion defect is noted only in the ipsilateral frontal territory. This is more visible on the corrected MTT maps. Both CBV and cCBV appear normal with only a slight defect in the area of the DWI abnormality (Figure 3.2.2.12). The area of cCBF and cMTT defects are confirmed to infarct on the follow-up study. When examining the cDelay maps we see that there is a negative shift (as indicated by the dark gray, where light gray represents zero) between the LMCA AIF and the right hemispheric voxels which appeared hypoperfused on the uncorrected map CBF. Furthermore, in cDelay, the delay in areas of low flow and prolonged MTT is greater than the surrounding areas. This is also consistent with simulation results (Figure 3.2.2.7) which showed delays are overestimated in low

flow conditions. The EOF for the SVD technique is quite large and heterogeneous for this patient. The areas of large EOF correspond to areas that appear artificially hypoperfused on the contralateral hemisphere. The EOF for the oSVD technique on the other hand is much smaller.

Figure 3.2.2.14 shows another case where AIF selection affects the output of the SVD technique, the perfusion studies of the 39 year old woman with a history of right ICA stenosis whose data was previously shown in Figure 3.2.1. The first two rows show the results without correction using an LMCA AIF and a RMCA AIF. The last two rows show the perfusion maps using oSVD. The EOF for the SVD techniques are shown on the same scale. For clarity, the EOF for the oSVD techniques are shown using a different scale from SVD, but the same scale as one another. For both SVD and oSVD techniques, one sees a larger flow abnormality when using the contralateral LMCA for the AIF, though the disparity is less for the corrected technique than the uncorrected technique. This continued disparity may be due to differences in dispersion between the two AIFs, as seen in Figure 3.2.1, which the oSVD does not take into account. In addition, for the uncorrected technique, the MTT regions of abnormality strongly correspond to regions of delay in the Delay maps, leading one to suspect that the MTT maps are highly weighted by delay, consistent with our simulation results. For the corrected technique, a similar correlation with delay is seen but not as strong, especially when using the RMCA as the AIF, as evidenced by the larger region of cDelay defect than cMTT defect. Interestingly, the EOF for the ipsilateral RMCA AIF seems to be much greater than for the LMCA. Both are heterogeneous and seem to have a dependence on underlying tissue. The EOF for the oSVD technique, on the other hand is much more homogeneous but again appears greater for the RMCA AIF.

Finally, we investigate the behavior of oSVD in examples of diffusion-perfusion mismatches in stroke to determine if oSVD is still sensitive to detecting areas of hypoperfusion without an accompanying DWI lesion. Figure 3.2.2.15 shows a pefusion study involving a 56-year old female patient imaged within four hours of presenting with symptoms of a right MCA stroke. Perfusion maps for both techniques were made using the same ipsilateral left MCA AIF. The EOF is larger in the SVD and appears to have more anatomic dependency than the EOF for the oSVD, which appears rather homogeneous. The EOF maps for SVD and oSVD are scaled differently to better show dependence on anatomy. This is a case when both oSVD and SVD show large flow defects despite the lack of DWI abnormality and minimal CBV abnormality. CBV maps are only shown once since both SVD and oSVD maps were identical within a scaling factor. The patient's lesion evolved into her perfusion defect, as demonstrated on the 22-day follow-up T2 FSE demonstrating that oSVD can show large MTT abnormalities when tissue infarction is likely even though DWI is normal. The 22-day follow-up T2-FSE appears distorted since during her hospital course, the patient ultimately required a hemicraniectomy in order to alleviate intracranial pressure due to brain swelling from the stroke.

Figure 3.2.2.16 shows the perfusion studies for a 65-year-old male patient imaged within 11 hours of presenting with symptoms of aphasia. This is an example of "diffusion-perfusion" mismatch where the perfusion defect does not evolve into the flow defect due to intervention with mechanical thrombolysis that resulted in reperfusion. Both CBF and cCBF show a larger area of hypoperfused tissue than the DWI lesion, however, the flow reduction in the cCBF is to a lesser extent than in the uncorrected maps (70% reduction in SVD compared to 40% reduction in oSVD). The four-month follow-up T2 FSE shows that the original DWI and CBV defects (arrowheads) did not evolve into the CBF or cCBF abnormality. Again we note the close

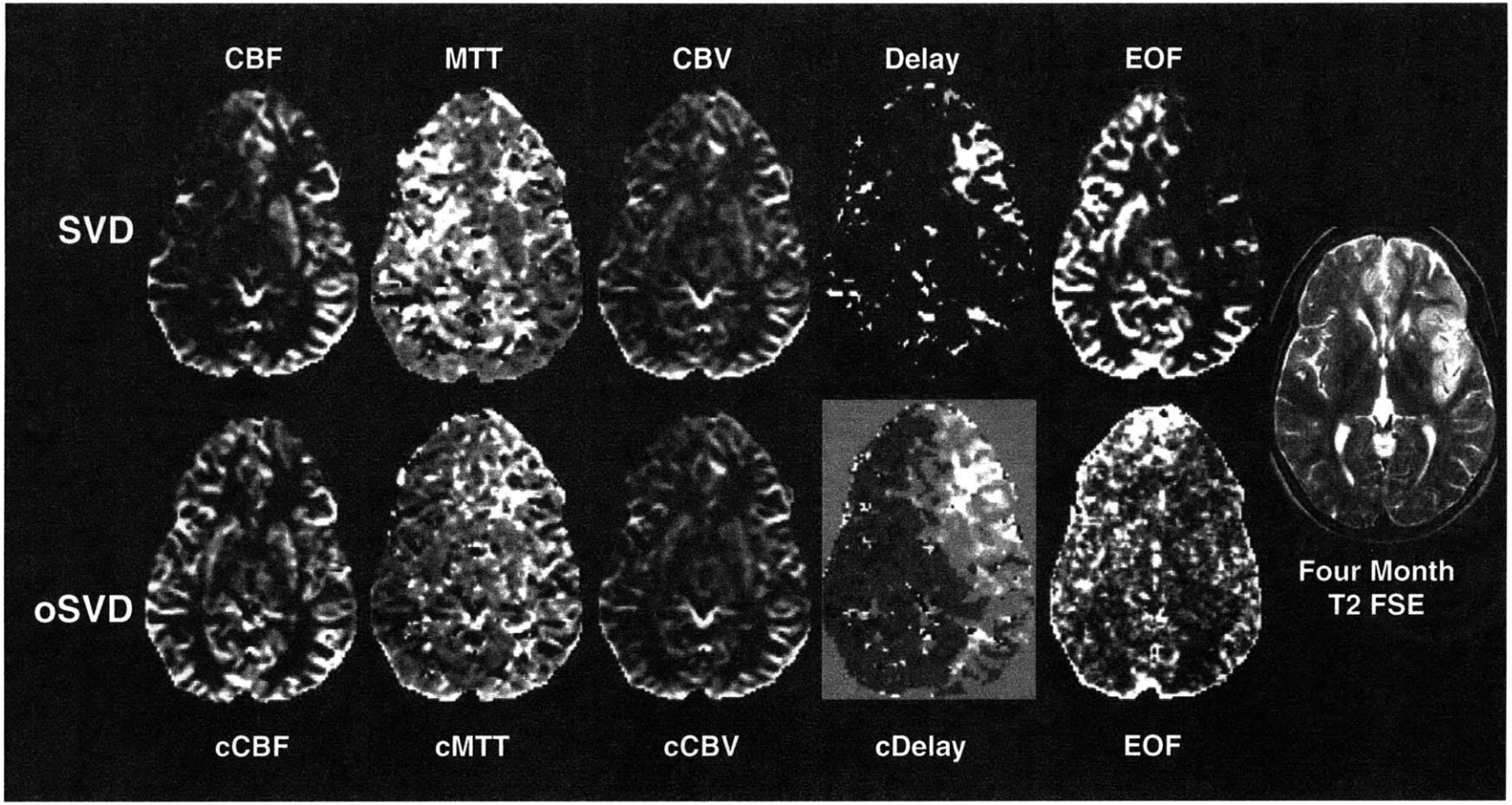

Figure 3.2.2.13 Example case where oSVD can compensate for SVD misprediction.
Perfusion maps for sickle cell patient shown in Figure 3.3.5 using both SVD and corrected SVD techniques. The perfusion abnormalities on the corrected maps (left frontal territory) are more consistent with the patient's clinical presentation than the maps made using standard techniques. This area is confirmed to have infarcted on the four month T2 FSE.

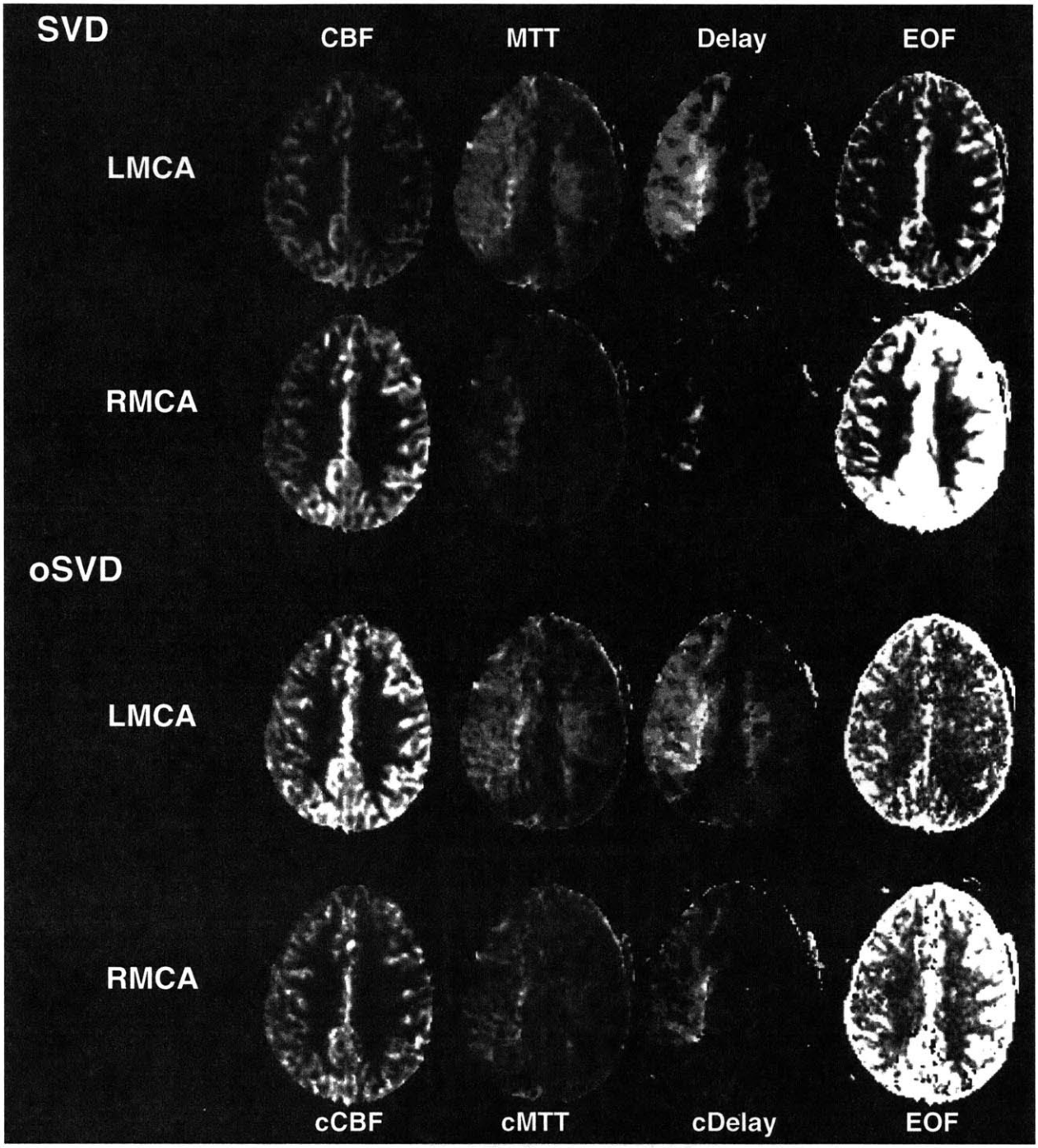

Figure 3.2.2.14 Example case of oSVD and SVD in a patient with carotid stenosis
Results of SVD and oSVD for a patient with right ICA stenosis. A mismatch between maps generated using the RMCA and LMCA as AIF are still seen though not as great as without correction. One also sees the close correspondence of Delay abnormality to areas of prolonged MTT on the uncorrected maps. EOFs for SVD are on the same scale for both LMCA and RMCA. The EOF for SVD and oSVD are on different scales (with EOF for SVD much larger than for oSVD) to better emphasize inhomogeneities within the map. The EOF for the ipsilateral RMCA is much larger than for the LMCA in both techniques.

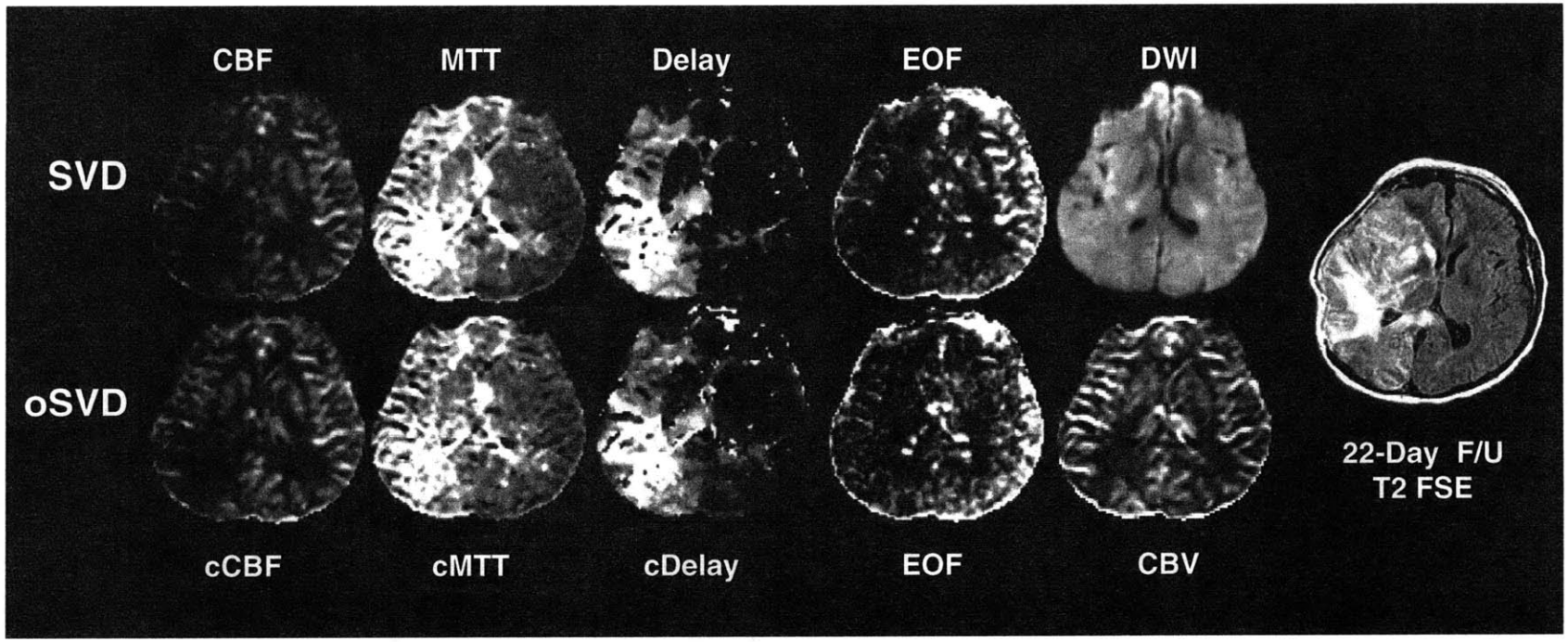

Figure 3.2.2.15 Example case with DWI/PWI mismatch where patient's lesion evolves into infarct.
SVD and oSVD perfusion studies for a 56-year-old woman imaged within 4 hours of presenting with symptoms of a RMCA stroke. The EOF is larger in the SVD and appears to have more anatomic dependency than the EOF for the oSVD. The EOF maps for SVD and oSVD are scaled differently to better show dependence on anatomy. This is a case when both oSVD and SVD show large flow defects despite the lack of DWI abnormality and minimal CBV abnormality. The patient's lesion evolved into her perfusion defect, as demonstrated on the 22 Day F/U T2 FSE demonstrating that oSVD can show large MTT abnormalities when tissue infarction is likely. The patient ultimately required a hemicraniectomy in order to alleviate intracranial pressure due to brain swelling.

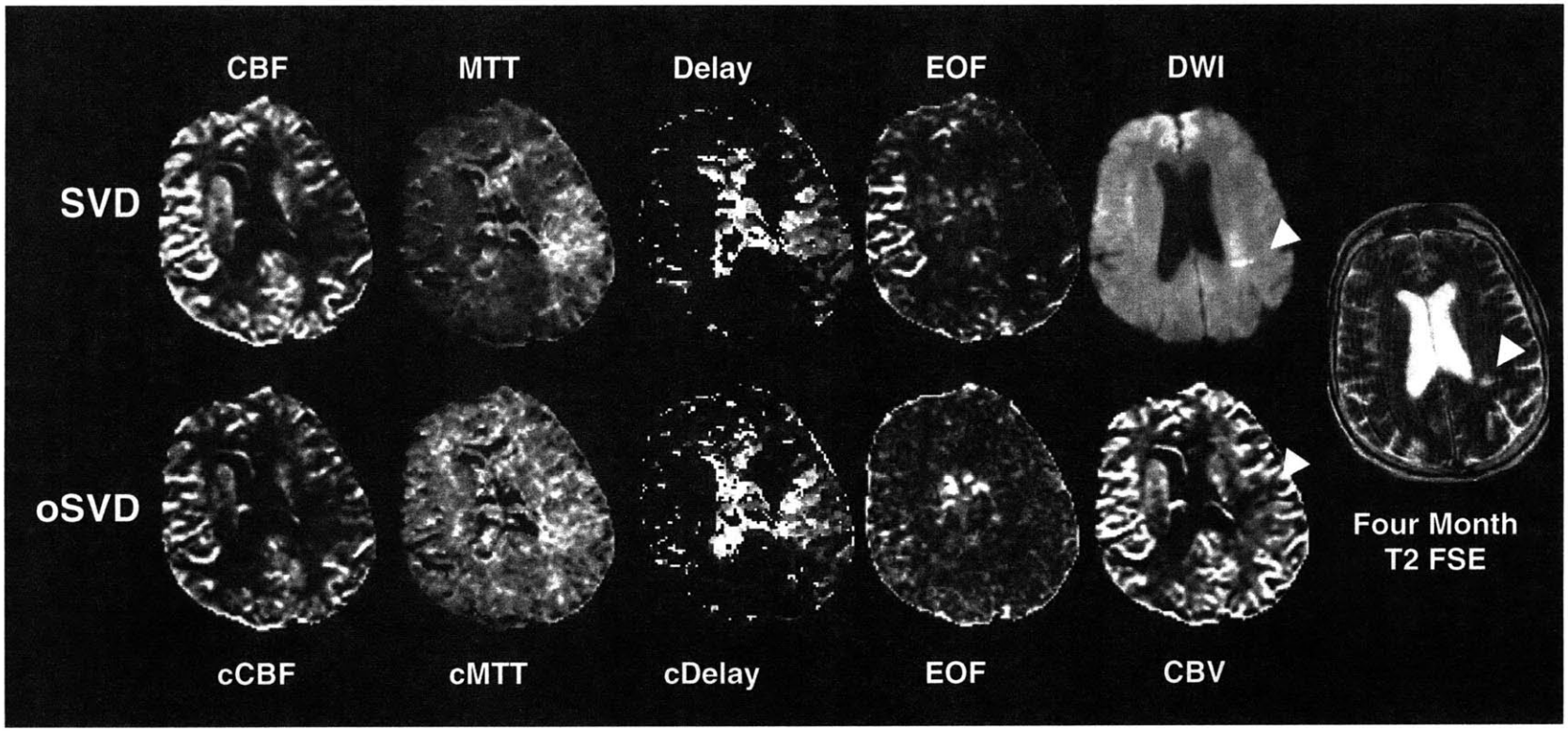

Figure 3.2.2.16 Example case with DWI/PWI mismatch with successful intervention.
SVD and oSVD calculated CBF and MTT maps for a 65-year-old male patient imaged within 11 hours of symptom onset. Both CBF and cCBF show a larger area of hypoperfused tissue than the DWI and CBV lesion, however, the flow reduction in the cCBF is to a lesser magnitude than in the uncorrected maps (70% reduction compared to 40% reduction). The EOF for SVD again shows a greater dependency on underlying tissue with a larger error in the contralateral hemisphere whereas the EOF for oSVD appears more homogeneous. The patient was successfully treated with mechanical thrombolysis resulting in reperfusion. The four-month follow-up T2 FSE shows that the original DWI and CBV defects (arrowheads) did not evolve into the CBF or cCBF abnormality.

spatial correlation of the Delay maps with the uncorrected CBF and MTT lesion abnormality. The EOF for SVD also again shows a greater dependency on underlying tissue with a larger error in the contralateral hemisphere whereas the EOF for oSVD appears more homogeneous.

Discussion

We have presented a model independent technique whose flow estimates are delay invariant. This technique does not compensate for dispersion but it is one step closer towards improving relative flow estimates. From Figures 3.2.2.3 and 3.2.2.4 one can conclude that at greater SNR circular deconvolution techniques are preferred despite the slightly greater variance and bias than SVD when no delay is present (Figure 3.2.2.5). Improved SNR can be attained with better MR instrumentation while the error in the standard SVD technique is inherent to its implementation. Due to the use of a single AIF for calculating flow in the whole brain, there will inevitably exist tracer arrival time differences between the AIF and tissue curves even in the absence of pathology. Therefore, a technique that is insensitive to tracer arrival delays is preferred.

Of the two deconvolution techniques that used block-circulant matrices examined here, the oSVD technique provides better performance in terms of flow estimate at both low and high flow rates (Figure 3.2.2.5) at low SNR. Although delay independent, oSVD has poorer performance in terms of bias assuming no delay as a function of signal to noise compared to standard deconvolution techniques. There may be alternate methods that can provide better solutions such as the Tikhonov-Miller (24) or Phillips-Twomey (25) method that uses regularization to impose smoothness constraints. Iterative algorithms which do not require calculation of the inverse of close to singular matrices may also prove useful in minimizing the oscillations due to the circular deconvolution (20). Such future investigations into optimizing circular deconvolution techniques may result in methods that provide better flow estimates at low SNR.

3.3 Conclusions

This chapter has demonstrated that techniques that use the standard SVD technique with standard deconvolution to estimate flow are likely contaminated by delay. Therefore, CBF and MTT maps are probably more accurately considered delay-weighted CBF and MTT maps. We have shown that delay insensitive CBF estimates using oSVD may provide results that are potentially more robust than delay sensitive techniques in both normal subjects and in many different pathology cases. To determine if oSVD provides more accurate flow estimates, correlation with PET flow values in humans should be performed.

With flow estimates free from tracer arrival delay contamination, improved identification of salvageable tissue may be possible. Due to tracer arrival delay, the existing SVD technique may produce estimates of flow suggesting ischemia in regions that was merely oligemic. This in turn may contribute to the large sensitivity but lack of specificity in traditional MTT maps. One may argue that clinically what is desired is a sensitive indicator of tissue at risk of infarction and therefore delay contamination in CBF and MTT maps are potentially clinically useful features. The utility of decoupling flow from delayed arrival times in clinical diagnosis has yet to be proven by a large retrospective study. We speculate that the cDelay maps presented here can continue to provide sensitivity while at the same time the cCBF maps may be able to provide a more specific indicator of ischemic tissue at risk of infarction. The cDelay maps may prove of

continued use in qualitative assessment while cCBF may be of use in quantitative scientific investigation.

The clinical results presented here are clearly preliminary and additional studies involving a larger cohort of patients are necessary to better determine the accuracy of oSVD perfusion maps. Retrospective analysis of perfusion studies with follow-up MRIs need to be performed where lesion volumes identified by cCBF, cDelay, CBV, CBF and MTT are evaluated and compared for sensitivity and specificity. Decoupling delay from flow may enable clinicians to better distinguish regions that is downstream from an occlusion that may be oligemic from tissue that is truly ischemic and therefore at a higher risk of infarction. This in turn can potentially lead to better understanding of the pathophysiological events underlying the ischemic process and ultimately better prediction of salvageable tissue in human cerebral ischemia.

3.4 References

1. Astrup J, Siesjo BK, Symon L. Thresholds in cerebral ischemia - the ischemic penumbra. *Stroke*. 1981;12:723-725.

2. Siesjo BK. Cerebral circulation and metabolism. *J Neurosurg*. 1984;60:883-908.

3. Sorensen AG. What is the meaning of quantitative CBF? *AJNR Am J Neuroradiol*. 2001;22:235-236.

4. Baird AE, Warach S. Magnetic resonance imaging of acute stroke. *J Cereb Blood Flow Metab*. 1998;18:583-609.

5. Østergaard L, Chesler DA, Weisskoff RM, Sorensen AG, Rosen BR. Modeling cerebral blood flow and flow heterogeneity from magnetic resonance residue data. *J Cereb Blood Flow Metab*. 1999;19:690-699.

6. Calamante F, Gadian DG, Connelly A. Delay and dispersion effects in dynamic susceptibility contrast MRI: simulations using singular value decomposition. *Magn Reson Med*. 2000;44:466-473.

7. Villringer A, Rosen BR, Belliveau JW, Ackerman JL, Lauffer RB, Buxton RB, Chao YS, Wedeen VJ, Brady TJ. Dynamic imaging with lanthanide chelates in normal brain: contrast due to magnetic susceptibility effects. *Magn Reson Med*. 1988;6:164-174.

8. Rosen BR, Belliveau JW, Chien D. Perfusion imaging by nuclear magnetic resonance. *Magn Reson Q*. 1989;5:263-281.

9. Todd-Pokropek A. Estimating blood flow by deconvolution of the injection of radioisotope tracers. In: Rescigno A., Boicelli A., eds. *Cerebral Blood flow: mathematical models, instrumentation, and imaging techniques,*. New York: Plenum Press, 1988; 107-119.

10. Lassen NA, Perl W. *Tracer kinetic methods in medical physiology*. New York: Raven Press, 1979.

11. Meier P, Zierler KL. On the theory of the indicator-dilution method for measurement fo blood flow and volume. *J Appl Phys*. 1954;6:731-744.

12. Østergaard L, Weisskoff RM, Chesler DA, Gyldensted C, Rosen BR. High resolution measurement of cerebral blood flow using intravascular tracer bolus passages. Part I: Mathematical approach and statistical analysis. *Magn Reson Med*. 1996;36:715-725.

13. Porkka L, Neuder M, Hunter G, Weisskoff RM, Belliveau JW, Rosen BR. Arterial input function measurement with MRI. *Proc. SMRM, 10th Annual Meeting*, San Francisco 1991; 120.

14. Sorensen AG, Wu O, Copen WA, Davis TL, Gonzalez RG, Koroshetz WJ, Reese TG, Rosen BR, Wedeen VJ, Weisskoff RM. Human acute cerebral ischemia: detection of changes in water diffusion anisotropy by using MR imaging. *Radiology*. 1999;212:785-792.

15. Strang G. *Linear Algebra and Its Applications*. Third Edition San Diego: Harcourt Brace Jovanovich, 1988.

16. Weisskoff RM, Zuo CS, Boxerman JL, Rosen BR. Microscopic susceptibility variation and transverse relaxation: theory and experiment. *Magn Reson Med*. 1994;31:610-610.

17. Stewart GN. Researches on the circulation time in organs and on the influences which affect it. *J. Physiol*. 1894;Parts I-III:

18. Østergaard L, Sorensen AG, Chesler DA, Weisskoff RM, Koroshetz WJ, Wu O, Gyldensted C, Rosen BR. Combined diffusion-weighted and perfusion-weighted flow heterogeneity magnetic resonance imaging in acute stroke. *Stroke*. 2000;31:1097-1103.

19. Smith AM, Grandin CB, Duprez T, Mataigne F, Cosnard G. Whole brain quantitative CBF, CBV, and MTT measurements using MRI bolus tracking: implementation and application to data acquired from hyperacute stroke patients. *J Magn Reson Imaging*. 2000;12:400-410.

20. Lagendijk RL, Biemond J. *Iterative identification and restoration of images*. Boston: Kluwer Academic Publishers, 1991.

21. Oppenheim AV, Schafer RW. *Discrete-time signal processing*. Englewood Cliffs, New Jersey: Prentice Hall, 1989.

22. Gobbel GT, Fike JR. A deconvolution method for evaluating indicator-dilution curves. *Phys Med Biol*. 1994;39:1833-1854.

23. Henkelman RM. Measurement of signal intensities in the presence of noise in MR images. *Med Phys*. 1985;12:232-233.

24. Tikhonov AN, Arsenin VY. *Solutions of Ill-posed problems.* New York: Wiley, 1977.

25. Twomey S. On the Numerical solution of Fredholm Integral equations of the first kind by the inversion of the linear system produced by quadrature. *J. Ass. Comput. Mach.* 1963;10:97-101.

Chapter 4

Combining diffusion & perfusion weighted imaging

One side will make you grow taller,
And the other side will make you grow shorter.

—Lewis Carroll
(*Alice's Adventures in Wonderland*)

Efforts to limit infarction in acute stroke patients might gain significantly from an accurate means of identifying hypoperfused yet viable brain tissue. Diffusion-weighted (DWI) and perfusion-weighted (PWI) magnetic resonance (MR) imaging have been shown to be highly sensitive and specific in diagnosing acute human cerebral ischemia (1-8). These imaging techniques appear to provide superior early identification of regions likely to infarct, compared to conventional MR or CT imaging (1-4, 9). However, the prediction of tissue and clinical outcome from specific imaging characteristics remains challenging. Although studies have found correlations between acute DWI and PWI lesion volumes with patients' clinical and follow-up imaging outcomes (10-15), the ability to predict clinical or tissue outcome in individual patients using a single modality still appears limited, perhaps due to the effects of stroke location and co-morbid factors.

Attempts have been made to combine DWI and PWI by comparing lesion volumes identified by the two techniques. "Diffusion-perfusion mismatches," in which the lesion volumes identified by one modality are larger than those by the other, have been reported by several groups (11-14, 16). Many groups have reported greater lesion enlargement of the acute DWI lesion volume in cases where the acute PWI volume is larger (1, 13-21) than the DWI lesion. In cases where the acute PWI lesion was smaller than the DWI lesion, total lesion growth was not as great (13-15, 22). Based on these observations, many have hypothesized that these DWI-PWI mismatches may allow identification of salvageable tissue in individual patients.

This "mismatch", however, is typically between the size of lesion volumes rather than between DWI and PWI values on an individual voxel basis. Due to heterogeneity in both ADC (12, 22-25) and flow values (14, 16, 19, 22) within acute ischemic tissue, volumetric approaches comparing gross differences in DWI and PWI lesion volumes may oversimplify the complex task of assessing tissue viability in different regions within ischemic tissue. A voxel-by-voxel analysis, such as one developed by Welch and colleagues (23-26), may provide a more sensitive approach for identifying salvageable tissue. Their studies demonstrated that a combination of T2 and ADC information provided better prediction of cellular necrosis than algorithms that used them separately and that a voxel-by-voxel analysis may better demonstrate the underlying heterogeneity in the lesion.

A natural extension of these tissue signature algorithms is the inclusion of perfusion information. However, assessing the signatures' significance becomes complicated since each additional parameter leads to an exponential increase in the number of "signatures." Furthermore, assuming only discrete states ignores the variances intrinsic to the data. A more complete algorithm may be one in which inputs are treated as random variables and the output is the probability of infarction for each given tissue voxel. In this study, a strategy was investigated that used statistical algorithms where the output is not a map of stages of infarction but risk of future infarction.

This chapter is divided into three sections. The first section seeks to determine whether algorithms that combine diffusion and perfusion information provide more sensitive and specific predictors of tissue outcome than algorithms using only subsets of this information. In addition, it also examines whether a **Generalized Linear Model** (GLM) algorithm provides an improved indicator of which tissue is at risk of infarction over thresholding-based approaches. Both questions were investigated by retrospectively applying the different techniques to diffusion and perfusion indices acquired from acute stroke patients and comparing the algorithms' voxel-by-

voxel performances in predicting which tissue will proceed to infarction. The second section investigates **Generalized Additive Models** (GAMs) whose predictions are based on non-linear functions of input diffusion and perfusion parameters in order to take into consideration observed non-linear behavior of diffusion and perfusion values. The third section investigates non-linear combinations of input parameters using a **Hierarchical Mixture of Experts**. It is hypothesized that our initial models were limited in using a single model for all tissue regions although it has been observed that different tissue regions, e.g. gray matter vs. white matter, have different diffusion and perfusion characteristics even in normal conditions. By allowing for combinations of experts, we hypothesize better estimation of tissue likely to infarct may be obtained.

4.1 Generalized Linear Models[4]

Subjects and Methods

Patient Selection

Diffusion- and perfusion-weighted images of patients with hyperacute cerebral ischemia acquired within twelve hours of symptom onset between the years August 1994 and August 1997 were examined retrospectively (n=94). To avoid potential confounds due to different types of ischemic damage and to obtain a relatively homogenous population of stroke patients, this study was limited to patients with clinical signs suggestive of a major cerebral artery occlusion. This study therefore only included Trial of ORG 10172 in Acute Stroke (TOAST) classification subtypes of large artery atherosclerosis, cardioembolism, stroke of other determined etiology and stroke of undetermined etiology (28). Subtypes of small vessel occlusion and non-cerebral artery occlusions were excluded (n=32). Other exclusion criteria included treatment with thrombolytic or neuroprotective agents (n=10) and non-availability of acute diffusion or perfusion studies due to motion or equipment induced artifacts (n=4). Patients were excluded if a follow-up (F/U) axial T2-weighted fast spin echo (FSE) imaging study five days or later was not available to confirm extent of lesion volume (n=34). A total of fourteen patients satisfied these inclusion criteria. Diffusion and perfusion findings in 9 out of 14 of these patients have been reported previously (1, 12, 18, 19). Table 4.1.1 summarizes their demographics and stroke subtype classifications.

Image Acquisition

Imaging was performed on a 1.5T General Electric Signa MR instrument, with 5.4.2 software (General Electric Medical Systems, Waukesha, WI) and retrofitted with echo planar imaging (EPI) capabilities via an Advanced NMR Systems (Wilmington, MA) hardware upgrade, that included the "catch and hold" modification. Table 4.1.1 summarizes the MR acquisition parameters for the patients. Each patient was also imaged with conventional sequences that included sagittal T1 localizers, axial T2 weighted fast spin echo (FSE), fluid attenuated inversion recovery (FLAIR) or proton-density (PD), 2D phase contrast MR angiography (MRA) and post-contrast axial T1 weighted images. The Acute Stroke Protocol used for imaging patients was similar to those published in previous reports (1, 12, 19).

Multi-slice axial diffusion-weighted images were acquired by either sampling three orthogonal directions at b-values of 1010 s/mm^2 (n=3) (1) or sampling the full diffusion tensor at b-values of

[4] Parts of this section have been reprinted with modifications from (27) with permission from Lippincott, Williams & Wilkins © 2001.

1221 s/mm^2 (n=11) (29) using single-shot pulsed field gradient spin echo EPI. The duration of the diffusion gradient in each single shot diffusion weighted image was either 42 ms (3-direction) or 47 ms (full-tensor) with intertemporal pulse offset of 5 ms resulting in b-values of 1010 s/mm^2 (3-directions) or 1221 s/mm^2 (full-tensor) respectively. A low b-value (b=3 s/mm^2) was used in place of crusher gradients for the non-diffusion-weighted image. This low b-value image was used as the initial T2-weighted image. For sequences sampling three directions, echo times were TE=108 ms (n=2) or 155 ms (n=1). For the seven single-shot full diffusion tensor sequence, TE=118 ms. For all images, a repetition time of TR=6000 ms was used and up to 20 axial slices were obtained with 6 mm slice thickness and 1 mm interslice gap. A fixed field of view (FOV) of 400 × 200 mm^2 and an acquisition matrix of 256 × 128 voxels was used. To increase the signal-to-noise ratio (SNR) of the images, three full-head diffusion weighted images were acquired and averaged. The isotropic diffusion weighted image (DWI), was formed from the geometric mean of the high b-value single-shot images. The ADC image was calculated from the slope of the linear regression fit of the log of the high and low b-value images versus their b-values.

Perfusion weighted images were acquired from dynamic susceptibility contrast images using either spin-echo (SE) (n=10) or gradient-echo (GRE) (n=4) EPI pulse sequences. Images were acquired during the first pass of a bolus of 0.1 mmol/kg (GRE) or 0.2 mmol/kg (SE) of body weight of gadopentetate dimeglumine (Magnevist; Berlex Laboratories, Wayne, NJ) contrast agent. The bolus was injected approximately 10 seconds after the start of imaging at a rate of 5 ml/s using a MRI-compatible power injector (Medrad, Pittsburgh, PA) through an 18-gauge antecubital catheter. The contrast agent was followed by at least 15 ml of normal saline injected at the same rate of 5 ml/s. The imaging sequence consisted of either 51 single-shot echo planar images over a volume of 10 slices for a total of 510 images (n=3) or 46 single-shot images over a volume of 11 slices for a total of 506 images (n=11). With a TR=1500 ms, the total acquisition time was 83 seconds (51 time points) or 69 seconds (46 time points). Echo times were TE=75 ms (SE) and TE=50 ms (GE). The FOV was 400 × 200 mm with an acquisition matrix of 256 × 128. Images were acquired with a slice thickness of 6 mm and a 1 mm interslice gap. From the dynamic susceptibility contrast images, concentration-versus-time curves were calculated on a voxel-by-voxel basis utilizing the linear relationship between changes in transverse relaxation and concentration of contrast agent (30, 31). Relative regional cerebral blood volume (CBV) values were then obtained for each voxel by numerically integrating the concentration-versus-time curve (31, 32). Relative cerebral blood flow (CBF) values were obtained for each voxel as the height of the deconvolved tissue response function with an arterial input function (33). The arterial input function was measured directly from the susceptibility contrast images (34) in voxels of tissue encompassing the cerebral artery in the normal contralateral hemisphere. From the central volume theorem, the mean transit time (MTT) for each voxel was then calculated by taking the ratio of CBV to CBF (33).

Coregistration

The volumetric diffusion, perfusion and follow-up data were spatially coregistered utilizing an automated image registration software package, AIR 3.08 (UCLA, CA) (35, 36). The initial low b-value T2-weighted EPI, ADC, DWI and follow-up T2-weighted FSE images were coregistered to the same dimensions (128×128×11 or 128×128×10 voxels), orientation and coordinates as the perfusion images using an affine, twelve-parameter transformation model and trilinear

interpolation. Voxels from "normal" appearing gray matter in the unaffected, contralateral hemisphere from the coregistered initial T_2 images were outlined prior to generation of the predictive maps. For all six acute-stage images, voxel values were normalized by dividing by the mean of these outlined regions to produce "relative" values (rT2, rADC, rDWI, rCBF, rCBV, and rMTT).

Development of Generalized Linear Model Algorithms

In the generalized linear model (GLM) algorithms, tissue outcome was modeled as a binary variable (infarcted/non-infarcted), P, where the value 1 represented infarcted tissue and value 0 non-infarcted tissue. In a GLM, for a binary variable, the probability of tissue infarcting can be represented by the logistic function:

$$P = \frac{1}{1 + e^{-\eta(\mathbf{x})}} \tag{4.1.1}$$

where $\eta(\mathbf{x})$, the predictor is a linear function of its input parameters, $\mathbf{x}$,

$$\eta(\mathbf{x}) = \beta^T \mathbf{x} + \alpha \tag{4.1.2}$$

and β is the vector of calculated coefficients and α the bias or intercept term for the GLM. The α term provides the base value for P if all of the input parameters, $\mathbf{x}$, are zero. The β coefficients can be interpreted as the multiplicative effects on P due to changes in the input parameters (37).

For calculating the coefficients in the GLM algorithms, a supervised approach was utilized. Using commercial image processing software (Alice, Hayden Image Processing Solutions, Boulder, CO), training regions were selected by outlining brain tissue volumes that were clearly infarcted or non-infarcted in the ipsilateral hemisphere in the coregistered follow-up axial T_2 FSE images by a neuroradiologist blinded to the predictive map results. Care was taken to avoid including regions demonstrating chronic changes on T_2, such as old stroke lesions or periventricular white matter abnormalities. Selection of "normal" voxels was also limited to the ipsilateral hemisphere in slices that showed evidence of infarction. Combinations of initial rT2 EPI, rADC, rDWI, rCBF, rCBV and rMTT values from these outlined training regions were used as the input vector, $\mathbf{x}$, in the training stage. Because GLM algorithms assume independent observations, only every other voxel in the selected ROIs was sampled for the training data in order to reduce correlation. The coefficients for the GLMs, β, were calculated using an iterative reweighted least squares (IRLS) algorithm in S-PLUS 3.4 (StatSci, Seattle, WA). Selection of covariates was based on the Akaike Information Criterion (AIC) whereby terms were included if their addition resulted in reductions in prediction error values that were a function of both training error and complexity (38). The AIC therefore provided an objective means to evaluate the trade-off between minimizing residual training error and increased complexity (38). The algorithm with the minimum AIC is therefore one with the minimum number of parameters and minimum training error. Automatic parameter selection was not utilized because all the input parameters were not independent with MTT=CBV/CBF and DWI=T_2 exp(-b ADC). Therefore,

Table 4.1.1 Patient demographics, vascular territory, presenting symptoms, stroke subtype, imaging times and follow-up lesion volume. Unless otherwise noted, all diffusion sequences were acquired axially at TR=6000, b-value=1221 s/mm^2 up to 20 slices and perfusion sequences with TR/TE=1500/75 ms, 11 slices and 46 timepoints.

Patient	Age/ Sex	Vascular Territory	Symptoms	TOAST Classification	Initial DWI/PWI (hrs)	F/U T2 (days)	F/U T2 Volume (cm^3)
1	78/F	LMCA	Aphasia	Cardioembolism	4	5	86.7
2	77/F	LPCA	Amnestic Syndrome	Cardioembolism	4	6	0.41
*3	58/M	LMCA	R hand weakness & slurred speech	Cardioembolism	6	5	5.3
*†4	64/F	RACA	L hand & L leg weakness	UC	5.5	7	2.2
5	69/M	LPCA	R homonymous hemianopia & pure alexia w/o agraphia	Cardioembolism	3	5	22.9
†6	79/M	LMCA	R hemiplegia &mutism	LAA	7	8	130.1
7	33/M	LMCA	R hemiplegia&aphasia	LAA	4	178	83.9
8	32/M	LMCA	R hemiplegia&mutism	UC	5	44	58.7
9	65/M	RMCA	L weakness & hemineglect	LAA	10	379	96.6
*10	61/M	RMCA	L hemiparesis	Cardioembolism	3	11	1.2
‡11	72/M	LMCA	Aphasia	Cardioembolism	6	54	21.7
†12	80/F	RMCA	L facial droop & pronator drift	OIC (balloon occlusion)	11	7	32.8
‡13	45/M	RMCA	L hemiparesis &plegia of leg	OIC (dissection)	4	57	18.9
†14	45/M	LMCA	R homonymous hemianopia, R hemiparesis	OIC (dissection)	7	58	92.2

LAA=Large artery atherosclerosis; OIC=Other identified cause; UC=Undetermined cause

* DWI sampled in 3 directions, b-value=1010 s/mm^2. PWI consists of 10 slices and 51 timepoints; † Gradient Echo EPI sequences used for PWI at TR/TE=15000/50 ms; ‡ Early spontaneous reperfusion (<15 hours) as determined by serial MR perfusion studies.

when selecting covariates, independent parameters, rT_2, rADC, rCBF and rCBV were considered first for inclusion followed by the higher order covariates of rDWI and rMTT. For purposes of comparing the two techniques, combinations of DWI and PWI identical to those created for the thresholding algorithms were generated for the GLM algorithms.

To validate the performance of the GLMs, a jack-knifing approach was followed wherein the coefficients for each patient's algorithms were calculated using the other patients in the study as training data (39). Jack-knifing was used to avoid bias that would otherwise occur if the algorithm's performance was evaluated on the same data that was used to train the algorithm. Using the calculated coefficients, the risk of a voxel of tissue going on to infarction was calculated using Equations (4.1.1) and (4.1.2). The 95% confidence intervals for the computed risks were computed from the parameters obtained from S-PLUS 3.4.

To evaluate the jack-knifing results for the GLM algorithms, we compared the computed coefficients for each of the training datasets to determine if they were significantly different ($P \leq 0.05$) from the coefficients obtained using a dataset containing data from all patients. The average of the coefficients of the GLM algorithms obtained from the 14 training data subsets was also compared with the coefficients of the aggregate GLM algorithm. Two-tailed Z-tests were used for the statistical comparisons.

Thresholding Algorithms

For the thresholding algorithms, a strategy similar to that reported by Welch (23) was followed. Tissue was classified as abnormal if the initial diffusion or perfusion values were greater than a specified number of standard deviations from the mean value measured in the contralateral non-infarcted gray matter regions. We generated tissue signature maps using images calculated from the diffusion study (T_2+ADC+DWI), images calculated from the perfusion study (CBF+CBV+MTT), and combinations of images from both studies. For the combined study, we generated signature maps using combinations of T2 and ADC with one perfusion parameter (CBF, CBV or MTT) and all six parameters (T2+ADC+DWI+CBF+CBV+MTT). The combinations of the parameters used for the thresholding algorithms were selected to be identical to the combination of parameters used in the GLM algorithms for the purpose of comparing the two techniques. For creating signature maps, a threshold of 2 standard deviations from the mean of the contralateral values was used. Each of the resulting signatures was taken to represent a different "state" of infarction. Voxels not meeting any of the threshold criteria were given a "normal" signature. For the thresholding algorithms, which are based on an unsupervised approach not requiring training data from other subjects, the non-normalized datasets were used.

Evaluation of Algorithm Performance

For evaluating the accuracy of the thresholding and GLM algorithms, the same infarcted and non-infarcted regions used in the training of the GLM algorithms were used. The performance of each of the algorithms was evaluated on its ability to accurately discriminate the infarcted from non-infarcted regions in the ipsilateral hemisphere. By comparing the predicted maps with lesions demonstrated on follow-up conventional MR images, the number of voxels predicted to infarct that actually did infarct (true positives or TP), and the number that did not infarct (false positives or FP) were tabulated. In addition, we tracked the number of voxels predicted not to infarct that remained non-infarcted (true negatives or TN) as well as those that became infarcted

(false negatives or FN). From these counts, the algorithm's sensitivity or true positive ratio, TPR=TP/(TP+FN), and specificity or true negative ratio, TNR=TN/(TN+FP), were calculated. Receiver operating characteristic (ROC) curves were then generated for each algorithm by plotting TPR (sensitivity) against the false positive ratio (FPR) (1-specificity). For thresholding algorithms, the number of standard deviations was varied from -5 to 5 in 0.1 increments for all parameters except MTT. For MTT cutoff values ranged from -10 to 10 standard deviations in 0.2 increments due to its larger range of values. For the GLM algorithms, the probability cutoffs for classifying tissue to be infarcted were varied from 0 to 1 in 0.01 increments.

The area under the ROC curves (AUC) has been shown to represent the probability that an image will be correctly ranked normal or abnormal and therefore used to assess the performance of diagnostic systems (40). The AUC for the ROC curves for each patient was calculated using numerical integration. The AUCs for the different algorithms were compared by paired one-tailed Wilcoxon signed-rank tests. Values $P \leq 0.05$ were considered significant in all statistical analysis. The performances of the algorithms were also compared at their optimal operating points (OOPs) on the ROC curves (41). As defined by Halpern, (41) the OOP is the point where the ROC curve is tangent to the highest line of slope:

$$\frac{(\text{prevalence of disease})}{1-(\text{prevalence of disease})} \times \frac{(\text{cost of false-positive result})}{(\text{cost of false-negative result})}.$$

By assuming equal prevalence of infarcted (0.5) and non-infarcted (0.5) voxels and equal costs of false-positives and false-negatives, the OOPs for the ROC curves were determined numerically by finding the points on the ROC curves where the slope=1.

Results

Generalized Linear Model Algorithms

Based on the Akaike Information Criterion (AIC), GLM algorithms using different combinations of the possible six input parameters were evaluated and compared using data from all fourteen patients. Out of the independent parameters, rCBF resulted in the greatest reduction in the AIC, followed by rT_2, then rADC and finally rCBV. Adding the higher order terms, rDWI and rMTT resulted in a further reduction of AIC and were therefore included in the combined diffusion and perfusion GLMs. Therefore, the optimal GLM algorithm by the AIC requires all six parameters. However, for the purpose of comparison, the GLM coefficients for all possible 63 GLMs were calculated. A subset of these 63 GLMs that performed best in terms of sensitivity and specificity are shown in Table 4.1.2 along with the standard errors for the estimates of each parameter. The coefficients and intercepts for the aggregate GLM algorithm were not significantly different ($P>0.5$) from the mean of the coefficients across the 14 subjects. However, the coefficients and intercepts for some parameters in individual patients showed significant differences ($P \leq 0.05$) from the aggregate GLM algorithm demonstrating the potential effects of training data on algorithm development.

Table 4.1.2 Coefficients of GLM algorithms for all 14 subjects.

Algorithm	α	rT_2	rADC	rDWI	rCBF	rCBV	rMTT
rT_2+rADC+rDWI	-10.0±0.2	-2.9±0.2	4.9±0.2	6.7±0.2	...	...	...
rCBF+rCBV+rMTT	-1.2±0.06	...	...	...	-1.2±0.09	-0.02±0.06	0.6±0.03
rT_2+rADC+rMTT	-3.6±0.06	4.4±0.08	-3.5±0.07	...	...	...	0.9±0.02
rT_2+rADC+rCBF+rCBV	-1.6±0.05	4.4±0.08	-3.3±0.07	...	-3.0±0.06	1.2±0.04	...
Combined Algorithm	-11.7±0.2	-3.0±0.2	5.9±0.2	7.1±0.2	-1.2±0.1	0.05±0.06	0.7±0.03

The columns labeled rT2, rADC, rDWI, rCBF, rCBV and rMTT represent the mean and standard error of the weighting coefficient for each respective parameter when utilizing all 14 patients for the training data set. The column labeled α is the bias or intercept term. Dashed lines indicate the parameter was not used for a particular multivariate algorithm. Each row represents the coefficients for the different GLM algorithms investigated.

Table 4.1.3 Optimal operating points for thresholding and GLM algorithms.

	Algorithm	Cut-off Values	Specificity	Sensitivity
Thresholding	T2+ADC+DWI	2.2	0.87	0.54
	CBF+CBV+MTT	1.6	0.64	0.72
	Combined Algorithm	2.7	0.83	0.66
GLM	T2+ADC+DWI	34	0.90	0.50
	CBF+CBV+MTT	28	0.65	0.71
	Combined Algorithm	32	0.84	0.66

OOPs for each model and their associated cut-off values used for classification of infarcted and non-infarcted voxels are shown. The cut-off values are in number of standard deviations for the thresholding algorithm for all parameters with the exception of MTT. The cut-off threshold of MTT was twice the standard deviations of the other five parameters. The cut-off values for the GLM algorithm are in percent risk of infarction. The third column and fourth represents the specificities and specificities at the OOPs for each of the algorithms.

ROC Analysis

Figure 4.1.1 shows the ROC curves of the pooled results from the (A) thresholding and (B) GLM methods across all fourteen patients for the multivariate and univariate GLM algorithms. For both approaches, the multivariate GLM algorithms performed better than the univariate GLM algorithms as measured by higher ROC curves. Furthermore, GLM algorithms that combined diffusion and perfusion data performed better than the rT_2+rADC+rDWI or rCBF+rCBV+rMTT GLM algorithms as shown by the higher ROC curves.[5] The full six-parameter "Combined Algorithm" has a higher ROC curve than GLM algorithms using only rT_2+rADC+rMTT or rT_2+rADC+rCBF+rCBV parameters, consistent with the AIC results. For the diffusion and perfusion based GLM algorithms, the multivariate algorithms provided the best performance in terms of ROC curves and therefore the univariate diffusion and perfusion studies are not discussed in further detail in this study. Out of the combined algorithms, the algorithm using all six parameters provided the best performance and therefore the other combined algorithms are also not discussed in the remainder of this study.

Algorithms using only perfusion imaging appear to have greater sensitivity in regions of low specificity (FPR>0.3). For algorithms using only diffusion imaging, the reverse appear true, that is the diffusion-based algorithm had greater sensitivity than perfusion-based algorithms in ranges of high specificity (FPR<0.3). When perfusion and diffusion values are combined concurrently, an overall increase in sensitivity is obtained. Table 4.1.3 shows the specificities associated with the OOPs for both thresholding and GLM algorithms along with their corresponding sensitivities. The OOPs are comparable for both thresholding and GLM algorithms. For both algorithms, from the ROC curves shown in Figure 4.1.1, the "combined algorithms" have the greatest sensitivities at each of the specificities listed in Table 4.1.3.

From Figure 4.1.1, one sees that both thresholding and GLM methods produce similar ROC curves when pooling results across the fourteen subjects. ROC curves were also generated on an individual patient basis and the area under the curves (AUC) calculated. The differences between the multivariate algorithms' AUCs were calculated for the thresholding and GLM algorithms. For the thresholding algorithm, the "Combined Algorithm" had significantly higher AUCs than the diffusion-based algorithm (T2+ADC+DWI) (P=0.02) indicating better overall performance of the combined threshold algorithm over the initially proposed diffusion-only thresholding algorithm (23-26). The difference between the "Combined Algorithm" and CBF+CBV+MTT threshold algorithms were not significant (P=0.21). No significant difference was found between the performances of threshold algorithms based purely on diffusion (T2+ADC+DWI) and those based purely on perfusion (CBF+CBV+MTT) (P=0.52). For the GLM algorithms, the "Combined Algorithm" showed a significant improvement over diffusion based algorithms (rT2+rADC+rDWI) (P=0.02) and perfusion based algorithms (rCBF+rCBV+rMTT) (P=0.04). There was no significant difference between multivariate diffusion and multivariate perfusion GLM algorithms (P=0.50). The lack of difference between the diffusion and perfusion algorithms for both GLM and thresholding algorithms is most likely because diffusion algorithms have lower sensitivity at low specificity than perfusion algorithms but higher sensitivity at high specificity which may in turn translate into equivalent AUCs.

[5] In the interest of clarity, only the ROC curve of the single diffusion, perfusion combinations with the highest curve is shown. This was the model combining T2, ADC and MTT.

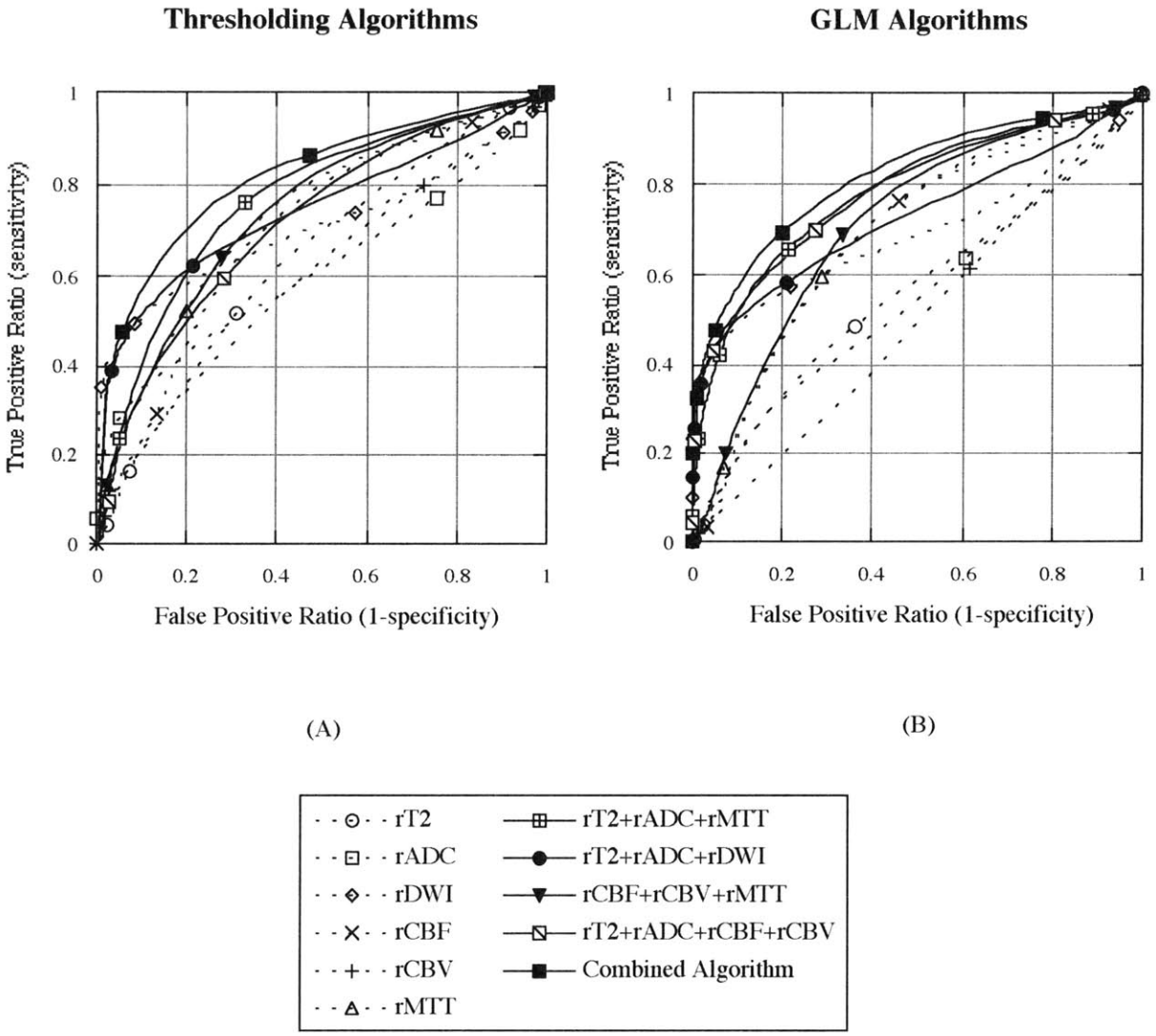

Figure 4.1.1 Performance of (A) thresholding and (B) GLM methods pooling results across fourteen patients. For both methods, the perfusion-based maps (rCBF+rCBV+rMTT) appear more sensitive than the diffusion based maps (rT_2+rADC+rDWI) at values of high FPR. The multivariate algorithms tend to have a higher ROC curve than the univariate algorithms. When diffusion and perfusion data are combined either singly (rT_2+rADC+rMTT) or multiply (rT2+rADC+rCBF +rCBV or "Combined Algorithm"), an overall increase in sensitivity in areas of high specificity (FPR<0.2) is seen.

Differences between the AUCs for the GLM algorithms and their corresponding threshold algorithm counterparts were calculated and compared. The GLM and thresholding algorithms using diffusion data (P=0.33), perfusion data (P=0.64) or combined algorithms (P=0.27) performed comparably.

Example Cases

Figure 4.1.2 shows the acute imaging studies and thresholding maps for Patient 14. The tissue signature maps are the results of using only hyperacute diffusion data (T2+ADC+DWI), hyperacute perfusion data (CBF+CBV+MTT) and combining all six input parameters ("Combined Algorithm"). The diffusion-based algorithm, though identifying a smaller region at risk of infarction in the ipsilateral hemisphere than either the perfusion-based algorithm or "Combined Algorithm", also demonstrates an abnormal signature in the contralateral hemisphere. Abnormal tissue signatures in the perfusion-based algorithm are predominantly limited to the ipsilateral hemisphere although they encompass an area much greater than the follow-up infarct volume. Because misclassifications are cumulative in the thresholding algorithms, the results in the combined diffusion and perfusion algorithms have similarly high sensitivity but poor specificity as that shown for the perfusion based algorithms. However, a greater number of tissue states exist in the combined algorithm resulting in greater heterogeneity than those based on algorithms incorporating only diffusion or perfusion information.

Figure 4.1.3 shows the results of the GLM algorithms using the same imaging data as shown in Figure 4.1.2. One again observes that algorithms utilizing diffusion alone (rT2+rADC+rDWI) underestimate the follow-up infarct volume. Maps using only perfusion information (rCBF+rCBV+rMTT) overestimate the follow-up infarct volume. The "Combined Algorithm", however, predicts an area at high risk of infarction, as evidenced by the red-yellow region, that correlates well with the follow-up lesion areas as demonstrated on the two month follow-up T2 FSE image shown in Figure 4.1.2. In addition, for all algorithms, the regions predicted to be at high risk of infarction are predominantly localized to the ipsilateral hemisphere as compared to the results of the thresholding algorithm.

The results of applying the statistical algorithms to a patient with early reperfusion as defined by follow-up perfusion studies are shown in Figure 4.1.4. The acute MRI studies for Patient 11 appear normal with the exception of decreased CBF and increased MTT in the left temporo-parietal lobe. The imaging study eight hours later show a slight diffusion abnormality in the area shown abnormal in the initial perfusion study. However, the remaining perfusion defects appear to have resolved as demonstrated by the CBF and MTT maps, suggesting the occurrence of spontaneous reperfusion. Both the thresholding and the GLM based risk maps over predict the follow-up infarct volume in the two-month follow-up T2 FSE. The resolution of much of the abnormalities in the follow-up imaging study was consistent with the patient's improved clinical outcome.

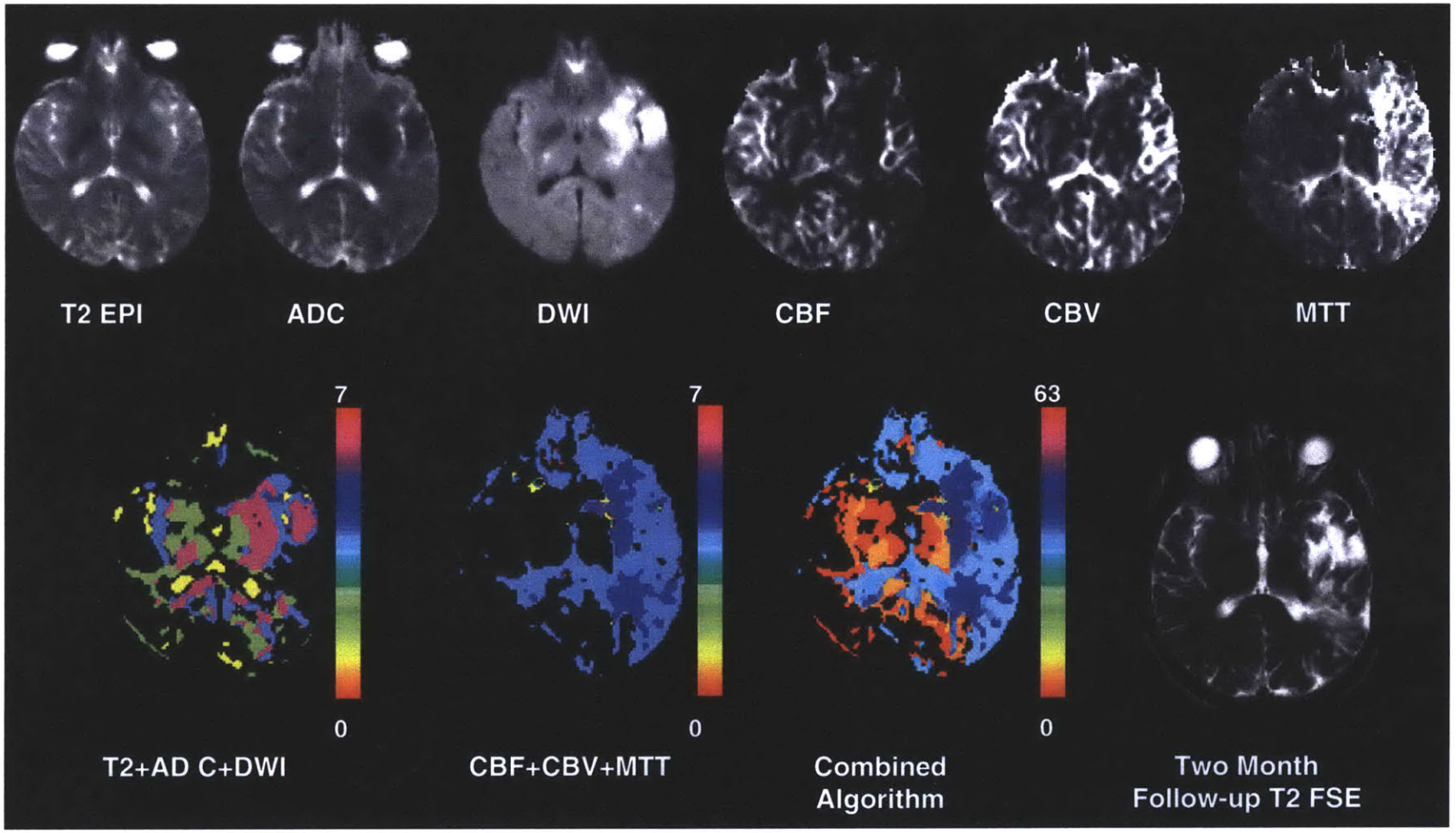

Figure 4.1.2 Initial imaging data and thresholding results for Patient 14. Shown are the acute diffusion and perfusion studies acquired within 7 hours since patient was last seen asymptomatic. Signature maps were created using initial T_2, ADC and DWI data, initial CBF, CBV and MTT values and combining all six variables T_2, ADC, DWI, CBF, CBV and MTT. The first two signature maps have 8 possible signature values, and the last maps 64 values as indicated by the different colors in the adjacent color bars. Each color represents a different tissue signature or state. The two-month follow-up T2 FSE image is shown for comparison.

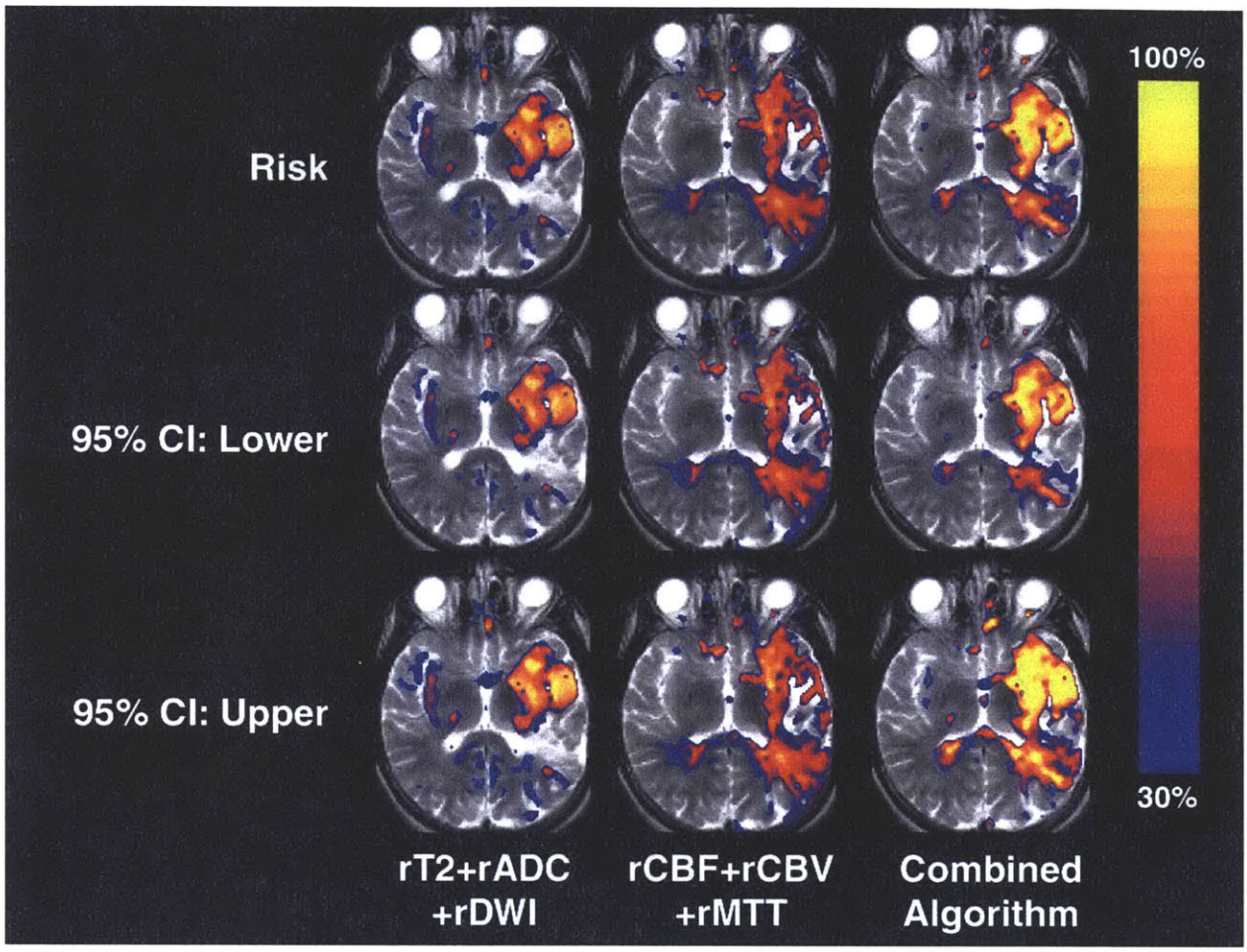

Figure 4.1.3 Predicted risk of infarction maps overlaid on the two-month follow-up T2 FSE for Patient 14. The maps were generated from the hyperacute data shown in Figure 4.1.2. Overlaid values are the probability tissue will go on to infarction, with blue areas at low risk of infarctions and yellow areas at high risk of infarction. The first row shows the probability of tissue becoming infarcted. The second and third rows are the lower and upper 95% confidence limits respectively for the risk estimates shown in the first row. For clarity, voxels with less than 30% probability of becoming infarcted are not shown. The first column are the results of using only diffusion data as predictors (rT2+rADC+rDWI), second column are the results of using only perfusion data as predictors (rCBF+rCBV+rMTT) and the third column are the results of combining all six input parameters (rT2+rADC+rDWI+rCBF+rCBV+rMTT). The area at risk depicted by the third column correlates best with the two-month follow-up lesion area shown in Figure 4.1.2.

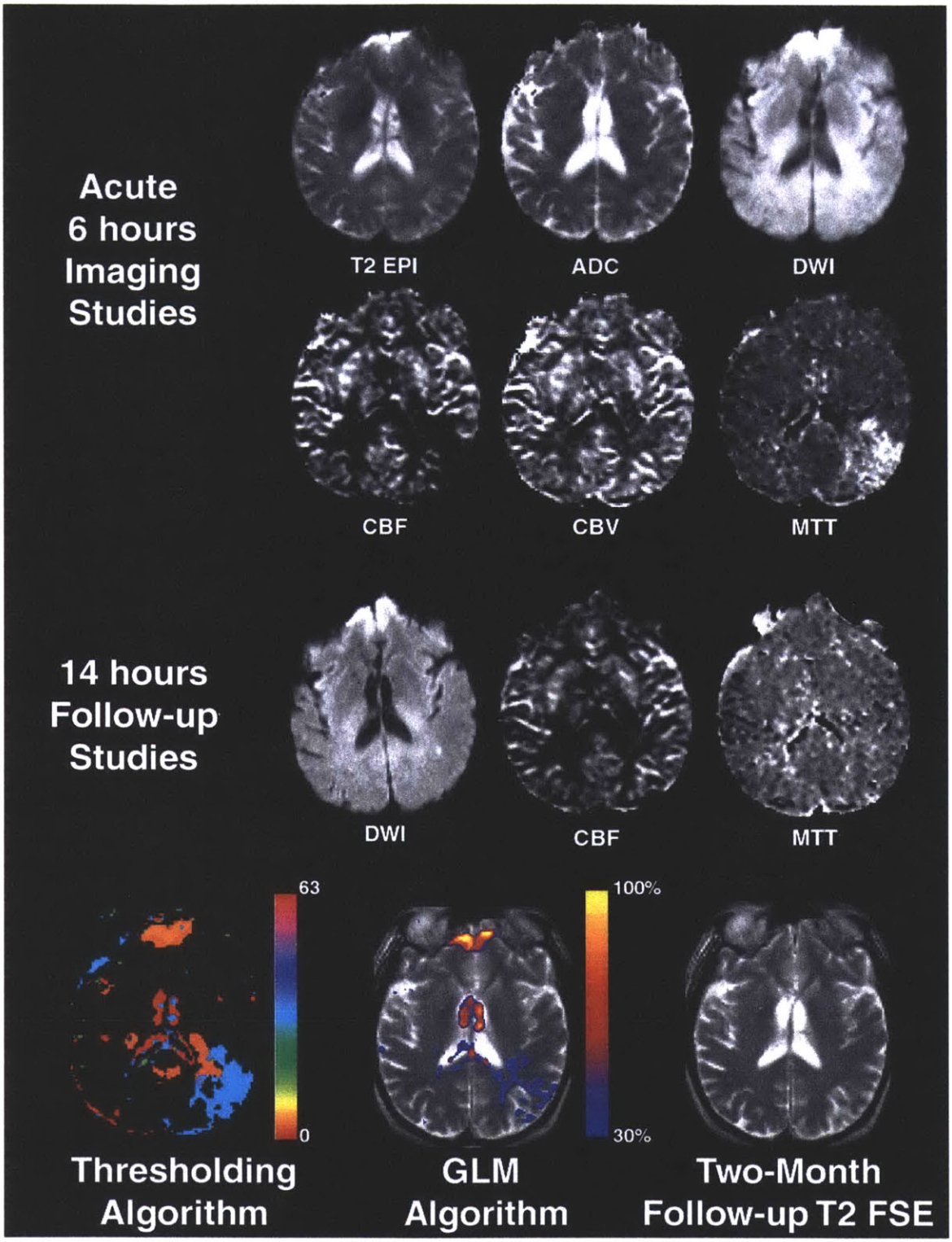

Figure 4.1.4 Predicted risk of infarction maps for a patient with early spontaneous reperfusion. Both the thresholding and the GLM based risk map over predict the follow-up infarct volume as reflected by a two-month follow-up T2 FSE.

Discussion

Our results demonstrate the feasibility of generating, on a voxel-by-voxel basis, quantitative predictive maps of tissue outcome utilizing acute MRI images. These results are consistent with earlier studies that show that tissue predictive algorithms can combine on a voxel-by-voxel basis multiple image modalities successfully into a single map of tissue status (23-26). This study extends these earlier algorithms in two ways. First, the algorithms based on thresholding were extended to include perfusion information. Second, tissue signature algorithms were extended to provide a voxel-by-voxel prediction of the viability of brain tissue in a "risk maps" using a generalized statistical approach.

Combined diffusion and perfusion algorithms

By extending tissue signature algorithms based on thresholding to include perfusion information, our results show that such inclusion improves the predictive power of signature maps. While only a trend towards improved performance was demonstrated in the case of the combined thresholding algorithm over the perfusion-based algorithm (P=0.21), we believe that further optimization of the threshold approach and refinement in interpretation of results would improve its utility. Although statistical significance was not found in the AUCs for the multivariate diffusion-based algorithm compared to the multivariate perfusion-based algorithm using either thresholding or GLM, the ROC curves demonstrate the difference between the diffusion-based and perfusion-based algorithms in their tradeoffs between sensitivity and specificity, a characteristic not evident in simple AUC indices (42). Diffusion-based algorithms were observed to have higher sensitivity in regions of high specificity or low FPR whereas perfusion-based algorithms have higher sensitivity in regions of low specificity. Combined algorithms appear to provide the best trade-off in terms of maintaining high sensitivity at high specificity.

The high specificity of diffusion-based algorithms is not unexpected due to the association between high risk of infarction and changes in diffusion parameters which are believed to detect tissue with altered cellular water homeostasis caused by severe energy depletion and breakdown in Na+-K+ pump activity (22, 26). The level of sensitivity of diffusion-based algorithms is time dependent; less sensitive at very early imaging times before DWI reaches its maximum, and more sensitive hours later when DWI lesion size approaches the "final" infarct size. However, a simple reduction of ADC may not be a marker for irreversibly injured tissue and indeed a set "threshold" for irreversible ADC reductions may be difficult to determine as the threshold varies as a function of depth and duration of ischemia (22). The perfusion parameters, on the other hand, presumably reflect the state of nutritive flow to the voxel of tissue. The lack of specificity but high sensitivity in perfusion-based algorithms may be attributed to the presence of metabolically viable hypoperfused tissue at flow levels below the threshold for electrical neuronal failure (43). The likelihood for tissue to infarct is a combined function of the degree and the duration of blood flow reduction, which have been shown to vary spatially and temporally (43-46). Therefore, perfusion-based algorithms may also have a similar level of time-varying sensitivity and specificity, which varies on a voxel-by-voxel basis.

GLM algorithms

Of the two techniques examined in this study for combining diffusion and perfusion information, the GLM method may provide results that are straightforward to interpret as additional

parameters are included in the algorithm. In initial thresholding algorithms, a key feature was the ability to assign each tissue signature based on imaging to a possible physiologic state of the tissue. However, with the addition of multiple parameters, each additional term exponentially complicates output interpretation since the signature maps create additional states whose biological significance is not necessarily clear. Nevertheless, thresholding algorithms may provide unique insight regarding heterogeneity of the ischemic lesion at any single point in time. Further investigations correlating evolution of these signatures with histology may provide insight into the pathophysiologic significance of the different signatures. GLM algorithms, on the other hand, provide the risk of the tissue infarcting as a continuous variable that ranges between 0 and 1 and therefore, as stroke evolves, the risk of individual voxels of tissue can be monitored quantitatively by a single variable. The recruitment of voxels in the presumed "ischemic penumbra" might therefore be quantified as the change in risk in the peripheral areas from low probability to high probability over time.

In this study, algorithms were trained on data from patients who did not receive thrombolytic or neuroprotective therapy. The two patients with spontaneous reperfusion were specifically not excluded from the training set since their inclusion were believed to be a better reflection of the naturally occurring ischemic stroke patient population where spontaneous reperfusion has been detected within 24 hours after symptom onset in 24% of patients using transcranial doppler ultrasound (47). Therefore, these algorithms' predictions seem likely to be based on the natural evolution of ischemic tissue undergoing infarction. However, the training set is small, and therefore does not yet capture the full range and frequency of stroke evolution possibilities. For example, if in a new patient an event occurs to interrupt the progression of ischemic damage as quantified from the training patient data, the probability of infarction of individual tissue regions may change greatly. This was apparent in the case of Patient 11, who exhibited spontaneous reperfusion (Figure 4.1.4). For such circumstances progression of infarct lesion size have been shown to be diminished (15, 48-50). A similar change in probabilities might be seen after successful therapeutic reperfusion, or after administration of an effective neuroprotective agent. This method therefore appears to provide a technique that might be used to monitor this change in risk quantitatively. Were this approach to be validated, the GLM approach could become a useful statistical method for evaluating the efficacy of novel therapies, and possibly even develop into a tool to help guide the choice of appropriate therapy for individual patients.

Future investigation

These results demonstrate in a preliminary fashion the feasibility of combining diffusion and perfusion information into a single index of tissue risk. While collection of additional patient data will make the specific algorithm parameters more robust, this would not necessarily change the methodology presented for analyzing and quantifying this natural history data. On the other hand, there are still many avenues of investigation for improving these algorithms. Clearly, the retrospective aspect of this study limited the models. As demonstrated by the large variance of lesion volumes and etiologies across patients in this report, prospective studies involving a greater cohort of patients with standardized MR acquisition parameters and follow-ups at set intervals are needed to further test the validity of the algorithmic approaches described here. For example, an overestimation of "final" lesion volumes in some patients may have occurred due to the possible presence of vasogenic edema at five-days post-ictus (51) resulting in the use of wrongly classified voxels in the training and evaluation of our algorithms. In addition,

inaccuracies in the coregistration may have introduced errors in both algorithm development and evaluation. Although intrasubject studies have shown the average misregistration size to be less than 1 mm, less than the voxel dimensions used in this study, the maximum misalignment has been reported to be as large as 3.8 mm (36). This suggests that the GLM algorithms' results may be inaccurate for cases involving small infarct volumes. The addition of acute clinical variables as covariates may also improve GLM models' performances as has been demonstrated by another study that predicted clinical outcome by combining imaging data with initial clinical variables (52).

A priori assumptions in algorithm design, principally that the risk of infarction changes linearly with the covariates, may also have negatively impacted the performance of both thresholding and GLM algorithms. Several studies have shown that the risk of infarction does not change linearly for some of the algorithm variables. For example, ADC has been well documented to first decrease in acute cerebral ischemia before pseudonormalizing and increasing in the chronic stage (9). This non-linear behavior may also hold true for perfusion metrics even in the hyperacute stage. Recent studies have found both increased and decreased CBV in acutely imaged lesions (<12 hours) that become infarcted as shown by follow-up MR studies (16, 19). The GLM algorithms used in this study assume linear behavior. This suggests that additional investigations of algorithms that take into consideration the nonlinear behavior of covariates may provide improved performance.

Finally, there are a few additional technical limitations to our approach. Our models are almost certainly limited because they do not account for the intrinsic anatomic variations in both normal and pathophysiologic conditions. For instance, white matter may be misclassified as territory at risk of infarction since its normal flow values fall within the ischemic range for gray matter. Expert models that can differentiate white from gray matter, perhaps taking into consideration fractional anisotropy, and apply the appropriate tissue specific model to obtain an assessment of infarction risk can potentially compensate for this limitation.

4.2 Generalized Additive Models

Predictive models which combined diffusion and perfusion MRI have been previously shown to provide more sensitive and specific detection of areas at risk of infarction in hyperacute cerebral ischemia than models utilizing diffusion or perfusion alone (27). However, these combined models had an optimal operating point of 66% sensitivity and 84% specificity. One of the limitations of these models was the assumption of a linear dependence of the risk of infarction on their input parameters. Several studies (19, 23), however, have suggested that the risk a voxel will infarct may depend nonlinearly with measured diffusion and perfusion values. In particular, areas that are infarcted in follow-up exams have been observed acutely to contain both abnormally high ADC values, representing tissue that has already infarcted, and abnormally low ADC values, representing tissue at risk of infarction (9, 23). Areas that are infarcted on follow-up imaging studies have also been observed to consist of both low and high CBV values at the acute stage (19). Therefore, models that do not take into consideration these pathophysiologic variations may not perform optimally. This problem can potentially be overcome by using different sets of models for handling different cases. In prospective studies, however, the decision of which model is appropriate may not be clear. Instead, models whose functional form are derived from their data, such as generalized additive models (GAM) (53), may provide better

estimates of infarction state over models that assume an *a priori* linear dependence, such as generalized linear models (GLM). The aim of this study therefore was two-fold: (1) to extend linear predictive MRI models by generalizing them to handle nonlinear behavior and (2) to examine if GAM algorithms provide an improved estimate of the risk of infarction over GLM models.

Subjects and Methods

Patient inclusion criteria are the same as that reported in Section 4.1 describing the development of GLM models. Using the imaging protocol and techniques described in the previous section, maps of the EPI T2 image (T2), isotropic diffusion weighted image (DWI), apparent diffusion coefficient (ADC), relative cerebral blood flow (CBF), relative cerebral blood volume (CBV), and mean transit time (MTT) were calculated on a voxel-by-voxel basis. The diffusion and perfusion maps were spatially coregistered using an automated image registration software package, AIR 3.08 (35). Intensity values in each image were normalized by the mean value of normal appearing regions in the contralateral hemisphere as described in Section 4.1 to reduce "relative" values (rT2, rADC, rDWI, rCBF, rCBV, and rMTT).

Based on the results of the previous section which showed the best model in terms of the Akaike Information Criterion included all covariates, GLM and GAM models of risk of tissue infarction were generated combining T2, ADC, DWI, rCBF, rCBV, and MTT as input parameters. Models were also generated using only independent parameters as input in order to evaluate the effects of dependent variables on the results. The coefficients for the GLM and GAM for each patient were calculated using the same jack-knifing approach described in the previous section to avoid bias. For both algorithms, tissue outcome was modeled as a binary variable (infarcted/non-infarcted), P, where the value 1 represented infarcted tissue and value 0 non-infarcted tissue. For the GLM, coefficients were calculated using:

$$P = \frac{1}{1 + e^{-\eta(\mathbf{x})}} \tag{4.2.1}$$

where $\eta(\mathbf{x})$, the predictor is a linear function of its input parameters, $\mathbf{x}$,

$$\eta(\mathbf{x}) = \alpha + \sum_i \beta_i x_i \tag{4.2.2}$$

and β_i are again the elements of the vector of calculated coefficients and α the bias or intercept term for the GLM. For the GAM, Equation 4.2.2 is generalized to no longer assume a linear relationship:

$$\eta(\mathbf{x}) = \alpha + \sum_i f_i(x_i) \tag{4.2.3}$$

where $f_i(x_i)$ is a nonparametric function of x_i, which for this study was a cubic B-spline. The risk of infarction for each voxel was then calculated using the new predictor. The parameters for the GAM for each patient were calculated using the other 13 patients' data for training using a supervised learning algorithm using S-PLUS 6.0 (Insightful, Seattle, WA).

The performances of the GAM and the GLM models were evaluated using the same ROC analysis techniques described Section 4.1. The AUC for the ROC curves for each patient was calculated using numerical integration. The AUCs for the GAM and the GLM were compared using a paired one-tailed Wilcoxon signed-rank test. $P<0.05$ was considered significant.

Results

Figure 4.2.1 shows the calculated $f_i(x_i)$, the relative contribution of x_i to the total additive predictor for the GAM for each of the covariates when using a model consisting only of the independent parameters. In dashed lines, the GLM weighting parameters are also shown in which each $f_i(x_i)$ was assumed to be a linear operator. The predictor, $\eta(x)$, is the summation of the individual $f_i(x_i)$ terms for a given rT2, rADC, rCBF and rCBV values plus an alpha onset (α=-1 for both models). From the graphs, the risk of infarction increases with rT2. At very high values, the risk of infarction for rT2 decreases slightly in the GAM. For rADC, low values of rADC are associated with increased risk of infarction for both GAM and GLM. However, for GAM models, normal to high values are do not reduce the risk of infarction whereas in the GLM, normal to high rADC reduces the predicted risk of infarction. For rCBF, the GLM and GAM perform similarly except for high rCBF values. In the GAM, the estimated risk of infarction for high rCBF values is not further reduced as compared to the GLM. For rCBV, increasing values are associated with increasing risk of infarction for both GAM and GLM. However, high rCBV values will not further increase the risk of infarction in the GAM as compared to the GLM.

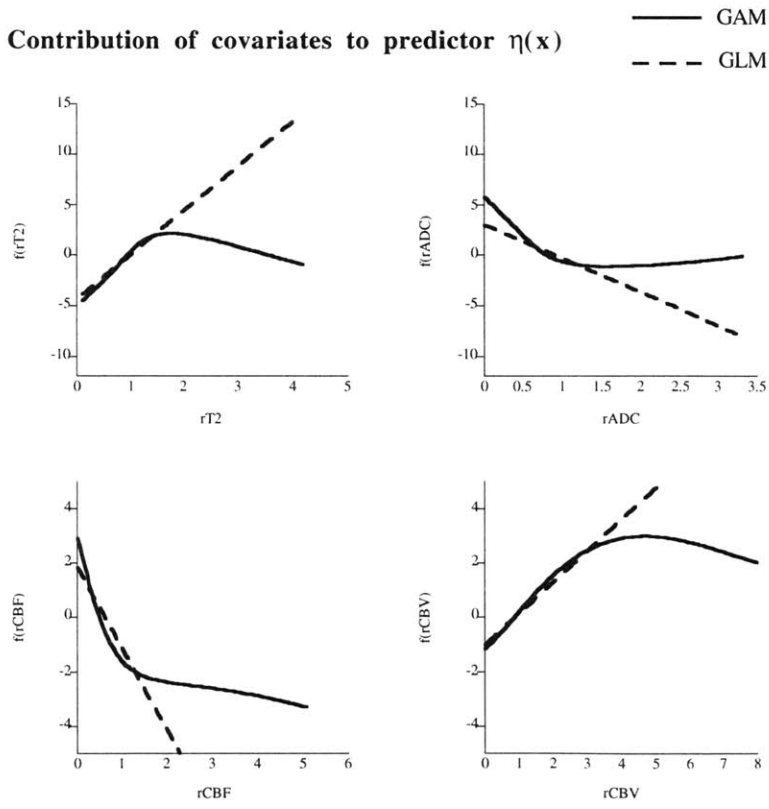

Figure 4.2.1 Transformation functions $f_i(x_I)$ for rT2, rADC, rCBF and rCBV in a GAM model consisting only of independent parameters. In dashed lines, the GLM weighting parameters are also shown. Note the non-linear behavior of $f_i(x_I)$ where input values above a cutoff value do not contribute greatly to risk of infarction as it would if a linear operator was assumed.

Figure 4.2.2 shows the $f_i(x_i)$ and β for models using all input parameters. In this case rT2 values closely follow the same functional form as the GLM for values within physiologic range. Non-linear behavior is observed for rADC and rDWI where normal and low values of rDWI and rADC have lower

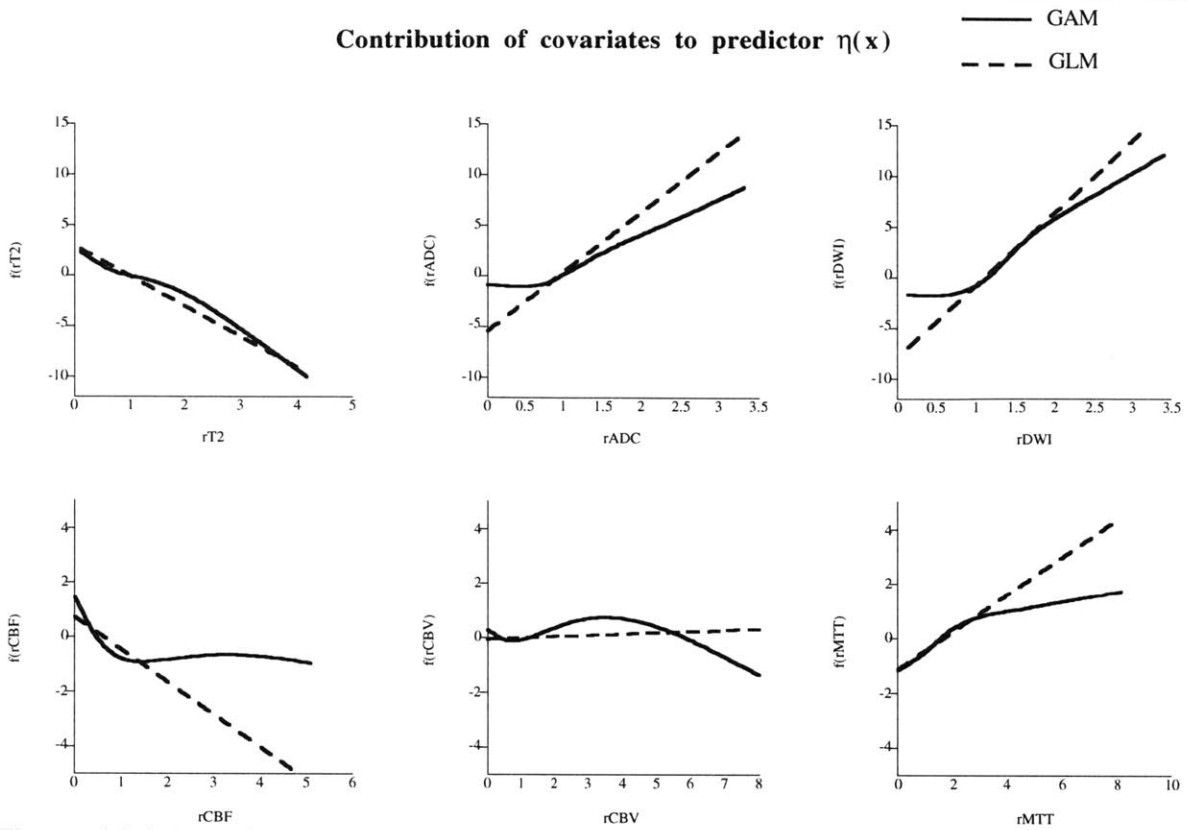

Figure 4.2.2 Transformation functions $f_i(x_i)$ for all six input parameters in a GAM model. In dashed lines, the GLM weighting parameters are also shown.

contributions to the risk of infarction in the GAM than in the GLM. The behavior of rADC and rT2 behave opposite than in Figure 4.2.1 which is potentially due to the presence of the non-independent parameter of rDWI, a mathematical combination of rADC and rT2. For rCBF values, low values will produce a higher risk of infarction as can be inferred by the negative slope. Comparable performance is again seen between the GLM and GAM models except for normal to high CBF values where the GAM again exhibits nonlinear behavior. Non-linear behavior is also seen with rMTT, where comparable behavior is demonstrated for GAM and GLM for lower values. However, for high rMTT values, in the GAM, the slope is reduced compared to the GLM. With the introduction of rMTT, the contributions of both rCBF and rCBV to the estimated risk of infarction are reduced with rCBV's contribution becoming non-significant. In the GAM, a non-linear transformation function is observed for rCBV.

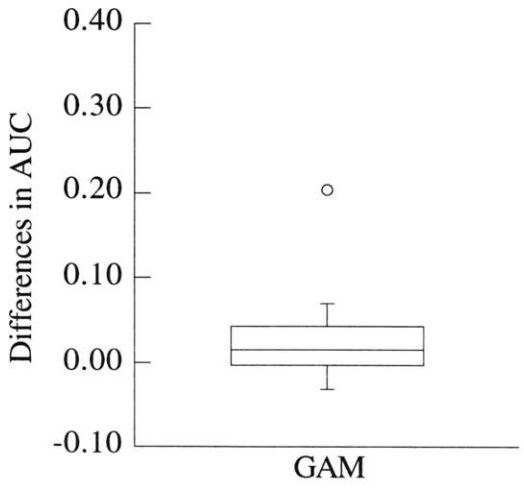

Figure 4.2.3 Boxplot of differences between the AUCs for the GAM versus the GLM for 14 patients. The GAM had significantly higher AUC than the GLM (P=.034).

Figure 4.2.3 shows the boxplot of the differences between the AUCs for the GAM versus GLM for the 14 patients. The GAM had statically significantly higher AUC than the GLM (P=0.034). The optimal operating points for both GAM (specificity=79% sensitivity=70% using a cutoff of 29%) and GLM were comparable (specificity=84%, sensitivity=66% using a cutoff of 32%).

Figure 4.2.4 shows an example case where GAM models provide better prediction of tissue that eventually infarcts for a 33-year-old patient whom was imaged within 4 hours of presenting with symptoms (Patient 7 in Table 4.1.1). Also shown are the acute imaging parameters. Both GAM and GLM were thresholded at a risk of 30%. The GAM shows improved performance over the GAM especially in the area surrounding the core of the infarct. However, the GAM provides poorer performance in non-tissue regions as reflected by spots along edge of the brain.

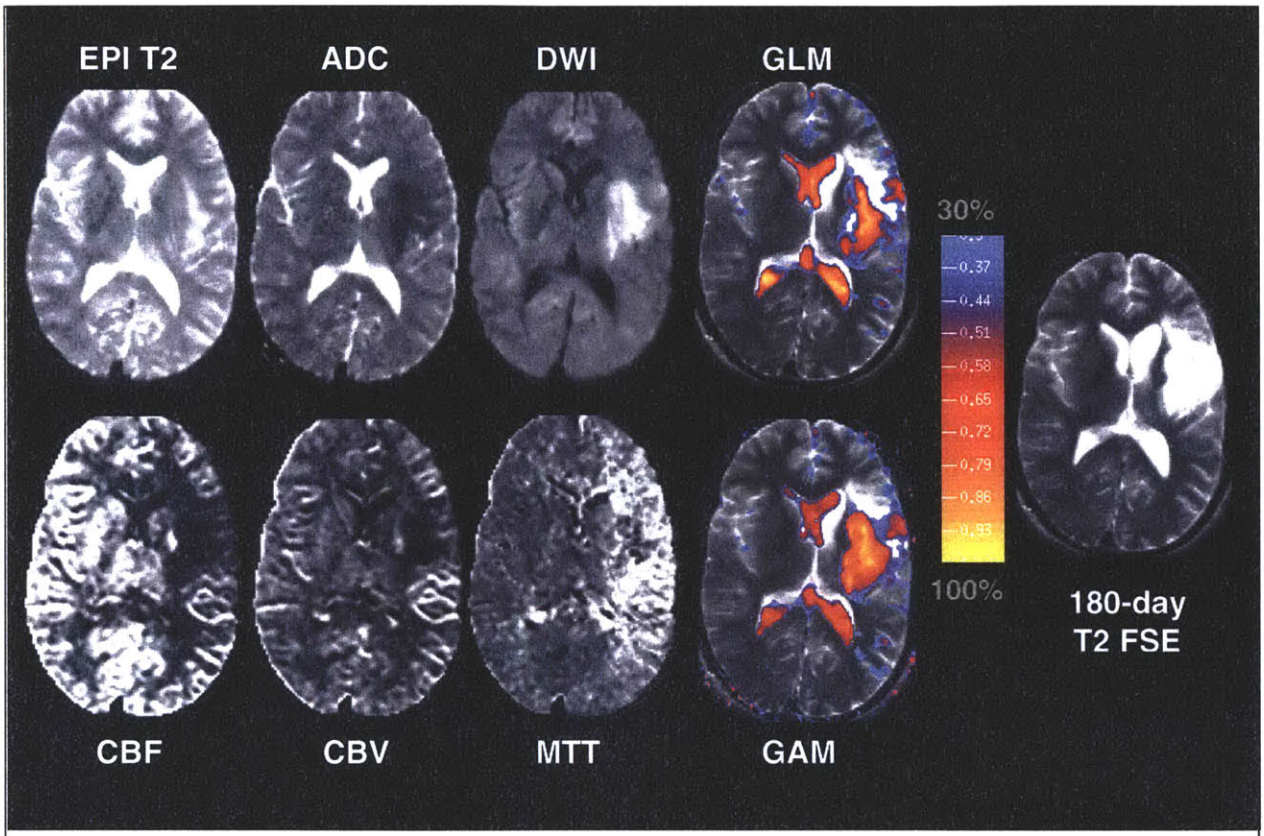

Figure 4.2.4 Initial imaging data of acute stroke patient acquired within 4 hours of symptom onset and predicted risk of infarction by GLM and GAM thresholded at their optimal operating point of 30%. The GAM provides a better estimate of the lesion volume especially in the periphery of the initial lesion volume.

Discussion

This study has demonstrated that the GAM, besides providing a more flexible model, may also provide a more accurate estimate of risk of infarction than the GLM. The GAM may be of most benefit over GLM in cases where biphasic behavior of the input parameters exists. This study has also shown that the GAM may be useful in identifying non-linear behavior and may provide insight into physiologic variation of risk of infarction with rT2, rADC, rDWI, rCBF, rCBV and

rMTT. For rADC, in models consisting only of independent parameters (Figure 4.2.1), high values of rADC in the GLM models reduce the estimated risk of infarction whereas in the GAM models they have little effect. This apparently contradicts the well-documented association of elevated ADC with infarct lesion in the chronic stage. However, since the study was *a priori* limited to hyperacute stroke patients presenting within 12 hours, it is likely that the training data did not have enough representative points for the GAM to detect a positive correlation of risk of infarction with elevated ADC. We speculate that if future studies were to include chronic as well as acute stroke patients in their training data, a GAM algorithm may perform better than a GLM algorithm, which would not be able to take into consideration such non-linear behavior.

Besides providing a quantitative estimate of individual voxels of tissue's risk of infarction, both GLMs and GAMs may provide insight into the relative weights of the different input parameters in estimating the risk of infarction. For example, the diffusion parameters (rDWI, rADC and rT2) have the greatest weight in terms of estimating which tissue may become infarcted if the ischemic cascade is allowed to proceed unimpeded. These parameters are followed by the perfusion parameters (rCBF, rMTT and rCBV) in weight with rCBV being statistically insignificant in the combined algorithms used in this study. Care needs to be taken when examining the weighting parameters of the models, however, since the input parameters are not independent. As a result, aliasing and marginality constraints should be taken into account (37). For example, the combined diffusion coefficients (Table 4.1.2 and Figure 2.2.2) suggest that increased rADC and reduced rT2 are positive risk factors in the hyperacute state, which is inconsistent with the generally observed behavior of reduced ADC in the acute stroke setting (9, 12, 54). However, when GLM models using rADC and rT2 are examined without rDWI (Figure 4.2.1), the risk of infarction is negatively correlated with rADC, and positively correlated with rT2, both consistent with expected physiologic behavior. This inconsistency is likely due to the interactions of the non-independent variables, rDWI with rADC and rT2. Because the covariates are themselves correlated, the partial correlations may be different from the marginal correlations. In addition, parameters that are significant in univariate models may lose their significance when combined with other covariates, as in the case of rCBV when combined with rCBF and rMTT. For this reason, in the model selection process, care was taken to consider the independent covariates first before including the dependent variables, rDWI and rMTT, which are mathematical combinations of the other parameters. By analyzing the independent parameters first separately, one finds that each of the parameters contribute significantly to the models, and indeed may be useful in understanding the biological state of the tissue. Therefore, although rCBV information may not significantly improve the prediction of infarction in the combined diffusion and perfusion model, it may still be an independent indicator of tissue status and therefore useful for clinical decision-making.

One of the limitations of the GAM is its increased computational complexity due to its use of nonparametric functions that are derived from the data using smoothing functions (55). Piece-wise linear models may provide a compromise between computational complexity with modeling of non-linear behavior. Another limitation to both the GAM and GLM models is that both models do not take into account intrinsic anatomic variations in both normal and pathophysiologic conditions. The GAM models may still fail in distinguishing normal white matter from ischemic gray matter. Expert models that can differentiate white from gray matter from CSF may potentially compensate for this still existing limitation.

4.3 Hierarchical Mixture of Experts

A limitation of the GLM and GAM algorithms is that the intrinsic variations in both normal and pathophysiologic states are not taken into account. Utilization of a hierarchical mixture of experts (HME) system is postulated to provide better prediction than a single-layer GLM since measured DWI and PWI values show dependence on tissue type. Using a mixture of experts in which each tissue type will be analyzed by its own expert may improve the accuracy of the prediction. For example, normal white matter CBF values are at ischemic levels for gray matter and thus, white matter may need a different statistical model of infarction risk than gray matter. A mixture of experts approach may potentially handle this need for separate models. The purpose of this study is two-fold: (1) to develop predictive models using a hierarchical mixtures of experts architecture and (2) to compare the performance of HME models with the GLM models developed in Section 4.1. We hypothesize that a mixture of experts model will provide improved prediction of tissue outcome than a single-layer GLM. We tested this hypothesis by analyzing the predictive performance of both models on hyperacute stroke patients.

Subjects and Methods

HME Algorithms

The HME is a tree-structured architecture consisting of gating and expert networks (56), as shown in Figure 4.3.1. (For an in depth discussion of HMEs see (56).) Briefly, the gating networks calculate the *a priori* probabilities of which expert to use based on the values of the input vector **x**. Each expert generates an output μ_i based on the input vector {**x**} and target output vector **y**. The expert networks may themselves consist of other GLMs or HMEs. In this application, μ_{ij} is the probability of infarction. The expert networks are GLMs trained on a binary target vector **y**.

The gating networks are also GLMs utilizing a multinomial density function. The *a priori* probabilities of the top level i branches can be computed as:

$$g_i = \frac{e^{\zeta_i}}{\sum_k e^{\zeta_k}}$$

where

$$\zeta_i = \mathbf{v}_i^{\mathrm{T}} \mathbf{x},$$

that is also a function of the input vector. The lower levels j for each i level are computed similarly:

$$g_{j|i} = \frac{e^{\zeta_{ij}}}{\sum_k e^{\zeta_{ik}}}$$

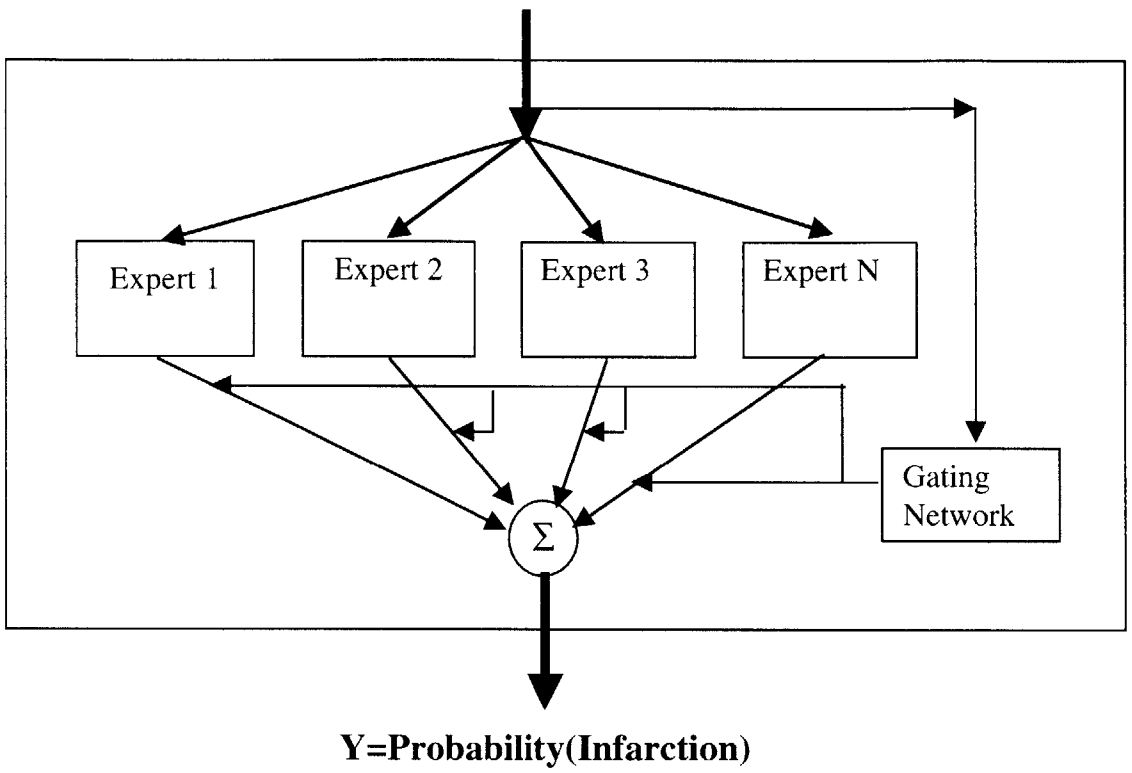

Figure 4.3.1 Architecture for a Hierarchical Mixture of Experts whose top layer consists of N experts. Each expert can be another HME or single layer GLM.

with

$$\zeta_{ij} = \mathbf{v}_{ij}^{\mathrm{T}} \mathbf{x}.$$

The output **Y** is then the sum of the output of the individual experts weighted by the gating functions:

$$Y = \sum_i g_i \sum_j g_{j|i} \mu_{ij}$$

where:

$$\mu_{ij} = \frac{1}{1 + e^{-\mathbf{W}_{ij}^{\mathrm{T}} \mathbf{x}}}.$$

For training, the posterior probabilities of each network can then be represented as follows:

$$h_i = \frac{g_i \sum_j g_{j|i} P_{ij}(y)}{\sum_i g_i \sum_j g_{j|i} P_{ij}(y)}$$

$$h_{j|i} = \frac{g_{j|i} P_{ij}(y)}{\sum_i g_i \sum_j g_{j|i} P_{ij}(y)}$$

where

$$P_{ij}(y) = \mu_{ij}^{y} \left(1-\mu_{ij}\right)^{1-y}$$

assuming **y** is the known output given an input vector **x**.

The Expectation-Maximization (EM) algorithm was used for updating the HME parameters as described in (56). As the expectation step, h_i and $h_{j|i}$ for the current parameters are calculated. In the maximization step, the parameters are updated using the t training samples as follows:

$$\mathbf{W}_{ij} = \arg\max_{\mathbf{W}_{ij}} \sum_t h_{ij}^{(t)} \ln P_{ij}(y^{(t)})$$

$$\mathbf{v}_i = \arg\max_{\mathbf{v}_i} \sum_t \sum_k h_k^{(t)} \ln g_k^{(t)}$$

$$\mathbf{v}_{ij} = \arg\max_{\mathbf{v}_{ij}} \sum_t \sum_k h_k^{(t)} \sum_l h_{l|k}^{(t)} \ln g_{l|k}^{(t)}$$

where $h_{ij}=h_i h_{j|i}$. These three network parameter equations can be solved using IRLS. For the weight parameters, $\mathbf{W}_{ij}$, a logistic function is used since each expert consists of a GLM. For the gating functions, $\mathbf{v}_i$ and $\mathbf{v}_{ij}$, a softmax function is used as the link function in order to handle the multinomial distribution of the gating networks. The EM steps are repeated until the parameter values converge.

A two-layer HME consisting of three experts at the top branch and four experts in each sub-branch was used resulting in a total of 12 experts. Each expert was a GLM model.

Patient Selection and Image Acquisition

Patient inclusion criteria are the same as that reported in the previous sections describing the development of GLM and GAM models. Using the imaging protocol and techniques described in the previous section, maps of the apparent diffusion coefficient (ADC), relative cerebral blood flow (rCBF), relative cerebral blood volume (rCBV), and mean transit time (MTT) were calculated on a voxel-by-voxel basis. The diffusion and perfusion maps were coregistered using an automated image registration software package, AIR 3.08 (35). Intensity values in each image were normalized by the mean of its contralateral hemisphere.

Two sets of training data were used to evaluate the potential of the HME to discriminate different tissue types. The first set of training data used the same data to train the GLM and GAM in Sections 4.1 and 4.2 (ROI). The second set of training data consisted of all outlined follow-up lesion values assigned the value 1 and all other tissue voxels in the image assigned the value zero (ALL). This dataset was also subsampled. The HME and the GLM were trained on the two-sets of data and performances evaluated using jack-knifing routines described in Section 4.1.

Evaluation of Algorithm Performance

ROC analysis as described in Section 4.1 was performed for the predicted infarct volumes from GLM and HME algorithms. Section 4.1 has already demonstrated the superior performance obtained by combining DWI and PWI values and as result, in this study, analysis will be limited to combined DWI and PWI models. The AUC for the ROC curves for each patient was calculated using numerical integration. The AUC for the ROC curves were compared using paired one-tailed Wilcoxon signed-rank test. $P<0.05$ was considered significant. The optimal operating points were also calculated and presented to the nearest significant digit.

Results

Figure 4.3.2 shows the boxplots of the differences between the AUCs for the HME versus the GLM when trained using user outlined lesions and normal regions constrained to the ipsilateral hemisphere (ROI) (same used in Section 4.1) and when trained using the whole brain (ALL). No statistical difference was found between the HME and GLM when trained using only the ipsilateral tissue data ($P=0.48$) whereas when trained using the whole brain the HME performed significantly better ($P=0.034$).

Figure 4.3.3 shows the HME and GLM prediction for Patient 1 using regional subsets (ROI) and the whole brain (ALL) for training. One sees that sees that the areas predicted to infarct appear brighter on the HME models, and hence with greater probability than the GLM model for both training data sets. In addition, the optimal operating points were found to be 30% and 5% when training with ROI and ALL respectively. It is also evident that training with data whose normal values were not constrained to the ipsilateral hemisphere (ROI), a better estimation of tissue outcome in the normal contralateral hemisphere as well as in CSF is obtained. One notes, however, that normal white matter continues to be misclassified as being at high risk of infarction. It should also be noted that all four models were able to acutely identify the volume of tissue that infarcted based on follow-up exam, albeit with different

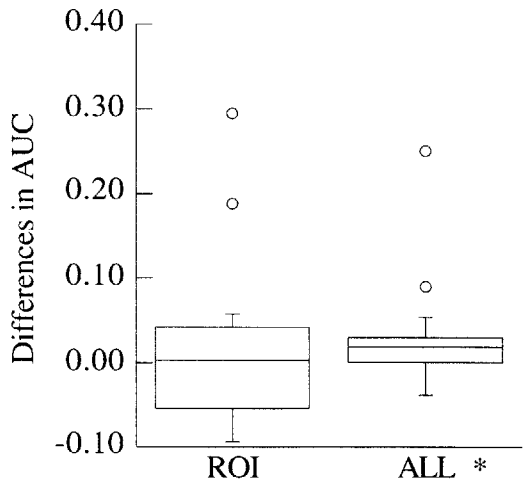

Figure 4.3.2 Boxplot of differences between AUCs for the HME and the GLM when using only regions (ROI) of ipsilateral tissue for training and using the whole brain for training (ALL). HME had significantly higher AUC ($P=0.034$) when training with the latter.

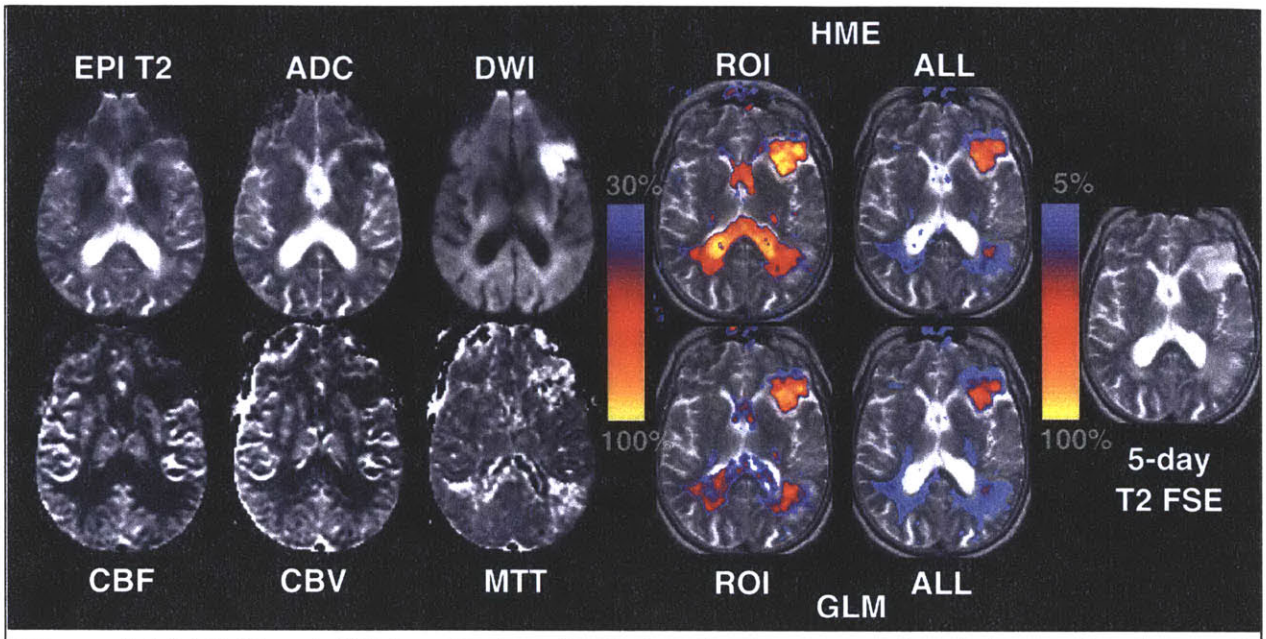

Figure 4.3.3 HME and GLM predictions for Patient 1 using user outlined abnormal and normal regions (ROI) for training and user outlined abnormal and the remaining brain as normal (ALL) for training. The optimal operating points for the two training sets are 30% and 5% for ROI and ALL respectively. The acute imaging data as well as the 5-day follow-up study are shown for comparison.

degrees of certitude, as reflected by intensity of the risk maps.

Discussion

Based on these preliminary results, we have shown the feasibility of using an HME for predicting tissue at risk of infarction. Furthermore, the HME architecture improves our estimate of tissue at risk of infarction over a single-layer GLM. We speculate that this is due to multiple experts handling different tissue subtypes. We have also demonstrated improved performance of models trained using the entire infarct volume and entire remaining brain tissue with greater specificity in identifying lesion volumes. When training with the infarct/remaining brain data sets (ALL), the HME has significantly higher AUCs than the GLM model (P=0.034). The models performed poorest for patients with small lesion volumes (Patients 2 and 10) perhaps due to errors in the co-registration process. Additional evaluation using a larger patient population involving larger volumes of tissue may provide a better assessment of the performance of these models.

With the continued poor risk assessment of normal white matter, one suspects that there does not exist enough information to segment normal white matter from gray matter other than using flow rates. However, normal white matter flow rates are equivalent to ischemic gray matter levels which results in white matter voxels' continued misprediction. We therefore speculate that the inclusion of anisotropy may help to segment gray and white matter tissue and therefore result in more accurate estimates. Future investigations can also involve using GAMs as the experts rather than GLMs, since based on the results of the previous section, GAMs appear to have more accurate performance.

4.4 Conclusions

Despite some limitations, we have shown that algorithms combining diffusion and perfusion information can assess the risk of infarction at the acute stage with greater sensitivity and specificity than algorithms using diffusion and perfusion information separately. Of the combined algorithms studied, the HME may provide the preferred approach due to its potentially greater ease of interpretation with its single index of risk and greater sensitivity and specificity trade-off. While further investigation and algorithm refinement is necessary, this method for quantitatively assessing the risk of infarction on a voxel-by-voxel basis shows promise as a technique for not only gaining insight into the natural spatial temporal evolution of ischemic damage in humans but also for evaluating the effects that novel therapies may have on this process.

4.5 References

1. Sorensen AG, Buonanno FS, Gonzalez RG, et al. Hyperacute stroke: Evaluation with combined multisection diffusion-weighted and hemodynamically weighted echo-planar MR imaging. *Radiology*. 1996;199:391-401.

2. Lutsep HL, Albers GW, DeCrespigny A, Kamat GN, Marks MP, Moseley ME. Clinical utility of diffusion-weighted magnetic resonance imaging in the assessment of ischemic stroke. *Ann Neurol*. 1997;41:574-580.

3. Barber PA, Darby DG, Desmond PM, Gerraty RP, Yang Q, Li T, Jolley D, Donnan GA, Tress BM, Davis SM. Identification of major ischemic change. Diffusion-weighted imaging versus computed tomography. *Stroke*. 1999;30:2059-2065.

4. Gonzalez RG, Schaefer PW, Buonanno FS, Schwamm LH, Budzik RF, Rordorf G, Wang B, Sorensen AG, Koroshetz WJ. Diffusion-weighted MR imaging: diagnostic accuracy in patients imaged within 6 hours of stroke symptom onset. *Radiology*. 1999;210:155-162.

5. Ueda T, Yuh WT, Maley JE, Quets JP, Hahn PY, Magnotta VA. Outcome of acute ischemic lesions evaluated by diffusion and perfusion MR imaging. *AJNR Am J Neuroradiol*. 1999;20:983-989.

6. Singer MB, Chong J, Lu D, Schonewille WJ, Tuhrim S, Atlas SW. Diffusion-weighted MRI in acute subcortical infarction. *Stroke*. 1998;29:133-136.

7. Lovblad KO, Laubach HJ, Baird AE, Curtin F, Schlaug G, Edelman RR, Warach S. Clinical experience with diffusion-weighted MR in patients with acute stroke. *AJNR Am J Neuroradiol*. 1998;19:1061-1066.

8. van Everdingen KJ, van der Grond J, Kappelle LJ, Ramos LM, Mali WP. Diffusion-weighted magnetic resonance imaging in acute stroke. *Stroke*. 1998;29:1783-1790.

9. Warach S, Chien D, Li W, Ronthal M, Edelman RR. Fast magnetic resonance diffusion-weighted imaging of acute human stroke. *Neurology*. 1992;42:1717-1723.

10. Tong DC, Yenari MA, Albers GW, O'Brien M, Marks MP, Moseley ME. Correlation of perfusion- and diffusion-weighted MRI with NIHSS score in acute (6.5 hour) ischemic stroke. *Neurology*. 1998;50:864-870.

11. Warach S, Dashe JF, Edelman RR. Clinical outcome in ischemic stroke predicted by early diffusion-weighted and perfusion magnetic resonance imaging: A Preliminary Analysis. *J Cereb Blood Flow Metab*. 1996;16:53-59.

12. Schwamm LH, Koroshetz WJ, Sorensen AG, Wang B, Copen WA, Budzik R, Rordorf G, Buonanno FS, Schaefer PW, Gonzalez RG. Time course of lesion development in patients with acute stroke: Serial diffusion- and hemodynamic-weighted magnetic resonance imaging. *Stroke*. 1998;29:2268-2276.

13. Barber PA, Darby DG, Desmond PM, Yang Q, Gerraty RP, Jolley D, Donnan GA, Tress BM, Davis SM. Prediction of stroke outcome with echoplanar perfusion- and diffusion-weighted MRI. *Neurology*. 1998;51:418-426.

14. Neumann-Haefelin T, Wittsack HJ, Wenserski F, Siebler M, Seitz RJ, Modder U, Freund HJ. Diffusion- and perfusion-weighted MRI. The DWI/PWI mismatch region in acute stroke. *Stroke*. 1999;30:1591-1597.

15. Beaulieu C, de Crespigny A, Tong DC, Moseley ME, Albers GW, Marks MP. Longitudinal magnetic resonance imaging study of perfusion and diffusion in stroke: evolution of lesion volume and correlation with clinical outcome. *Ann Neurol*. 1999;46:568-578.

16. Schlaug G, Benfield A, Baird AE, Siewert B, Lovblad KO, Parker RA, Edelman RR, Warach S. The ischemic penumbra: operationally defined by diffusion and perfusion MRI. *Neurology*. 1999;53:1528-1537.

17. Baird AE, Benfield A, Schlaug G, Siewert B, Lovblad KO, Edelman RR, Warach S. Enlargement of human cerebral ischemic lesion volumes measured by diffusion-weighted magnetic resonance imaging. *Ann Neurol*. 1997;41:581-589.

18. Rordorf G, Koroshetz WJ, Copen WA, Cramer SC, Schaefer PW, Budzik RF, Schwamm LH, Buonanno F, Sorensen AG, Gonzalez RG. Regional ischemia and ischemic injury in patients with acute middle cerebral artery stroke as defined by early diffusion-weighted and perfusion-weighted MRI. *Stroke*. 1998;29:939-943.

19. Sorensen AG, Copen WA, Ostergaard L, Buonanno FS, Gonzalez RG, Rordorf G, Rosen BR, Schwamm LH, Weisskoff RM, Koroshetz WJ. Hyperacute stroke: simultaneous measurement of relative cerebral blood volume, relative cerebral blood flow, and mean tissue transit time. *Radiology*. 1999;210:519-527.

20. Karonen JO, Vanninen RL, Liu Y, Ostergaard L, Kuikka JT, Nuutinen J, Vanninen EJ, Partanen PL, Vainio PA, Korhonen K, Perkio J, Roivainen R, Sivenius J, Aronen HJ. Combined

diffusion and perfusion MRI with correlation to single-photon emission CT in acute ischemic stroke. Ischemic penumbra predicts infarct growth. *Stroke*. 1999;30:1583-1590.

21. Darby DG, Barber PA, Gerraty RP, Desmond PM, Yang Q, Parsons M, Li T, Tress BM, Davis SM. Pathophysiological topography of acute ischemia by combined diffusion- weighted and perfusion MRI. *Stroke*. 1999;30:2043-2052.

22. Baird AE, Warach S. Magnetic resonance imaging of acute stroke. *J Cereb Blood Flow Metab*. 1998;18:583-609.

23. Welch KMA, Windham J, Knight RA, Nagesh V, Hugg JW, Jacobs M, Peck D, Booker P, Dereski MO, Levine SR. A model to predict the histopathology of human stroke using diffusion and T2-weighted magnetic resonance imaging. *Stroke*. 1995;26:1983-1989.

24. Nagesh V, Welch KMA, Windham JP, Patel S, Levine SR, Hearshen D, Peck D, Robbins K, D'Olhaberriague L, Soltanian-Zadeh H, Boska MD. Time course of ADCw changes in ischemic stroke: Beyond the Human Eye! *Stroke*. 1998;29:1778-1782.

25. D'Olhaberriague L, Welch KMA, Nagesh V, Gymnopoulos C, Mansbach HH, Hugg JW, Boska MD, Knight RA, Schultz LR, Levine SR, Chopp M. Preliminary clinical-radiological assessment of a MR tissue sigature model in human stroke. *J Neurol Sci*. 1998;156:158-166.

26. Jiang Q, Chopp M, Zhang ZG, Knight RA, Jacobs M, Windham JP, Peck D, Ewing JR, Welch KMA. The temporal evolution of MRI tissue signatures after transient middle cerebral artery occlusion in rat. *J Neurol Sci*. 1997;145:15-23.

27. Wu O, Koroshetz WJ, Ostergaard L, Buonanno FS, Copen WA, Gonzalez RG, Rordorf G, Rosen BR, Schwamm LH, Weisskoff RM, Sorensen AG. Predicting tissue outcome in acute human cerebral ischemia using combined diffusion- and perfusion-weighted MR imaging. *Stroke*. 2001;32:933-942.

28. Adams HJ, Bedndixen B, Kappelle J, Biller J, Love B, Gordon D, Marsh Er. Classification of subtype of acute ischemic stroke. Definitions for use in a multicenter clinical trial. TOAST. Trial of Org 10172 in Acute Stroke Treatment. *Stroke*. 1993;24:35-41.

29. Sorensen AG, Wu O, Copen WA, Davis TL, Gonzalez RG, Koroshetz WJ, Reese TG, Rosen BR, Wedeen VJ, Weisskoff RM. Human acute cerebral ischemia: detection of changes in water diffusion anisotropy by using MR imaging. *Radiology*. 1999;212:785-792.

30. Villringer A, Rosen BR, Belliveau JW, Ackerman JL, Lauffer RB, Buxton RB, Chao YS, Wedeen VJ, Brady TJ. Dynamic imaging with lanthanide chelates in normal brain: contrast due to magnetic susceptibility effects. *Magn Reson Med*. 1988;6:164-174.

31. Rosen BR, Belliveau JW, Chien D. Perfusion imaging by nuclear magnetic resonance. *Magn Reson Q*. 1989;5:263-281.

32. Weisskoff RM, Zuo CS, Boxerman JL, Rosen BR. Microscopic susceptibility variation and transverse relaxation: theory and experiment. *Magn Reson Med.* 1994;31:610-610.

33. Østergaard L, Weisskoff RM, Chesler DA, Gyldensted C, Rosen BR. High resolution measurement of cerebral blood flow using intravascular tracer bolus passages. Part I: Mathematical approach and statistical analysis. *Magn Reson Med.* 1996;36:715-725.

34. Rosen B, Belliveau J, Buchbinder B, Kwong K, Poorka L, Fisel R, Weisskoff R, Neuder M, Aronnen H, Cohen M, Hopkins A, Brady T. Contrast agents and cerebral hemodynamics. *Magn Reson Med.* 1991;19:285-292.

35. Woods RP, Cherry SR, Mazziotta JC. Rapid automated algorithm for aligning and reslicing PET images. *J Comput Assist Tomogr.* 1992;16:620-633.

36. Woods RP, Grafton ST, Holmes CJ, Cherry SR, Mazziotta JC. Automated image registration: I. General methods and intrasubject, intramodality validation. *J Comput Assist Tomogr.* 1998;22:139-152.

37. McCullagh P, Nelder JA. *Generalized Linear Models.* Second Edition. New York: Chapman and Hall Ltd, 1983.

38. Bishop CM. *Neural Networks for Pattern Recognition.* New York: Oxford University Press Inc., 1995.

39. Efron B. *The Jackknife, the bootstrap and other resampling plans.* Philadelphia: Society for Industrial and Applied Mathematics, 1982.

40. Hanley JA, McNeil BJ. The meaning and use of the area under a receiver operating characteristic (ROC) curve. *Radiology.* 1982;143:29-36.

41. Halpern EJ, Albert M, Krieger AM, Metz CE, Maidment AD. Comparison of receiver operating characteristic curves on the basis of optimal operating points. *Acad Radiol.* 1996;3:245-253.

42. Swets JA, Pickett RM. *Evaluation of Diagnostic Systems: Methods from Signal Detection Theory.* New York: Academic Press, 1982.

43. Siesjo BK. Cerebral circulation and metabolism. *J Neurosurg.* 1984;60:883-908.

44. Astrup J, Siesjo BK, Symon L. Thresholds in cerebral ischemia - the ischemic penumbra. *Stroke.* 1981;12:723-725.

45. Pulsinelli W. Pathophysiology of acute ischaemic stroke. *Lancet.* 1992;339:533-536.

46. Hossmann KA. Viability thresholds and the penumbra of focal ischemia. *Ann Neurol.* 1994;36:557-565.

47. Vang C, Dunbabin D, Kilpatrick D. Effects of spontaneous recanalization on functional and electrophysiological recovery in acute ischemic stroke. *Stroke*. 1999;30:2119-2125.

48. Jansen O, Schellinger P, Fiebach J, Hacke W, Sartor K. Early recanalisation in acute ischaemic stroke saves tissue at risk defined by MRI. *Lancet*. 1999;353:2036-2037.

49. Albers GW. Expanding the window for thrombolytic therapy in acute stroke. The potential role of acute MRI for patient selection. *Stroke*. 1999;30:2230-2237.

50. Wolpert SM, Bruckmann H, Greenlee R, Wechsler L, Pessin MS, del Zoppo GJ. Neuroradiologic evaluation of patients with acute stroke treated with recombinant tissue plasminogen activator. The rt-PA Acute Stroke Study Group [see comments]. *Ajnr: American Journal of Neuroradiology*. 1993;14:3-13.

51. Brant-Zawadzki M. Ischemia. In: Stark DD, Bradley WG, eds. *Magnetic resonance imaging*,. St. Louis: Mosby, 1988; 299-315.

52. Johnston KC, Connors AF, Jr., Wagner DP, Knaus WA, Wang X, Haley EC, Jr. A predictive risk model for outcomes of ischemic stroke. *Stroke*. 2000;31:448-455.

53. Hastie T, Tibshirani RJ. *Generalized Additive Models*. New York: Chapman and Hall, 1990.

54. Moseley ME, Kucharczyk J, Mintorovitch J, Cohen Y, Kurhanewicz J, Derugin N, Asgari H, Norman D. Diffusion-weighted MR imaging of acute stroke: correlation with T2-weighted and magnetic susceptibility-enhanced MR imaging in cats. *AJNR Am J Neuroradiol*. 1990;11:423-429.

55. Statistical Sciences. *S-PLUS Guide to Statistical & Mathematical Analysis, Version 3.3*. Seattle: StatSci, a division of MathSoft, Inc., 1995.

56. Jordan MI, Jacobs RA. Hierarchical mixtures of experts and the EM algorithm. *Neural Computation*. 1994;6:181-214.

Chapter 5

Evaluating novel acute stroke therapies with tissue signatures

It's a poor sort of memory that only works backwards.

—Lewis Carroll
(*Through the Looking Glass*)

The use of imaging to assess outcomes in clinical trials remains controversial, even though pre-clinical researchers in experimental models of cerebral ischemia commonly use it as an endpoint. A typical proposed imaging endpoint in stroke investigation is the comparison of infarct volumes between treatment and control groups. However, in humans, due to considerable inter-patient variability in stroke severity and location, large numbers of patients are often necessary in order to detect a statistically significant effect. Since intra-patient variability is presumably lower than the inter-patient variability, statistical power may be increased if one measures change in lesion size from baseline (1). Review of variability data from published studies indicate that when such a compare-to-baseline approach is used for the analysis of acute ischemic stroke, the sample size for detecting a given change can decrease by a factor of 5 or more (2). A logical extension would be to compare individual voxels to their baseline state. Such a method might provide even lower variability and thereby further increase the statistical power for detecting a treatment-related change.

With the advent of new MRI techniques such as diffusion weighted MR imaging (DWI) and perfusion-weighted MR imaging (PWI), early abnormalities can now be detected in the first few hours after the onset of stroke symptoms. Both animal and human imaging have confirmed that these techniques can identify tissue at risk of future infarction (2-12). These novel MR techniques provide information about blood flow, blood volume, metabolic state, and vascular permeability. However, the single best imaging modality for predicting tissue outcome has yet to be defined.

The mismatch between diffusion (DWI) and perfusion weighted imaging (PWI) has been proposed for use as an inclusion criterion in clinical trials because it has been hypothesized to be an imaging surrogate for salvageable tissue (1, 12). This "mismatch", however, is typically between the size of lesion volumes rather than between DWI and PWI values on an individual voxel basis. Due to heterogeneity in both ADC (12-16) and flow values (2, 12, 17, 18) within acute ischemic tissue, volumetric approaches comparing gross differences in DWI and PWI lesion volumes may oversimplify the complex task of assessing tissue viability. A voxel-by-voxel approach may be more sensitive in identifying salvageable tissue on an individual subject basis.

An approach that attempts to incorporate multiple imaging modalities has been termed a tissue signature model; an initial description of such an approach to stroke diagnosis included T2 weighted images and diffusion data (13). Since then, extensions to these models have been developed which incorporate tissue perfusion parameters to evaluate the natural evolution of stroke (19, 20). These models' predictions were validated either by histology in experimental animal models of stroke (20-22) or by follow-up imaging in retrospective human studies (15, 19, 23). They have been shown to be better predictors of infarct volume than using single individual modalities.

By predicting likelihood of infarction, tissue models can be used to evaluate the biological effect of a novel therapeutic agent. By comparing the infarct volume on follow-up imaging studies to the predicted infarct volume from baseline imaging, one can determine whether a treatment reduces the predicted infarct volume and in which areas. Specifically, if initial imaging data indicates that a given area of tissue (or voxel) has a 90% likelihood of proceeding to infarction in the absence of therapy, this indicates that 9 out of 10 times the tissue in that voxel will be

infarcted on follow-up imaging. If such a voxel does not proceed to infarction, it could be a one-in-ten chance occurrence. Alternatively, if hundreds such high-probability-of-infarction voxels do not infarct, that would suggest that tissue deemed likely to infarct based on the natural history of ischemic stroke, may potentially have responded to therapy.

We hypothesize that a novel intervention that reduces the amount of tissue that proceeds to infarction in a dose-dependent manner may result in a modification of the model accuracy. The expected outcome, infarction, may not occur, due to modification of the natural progression of the disease by the novel therapy. Specifically, we hypothesized that an efficacious treatment would produce a reduction in the predictive performance of tissue signature models as a function of effective dose. To test this hypothesis, this chapter examines the positive predictive performance of an extended tissue signature model (19) in a group of patients participating in a dose-escalation phase II study of a neuroprotective agent, basic fibroblast growth factor.

5.1 Preliminary evaluation of basic fibroblast growth factor (bFGF) using predictive tissue models

Subjects and Methods

Patient Enrollment and Treatment

Basic fibroblast growth factor (bFGF) is an 18 kiloDalton, 154 amino acid polypeptide that is found in the brain and has potent trophic effects on brain cells (24). In particular, bFGF protects brain neurons against a variety of toxins and insults, including anoxia, hypoglycemia, excitatory amino acids, free radicals, and nitric oxide, among others (25, 26). Preclinical studies have shown that the intracerebral or intravenous administration of bFGF reduces infarct size in animal models of stroke (27-30). This large protein, administered intravenously, crosses the damaged blood brain barrier to penetrate ischemic brain tissue (27). The mechanism of infarct reduction appears, in part, to depend on upregulation of anti-apoptotic proteins in the ischemic penumbra (31). As a result of these preclinical data, a human clinical safety trial of intravenous bFGF was undertaken.

Sixty-six patients were entered into a phase I/II trial of bFGF, Fiblast ® (Scios Inc., Mountain View, CA), in acute stroke at seven centers. This trial was a double-blind, randomized, placebo-controlled, dose-escalation, three month follow-up study of intravenous infusion of human recombinant bFGF in patients with major thromboembolic ischemic infarction within 12 hours of the onset of symptoms. Each patient or an appropriate family member provided informed consent. All procedures were approved by the hospital's Subcommittee on Human Studies. Patients were randomized to receive a 3-hour intravenous infusion of either placebo or one of six different doses of bFGF ranging from 9 to 150 μg/kg. Eleven patients were enrolled at this institution. Their demographics and lesion volumes are shown in Table 5.1. Four of the eleven patients were excluded due to incomplete acute data sets. Each of the remaining seven patients underwent serial diffusion and perfusion MR imaging prior to treatment according to the protocol described below within the first 12 hours of symptom onset, and follow-up imaging at discharge.

Image Acquisition

For this study, the imaging protocols described in Chapter 4 were followed.

Model Development

A generalized linear model (GLM) of risk of tissue infarction was used to generate estimates of risk of tissue infarction in patients with acute ischemic stroke due to large vessel embolic or thrombotic disease. In GLM models, tissue outcome, P, was modeled as a binary variable (infarcted/not infarcted). The risk of tissue becoming infarcted can then be estimated by the logistic function:

$$P = \frac{1}{1+e^{-\beta x}} \qquad \textbf{(5.1)}.$$

where P is an estimate of the risk of infarction, **x** represents the input vector consisting of the initial diffusion and perfusion imaging data and β is the vector of weighting coefficients for each parameter. The calculation of these coefficients have been described in the previous chapter and was derived from the analysis of acute and follow-up studies in fourteen patients not enrolled in treatment trials or treated with thrombolytic agents. Table 5.2 shows the coefficients used in the analysis in this study.

Table 5.2: Standardized coefficients of the GLM model.

α	rT_2	rADC	rDWI	rCBF	rCBV	rMTT
-11.7	-3.0	5.9	7.1	-1.2	0.05	0.7

The column labeled α term is an intercept term constant for all voxels. The other columns represent the weighting coefficient for each respective parameter.

Maps of the risk of infarction for the seven patients receiving initial DWI and PWI were calculated using coregistered initial data sets and the GLM model. Voxels were classified as likely to infarct if their risk were greater than a prespecified threshold or risk level. The number of voxels that was correctly predicted to infarct (true positives or TP) was counted as well as the number of voxels incorrectly predicted to infarct (false positives or FP). The positive predictive value (PPV) was obtained by calculating the ratio of TP/(TP+FP). The pre-specified risk level was selected based on previously reported results from fourteen patients not enrolled in the bFGF trial (19). From this previous study, the optimal operating point (32) of the GLM algorithm was found to occur at a probability cutoff of 32% assuming equal prevalence of infarcted and non-infarcted tissue voxels and equal costs of false positives and false negatives (19). At this risk threshold, the GLM algorithm achieved 66% sensitivity and 84% specificity. Therefore a risk threshold of 32% was used in this study.

The PPV of the model was calculated for each patient by comparing predicted infarct volume with the lesion volume demonstrated on an axial T2-weighted FSE study acquired prior to

Table 5.1 Patient demographics, bFGF dosage, acute DWI and follow-up (F/U) T2 FSE lesion volumes and NIH Stroke Scale scores at admission and at discharge and 3 month Barthel Index.

Patient	Age/ Sex	Dosage (μg/kg)	Initial Scan (hours)	Follow-up (days)	Initial DWI (cm^3)	F/U T2 (cm^3)	NIH SS (Initial)	NIH SSS (Discharge	Barthel (90-day)
1	68/M	Placebo	9	5	7	6	4	2	100
2	63/M	Placebo	9	6	55	88	9	2	100
3	79/M	9	8	7	18	14	15	5	75
4	80/F	27	9	7	102	207	15	11	35
5	75/F	75	6	4	20	26	6	1	100
6§	58/F	150	7	13	134	289	16	14	100
7§	74/M	150	8	19	25	16	17	12	20
8*	77/M	75	6	8	9	6	4	2	100
9*	41/M	3	3	3	31	52	2	2	(died)
10*	33/M	75	5	5	2	7	4	3	100
11*`	78/M	Placebo	9	7	169	148	18	20	(died)

*Incomplete initial MRI examinations.
§Gradient-echo EPI sequences used for PWI.

discharge. To assess PPV, matching volumes of lesion and "normal" voxels need to be selected. For example, a degenerate algorithm that classified all voxels as infarcted would do well in cases where the lesion volume is greater than the "normal" volume compared to cases with the reverse situation. The performance of the model would then depend on the size of the lesion volume and make interpatient comparisons infeasible. By *a priori* constraining the number of total normal voxels to equal the number of total abnormal voxels, a minimum performance of 50% is obtained in the case of degenerate models regardless of the size of the lesion volume. Follow-up T2 FSE lesion regions of interest for performance evaluation were selected by a neuroradiologist blinded to treatment regimen using a semi-automated image processing software (Alice, Hayden Systems/Parexel, Waltham, MA). For patients with very large infarcts (for example, greater than 100 cc) where the number of abnormal voxels was greater than the number of normal voxels in the ipsilateral hemisphere, in order to reduce without bias the number of abnormal voxels, care was taken to limit the lesion to areas that did not appear abnormal on the initial T2 scan. This was under the assumption that tissue already demonstrating T2 prolongation was likely already infarcted and therefore would not benefit from a neuroprotective agent. A matching number of non-infarcted voxels were selected in areas surrounding the lesion in the ipsilateral hemisphere that appeared normal in the follow-up T2 FSE.

Endpoints

Preliminary clinical efficacy was measured using change in NIH Stroke Scale score (NIH SSS) measured at admission compared to that reported at discharge. Patients were classified with an improved outcome if the NIHSSS decreased by more than four points. 2×2 contingency tables were computed for the placebo versus the bFGF treated patients and a two-sided Fisher's Exact test performed. $P<0.05$ was considered significant.

We first sought to correlate the dose of bFGF with total size of follow-up lesion volumes, a traditional imaging endpoint. Lesion volumes were selected and measured in the coregistered acute DWI and T2 follow-up using a semi-automated image processing software package (Alice, Hayden Systems/Parexel, Waltham, MA). Follow-up lesion volumes were plotted as a function of dose and linear regression performed to determine if a significant trend existed. We performed similar dosage analysis for percent change between initial DWI lesion volume and follow-up lesion volume. The dose of bFGF was also correlated with the positive predictive value of the GLM generated risk maps. Pearson's product-moment correlation was used to determine existence of correlation between the outcome variables and dosage level ($P<0.05$).

Results

None of the traditional outcome measures, clinical or imaging, were statistically significant most likely because of the wide variability in lesion volume and location, as well as the range of initial NIHSS scores in these seven patients (NIHSSS = 4 to 17, see Table 5.1). As shown in Table 5.3 and Table 5.4, there is a trend towards improved NIH SSS change in the bFGF treated patients compared to control for both the total eleven patients and the seven patients subset, but the trend is not significant ($P=1$). As shown in Figure 5.1 and Table 5.1, analysis of the volumetric measurement of lesion size at discharge for all eleven patients ($R=0.19$ $P=0.58$) or for the seven patient subset ($R=0.34$ $P=0.45$) as a function of dosage level also preclude drawing any statistically valid conclusions. In addition, as shown in Figure 5.2, assessment of the change of lesion volume from baseline DWI to follow-up for all eleven patients ($R=0.13$ $P=0.71$) or seven-

patient subset (R=0.12 P=0.8) also fail to demonstrate any statistically significant trends. This is again likely because of the small sample size. Furthermore, the trends in these figures suggest that with increasing dosage, the patients' lesion volumes grow.

Figure 5.3 summarizes the PPV for the seven-patient subset who had received acute DWI and PWI studies. A probability threshold of 32% risk was used for classifying abnormal and normal tissue. The PPV of the model decreases as the dosage increases (R=0.38 P=0.4) suggestive of a dose-dependent effect of bFGF. Statistical significance was not found again most likely due to the small number of patients used in this study.

Table 5.3: 2x2 Contingency table based on improved outcome for eleven patients.

	ΔNIH SSS ≥ 4	ΔNIH SSS < 4
Treated	4	4
Placebo	1	2

Table 5.4: 2x2 Contingency table based on improved outcome for subset of 7 patients used in GLM analysis.

	ΔNIH SSS ≥ 4	ΔNIH SSS < 4
Treated	4	1
Placebo	1	1

Figure 5.4 shows the GLM risk map for a patient randomized to receive placebo (Patient 2). The top row shows a subset of the input data to the model. The top row shows the predicted map overlaid on the initial DWI image. From the figures, one sees that the amount of tissue predicted to go onto infarction correlates well with the six-day follow-up lesion volume.

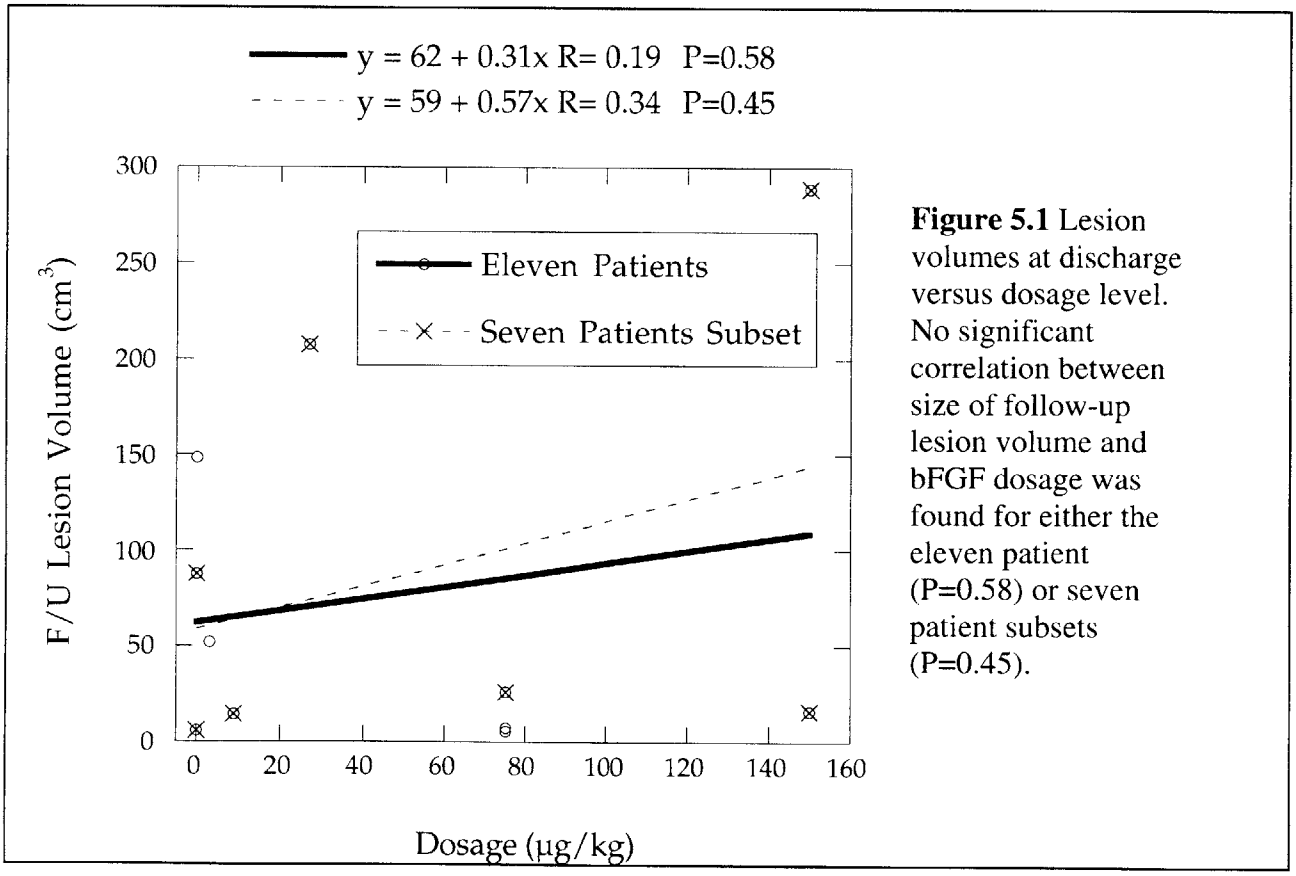

Figure 5.1 Lesion volumes at discharge versus dosage level. No significant correlation between size of follow-up lesion volume and bFGF dosage was found for either the eleven patient (P=0.58) or seven patient subsets (P=0.45).

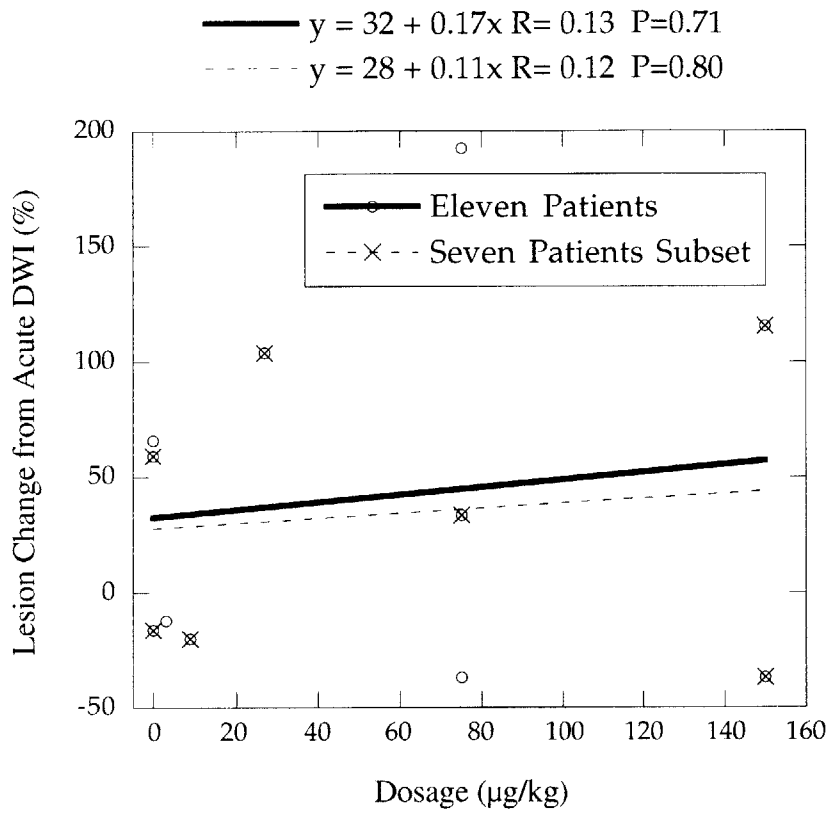

Figure 5.2 Percent change between initial DWI and follow-up lesion volumes. No significant trend was found between change in lesion volume as a function of dosage for either the eleven patient (P=0.71) or seven patient subset (P=0.80).

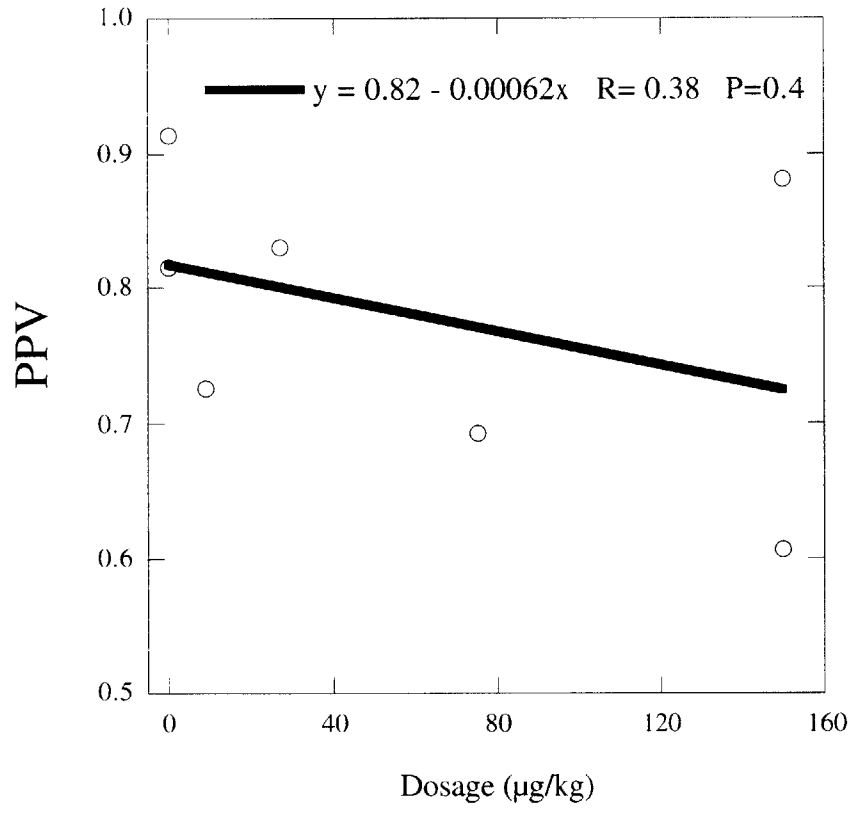

Figure 5.3: The PPV of GLM for bFGF treated patients versus dosage at a risk threshold of 32%. A downward linear trend (R=0.38 P=0.4) was found between increased dosage and PPV.

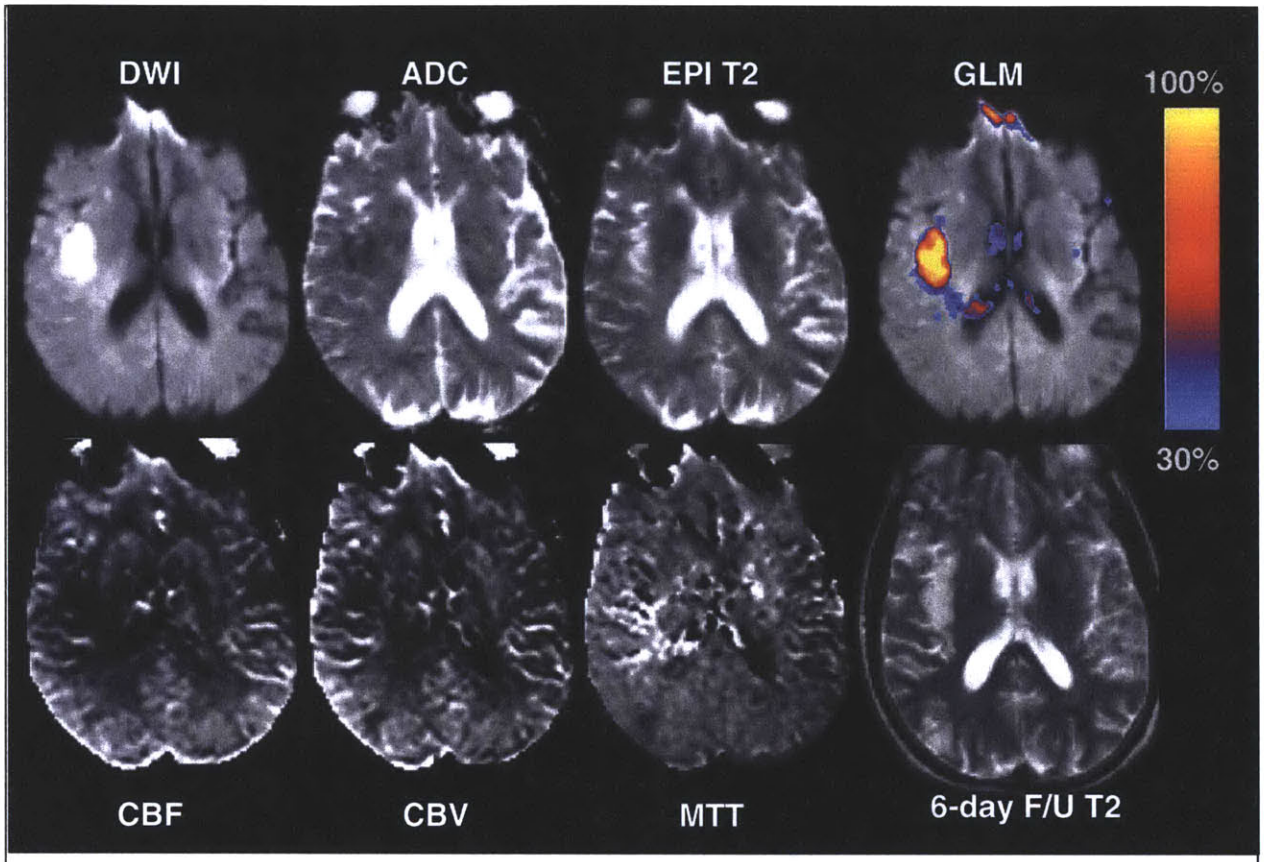

Figure 5.4 GLM input and output for a placebo patient imaged 9 hrs after onset of symptoms. The top row shows the predicted risk of infarction using only acute imaging data. For clarity, only voxels with greater than 30% risk of becoming infarcted are overlaid on the initial DWI. One can observe the good correlation of the area predicted to go on to infarction with the six-day follow-up T2 FSE.

Figure 5.5 shows the predicted risk map of infarction for Patient 7 who had been randomized to receive the full-dose of bFGF. One sees from the risk map an area at high risk of infarction which correlates to the initial DWI abnormality. However, the blue region surrounding the red "core" represents an area at risk of infarction that does not infarct as can be seen by the 19-day follow-up FLAIR. In this case, the GLM predicted a large area at risk of becoming infarcted that ultimately appears to have been salvaged. Despite the positive imaging outcome, the patient's clinical outcome, as determined by his 90-day Barthel Index of 20, was poor (see Table 5.1).

In comparison, Figure 5.6 shows the predicted risk map of infarction for Patient 6, who also had been randomized to receive the full dose of bFGF. For this patient, the predicted risk correlates well with the follow-up infarct volume. The PPV for this patient was 88% compared to 61% for Patient 7. However, unlike Figure 5.5, there does not appear to be a substantial region of tissue that is at lower risk of infarction (blue) than the initial DWI lesion. This suggests that there may have been very little tissue that would be able to respond to therapy. Interestingly, this patient had a favorable clinical outcome with a 90-day Barthel Index of 100, despite a larger lesion volume at discharge.

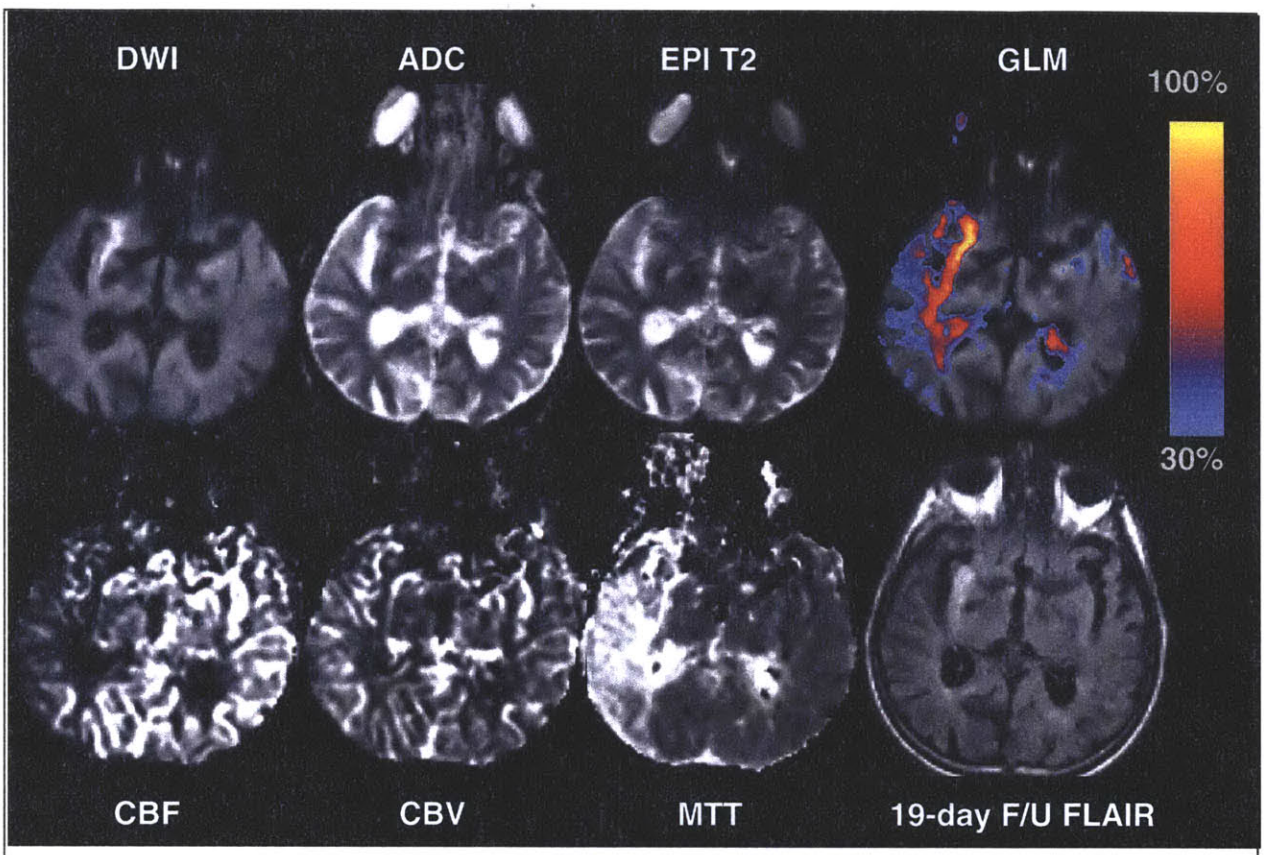

Figure 5.5 GLM input and output for Patient 7 who received 150 μg/kg of bFGF. The top row shows a much larger predicted infarct volume than what was demonstrated in the follow-up FLAIR.

Discussion

Our results confirm earlier studies that showed that diffusion and perfusion MRI in the hyperacute stage can reflect tissue at risk of infarction (2, 8, 16, 19, 33). Our results are also consistent with earlier demonstrations of a correlation between clinical outcome and imaging (8, 16, 17, 33-35). These results confirm that predictive models of tissue outcome can be constructed capturing the natural history of cerebral ischemia into a "risk map" (13, 19). We extend these earlier findings by applying a statistical predictive model of tissue outcome as a measure of treatment efficacy in the setting of a neuroprotective agent, and show that neuroprotective efficacy can be suggested with a small group of subjects.

Our results are clearly preliminary and therefore the conclusions that can be drawn are quite limited. Nevertheless, we speculate that using each patient's baseline study as his/her own control on a voxel-by-voxel basis shows increased statistical power compared to traditional endpoints and may show treatment efficacy even in a small group of subjects. We speculate that the primary reason for this increased statistical power is the reduction in variability that accrues from using each voxel as its own control. While imaging has been suggested as a surrogate endpoint

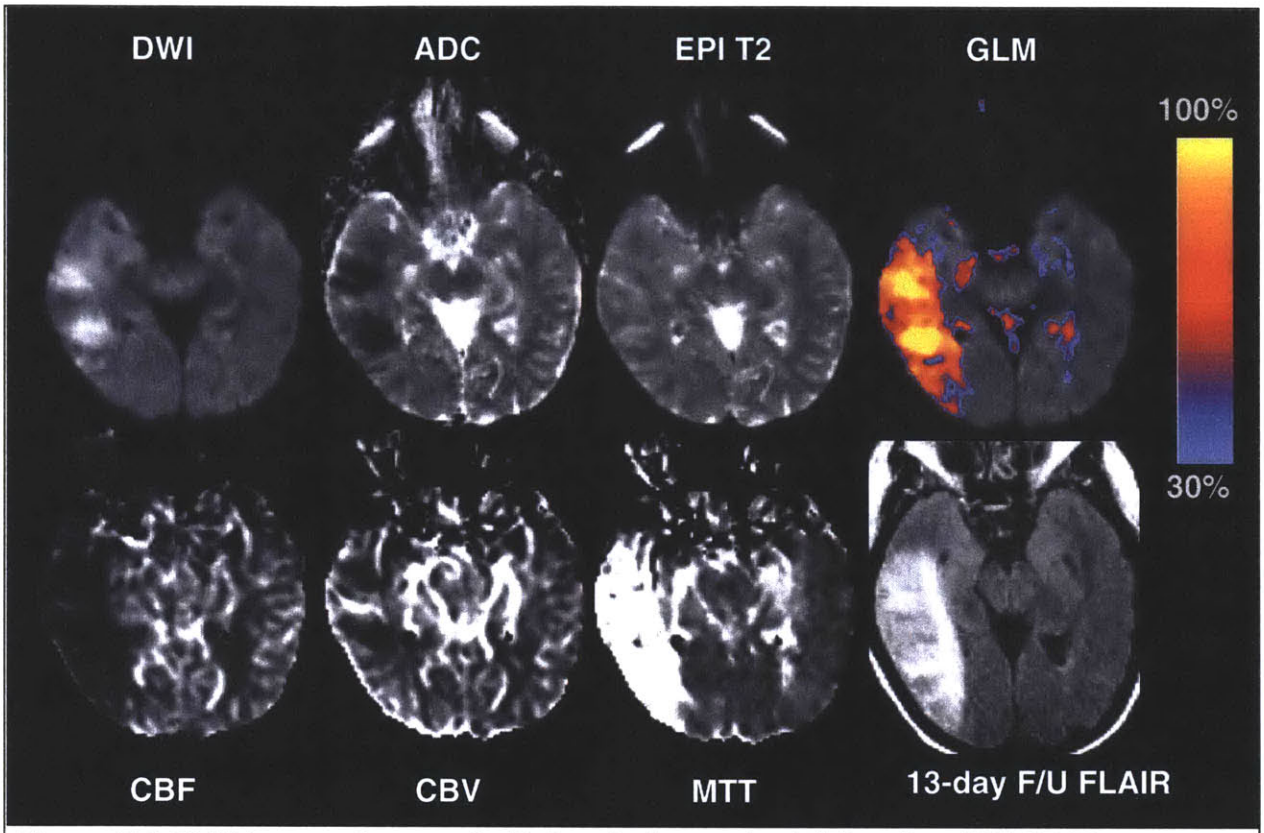

Figure 5.6 GLM input and output for Patient 6 who received 150 μg/kg of bFGF. The top row shows a much predicted infarct volume that matches well with the follow-up FLAIR. Unlike Figure 5.5, there does not appear a region of lower at risk of infarction tissue (blue areas) suggesting there may be little tissue that would respond to therapy.

for stroke trials in numerous studies, (8, 36-39), typically the endpoint is lesion volume size either on an absolute basis or occasionally in a change-from-baseline basis. Unlike pre-clinical stroke models in animals, where considerable effort has been expended to control as many variables as possible to generate reproducible lesions, in human stroke, the size of the lesion and its natural evolution can be highly variable. Perhaps due to the effects of stroke location and co-morbid factors, the high variability in lesion size between patients detracts in the ability of these volumetric techniques to detect differences based on treatment assignment.

Our results also suggest that MRI may be useful for testing biological hypotheses even in a small group of subjects. In the present case, the biological hypothesis was that bFGF reduces infarct size in humans. Such a hypothesis is well founded, since studies in animal models have shown that bFGF reduces infarct volume (27-30). Our results did not reach statistical significance due to the limited number of sample points, especially at the highest dosage level. However the trend of reduced positive predictive value as a function of dosage level may be an indication that bFGF in some manner may have modified the natural history of the disease in this patient. The recovery of tissue at intermediary values of risk is suggestive of some therapeutic efficacy of bFGF for non-irreversibly damaged tissue.

From a clinical imaging perspective, our findings suggest that "risk maps" indicating areas of tissue at risk of infarction can be created and used. This may be useful for consumers of imaging who are often faced with a variety of imaging techniques but who may not have time or ability to sort through the many different images that functional MRI can produce. Risk maps may therefore provide an objective quantitative method for *a priori* selecting regions of tissue for investigation in serial studies. Further studies where signature maps are applied retrospectively to select patients who will optimally benefit from therapy are awaited to test this hypothesis.

Nonetheless, our model has several important limitations. First, it cannot address safety issues; many neuroprotective agents appear to be effective in animals and even in humans, but have adverse safety profiles in humans. Safety can only be addressed through clinical testing. In fact, the phase III clinical trial of bFGF in North America was discontinued in 1999 due to significant drug side effects (40, 41). However, in the European trial, no significant side effects were reported and a small trend towards efficacy was reported using one third of the projected patients recruited (42, 43). Correlation of our model's results with traditional clinical endpoints has yet to be demonstrated. Despite the clear potential of such imaging techniques to identify promising therapies with small numbers of patients, we do not advocate that imaging be used as a sole clinical trial endpoint. Indeed, a preliminary study has shown that although a therapy may be effective in preserving brain tissue, it may not be effective in preserving functionality (44). One or more full-scale phase III clinical trials using traditional clinical endpoints will be needed before efficacy can be truly established. However, numerous unsuccessful phase III trials for acute cerebral ischemia have been performed (45, 46), and it is possible that imaging may rapidly identify inefficacious therapies while still in phase I or phase II.

Another limitation of our method is that the patient database that we used to train the generalized model is restricted to infarction resulting from large vessel occlusion. A more appropriate approach might be to use a group of patients from the placebo arm of a randomized clinical trial to perform the training of the extended tissue signature model, thus guaranteeing similarity between the placebo and the treatment arms. Furthermore, our model does not indicate the reason why tissue predicted to infarct does not. For example, in our training data, there were cases where the predicted signature map overestimated the lesion volume on follow-up MRI, as shown in Figure 4.1.4. In this case, it was determined that early spontaneous reperfusion occurred (< 14 hrs from symptom onset) which led to the over-determination of predicted lesion volume. Similarly, the reduction in PPV in the present study might be attributed to early spontaneous reperfusion. However, the observed trend towards dose-dependent reductions of PPV makes this possibility less likely. The decrease in PPV with increasing dose allows us to speculate that the bFGF played a role in decreasing infarct growth via a neuroprotective effect, rather than an all-or-nothing reperfusion effect. We speculate that such neuroprotective effects would be evident with clinical outcome measures if an appropriate sample size were used, assuming no safety issues were present.

Furthermore, the failure of our models to demonstrate a statistical significant effect may be in the selection of our metric, PPV, which used an *a priori* cutoff of 32% to classify infarcted and non-infarcted tissue. Indeed, it may be that a better use of the results of the GLM, which is a continuous variable, would be to take advantage of the continuous variable associated with each volume of tissue's risk of infarction. For example, from the predicted risk of infarction for Patient 6 shown in Figure 5.6, one observes very little salvageable tissue as compared to Patient 7 shown

in Figure 5.5 as indicated by regions of lower risk of infarction (blue). Therefore, one can speculate that a better hypothesis to test would be that tissue at moderate risk levels, as reflected by the predicted risk map, would have their outcome affected by intervention. Future studies that exploit this information are eagerly anticipated.

5.2 Conclusions

Although our results are clearly preliminary, they indicate the usefulness of MRI-based modeling techniques as an outcome measure. By using a change from baseline approach, we may be able to compensate for intrinsic patient and intralesional intervoxel variability. While further testing is clearly needed, our results imply that if this modeling approach is validated, efficacy determination might be possible using smaller numbers of patients than is required using traditional means. Such an assessment model could allow more rapid screening in smaller groups of patients, and thereby speed the development and evaluation of effective therapies for acute cerebral ischemia.

5.3 References

1. Stroke Therapy Academic Industry Roundtable II (STAIR-II). Recommendations for Clinical Trial Evaluation of Acute Stroke Therapies. *Stroke*. 2001;32:1598-1606.

2. Sorensen AG, Copen WA, Ostergaard L, Buonanno FS, Gonzalez RG, Rordorf G, Rosen BR, Schwamm LH, Weisskoff RM, Koroshetz WJ. Hyperacute stroke: simultaneous measurement of relative cerebral blood volume, relative cerebral blood flow, and mean tissue transit time. *Radiology*. 1999;210:519-527.

3. Moseley ME, Cohen Y, Mintorovitch J, Chileuitt L, Shimizu H, Kucharczyk J, Wendland MF, Weinstein PR. Early detection of regional cerebral ischemia in cats: comparison of diffusion and T2 weighted MRI and spectroscopy. *Magn Reson Med*. 1990;14:330-346.

4. Warach S, Chien D, Li W, Ronthal M, Edelman RR. Fast magnetic resonance diffusion-weighted imaging of acute human stroke. *Neurology*. 1992;42:1717-1723.

5. Chien D, Kwong KK, Gress DR, Buononno FS, Buxton RB, Rosen BR. MR diffusion imaging of cerebral infarction in humans. *AJNR Am J Neuroradiol*. 1992;13:1097-1102.

6. Warach S, Wielopolski P, Edelman RR. Identification and characterization of the ischemic penumbra of acute human stroke using echo-planar diffusion and perfusion imaging. *12th Annual Meeting of the Society of Magnetic Resonance in Medicine*, New York, NY 1993; 249.

7. Warach S, Gaa J, Siewert B, Wielopolski P, Edelman R. Acute human stroke studied by whole brain echo planar diffusion-weighted magnetic resonance imaging. *Ann Neurol*. 1995;37:231-241.

8. Warach S, Dashe JF, Edelman RR. Clinical outcome in ischemic stroke predicted by early diffusion-weighted and perfusion magnetic resonance imaging: A Preliminary Analysis. *J Cereb Blood Flow Metab*. 1996;16:53-59.

9. Sorensen AG, Buonanno FS, Gonzalez RG, et al. Hyperacute stroke: Evaluation with combined multisection diffusion-weighted and hemodynamically weighted echo-planar MR imaging. *Radiology*. 1996;199:391-401.

10. Baird AE, Benfield A, Schlaug G, Siewert B, Lovblad KO, Edelman RR, Warach S. Enlargement of human cerebral ischemic lesion volumes measured by diffusion-weighted magnetic resonance imaging. *Ann Neurol*. 1997;41:581-589.

11. Lutsep HL, Albers GW, DeCrespigny A, Kamat GN, Marks MP, Moseley ME. Clinical utility of diffusion-weighted magnetic resonance imaging in the assessment of ischemic stroke. *Ann Neurol*. 1997;41:574-580.

12. Baird AE, Warach S. Magnetic resonance imaging of acute stroke. *J Cereb Blood Flow Metab*. 1998;18:583-609.

13. Welch KMA, Windham J, Knight RA, Nagesh V, Hugg JW, Jacobs M, Peck D, Booker P, Dereski MO, Levine SR. A model to predict the histopathology of human stroke using diffusion and T2-weighted magnetic resonance imaging. *Stroke*. 1995;26:1983-1989.

14. Nagesh V, Welch KMA, Windham JP, Patel S, Levine SR, Hearshen D, Peck D, Robbins K, D'Olhaberriague L, Soltanian-Zadeh H, Boska MD. Time course of ADCw changes in ischemic stroke: Beyond the Human Eye! *Stroke*. 1998;29:1778-1782.

15. D'Olhaberriague L, Welch KMA, Nagesh V, Gymnopoulos C, Mansbach HH, Hugg JW, Boska MD, Knight RA, Schultz LR, Levine SR, Chopp M. Preliminary clinical-radiological assessment of a MR tissue sigature model in human stroke. *J Neurol Sci*. 1998;156:158-166.

16. Schwamm LH, Koroshetz WJ, Sorensen AG, Wang B, Copen WA, Budzik R, Rordorf G, Buonanno FS, Schaefer PW, Gonzalez RG. Time course of lesion development in patients with acute stroke: Serial diffusion- and hemodynamic-weighted magnetic resonance imaging. *Stroke*. 1998;29:2268-2276.

17. Neumann-Haefelin T, Wittsack HJ, Wenserski F, Siebler M, Seitz RJ, Modder U, Freund HJ. Diffusion- and perfusion-weighted MRI. The DWI/PWI mismatch region in acute stroke. *Stroke*. 1999;30:1591-1597.

18. Schlaug G, Benfield A, Baird AE, Siewert B, Lovblad KO, Parker RA, Edelman RR, Warach S. The ischemic penumbra: operationally defined by diffusion and perfusion MRI. *Neurology*. 1999;53:1528-1537.

19. Wu O, Koroshetz WJ, Ostergaard L, Buonanno FS, Copen WA, Gonzalez RG, Rordorf G, Rosen BR, Schwamm LH, Weisskoff RM, Sorensen AG. Predicting tissue outcome in acute human cerebral ischemia using combined diffusion- and perfusion-weighted MR imaging. *Stroke*. 2001;32:933-942.

20. Carano RA, Li F, Irie K, Helmer KG, Silva MD, Fisher M, Sotak CH. Multispectral analysis of the temporal evolution of cerebral ischemia in the rat brain. *J Magn Reson Imaging.* 2000;12:842-858.

21. Knight RA, Dereski MO, Helpern JA, Ordidge RJ, Chopp M. Magnetic resonance imaging assessment of evolving focal cerebral ischemia. Comparison with histopathology in rats. *Stroke.* 1994;25:1252-1261; discussion 1261-1252.

22. Jacobs MA, Zhang ZG, Knight RA, Soltanian-Zadeh H, Goussev AV, Peck DJ, Chopp M. A model for multiparametric mri tissue characterization in experimental cerebral ischemia with histological validation in rat: part 1. *Stroke.* 2001;32:943-949.

23. Jacobs MA, Mitsias P, Soltanian-Zadeh H, Santhakumar S, Ghanei A, Hammond R, Peck DJ, Chopp M, Patel S. Multiparametric MRI tissue characterization in clinical stroke with correlation to clinical outcome: part 2. *Stroke.* 2001;32:950-957.

24. Baird A. Fibroblast growth factors: activities and significance of non- neurotrophin neurotrophic growth factors. *Curr Opin Neurobiol.* 1994;4:78-86.

25. Mattson MP, Murrain M, Guthrie PB, Kater SB. Fibroblast growth factor and glutamate: opposing roles in the generation and degeneration of hippocampal neuroarchitecture. *J Neurosci.* 1989;9:3728-3740.

26. Mattson MP, Lovell MA, Furukawa K, Markesbery WR. Neurotrophic factors attenuate glutamate-induced accumulation of peroxides, elevation of intracellular Ca2+ concentration, and neurotoxicity and increase antioxidant enzyme activities in hippocampal neurons. *J Neurochem.* 1995;65:1740-1751.

27. Fisher M, Meadows ME, Do T, Weise J, Trubetskoy V, Charette M, Finklestein SP. Delayed treatment with intravenous basic fibroblast growth factor reduces infarct size following permanent focal cerebral ischemia in rats. *J Cereb Blood Flow Metab.* 1995;15:953-959.

28. Tatlisumak T, Takano K, Carano RA, Fisher M. Effect of basic fibroblast growth factor on experimental focal ischemia studied by diffusion-weighted and perfusion imaging. *Stroke.* 1996;27:2292-2297; discussion 2298.

29. Ren JM, Finklestein SP. Time window of infarct reduction by intravenous basic fibroblast growth factor in focal cerebral ischemia. *Eur J Pharmacol.* 1997;327:11-16.

30. Ay H, Ay I, Koroshetz WJ, Finklestein SP. Potential usefulness of basic fibroblast growth factor as a treatment for stroke. *Cerebrovasc Dis.* 1999;9:131-135.

31. Ay I, Sugimori H, Finklestein SP. Basic fibroblast growth factor (bFGF) decreases DNA fragmentation and increases bcl-2 expression following stroke in rats (abstr.). *Stroke.* 2000;31:282.

32. Halpern EJ, Albert M, Krieger AM, Metz CE, Maidment AD. Comparison of receiver operating characteristic curves on the basis of optimal operating points. *Acad Radiol.* 1996;3:245-253.

33. Tong DC, Yenari MA, Albers GW, O'Brien M, Marks MP, Moseley ME. Correlation of perfusion- and diffusion-weighted MRI with NIHSS score in acute (6.5 hour) ischemic stroke. *Neurology.* 1998;50:864-870.

34. Barber PA, Darby DG, Desmond PM, Yang Q, Gerraty RP, Jolley D, Donnan GA, Tress BM, Davis SM. Prediction of stroke outcome with echoplanar perfusion- and diffusion-weighted MRI. *Neurology.* 1998;51:418-426.

35. Beaulieu C, de Crespigny A, Tong DC, Moseley ME, Albers GW, Marks MP. Longitudinal magnetic resonance imaging study of perfusion and diffusion in stroke: evolution of lesion volume and correlation with clinical outcome. *Ann Neurol.* 1999;46:568-578.

36. Lovblad KO, Baird AE, Schlaug G, Benfield A, Siewert B, Voetsch B, Connor A, Burzynski C, Edelman RR, Warach S. Ischemic lesion volumes in acute stroke by diffusion-weighted magnetic resonance imaging correlate with clinical outcome. *Ann Neurol.* 1997;42:164-170.

37. Chua MG, Davis SM, Infeld B, Rossiter SC, Tress BM, Hopper JL. Prediction of functional outcome and tissue loss in acute cortical infarction. *Arch Neurol.* 1995;52:496-500.

38. Saver JL, Johnston KC, Homer D, Wityk R, Koroshetz W, Truskowski LL, Haley EC. Infarct volume as a surrogate or auxiliary outcome measure in ischemic stroke clinical trials. The RANTTAS Investigators. *Stroke.* 1999;30:293-298.

39. Warach S, Pettigrew LC, Dashe JF, Pullicino P, Lefkowitz DM, Sabounjian L, Harnett K, Schwiderski U, Gammans R. Effect of citicoline on ischemic lesions as measured by diffusion-weighted magnetic resonance imaging. Citicoline 010 Investigators. *Ann Neurol.* 2000;48:713-722.

40. Stroke Trials Directory. *Trafermin in acute ischemic stroke Fiblase Phase 3.* 2001;

41. Clark W, Schim J. Trafermin in acute stroke: results of a phase II/III randomized efficacy study. *Neurology.* 2000;54:A88.

42. Bogousslavsky J, Donnan G. Fibroblast (Trafermin) in acute stroke: results of the European-Australian phase II/III safety and efficacy trial. *Cerebrovasc Dis.* 2000;10:1-116.

43. Ay I, Ay H, Koroshetz WJ, Finklestein SP. Growth Factors and Cerebral Ischemia. In: Fisher Marc, Bogousslavsky Julien, eds. *Current Review of Cerebrovascular Disease*,. Fourth Philadelphia: Current Medicine, Inc., 2001; 25-33.

44. Reese T, Porszasz R, Baumann D, Bochelen D, Sauter A, Rudin M. Mismatch between infarct size and functional deficit in rat middle cerebral artery occlusion model of stroke:

cytoprotective treatment does not preserve brain function (abstr). *Proc Intl Soc Mag Reson Med Eighth Scientific Meeting*, Denver, CO 2000; 280.

45. De Keyser J, Sulter G, Luiten PG. Clinical trials with neuroprotective drugs in acute ischaemic stroke: are we doing the right thing? *Trends Neurosci.* 1999;22:535-540.

46. Muir KW, Grosset DG. Neuroprotection for acute stroke: making clinical trials work. *Stroke*. 1999;30:180-182.

Chapter 6

Conclusions

"Would you tell me, please, which way I ought to go from here?"

"That depends on where you want to get to," said the Cat.

"I don't much care where—" said Alice.

"Then it doesn't matter which way you go," said the Cat.

"—so long as I get *somewhere*," Alice added as an explanation.

"Oh, you're sure to do that," said the Cat, "if you only walk long enough."

—Lewis Carroll
(*Alice's Adventures in Wonderland*)

This dissertation extended and improved existing stroke imaging techniques to aid in the identification of tissue at risk of infarction, thereby furthering the ultimate goal of identifying and treating salvageable tissue. Chapter 2 extended techniques for imaging tissue status whereas Chapter 3 improved techniques for measuring perfusion status, both critical parameters in the assessment of tissue viability. Chapter 4 introduced a promising new framework for *in vivo* quantification of tissue viability in humans through the use of tissue risk maps where each voxel of tissue is given a probability value of risk of infarction based on its acute imaging studies. Chapter 5 demonstrated the potential of this new technique for evaluating novel therapies in a clinical trial setting since it is the means for evaluating changes in baseline risk of infarction on an individual voxel basis. Chapters 2 and 3 are linked to Chapters 4 and 5 in that all extend current imaging techniques for identifying tissue at risk of infarction with greater specificity and sensitivity on an individual voxel basis. This chapter summarizes the main findings in the previous chapters and suggests avenues for future investigations.

Chapter 2 extended diffusion weighted imaging in acute stroke patients to diffusion tensor imaging in order to gain insight into the brain's ultrastructure not assessable with measurements of mean diffusivity alone. Reductions in anisotropy were found in the core of infarcted DWI lesions (1) whereas elevations and preserved anisotropy were observed within reversible DWI lesions. We therefore speculate that anisotropy shows promise as a marker of salvageable tissue. This hypothesis remains to be proved with additional studies involving therapeutically treated patients that may lead to the better discrimination of reversibly from irreversibly injured tissue.

However, given that reversible ADC lesions are rare events (2), an alternate approach may be to evaluate changes in anisotropy in serial studies of patients demonstrating mismatches in diffusion and perfusion lesion volumes, which have been speculated to represent salvageable tissue. Serial studies which characterize ADC and FA evolution on an individual voxel basis in the area of mismatch may provide additional insight over previous volumetric based approaches (3, 4) due to the known temporal heterogeneity of ADC evolution (5, 6) and spatial heterogeneity of FA even in normal subjects (7). Techniques which takes into consideration white and gray matter differences may also better characterize anisotropy and ADC changes in acute stroke.

The foci of Chapter 2 were anisotropy and mean diffusivity changes in hyperacute stroke. Additional insight may be gained by investigating changes in the individual eigenvalues and eigenvectors in hyperacute stroke patients, for which both anisotropy and ADC are functions of. However, this evaluation can be complicated by noise where the principal eigenvector directions may change if reductions of diffusion show an orientation preference, e.g. along the principal eigenvector resulting in greatest reduction in the principal eigenvalue. Additional numerical simulations of anisotropic tissue would be needed to provide clarification of this complex interaction between noise and resulting bias from sorting of eigenvalues (8).

Chapter 3 improved current perfusion imaging techniques by providing a more robust method for estimating *in vivo* perfusion indices by decoupling delay-related flow biases from truly reduced flow that is less likely to benefit from therapy. This has important clinical implication in that it may aid in better discrimination of tissue with oligemic flow from ischemic flow. This in turn may lead to better understanding of the pathophysiological events underlying the ischemic process and ultimately better identification of salvageable tissue in human cerebral ischemia. This thesis demonstrates the possible confounding of results and underestimation of flow values

if delays in tracer arrival are not taken into consideration. The proposed delay-insensitive refinement using deconvolution with a block-circulant matrix may provide additional insight into the nature of the diffusion and perfusion mismatch, which given this study's findings may be delay-related. Monte Carlo simulation results and qualitative evaluation of human stroke patients suggest that the sensitivity of existing CBF and MTT measurements may be more due to differences in tracer arrival time than to hypoperfusion. This may explain why existing MTT maps have been found to be not specific identifiers of infarcted tissue (9). To further examine the accuracy of the relative flow measurements in the new technique as compared to the current SVD technique, it may be fruitful to compare values from both techniques to those measured using PET. Previous studies have shown a close correlation between PET and the existing technique but they have been in either normal volunteers (10) and normal pigs (11) or in acute stroke pigs (12) where tracer delay may not be as severe as in human cases.

It may be argued, however, that identifying vascular territory that is downstream from an occlusion, and hence, area that is at risk of infarction, may be desired over identifying only ischemic tissue that may no longer be therapeutically treatable. Additional studies remain to be performed to determine if there is a clinical benefit using delay-insensitive flow indices coupled with delay maps over delay-weighted CBF and MTT maps. The clinical results presented here are clearly preliminary and additional studies involving a larger cohort of patients are necessary to better determine the accuracy of new technique. We anticipate retrospective analysis of perfusion studies with follow-up MRIs can be performed where lesion volumes identified by the new and current techniques are evaluated and compared for sensitivity and specificity.

Chapter 4 introduced a novel framework for acutely assessing the risk of tissue infarction, by combining multiple diffusion and perfusion imaging parameters into a single index of risk. We showed that algorithms combining diffusion and perfusion information predict the risk of infarction with greater sensitivity and specificity than algorithms using diffusion and perfusion parameters separately. Of the combined algorithms studied, statistical maps of risk of infarction was the preferred approach due to their potentially greater ease of interpretation with their single indices of risk and greater sensitivity and specificity trade-off. We presented several different approaches ranging from a simple generalized linear model (GLM), to a non-parametric generalized additive model (GAM) and to a hierarchical mixture of experts (HME). Each of these techniques tried to compensate for limitations of simpler techniques. GLMs sought to provide a single index for risk of infarction as a continuous variable. GAMs took into consideration the non-linear behavior of diffusion and perfusion values. HMEs tried to compensate for variations in anatomy. The small number of patients and large variability in lesion volume outcome involved in this study limited the ability to demonstrate statistical significance between techniques. Nonetheless, even in our small patient population of fourteen patients, GAMs performed significantly better than GLMs and HMEs performed significantly better than GLMs when training with data not constrained to user outlined regions. With additional studies that include larger cohorts of patients in the training and evaluation of models, improved predictive models with greater sensitivity and specificity may be attained.

One of the advantages of these statistical models whose output is the risk of infarction is the ease by which additional parameters can be added to the model. The models do not assume any *a priori* physiological relevance to any of the input parameters. This in turn makes adding parameters straightforward. The parameters presented in Chapters 2 and 3 can therefore be

incorporated in future models. One of the limitations of the existing training data is that three of the fourteen patients were not acquired with full diffusion tensor imaging. In future investigations, we speculate that incorporation of anisotropy will aid in the discrimination of white from gray matter and therefore lead to better performance in the HME based models. With the new perfusion algorithms, greater specificity may be perhaps reached with greater import to CBF values than currently assigned due to its lack of specificity. Inclusion of delay maps may also be found a useful parameter. One may even be able to compare the new and current perfusion analyses algorithms for identifying tissue at risk of infarction by comparing the sensitivity and specificity of statistical models derived from their calculated parameters. Advances in development of models and of new applications are eagerly anticipated.

Statistical based tissue signatures, however, already show promise as techniques for not only predicting the natural evolution of ischemic damage but also for evaluating the effects that novel therapies may have on this process as our findings in **Chapter 5** suggest. Despite the limited number of patients involved in a preliminary study, a trend towards efficacy of a neuroprotective agent, basic fibrinogen growth factor, was found as a function of dosage, demonstrating the feasibility of using signature maps in clinical trials to evaluate the response of individual patients to therapy. We speculate that using each patient's baseline study as his/her own control on a voxel-by-voxel basis increased statistical power compared to traditional clinical endpoints and compared to change-from-baseline lesion endpoints and may show treatment efficacy even in a small group of subjects. We speculate that the primary cause for this increased statistical power is the reduction in variability that accrues from using each voxel in each patient as its own control thereby taking into account both interpatient and intervoxel variability.

For this initial study, however, we did not take advantage of the fact that the output of our models were continuous variables and used an *a priori* cutoff of 32% (13) for classifying infarcted from non-infarcted tissue, thereby obfuscating the gradations of risk our models provide. We speculate that a better approach would be to compare the risk of infarction after therapy to before in treated and control patients. This analysis could be further refined by limiting the analysis to tissue whose baseline risk of infarction was moderate and therefore more likely to respond favorably to therapy.

In conclusion, although much more remains to be done, the overall results of this dissertation demonstrate that imaging can be used to identify tissue at risk of infarction, which may aid diagnosis and prognosis by providing clinicians unique insight into the underlying pathophysiology of stroke.

References

1. Sorensen AG, Wu O, Copen WA, Davis TL, Gonzalez RG, Koroshetz WJ, Reese TG, Rosen BR, Wedeen VJ, Weisskoff RM. Human acute cerebral ischemia: detection of changes in water diffusion anisotropy by using MR imaging. *Radiology*. 1999;212:785-792.

2. Grant PE, He J, Halpern EF, Wu O, Schaefer PW, Schwamm LH, Budzik RF, Sorensen AG, Koroshetz WJ, Gonzalez RG. Frequency and clinical context of decreased apparent diffusion coefficient reversal in the human brain. *Radiology*. 2001;221:43-50.

3. Zelaya F, Flood N, Chalk JB, Wang D, Doddrell DM, Strugnell W, Benson M, Ostergaard L, Semple J, Eagle S. An evaluation of the time dependence of the anisotropy of the water diffusion tensor in acute human ischemia. *Magn Reson Imaging*. 1999;17:331-348.

4. Yang Q, Tress BM, Barber PA, Desmond PM, Darby DG, Gerraty RP, Li T, Davis SM. Serial study of apparent diffusion coefficient and anisotropy in patients with acute stroke. *Stroke*. 1999;30:2382-2390.

5. Nagesh V, Welch KMA, Windham JP, Patel S, Levine SR, Hearshen D, Peck D, Robbins K, D'Olhaberriague L, Soltanian-Zadeh H, Boska MD. Time course of ADCw changes in ischemic stroke: Beyond the Human Eye! *Stroke*. 1998;29:1778-1782.

6. Schwamm LH, Koroshetz WJ, Sorensen AG, Wang B, Copen WA, Budzik R, Rordorf G, Buonanno FS, Schaefer PW, Gonzalez RG. Time course of lesion development in patients with acute stroke: Serial diffusion- and hemodynamic-weighted magnetic resonance imaging. *Stroke*. 1998;29:2268-2276.

7. Pierpaoli C, Jezzard P, Basser PJ, Barnett A. Diffusion Tensor MR Imaging of the Human Brain. *Radiology*. 1996;201:637-648.

8. Pierpaoli C, Basser PJ. Toward a Quantitative Assessment of Diffusion Anisotropy. *Magnetic Resonance in Medicine*. 1996;36:893-906.

9. Sorensen AG, Copen WA, Ostergaard L, Buonanno FS, Gonzalez RG, Rordorf G, Rosen BR, Schwamm LH, Weisskoff RM, Koroshetz WJ. Hyperacute stroke: simultaneous measurement of relative cerebral blood volume, relative cerebral blood flow, and mean tissue transit time. *Radiology*. 1999;210:519-527.

10. Østergaard L, Johannsen P, Host-Poulsen P, Vestergaard-Poulsen P, Asboe H, Gee AD, Hansen SB, Cold GE, Gjedde A, Gyldensted C. Cerebral blood flow measurements by magnetic resonance imaging bolus tracking: comparison with [(15)O]H2O positron emission tomography in humans. *J Cereb Blood Flow Metab*. 1998;18:935-940.

11. Østergaard L, Smith DF, Vestergaard-Poulsen P, Hansen SB, Gee AD, Gjedde A, Gyldensted C. Absolute cerebral blood flow and blood volume measured by magnetic resonance imaging bolus tracking: comparison with positron emission tomography values. *J Cereb Blood Flow Metab*. 1998;18:425-432.

12. Sakoh M, Rohl L, Gyldensted C, Gjedde A, Ostergaard L. Cerebral blood flow and blood volume measured by magnetic resonance imaging bolus tracking after acute stroke in pigs: comparison with [(15)O]H(2)O positron emission tomography. *Stroke*. 2000;31:1958-1964.

13. Wu O, Koroshetz WJ, Ostergaard L, Buonanno FS, Copen WA, Gonzalez RG, Rordorf G, Rosen BR, Schwamm LH, Weisskoff RM, Sorensen AG. Predicting tissue outcome in acute human cerebral ischemia using combined diffusion- and perfusion-weighted MR imaging. *Stroke*. 2001;32:933-942.